The University of Nottingham
UNITED KINGDOM · CHINA · MALAYSIA

Nottingham Centre for Geomechanics

Physical Model Tests and Numerical Simulation for Assessing the Stability of Tunnels

Han-Mei Chen

Thesis submitted to The University of Nottingham

For the degree of Doctor of Philosophy

July 2014

This thesis is dedicated to

my grandma, my parents and my husband.

ABSTRACT

Nowadays, numerical modelling is increasingly used to assess the stability of tunnels and underground caverns. However, an analysis of the mechanical behaviour of existing brick-lined tunnels remains challenging due to the complex material components.

One promising approach is to carry out a series of small-scale physical tunnel model tests representing the true behaviour of a prototype under extreme loading in order to validate and develop the corresponding numerical models. A physical model test is advisable before any field study, which might be dangerous and costly. During the tests, advanced monitoring techniques such as the laser scanning and photogrammetry would be used to register tunnel deformation and lining defects. This investigation will show how these may substitute or supplement the conventional manual procedures.

Simultaneously, numerical models will be developed, primarily using FLAC and UDEC software, to simulate the physical models after comparing their results. In this way, numerical simulations of physical models would be achieved and verified. These numerical models could then be applied to the field study in the future research, enabling accurate prediction of the actual mechanical behaviour of a masonry tunnel, in combination with advanced monitoring techniques.

ACKNOWLEDGEMENTS

Firstly, I am heartily grateful to my supervisor Prof. Hai-Sui Yu and Dr. Martin Smith who continuously support and encourage me throughout this research project. I am greatly indebted to them whose guidance was invaluable to me.

I would also like to cherish the memory of my supervisor Dr. David Reddish who passed away for his academic guidance and care. Without him, I would not be able to enjoy my work as I am. I would also like to express my gratitude to the senior experimental officer Dr. Nikolaos Kokkas and the former research fellow Dr. Philip Rowsell for their advice and assistance on my research.

I am thankful to all technicians working in the Nottingham Centre for Geomechanics and the laboratory of Civil Engineering for providing their assistance throughout the experimental work.

Finally, my sincere thanks go to my family members and friends who always supporting me during the PhD course in The University of Nottingham, UK.

TABLE OF CONTENTS

CHAPTER 1 INTRODUCTION

1.1 Challenges

Most railway tunnels made of brickworks in UK were built decades ago; some are even over a hundred years old. They are subjected to degradation such as spalling, perished mortar and loose bricks during their service life. Tunnels can also be subjected to ground stresses, which could cause severe deformation and damage to the tunnel brickwork support. Degradation and tunnel deformation are major threats to the tunnel's durability and can lead to a collapse if not controlled. It is noted that this project is concentrated on the study of railway tunnels, especially their brickwork supports.

Therefore, it is important that the stability and deterioration of these tunnels be assessed by regular/frequent monitoring work. There are also benefits (such as cost, life expectancy and so on) by building numerical models to analyse and predict the mechanical behaviour of long-term tunnels before serious problems occur.

Tunnel monitoring has predominantly been a manual procedure, which is time-consuming and subjective, giving rise to variance in the standards and quality of examination.

Although several numerical modelling approaches to old tunnel masonry structures have been proposed (Idris, 2008 and 2009), the modelling and the mechanical behaviour analysis of existing brick-lined tunnels remain challenging due to the complex material components.

1.2 Aim

The overall aim of the PhD research is to assess the stability of brick-lined tunnels through physical and numerical modelling.

1.2.1 Objectives

1) Review of existing problems with brick-lined tunnels and methods for maintaining and monitoring the condition of the tunnels;
2) Investigate the stability of small-scale physical models of brick-lined tunnels. Advanced monitoring techniques will be used to investigate;
3) Investigate the use of numerical modelling of brick-lined tunnels;
4) Assess, analyse and evaluate physical modelling and numerical simulation;
5) Assess the stability of brick-lined tunnels through the two approaches used.

1.2.2 Methodology

The methodology adopted for the project is as follows:

1) Literature review is undertaken to develop understanding and background knowledge (Objective 1);
2) Laboratory trials are designed, experiments performed are to fulfill objective 2;
3) Numerical simulation using FLAC and UDEC performed is to match the physical lab trials (Objective 3);
4) Advanced monitoring techniques are used to compare with traditional approaches;
5) Results from 2), 3) and 4) are produced and analysed, comparisons are made;
6) Conclusion are drawn.

This can be explained by Figure 1.1.

It is noted that these physical model tests are not required to replicate the real tunnels with various conditions, but should provide similar boundary and loading conditions, which are easily measured and assessable.

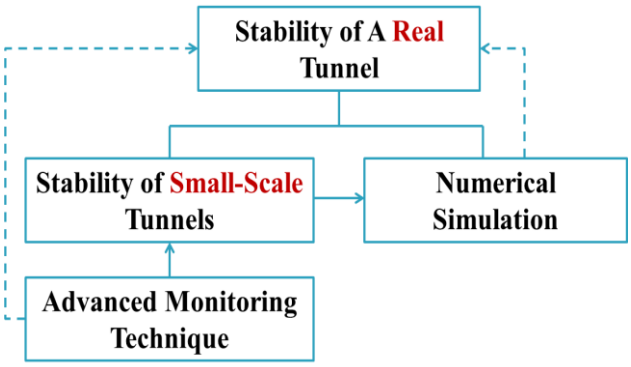

Figure 1.1 The methodology of the overall research

1.3 Structure of the thesis

The thesis consists of five chapters.

Chapter 1 introduces the current problems associated with tunnel stability. The main objectives and an outline of the report are also presented.

Chapter 2 reviews tunnel stability concerns, including tunnel instability phenomena and their causes, permanent linings as structure support and maintenance, etc. In addition, different existing monitoring methods have been proposed, followed by an outline of various numerical simulation approaches and their characteristics as well as brickwork properties. The modelling of tunnel masonry structures, multi-ring masonry arch bridges and masonry building structures has also been reviewed.

Chapter 3 reports a series of small-scale physical tunnel models which have been designed, prepared and tested, including the post-processing and analysis of monitoring equipment, as well as the loading process of the physical models.

Chapter 4 demonstrates the modelling of the physical model, by both FLAC and UDEC software, for the application of the finite difference method and distinct element method respectively. The accuracy of the numerical models using these two methods has been verified by the physical model results produced and reported in Chapter 3 as part of the research, A comprehensive parametric analysis is used to identify the influence of both stiffness and strength parameters in the relevant numerical procedures. Initially, a programme of material testing in the laboratory has been conducted as a reference to the numerical modelling.

Chapter 5 draws the conclusions of the work and proposes potential future research directions in both physical model tests and numerical simulations.

CHAPTER 2 LITERATURE REVIEW

2.1 Introduction

This literature reviews tunnel stability concerns, existing problems with brick-lined tunnels and methods for maintaining and monitoring the condition of the tunnels. Furthermore, tunnel masonry structures and their properties have been reviewed, followed by an outline of various numerical simulation approaches, as well as the numerical modelling of tunnel masonry structures, multi-ring masonry arch bridges and masonry building structures.

2.2 Stability concerns of tunnels

2.2.1 Terminology in tunnelling

The various locations on the tunnel cross-section are denoted by the indicated names, as Figure 2.1 shows.

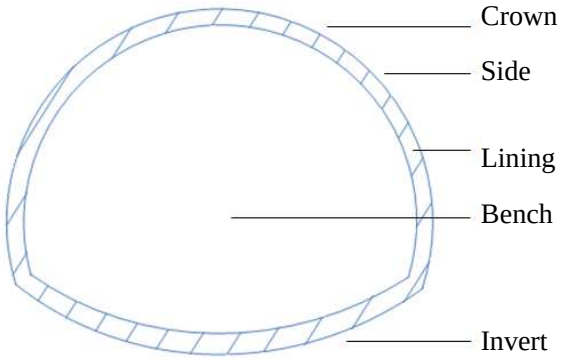

Figure 2.1 Parts of a tunnel cross-section (Kolymbas, 2005)

Other terms defined below are also useful in this research.

Transverse direction: in the horizontal plane, normal to the axis of the tunnel.

Longitudinal direction: in the direction of the tunnel axis.

Profile: the shape of a tunnel cross section, such as circular, rectangular, mouth or horseshoe.

Tunnel heading: the workface at the front of the tunnel where soil excavation is being made (NG et al., 2004).

2.2.2 Permanent linings

1) Introduction

Linings (permanent) are always expected in soft ground tunnels and are often used in rock tunnelling. They play a crucial role in the stability of tunnels and are constructed for several reasons (Megaw et al., 1981):

a) To provide sufficient structural support
b) To eliminate or reduce water ingress or seepage
c) To provide an internal surface and accommodate the operational tunnel profile

2) Structural support

After the excavation of a tunnel, the initial stable equilibrium of the ground is disturbed and stress redistribution starts to take place. With the addition of support structures, a new stress pattern will be set up.

The need for support depends on the actual conditions. In soft, plastic ground, the development of hydrostatic pressure makes it essential to build up support to carry the whole overburden pressure. In homogeneous rock, structural support seems to be unnecessary; an arching action of stress will develop efficiently to support the tunnel.

The timing of the support construction is critical to restrain any deformation that may cause collapse. It is largely judged by working experience associated with the ground properties. The stress redistribution after support construction would establish a new and stable equilibrium.

3) Operational tunnel profile

The shape of a tunnel profile usually depends on the ground conditions and the operational function of the tunnel.

An arch is ideal to support pressure and is widely used for the tunnel roof. The tunnel profile might be completed with vertical sidewalls to form a horseshoe, a whole circle or an ellipse.

The horse-shoe cross section often appears in railways. In these tunnels, the development of lateral stress requires a lining to carry loads. The sidewalls need to be anchored at the toe, where the stresses are largely concentrated.

The structural advantage of the circular form is the ability to endure loads from all directions in the ground. Thus, this form is usually adopted for the carrying of water or sewage, excavated by a shield machine or a full-face machine. Other forms, such as rectangular design are normally used in highway tunnels.

4) Principal materials for permanent lining

For bored tunnel linings, the principal materials are (Megaw et al.,1981):

a) Concrete
   - In situ concrete

- Sprayed concrete
- Segmental rings of precast concrete

b) Cast-iron and steel
   - Segmental rings of bolted cast-iron
   - Segmental linings of welded steel

c) Brickwork and masonry

In situ concrete

Concrete placed in situ is designed to accommodate any shape of cross section on an extensive scale. It is also ideal for the filling of the overbreak after excavation and unbounded voids between the lining and the raw tunnel surface. Using a travelling shutter behind the working face, concrete is cast in time for tunnel support.

Sprayed concrete

Combined with rock bolts, steel arches or mesh reinforcement, sprayed concrete is widely utilised nowadays. It plays an essential role in the New Austrian Tunnelling Method (NATM), whose principle is to control the development of stresses and deflections as well as their interaction with lining supports.

Segmental rings of precast concrete

All circular segmental rings provide an immediate supporting structure of great strength and useful flexibility. The principal design and dimensions of cast-iron and precast concrete segments are similar. Compared with cast-iron segments, the cost of materials and fabrication of precast concrete segments is much less. Furthermore, the superior rigidity of precast concrete segments enables them to endure damage during

handling and jacking as well as after erection. Therefore, precast concrete segments have become the first major substitute for segmental linings of cast-iron.

Segmental rings of bolted cast-iron

The circular shape is mostly used for cast-iron segments, whereas an ellipse form is sometimes adopted in sewers. Cast-iron has adequate compressive strength but relatively low tensile strength and is brittle. When used in circular tunnel rings, most of the ground loadings are direct compressive stresses with few tensile stresses and bending moments.

Segmental linings of cast-iron seem to perform better in terms of water tightness and operational convenience than those of precast concrete.

Segmental linings of welded steel

Steel material is not widely used in the world of segmental linings. Because of the extra strength in tension and bending, it is sometimes utilised in cases of abnormal loadings imposed by adjacent structures etc. The corrosion resistances in the ground for steel and cast-iron are similar.

Brickwork and masonry

Neither brickwork nor masonry is still employed as the structural lining material of a tunnel today. This is in contrast to the early railway age, around the nineteenth century, when most British railway tunnels were built with bricks that had often been manufactured on site. The term ‘English method’ refers to alternating excavation and timbering with bricklaying in brick-lined tunnel construction.

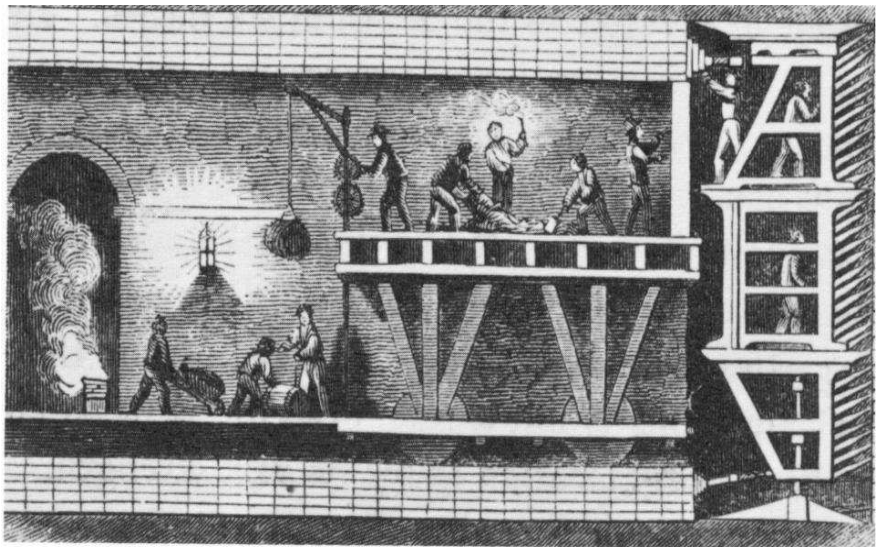

Figure 2.2 Diagram of the tunnelling shield used to construct the Thames Tunnel (Wikipedia, 2013)

In 1818, Sir Marc Isambard Brunel patented a tunnelling shield inspired by the shipworm. Workers worked in separate compartments of a reinforced shield of cast iron, digging at the tunnel-face. Periodically, the shield could be driven forward by large jacks and the opened tunnel surface behind it could be covered with cast iron lining rings (see Figure 2.2).

Brunel's invention provided the basis for subsequent tunnelling shields and it was used to build his greatest achievement ‘the Thames Tunnel’, completed in 1842 and remaining in use today as part of the London Underground System.

As the shield moved forward, bricklayers followed and lined the walls. The tunnel required over 7,500,000 bricks. (Wikipedia, 2013)

For most existing tunnels, such as railway and sewer tunnels more than 100 years old, maintenance is the most important issue. The repair of these linings may range from

re-pointing, local replacement of bricks to reconstruction that is more expensive (Megaw, 1981).

2.2.3 Hazards

1) General introduction

Tatiya (2005) defined the term ‘Hazard’ as danger, risk. It is the potential to cause losses/harm to man, machine, equipment, property assets or the environment, or a combination of these.

Figure 2.3 shows the classification of hazards, whereby hazards are divided into two groups: natural and man-made.

Excavation and underground operations are full of hazards as they are fighting against nature. Hazards could easily turn into disasters with massive injuries, fatalities and significant loss of possessions. Efforts can be made to minimise or even eliminate some of them (Tatiya, 2005).

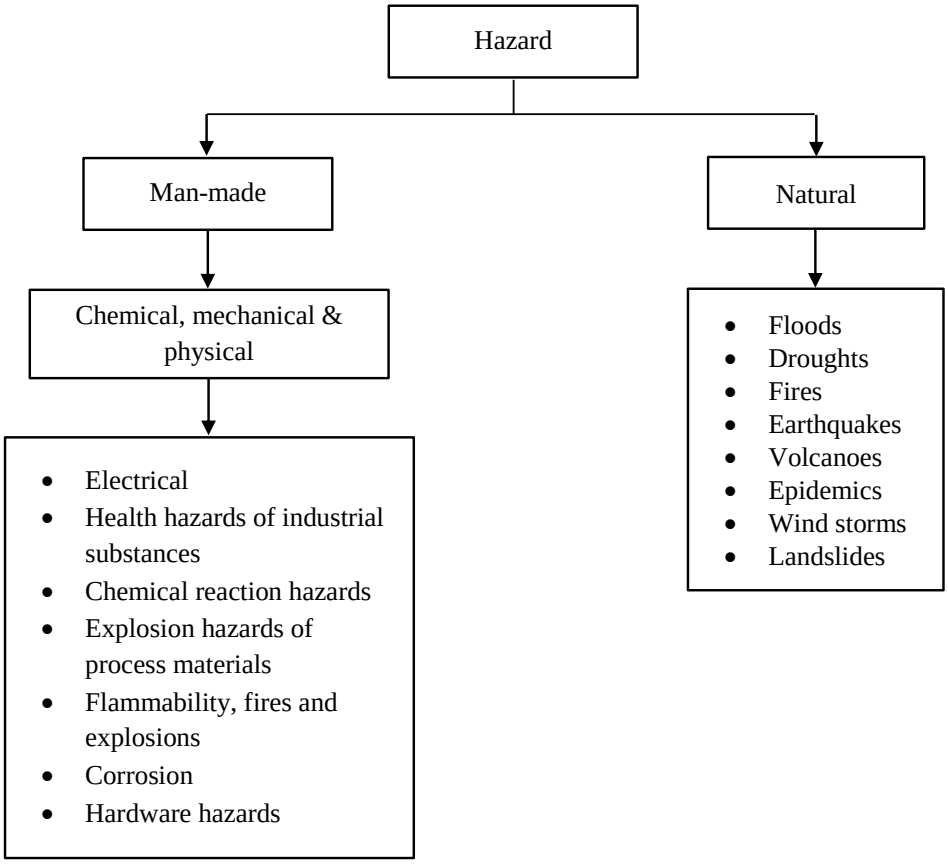

Figure 2.3 Classification of hazards (Tatiya, 2005)

2) Instability

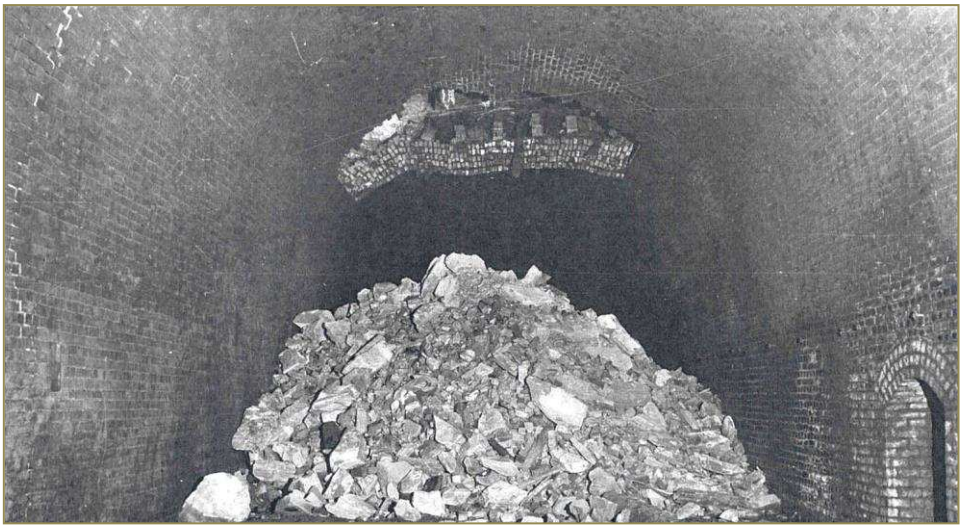

Figure 2.4 The collapse of Duckmanton Tunnel (1959) (Courtesy of Network Rail Ltd.)

One of the biggest hazards in tunnels is the instability phenomenon. It consists of five primary categories: tunnel collapses (as seen in Figure 2.4), disorders, convergences, differential settlements and floods (Idris et al., 2008).

3) Tunnel ageing phenomenon

As time goes by, physical, chemical and biological processes develop inside the masonry structure of the tunnel, which may lead to a series of instability problems and tunnel hazards.

4) Disorder

As one of the five primary categories of tunnel instability phenomena (Idris et al., 2008), disorder refers to deterioration and damage in tunnels, which is proved to be strictly correlated with the ageing phenomenon. It includes longitudinal or transverse structural cracks, convergence and partial masonry collapse. Some common disorder phenomena in brick-lined tunnels are shown here:

Lining distortions

Figure 2.5 A typical tunnel deformation (Courtesy of Geodetic System Ltd.)

A typical distortion of lining can be seen in Figure 2.5.

Linings, subject to large external loads in different positions, can lead to various deformations, with compression and tension experienced at certain sections (see Figure 2.6).

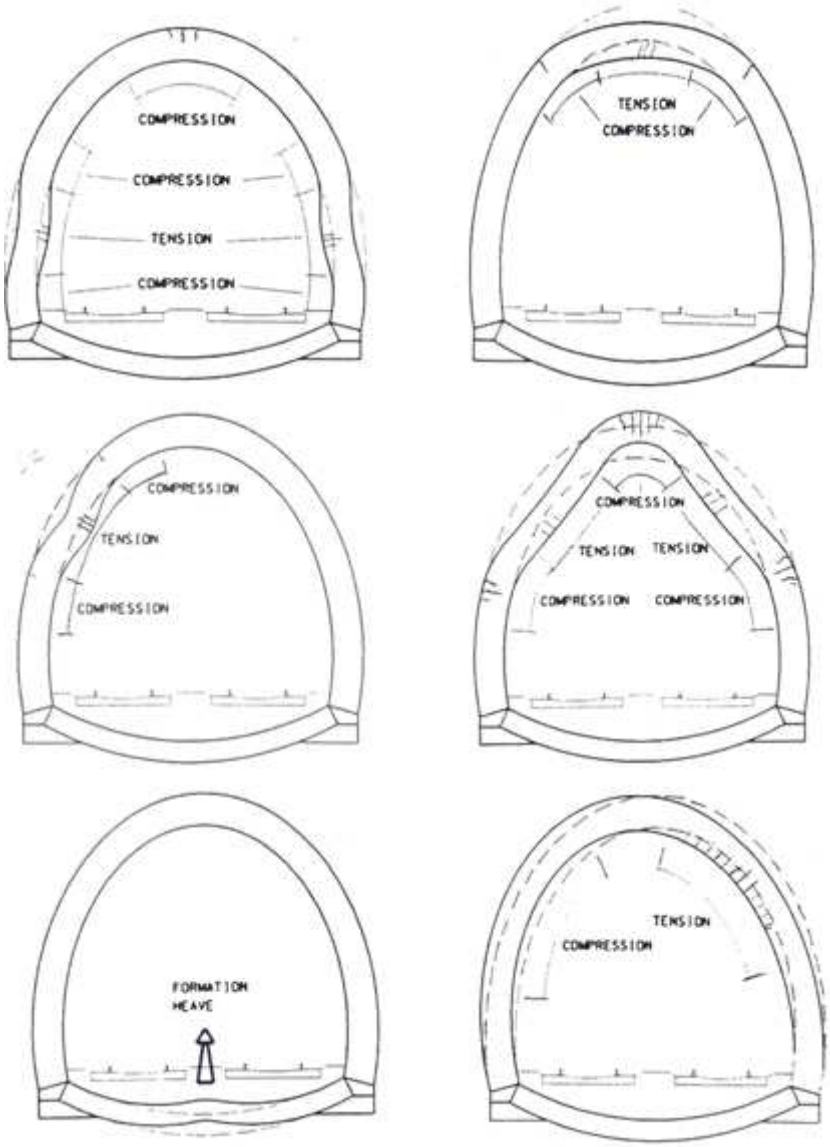

Figure 2.6 Types of lining deformation (Courtesy of Network Rail Ltd.)

Spalling of the surface

Spalling means the breaking away of fragments from the surface of a wall (Lenczner, 1972). It usually happens in brickwork tunnels and results from the action of sulphurous fumes and water on the jointing material (see Figure 2.7). In such linings, with a large number of mortar joints and bricks from different batches, it is

impossible to ensure a uniform quality of all bricks and mortars. Therefore, spalling is often local and brings about some patchy areas after maintenance.

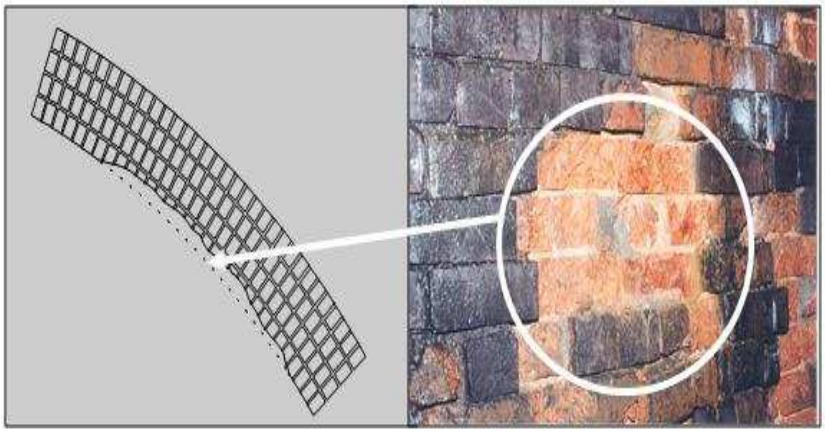

Figure 2.7 The phenomenon of spalling (Courtesy of Network Rail Ltd.)

Ring separation

The term '*Ring separation'* is the phenomenon when patched repairs in outer layers of bricks subsequently fail when tunnels move and deform. Most tunnels in the UK were built a long time ago. Their linings (made of brickwork in the past) have been subject to years of patch repairs. In many cases, the lining part is not in close contact with the main body of a tunnel. Thus, ring separation is likely to occur as shown in Figure 2.8.

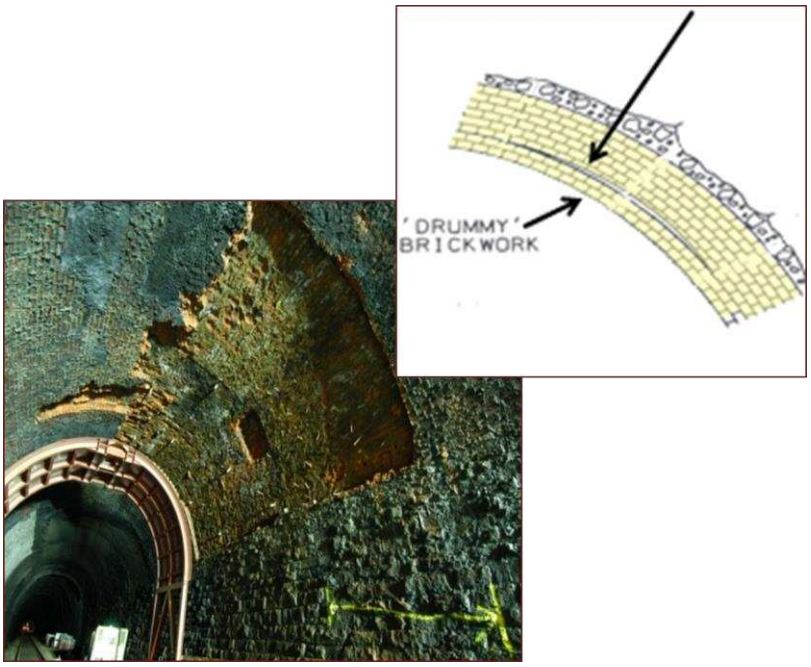

Figure 2.8 The phenomenon of ring separation (Courtesy of Network Rail Ltd.)

Open joints and the loosening of bricks

Figure 2.9 Open joints and weathered mortar (Courtesy of Network Rail Ltd.)

This is caused by the loss of mortar in two extreme ways. Dry conditions or weathering could transform the mortar into powder which then falls out; excessively damp conditions might wash the mortar out (see Figure 2.9).

Cracking

Figure 2.10 Cracks between bricks and mortars (Courtesy of Network Rail Ltd.)

Cracks are mostly likely to develop through changes due to external loads, which could be observed at the portals and recesses in the linings (see Figure 2.10). Cracks seem to be perpendicular to the tunnel axis if there are any changes in the loads or in the cross-section. Alternatively, longitudinal cracks parallel to the tunnel axis may appear along the crown or the spring line. The immediate cause of these cracks is unexpected excessive loads.

Cracks may also develop along the bottom of the tunnel walls, indicating the settlement of the foundations. Short cracks indicate local overstress, defects in the lining materials or poor workmanship.

One of the inspections is to monitor the size changes of cracks over a given time. Traditionally, the cracks' ends and widths are marked. As such, any changes in length and width could be measured between markers. (Széchy, 1967)

5) Causes of disorders in tunnels

For unlined tunnels, disorders result from loose pieces of rock due to blast or vibration from locomotives. If rock falls, it may damage or obstruct the track or cause injury to personnel.

For tunnels with lining support, the main disorders are lining distortions, cracks and spalling on the tunnel lining.

There are some major causes of disorders in tunnels:

Deterioration due to defective materials and construction methods

Old building materials like soft sandstone and limestone with marl have a much lower resistance to water, frost, smoke and atmospheric pollution than modern high strength and well compacted concrete.

Poor construction methods and workmanship can also result in later deterioration. Particularly in the past, the tunnel lining was not built up immediately against the excavated ground face and voids between them were poorly grouted or left ungrouted.

Deterioration caused by water

The influence of water damage in tunnels is enormous which could damage tunnels in different ways.

Even clean and unpolluted water could dissolve some chemicals, leading to trouble. For instance, the carbonate and chloride content (CO_3^{2-}, Cl^-) could invade the

concrete and metal structural supports and the sulphate content (SO_4^{2-}) may attack the concrete, the cement mortar or the lime in some lining joints.

One physical hazard from water is a softening action on the surrounding cohesive materials, which causes a reduction in strength and an increase in compressibility. For example, excessive settlement could occur as a result of the softening of the ground under the walls, accompanied by tunnel distortion and cracks in the arch.

In railway tunnels, the most severe damage results from another physical effect of water. The water resulting from frost would affect not only the quality of the lining but also that of the railway tracks, partly through the formation of icicles (as water dripping on the rails and freezing up) and partly through the freezing of the ballast, which is less elastic and creates unpredictable, uneven support conditions. These may cause broken rails and derailed trains. Short tunnels suffer more from frost, particularly near the portals.

Damage due to smoke

Smoke is significantly dangerous to iron members. A large amount of sulphur dioxide (SO_2) is the product of combustion from steam or diesel locomotives and it greatly accelerates the corrosion of iron in a damp atmosphere. Furthermore, SO_2 in smoke, accompanied by water, gives rise to acid attack on cement and lime.

Damage caused by overburden

The most dangerous overburden form is the actual overburden pressure in deep tunnels. Deformations and cracks due to actual overburden pressures are likely to occur in limestone and clay marl tunnels.

Tunnel portals are subjected to significant additional pressure because of progressive weathering and the sliding of the nearby supported slopes (Széchy, 1967).

6) Collapses

Collapse, a major tunnelling instability, is often reported by prior deformation, cracks, tunnel lining spalling and ground subsidence. Another cause of collapse is the crossing of undetected weak zones, e.g. faults, discontinuity of rock slopes or old shafts filled with loose, cohesionless materials and water. Many collapses can be avoided by installing additional supports such as rockbolts (Kolymbas, 2005).

Table 2.1 clearly shows some of the incidents of tunnel collapse to have occurred over the centuries in Britain.

Table 2.1 Incidents of tunnel collapse through the centuries (Courtesy of Network Rail Ltd.)

Example of Tunnel Collapses:	
Abernant - in 1870's	Poor construction, not solid backed, ground movement
Black-Boy - 1865	Collapse – train ran into it – voids above – dynamic impact
Betchworth - 1887	Unfavourable ground – fine running sand - inadequate lining
St Katherine's - 1895	Water formed cavity above crown, rotted timbers, brick ring fell
Dove Holes - 1872	Heavy rain, landslip, train hit collapsed tunnel section, several injured
Bramhope - 1854	Train hit fallen rock/masonry from roof, uncoupled & caused crash
Cockett - 1899	Dewatering mine below, crushing crown bricks, 600Tonne collapse
Bradway - 1922	Filled shafts collapsed into tunnel – rainstorm – single skin brick lining
LUL - 1922	Tunnel enlargement, wet area of ground, temp works disturbed by train
Cofton - 1928	Poor construction, uneven loading, works taking place, 4 dead 3 injured
Clifton Hall - 1953	Shaft Collapse – 2 fatalities – houses above collapsed
Duckmanton - 1959	Crown Collapse – voids above - dynamic impact
Penmanshiel - 1979	Geology / Overloaded Lining – during works – 2 killed
Strood - 2002	Chalk Fall – Unlined section – train de-railment
Gerrard's Cross - 2005	Collapse during construction

2.2.4 Regular inspection

The crucial work before maintenance is regular inspection for two reasons (Kolymbas, 2005):

1) Examination of design work

Certain measurements after construction should be executed to compare the results with the designed one. If there is a large discrepancy between predicted and measured values, revised constructions should be added, according to the tunnel conditions.

2) Indication of incoming hazards

Conventionally, certain inspectors and engineers carry out a series of major inspection schemes on a yearly basis manually. Regular inspection has been proved to be an efficient means of identifying potential hazards, e.g. damage and collapses. The lining part needs to be examined primarily.

2.2.5 Maintenance

A great number of British railway tunnels were built nearly 100 years ago; some are even older. Over this long period, tunnels have suffered from the frequent vibration of passing trains and a continuous smoky atmosphere, causing deterioration of the structures, e.g. the inner surface of the lining.

In the UK, few new railway tunnels are currently under construction. Therefore, the major work on tunnels is largely concerned with maintenance. For those brick-lined tunnels with inherently weak bricks, some maintaining methods are listed:

1) Spalling of the surface

The usual solution is to cut out the total defective area and substitute with new bricks. More advanced and efficient ways are proposed such as guniting, using a mixture of cement, sand and water to spray on the spalling surface under pneumatic pressure.

2) Open joints and the loosening of bricks

Repointing could make up for the defects. Grouting could provide another solution under appropriate conditions.

3) Cracking and bulging

Minor cracks can be pasted with plaster. Larger cracks need to be monitored over a period. If there are no further signs of an increase, these cracks could be closed to avoid more damage (Széchy, 1967).

2.2.6 Summary

Permanent linings are primarily proposed as the structural supports in most tunnels. Next, instability phenomena in tunnels, particularly lining disorders due to the ageing phenomenon, are introduced in this section. Some maintenance methods follow.

2.3 Tunnel monitoring methods

2.3.1 General introduction

There are some conventional and progressive non-destructive measuring methods to monitor tunnel distortions and convergence, as well as the existing state of lining. The details of these approaches are introduced in the following sections.

2.3.2 Monitoring tunnel distortions and convergence

By setting a series of target points and monitoring them at regular times, the internal profile of the tunnel could be observed. The deformation status of the profile could be obtained by comparing the previous profile with the current one.

1) Conventional contact measuring methods

The monitoring of convergence is usually carried out with the help of pins (target points) fixed on the tunnel wall soon after the excavation. Conventionally, the distance between pins is measured with invar wire and steel tapes (see Table 2.2). Tape extensometers (see Table 2.2) are also used to measure the distance between the target points on the tunnel wall.

2) Non-contact measuring methods

Nowadays, non-contact measuring methods are widely used in measuring work, such as total stations, an optical tachymeter (or tacheometer) and the photogrammetric method (i.e. evaluation of stereo images).

For most instruments, the fixed target points describing a cross section could be recorded, processed and presented as X, Y, Z coordinates. By comparing consecutive

images, the information on tunnel displacements and convergence would be obtained as well as the thickness of the lining support after excavation (Kolymbas, 2005). The methods are listed below:

Geodetic tachymeter (Total station)

A geodetic tachymeter is an electronic/optical theodolite with integrated device for distance measuring. It is also called 'total station'.

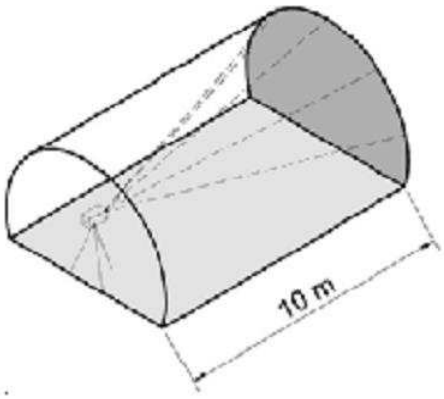

Figure 2.11 Monitoring of convergence with a laser tachymeter (Kolymbas, 2005)

The electronic tachymeter works as a combination of an electronic theodolite to measure angles and an Electro-magnetic Distance Measurement (EDM) system to read distances from the instrument to a particular point. Optical and laser tachymeters (see Figure 2.11) share similar principles to perform distance and profile measurement. The accuracy of the laser tachymeter is more acceptable for many geodetic applications (Clarke et al., 1992).

Routine geodetic surveying uses total stations to measure the movement of tunnel walls in three dimensions, with several 3D optical reflector targets (typically at the

crown, spring-line and occasionally at the side of the bench) installed at sections along the tunnel (e.g., 15 – 20 m between sections). The measurement of these targets is gained by placing the total station on the brackets bolted on the tunnel wall and moving the instrument forward. The coordinates of the targets are obtained from each instrument position. Any deformation of the tunnel would be noticed at regular tunnel inspections. Due to fuel emissions or dust, the precision of the measurements might be reduced in tunnels (Kavvadas, 2005).

Tunnel profilometer

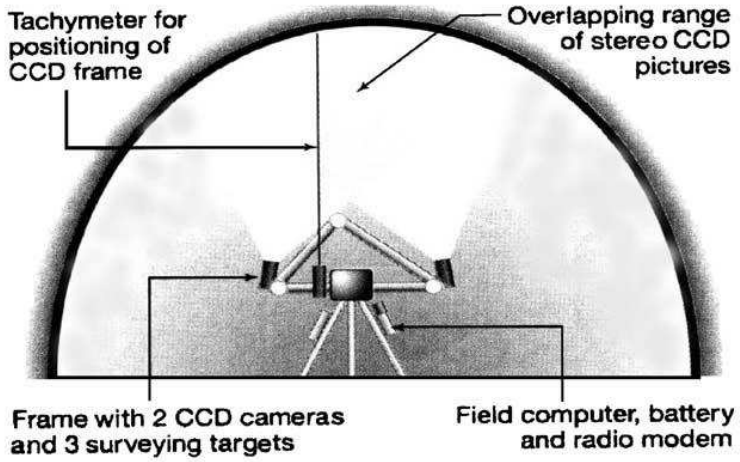

Figure 2.12 Typical features of the DIBIT tunnel profilometer (Kavvadas, 2005)

As digitised photogrammetric measuring instruments, tunnel profilometers (or tunnel scanners) are applied to measure the profile of tunnels with the help of powerful uniform illumination. There are two CCD (Closed-circuit Digital) cameras fixed on a portable frame in the system (see Figure 2.12). Digital images are taken and automatically stored in a field computer. Then, 3D coordinates of the surveyed tunnel surface are provided after processing with an accuracy of ± 5 mm. Although this level of accuracy is low compared to routine geodetic surveying (± (2 - 3) mm,

see Table 2.2), the advantage of recording a very large number of points on the tunnel wall can outweigh the low accuracy for many applications (Kavvadas, 2005).

Profile-image method

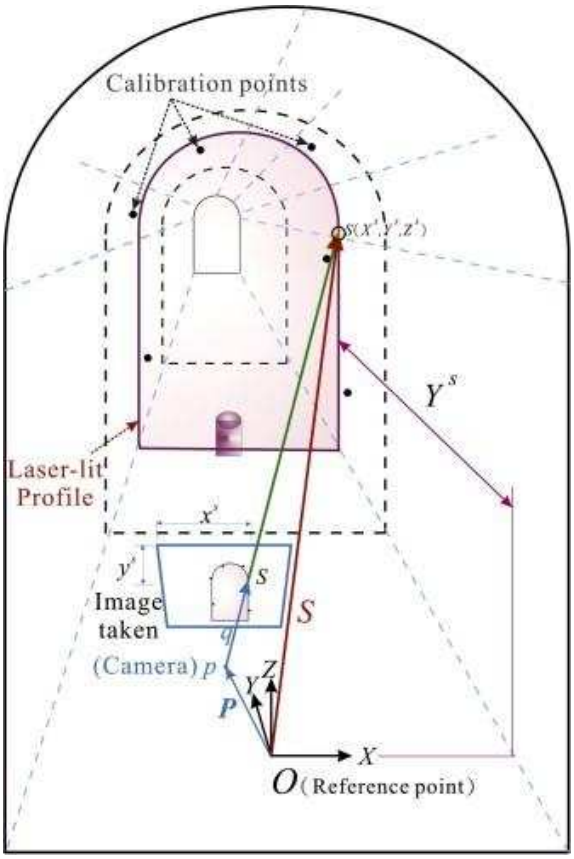

Figure 2.13 Illustration of imaging geometry of profile-image method for the tunnel wall (Wang et al., 2010)

Wang et al. (2009) have proposed a profile-image method to improve the precision and speed of the tunnel profile measurement. A line laser device is used as illumination to beam any profile along the tunnel. Using a digital camera, six calibration points with known coordinates in space down the tunnel can help to determine the relative six points with coordinates located on the same plane of the laser-lit profile, in one image. Thus, a profile of any section of a tunnel can be obtained (see Figure 2.13).

This method could measure the profile more precisely under poor conditions, such as a moist environment. The limitations should be addressed in future work, for example, the diffusion of a laser beam (width of the beam) when applied in a large tunnel (Wang et al., 2010).

Similarly, the LaserFleX™ system (see Figure 2.14) mounted on a vehicle offers a continuous structure profile measurement (Balfour Beatty Rail Ltd., 2006).

Figure 2.14 Examination in process using LaserFleX™ (Courtesy of Balfour Beatty Rail Ltd.)

Summary

The resolution and system accuracy of these profile-measuring methods are listed in Table 2.2 (Kolymbas, 2005; ES&S Ltd., 2009; Leica Geosystems Ltd., 2009).

Table 2.2 Methods for monitoring of convergence

Method	Manufacturer	Resolution (mm)	System accuracy (mm)
Invar wire	SolExperts	0.001	± 0.003
Steel tapes	Interfels	0.01	± 0.05
Tape extensometer	ES & S	0.02	± 0.02
Geodetic tachymeter	e.g. Leica	1	± (2 - 3)
Tunnel profilometer	DIBIT, GEODATA	1	± 5
Profile-image method	————	————	± (5 - 10)

2.3.3 Identifying damaged defects on tunnel shells

One of the main tasks in tunnel examination is to identify all types of defects in the whole tunnel shell, such as leaks, cracks, corrosion, cavities and water seepage. Here are some common methods:

1) Conventional contact measuring methods

The tunnel profile is usually divided into 5 parts: the crown, two upper sidewalls and two lower sidewalls. One inspector is responsible for detecting one part of the tunnel. The tunnel lining is tapped with a hammer to identify loose bricks, internal voids, hollowness, cracks, damp patches, bulges or any other defects as Figure 2.15 shows (Péquignot, 1963).

Figure 2.15 Manual work with devices (Courtesy of Network Rail Ltd.)

2) Non-contact measuring methods

There are several types of non-contact and non-destructive investigation techniques for identifying defects. These include:

a) Mechanical oscillation techniques

b) Radiation techniques

c) Electric and electronic techniques

d) Optical techniques

Each type consists of several techniques, listed in Table 2.3.

Table 2.3 Advantages and disadvantages of various techniques for existing non-destructive investigation of tunnels (Haack et al., 1995)

Techniques		Mainly Applied for:	Value for Tunnel Application	Problems With:	Advantages
Mechanical Oscillation Techniques	Structural dynamic methods (direct vibration)	Bridges; buildings aboveground	Very low	Uneven wall thickness; rock in homogeneity; varying groundwater level	None
	Seismic reflection	Geological investigation; determination of layer thickness	Low	Accuracy; speed	Only connected with very large cavities behind the tunnel lining
	Micro seismics and sonic emission analysis	Coal mines; laboratory tests	Very low	Reproducibility; accuracy	Investigation of structure-borne noise
	Ultrasonics –reflection and indirect surface transmission	Steel construction; mechanical engineering; pipelines; tanks	Very low	Coupling to test ground, concrete inhomogeneity; speed of diffusion by aggregates; accuracy	None
Radiation Techniques	Gamma ray backscatter	Road construction, earth construction; investigation of moisture content and density	Very low	Speed; penetration depth	None
	Neutron backscatter		Low	Speed, penetration depth	Indication of moisture content point-by-point

Techniques		Mainly Applied for:	Value for Tunnel Application	Problems With:	Advantages
Electric and Electronic Techniques	Eddy current methods	Electricity conducting metals; crack detecting for pipelines, indication of reinforcement	Low	Speed, non-conducting materials; penetration depth.	Indication of reinforcement
	Georadar	Ground investigation of bridges and tunnels	High	Evaluation; reflection by metallic cladding; speed	Good penetration depth
	Electrical potential methods	Detection of corrosion of reinforcement	Low	Speed; penetration depth	Detection of corrosion
Optical Techniques	Infrared thermography combined with visual determination	Check of thermal insulation; tunnels	Very high	Certain tunnel climates; evaluation; heat release of installations	Detection of cavities and moist patches, cracks, etc.; high speed
	Multispectral analysis	Monuments, buildings, tunnels	High	Speed; vibration; demand of powerful lighting; evaluation; penetration depth	Detection of small and dry cracks

3) Highly valuable techniques for tunnel investigation:

The highly valuable methods (Georadar, Infrared thermography and Multispectral analysis) for tunnel application, as shown in Table 2.3, are discussed in the following sections:

Georadar

In principle, georadar can detect anomalies in ground mass or structures like bridges and tunnels and can identify defects by noticing variations in the transit times for the reflected signal.

Since the reflection angle of the georadar unit is around 60°, defects could be identified before the georadar is located above. As the georadar moves towards one defect, the signal's transit times become shorter and shorter. The transit times would increase again as the georadar moves away from the defect. Finally, a transit time curve is obtained, showing a defect. However, not all of the disturbances showed were really damaged. In some other cases, defects could not be identified. (Haack et al., 1995).

Infrared thermography

Some tunnels have been investigated using an infrared scanner. The scanner makes full use of infrared thermography technology. It is an optic-electronic measuring device installed on a moving vehicle (see Figure 2.16). The scanner basically surveys the whole part of the tunnel lining. Moist patches in the tunnel shell and water seepage behind the tunnel shell could be recognised (Haack et al., 1995).

The use of georadar and infrared thermography for the inspection of a tunnel remains uncertain and incomplete with regard to the detection of defects. Some defects, such as corrosion and dry cracks cannot be detected properly (Haack et al., 1995). Thus, there is a need to develop investigatory methods.

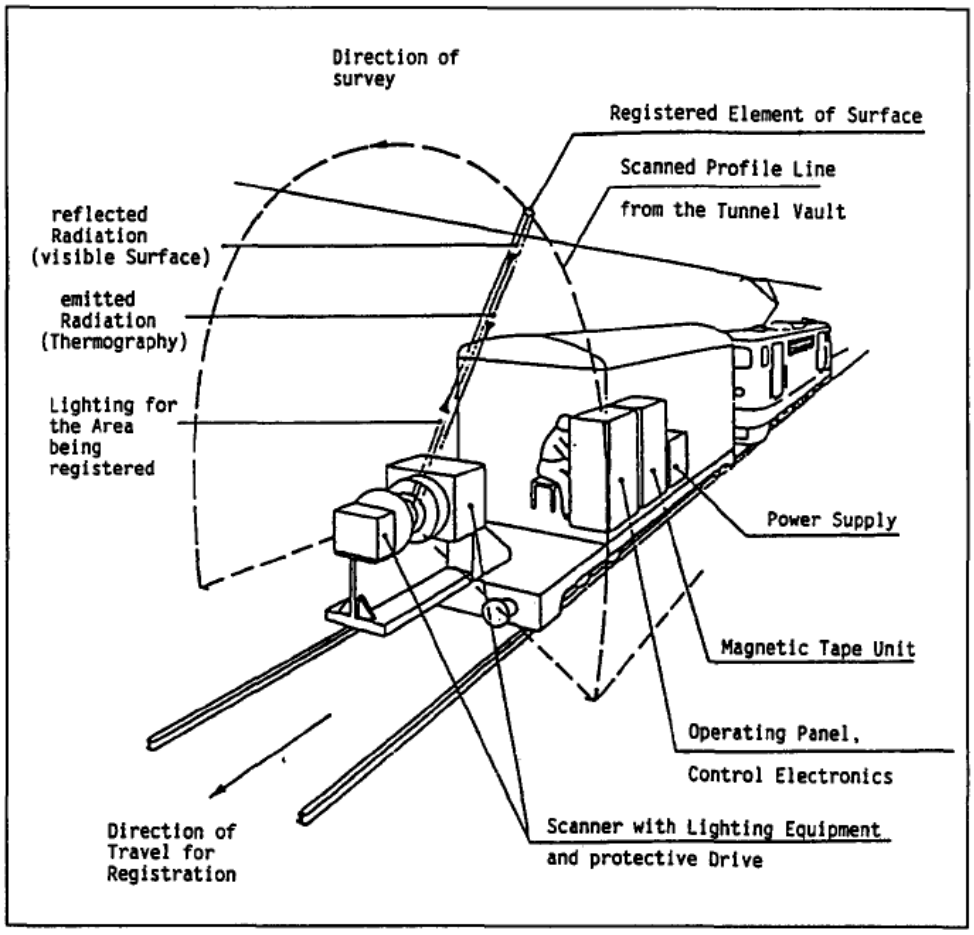

Figure 2.16 Tunnel inspection using an infrared scanner (Haack et al., 1995)

Multispectral analysis

In the process of multispectral analysis, photos of a surface are taken in a similar way to colour photography. Normally, there are six filters to separate some spectral areas from the entire light spectrum. For the same section of a structure, one shot is taken per filter.

A multispectral projector is used to superimpose these pictures taken of the same section with different filters. In this way, information about the surface areas would display a change in colour, thereby revealing some surface defects that are invisible to the human eye. Multispectral analysis has been employed to detect lining cracks in experimental tests by highlighting the thin cracks as bright lines against a dark background. The high resolution of this method could detect fine cracks as small as 0.5 mm. In addition, more defects, such as moist patches and deposits of carbonate could be recognised.

The multispectral analysis method may be excellent for identifying fine cracks in tunnel shells but it could not widely cover most work of defect inspection in tunnels (Haack et al., 1995).

Discussion

A series of tests on an experimental wall (Haack et al., 1995) used the above three methods respectively. It indicated that these three methods do complement one another for tunnel defect inspection. Under certain circumstances, it was advisable to use all three methods, which seemed to be relatively complex. Due to the limitations of these methods, more efficient and advanced techniques for tunnel examination are needed with some requirements:

a) High speed
b) High accuracy
c) Detection of all kinds of defects

In the following section, two advanced techniques (A laser scanning system and photogrammetry) are proposed for inspecting defects on tunnel shells.

4) Laser scanning system (LiDAR)

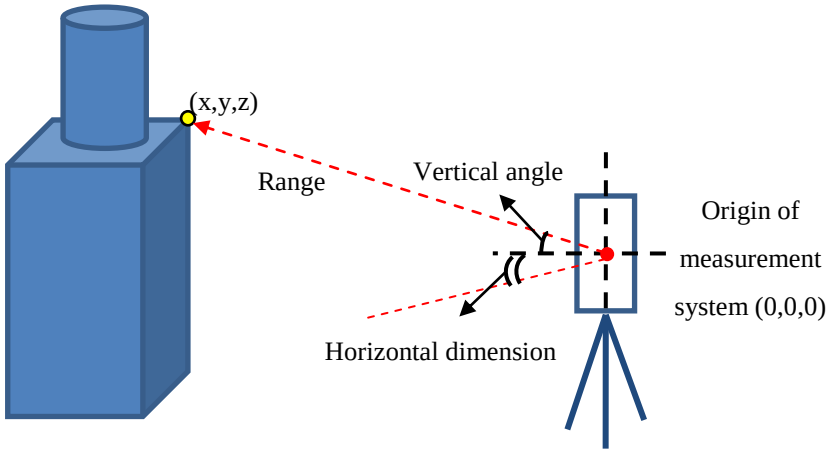

Figure 2.17 The principle of Lidar

Technology description

The use of laser scanners to determine distances to objects is based on a similar principles as ordinary radar, although 'laser radar' or 'Lidar (Light Detection and Ranging)' systems send out a narrow pulsed beam of light rather than broad radio waves (Figure 2.17). The systems uses the principle of either phase measurement or the speed of light and very precise timing devices to calculate the distance between a laser emitter/receiver device and an object reflecting the beam (Turner et.al, 2006). Horizontal direction and vertical angle to the target point are recorded as well.

A series of closely spaced target points on the object are targetted by the laser scanner and located by the range and orientation from the instrument position. The devices are capable of generating dense "clouds of points" that could be processed to yield three-dimensional [x, y, z] coordinates of the features being scanned. These ground-based laser scanners do have a benefit as being able to measure vertical, or

near-vertical objects that could not be visible so cannot be accurately measured from airborne sensors (Turner et.al, 2006).

A major advantage of this technique is that real objects can be represented more adequately in three dimensions than the use of a single picture or collection of pictures. Scanning can also provide a higher level of detail together with good metric accuracy. It operates automatically and without any contact (Guarnieri et.al, 2004).

Current applications

Figure 2.18 A typical laser scanner (Courtesy of Plasser American Ltd.)

Laser scanning technology seems to be a very promising alternative for many kinds of surveying applications. Airborne and ground-based laser scanners acquire a huge amount of 3D data very quickly, which can be profitably combined with coloured high-resolution digital images to provide a 3D representation of the environment. These models are currently used for cultural heritage, industrial, land management and also medical applications (Guarnieri et.al, 2004).

For distance measurement, a semi-conductor laser in the sensor head is modulated with high frequency in a sine-wave form and guided vertically upward by means of an oscillating mirror. When the laser beam hits the contact wires to be measured and/or other objects, it is reflected and the phase shift is measured by a detector.

Then the distance can be calculated from the phase shift of the emitted and reflected laser light (Plasser American Ltd., 2010).

To measure the horizontal position the laser beam is deflected laterally by ± 35° by means of a mirror oscillating at 50 Hz. The specific distance is then measured in relation to the associated angle. The horizontal position can be calculated from the determined distance and angle (Plasser American Ltd., 2010). This is also similar to the measurement of the vertical position.

Current railway applications

A high-speed and non-contact measuring system by laser scanners has been set up. Typically, the laser scanner is used for (Plasser American Ltd., 2010):

a) Track geometry measurement (track gauge, longitudinal level of both rails, cross level, twist)
b) Measuring speed
c) Rail profile measurement (corrugations, rail breaks or rail joints, worn-down welds, ball indentations, wheel burns, missing clips or fastenings), of which railway structures include tunnels, overbridges, under-bridges, platforms, signals and station canopies.
d) Ballast profile measurement
e) Clearance gauge measurement
f) Geometrical measurement of the contact wire (height and stagger of contact wire, the position of catenary masts, the position of distance marking and the position of structures such as bridges)

Potential applications

There is potential for monitoring the performace of objects such as tunnel deformation, automatic calculation of embankment/cutting slopes and angles, vegetation coverage, tree positioning, all which would be of benefit to the railways.

Further research and development

Future work could focus on the development and comparison of processing algorithms in order to improve the accuracy of the surface displacement maps (Schulz et al, 2005).

Further evaluation of 3D laser scanner development and data analysis procedures are needed, conducting instrument comparisons with field-testing facilities, which have been used to test some well-documented rock slopes and to verify laser data collection procedures.

Additional experiments should be undertaken to compare ground and airborne laser scanning data to determine the scale effects. It is also important to study the advantages of integrating laser scan data with the interpretation of optical imagery further, especially the high-resolution digital photographs now available with several scanners.

Of further interest is to investigate whether the intensity of the reflected laser returns in combination with information on the orientation can for example on a local rock surface, provide information that might assess the roughness and weathering of individual discontinuity sets (Turner et.al, 2006).

5) Photogrammetry

Technology description

Photogrammetry is the technique of measuring objects (2D or 3D) using photographs, which may also be imagery stored electronically on tape or disk taken by video, digital cameras or radiation sensors, such as scanners. The most important feature is the fact that the objects are measured quickly without being touched. Therefore, the term 'remote sensing' is sometimes used instead of photogrammetry. (see Figure 2.19) It is a well establish technology although digital photogrammetry has made significant benefits in automation of the techniques (Mcglone et al., 2004)

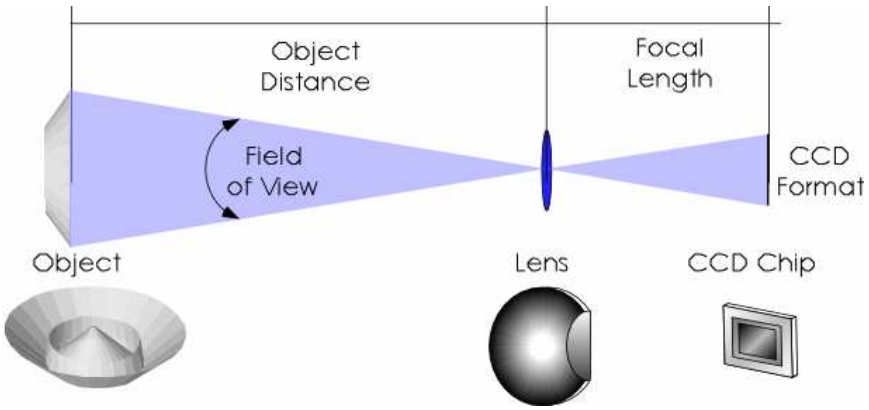

Figure 2.19 The principle of photogrammetry (Courtesy of Geodetic Systems Ltd.)

Classification of photogrammetry

Principally, photogrammetry can be divided into two groups.

a) Depending on the lens-setting:
    - Far range photogrammetry (with camera principal distance/focal length setting to infinity)

- Close range photogrammetry (with camera principal distance/focal length settings to finite values).

b) Another grouping could be:

- Aerial photogrammetry (mostly far range photogrammetry)
- Terrestrial photogrammetry (mostly close range photogrammetry).

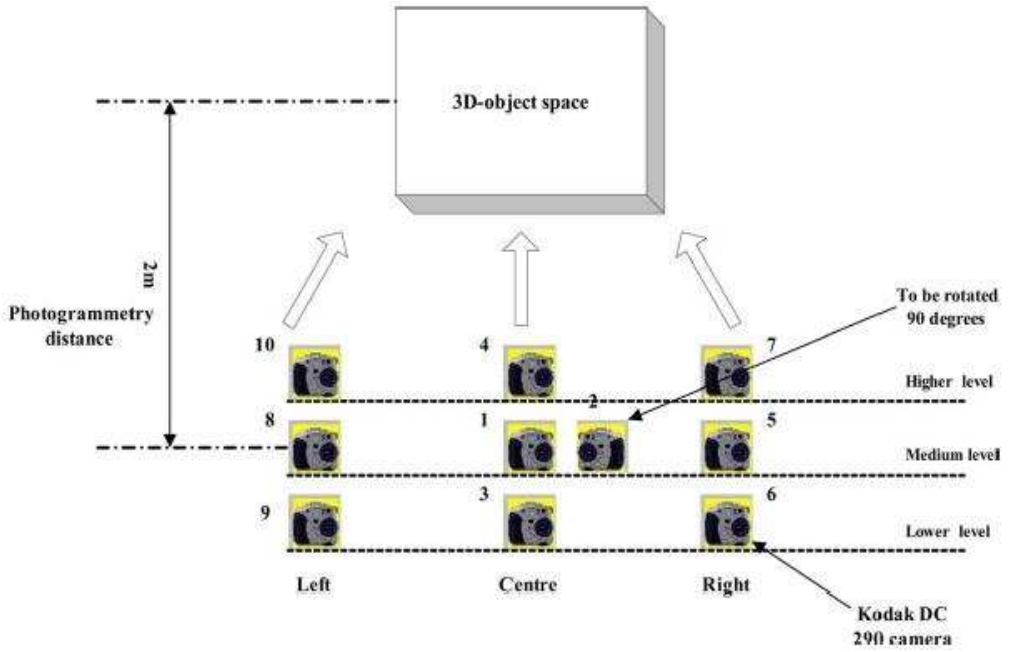

Figure 2.20 Digital cameras at different positions in photogrammetry (Courtesy of Geodetic Systems Ltd.)

Photogrammetry uses several camera stations located in different places and associated with custom-calibrated lenses and cameras to optimise the intersective geometry of the light rays (see Figure 2.20). Mathematical techniques are used to complete the coordinates of the points at the interesting rays and optimised positions are calculated when redundancy of measurements occur.

Current applications

The applications of the photogrammetry technique are widespread nowadays. The technique is mainly utilised for object interpretation and measurement.

In civil engineering, it has provided useful information on the cracking behaviour of reinforced concrete, including crack width, displacement, etc. under different loading conditions (Pease, 2006) as well as short and long time load tests of civil engineering materials (Hampel, 2003).

Photogrammetry is used as a fundamental tool to generate Digital Terrain Models (DTMs) without any objects like vegetation and buildings, starting from Digital Surface Models (DSMs) (Bitelli et al., 2004). From the images taken, it is possible to generate DTMs and DSMs of objects (e.g. topographic surfaces, road mapping, historical heritage modelling), contours, cross-sections, as well as joint and minor fracture zone orientations, etc. (Martin et al., 2007).

Aerial photogrammetry is mainly used to produce topographical or thematical maps, engineering surveys, digital terrain models and to provide a good source of historical data. The users of close-range photogrammetry are often architects and civil engineers (to supervise buildings, document their current state, deformations or damages), archaeologists, surgeons (plastic surgery) or police departments (documentation of traffic accidents and crime scenes), to mention just a few.

Current railway applications

Photogrammetry has mainly been applied to measure rail tunnel profiles as well as deformation mornitoring. The applications have been viewed with great interest as

the DTMs have a variety of further uses: landslide prediction, slope measurement and heights of embankments, rolling stock clearence, etc. It is also possible to generate models oftracks, rails and infrastructure.

Further research and development

An improvement of photogrammetry is considered in further study with lasers to measure the profile and deformation of tunnels, especially in bad conditions (penetration, dirt, degragation and erosion, etc.)

2.3.4 Final discussion

Conventional contact inspection procedures still play an essential role in the monitoring of tunnels. They might be accurate enough, but they are rather time-consuming, potentially destructive to tunnels and easily affected by human errors etc.

The advanced and automated non-contact testing methods, such as digital photogrammetry and laser scanners could improve or substitute conventional tunnel inspection procedures.

2.4 Masonry structure review

2.4.1 Introduction to masonry structures

As one of the most popular and oldest architectural materials, masonry plays an important role, particularly in tunnels, bridges and historical buildings.

This research focuses on the numerical modelling of old brick-lined tunnels. As a masonry structure, the brickwork forms the tunnel support. Trying to understand and simulate the brickwork ageing process is challenging. Therefore, it is worthwhile

starting by understanding more about the properties of brick, mortar and the composite brickwork separately in the following section.

2.4.2 Brick bond patterns

1) Brickwork wall

Terms of brickwork wall

Before introducing various types of bond patterns, terms with general application to brickwork should be reviewed, as defined by McKay (1968).

Bed: The lower surface of a brick when placed in position;

Header: The end surface of a brick;

Stretcher: The side surface of a brick;

Face: A surface of a brick, such as the bed face, header face and stretcher face;

Course: A complete layer of bricks; a heading course consists of headers and a stretching course comprises stretchers;

Bed joints: Mortar joints, parallel to the beds of the bricks and therefore horizontal in general walling;

Cross or vertical joints: These are between the ends of bricks in general walling, perpendicular to the beds of the bricks.

Different types of brickwork wall

Five popular bond patterns of brickwork wall are listed below (1, McKay 1968) and illustrated in Figure 2.21.

The American, or common bond: It is a variation of the stretcher bond. This bond has a course of full-length headers at regular intervals that provide the structural bond as well as the pattern. Header courses usually appear at every fifth, sixth or seventh course, depending on the structural bonding requirements.

English, or cross bond: It consists of alternating courses of headers and stretchers. It is the strongest bond as the bricks are well lapped. Each alternate header is positioned centrally over a vertical joint.

Flemish bond: This comprises alternating headers and stretchers in each course. The headers in every other course are positioned centrally over and under the stretchers in the courses in between. It is not as strong as English bond due to the large number of short, continuous joints.

Stack bond: There are no overlapping units in any course and all vertical joints alignment. This pattern usually bonds to the backing with rigid steel ties, when available.

Stretcher or running bond: This consists of stretchers in every course. Since the bond has no headers, metal ties are usually employed to form the structural bond.

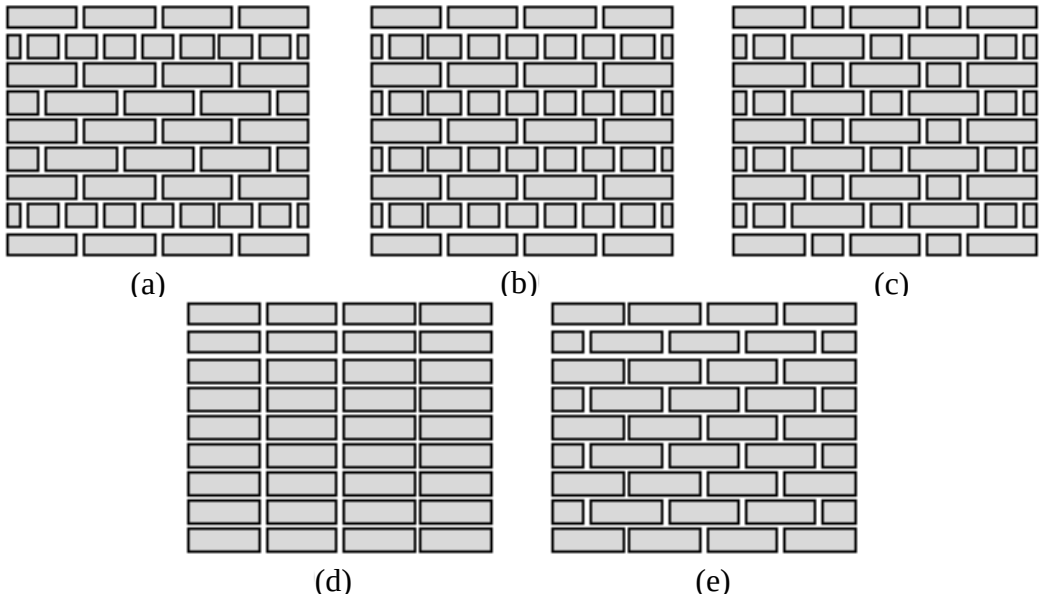

Figure 2.21 Different arrangements for brick masonry: (a) American bond; (b) English bond; (c) Flemish bond; (d) Stack bond; (e) Stretcher bond. (Lourenço, 2008)

2) Brick arch

General introduction to the brick arch

A typical brick arch consists of wedge-shaped bricks jointed with mortar and spans an opening. It supports the weight above to a large extent by transmitting the pressure downwards to the bottom, thus constituting a comprehensive application in the architecture and engineering fields.

Terms of arches

Common terms of arches are shown below (McKay, 1968).

Ring or Ring Course: The circular course or courses comprising the arch;

Extrados: The external curve of the arch;

Intrados: The inner curve of the arch;

Face: The outer surface of the arch between the intrados and extrados;

Crown: The highest point of the extrados;

Bed joints: The joints between the bricks, which radiate from the centre;

Voussoirs: The wedge-shaped bricks that comprise an arch;

Key brick: It is the central voussoir in a brick arch, which is usually the last voussoir to be placed in position. The key shown in the middle picture of Figure 2.22 comprises two bricks.

Classification of brick arches

McKay (1968) classified brick arches according to their shape and the materials and workmanship employed in their construction.

a) Shapes — including flat, segmental, semi-circular, circular, semi-elliptical, elliptical and pointed types.
b) Materials and Workmanship — consisting of either rubber bricks (coloured soft bricks, made of rubber), purpose-made bricks, ordinary or standard bricks cut to wedge shape (axed bricks), or standard uncut bricks (rough bricks).

This research concentrates on a rough brick semi-circular arch to form a horse-shoe tunnel (see Section 3.5 in details).

Different types of semi-circular brick arches

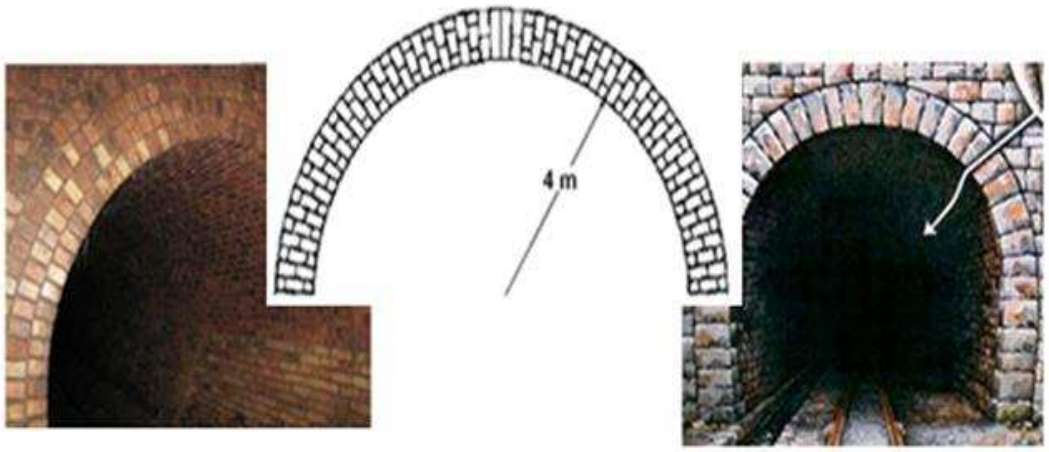

(a) (b) (c)

Figure 2.22 Different kinds of semi-circular brick arches: (a) Multiple-ring arches with uncut rectangular bricks; (b) Multiple-ring arches with wedge-shaped bricks laid in radial orientation; (c) single ring arch

Figure 2.22 shows three common semi-circular arches of railway tunnels. This research uses a similar arch type to the one as shown in Figure 2.22 (a).

2.4.3 Brick/Mortar/Brickwork properties

1) Brick properties

Physical properties

The dimensions and dry mass density of each brick type are slightly different. The dimension of a normal brick would not exceed 337.5 × 225 × 112.5 mm (L × W × H). The discrepancy between the dimensions of bricks from one batch would normally not exceed 0.5% of the average dimension. Bricks may be wire cut, with or without

perforations, pressed with single or double frogs or cellular (Vermeltfoort et al., 2005).

During the manufacture of bricks, countless fine pores are formed inside which influence almost every important property of the brick, such as compressive strength, modulus of elasticity, thermal conductivity, moisture expansion and frost resistance. The term porosity is used to represent the volume of pores out of the overall volume of the brick substance (Lenczner, 1972).

The water absorption properties of bricks are rather important for mortar workability and bonding. As such, the Initial Rate of Absorption (IRA) and total absorption are established for each type of brick. The IRA is measured for a unit in the first minute that it is immersed in water. Some research has shown that the IRA was inconsistent in relation to the bond. Therefore, it is usually recommended that the total absorption is used since this seems to be more appropriate (Sutcliffe, 2003).

In this way, the long-term suction properties could also be established by registering the water quantity absorbed over a given period. These absorption quantities may be able to give an indication of the pore volume of the brick (Vermeltfoort et al., 2005).

Elastic properties

The stress/strain relationship of a brick is almost linear up to the point of fracture. Young's modulus of bricks varies from 3.5 kN/mm^2 to 34 kN/mm^2. (Lenczner, 1972)

Compressive properties

Different manufacturing approaches and procedures produce different brick structures with different strengths. For instance, the final strength of material such as

clay-brick depends on the final temperature. The higher the temperature is, the higher the strength will be, since more minerals melt.

The compressive strength of bricks could be tested with a brick unit or several layers of bricks glued together, which are then loaded on the bedding surface and the brick face. The deviation in strength is believed to be due to the anisotropy in the material (Vermeltfoort et al., 2005).

Tensile properties

Due to the relatively high porosity and brittleness of bricks, the tensile strength is generally weak (Lenczner, 1972).

Detailed tensile tests could be tested on single bricks, providing lateral confinement at the end of the specimen (Vermeltfoort et al., 2005).

Durability of bricks

The durability of bricks is closely related to the resistance to chemical attack, moisture penetration and frost action. Among the agents causing chemical attack, efflorescence is probably the most common one. Salt is an essential material for efflorescence. Soluble salts contained in most clay bricks, combined with water could increase the occurrence of efflorescence. The sulphate, carbonate or chloride content (SO_4^{2-} , CO_3^{2-} , Cl^-) of other agents like soot or water could also attack the bricks (Lenczner, 1972).

2) Mortar properties

Physical properties

Modern masonry mortars are often made of cement, lime (conforming to BS 890), sand and water in specific proportions (Sutcliffe, 2003).

Elastic properties

The elastic properties of mortar would significantly affect the elastic properties and strength of the brickwork. The compressive strength of a brick is greater than that of mortar. When bricks and mortar are bonded together as brickwork, they are forced to strain equally, causing the bricks to move into a state of tension (Lenczner, 1972).

Compressive properties

Mortar compressive strength is affected by the cement content of the mix, the water/cement ratio, the proportion of cement to sand and the properties of the sand. For instance, high cement content and a low water/cement ratio would yield a mixture of high compressive strength. To some degree, coarse sand seems to yield at a higher strength than fine sand (Lenczner, 1972).

The curing (moisture) conditions of the mortar affect its mechanical properties. Mortar that is too dry or too wet has a negative effect on strength (Vermeltfoort et al., 2005).

Tensile properties

The tensile bond strength is the adhesive strength between the mortar and the brick, and is influenced by both of them. The tensile strength is typically measured by

separating sandwich brick assemblies in the laboratory to determine the tensile force (Lenczner, 1972).

Durability of mortars

The presence of excess calcium chloride in mortar may accelerate its deterioration and encourage efflorescence. The mortar may also suffer from sulphur compounds in a smoky atmosphere. It is advisable to mix sulphate resisting Portland cement in mortar for better durability.

3) Composite brickwork properties

The properties of the composite strongly depend on the properties of the components: the brick, the mortar, and their complex interactions (Sutcliffe, 2003). Unreinforced brickwork was tested under different loading conditions to study the behaviour.

The strength of brickwork in compression

The failure mechanism of brickwork under vertical stress σ_y is illustrated in Figure 2.23. When under a great axial compression load, lateral strains are experienced by both brick and mortar. Since strains in mortar are normally larger than those in bricks, the brick is consequently put into a state of lateral tension and the mortar into lateral compression.

Typical failure in brickwork may occur in the form of vertical splitting as the tensile stress in the brick reaches its ultimate tensile strength (see Figure 2.24).

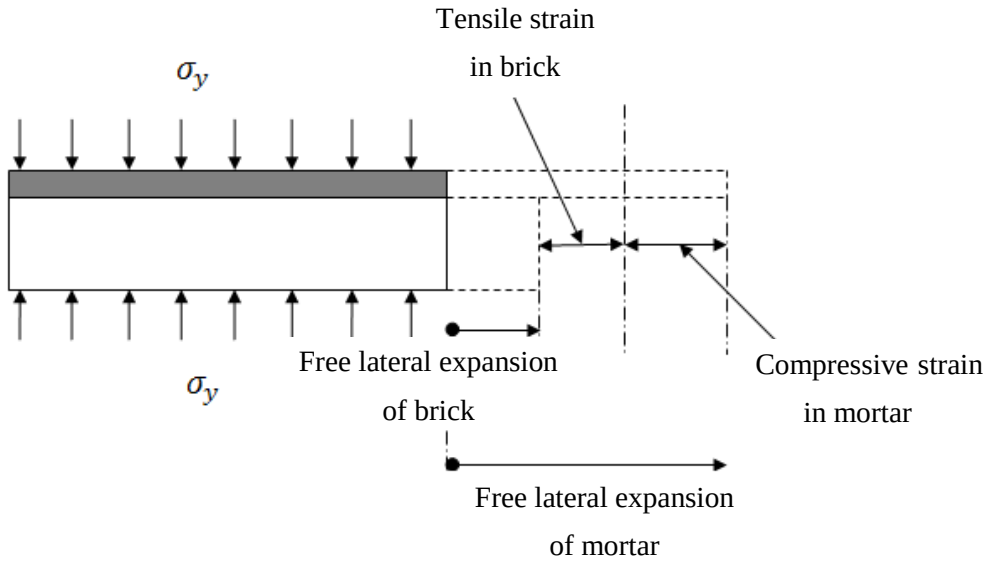

Figure 2.23 Lateral expansion of brick and mortar under vertical stress (Lenczner, 1972)

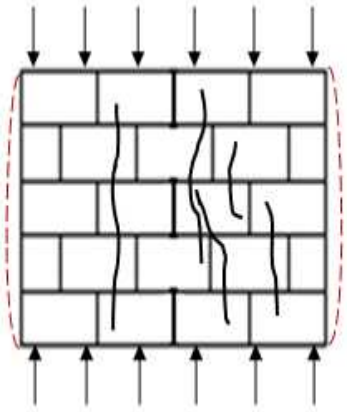

Figure 2.24 Typical failure pattern in a brickwork wall (Lenczner, 1972)

Here are the main factors affecting the compressive strength of brickwork:

The strength of the bricks: Hendry et al. (1998) observed that the compressive strength of brickwork was smaller than that of the bricks given by a standard compressive test. Furthermore, Lenczner (1972) indicated that the brickwork

strength was almost proportional to the square root of brick strength after tests at 28 days.

The strength of the mortar: The brickwork strength is much higher than the cube crushing strength of the mortar used (Hendry et al., 1998). The strength of brickwork is approximately proportional to the fourth root of mortar strength with constant brick strength (Lenczner, 1972).

Other factors: A number of other factors would affect brickwork compressive strength; for example, the density of bricks, the dynamic modulus of the mortar, time of curing, thickness of mortar bed joints, water suction of the bricks, the brickwork bonding pattern and workmanship (Lenczner, 1972).

The strength of brickwork in tension

Tensile failure modes of brickwork in uni-axial tension parallel or perpendicular to the bed joints are listed below (Sutcliffe, 2003):

a) Crogged or stepped tensile failure of joints (Mortars weaker than bricks - see Figure 2.25 (a))
b) Vertical tensile failure of bricks and joints (Bricks weaker than mortar - see Figure 2.25 (b) and (c))
c) Horizontal bed joint tensile failure of mortar joints (Weak mortar and brick / mortar bond - see Figure 2.25 (d))

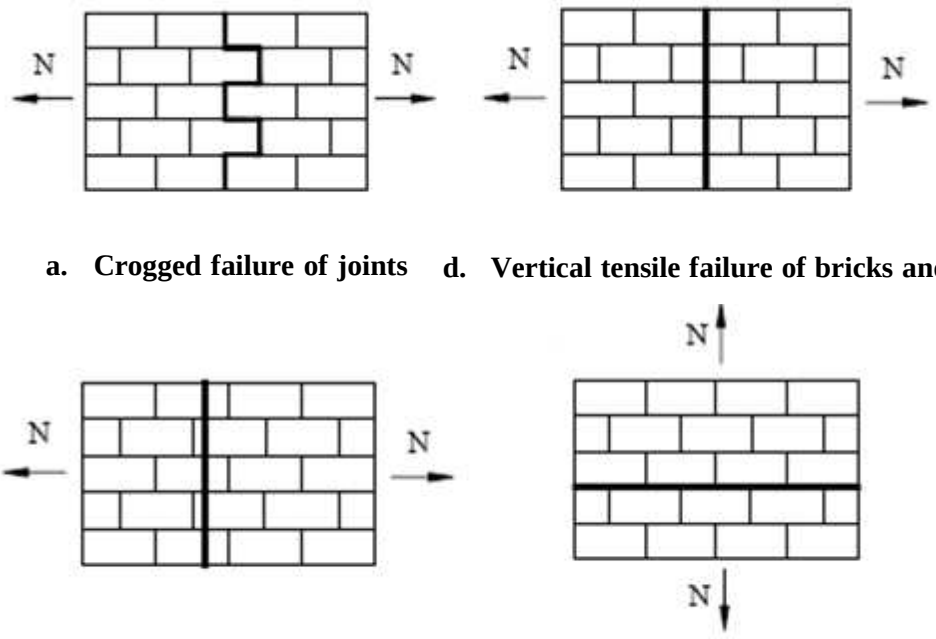

a. Crogged failure of joints **d. Vertical tensile failure of bricks and joints**

c. Vertical tensile failure of bricks **b. Horizontal bed joint failure of joints**

Figure 2.25 Tensile failure modes (Sutcliffe, 2003)

The tensile bond strength of brickwork is dependent on (Sutcliffe, 2003):

a) Suction of the bricks and water retention of the mortar
b) Mortar composites
c) Workmanship, including fullness of joints and cleanliness of jointing surfaces

The strength of brickwork in shear

Shear strength is critical for brickwork walls under lateral loads. The possible failure of a masonry shear wall would occur in such modes (Lenczner, 1972; Sutcliffe, 2003):

a) Direct tensile failure at the wall heel
b) Shear sliding along a bed joint
c) Diagonal tensile failure of the wall

d) Compressive or crushing failure at the wall toe

Mohr-Coulomb relationship in Equation (2.1) could deduce that:

The resistance of brickwork to horizontal shear would increase as the normal load increases.

The shear strength of the joint is also highly related to both shear bond strength (c) and friction between bricks and hardened mortar.

$\tau = c + \mu \cdot \sigma_n$ ……...……..… **(2.1)**

Where

$\tau =$ Joint shear strength;

$c =$Shear bond strength;

$\mu =$ Coefficient of friction;

$\sigma_n =$ Compressive stress normal to the joint

Many factors affecting the tensile bond strength of brickwork are also related to the shear bond strength (c) of brickwork (Sutcliffe, 2003):

Brick properties: Compressive strength, roughness of the contact surface, suction (initial rate of absorption and total absorption) and moisture content;

Mortar properties: Compressive strength, mortar composites and ratios, flowability, water retentivity;

Other factors: Brickwork prism compressive strength, joint thickness, curing conditions.

2.5 Numerical modelling review

2.5.1 Introduction to numerical simulation strategies

There are three basic numerical simulation approaches for masonry structures at present (Idris et al., 2008), as can be seen in Figure 2.26.

1) Detailed micro-modelling

Bricks and mortar in the joints are represented by continuum elements, while the brick / mortar interface is represented by discontinuous elements.

2) Simplified micro-modelling

The continuum part of detailed micro-modelling expands to zero thickness interfaces.

3) Macro-modelling

The brickworks are assumed to be on an equivalent continuum.

Both simplified micro-modelling and macro-modelling are to be used in this research and compared with each other.

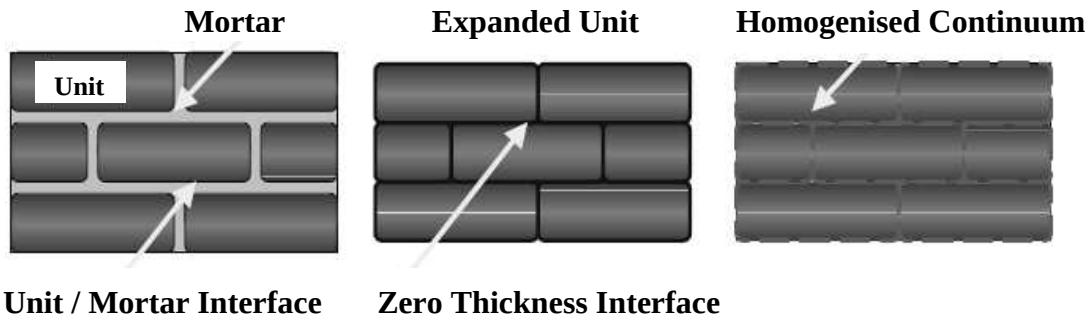

(a) Detailed micro-modelling; (b) Simplified micro-modelling; (c) Macro-modelling

Figure 2.26 Basic approaches to masonry structures (Idris et al., 2008)

2.5.2 Numerical analysis of masonry structures

Numerical analysis of masonry structures in tunnels, bridges and buildings is presented in the following sections:

1) Numerical analysis of masonry tunnels

Introduction

In tunnelling, numerical models are built to analyse and predict the mechanical behaviour of the surrounding areas, the support (e.g. linings, rockbolts) and the ground. Thus, the stability of tunnels could be assessed efficiently for optimum construction as well as maintenance. Numerical simulations are also used for sensitivity analyses to show the effects of different parameters on tunnel stability. However, the results by numerical simulation are not convincing without being validated. The validation process is often undertaken by experimental work. Therefore, the preparation of physical model tests in the laboratory is necessary to simulate the failure of real world tunnels for validation.

Masonry structures, typically stone blocks and brickworks support the majority of old tunnels. Due to the vaulted section shape of these tunnels (see Figure 2.27), the masonry structure is mainly loaded in compression.

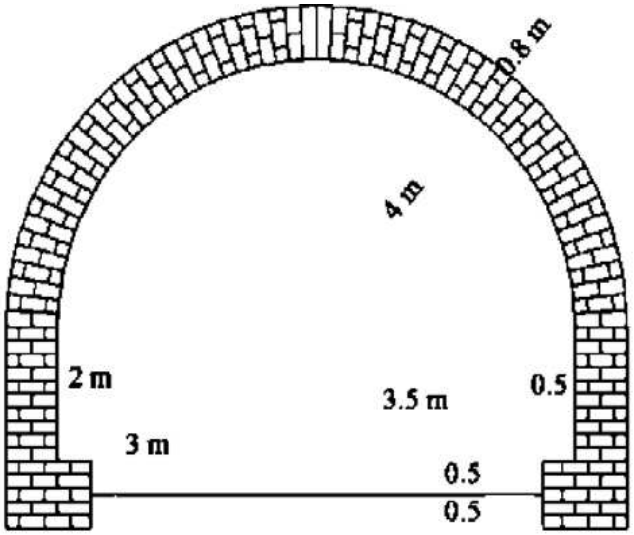

Figure 2.27 A typical vaulted masonry tunnel (Idris et al., 2008)

Literature review

Although several modelling approaches to masonry structures are currently under development by researchers, there are few publications focussed on the analysis of ancient tunnel masonry structures.

A tunnel masonry structure is a discontinuum, which consists of blocks bonded to each other by mortar in the joints. Furthermore, there is an interface between the surrounding soil and the masonry structure. Three basic modelling approaches (detailed in Section 2.5.1) to masonry structures have now been identified (Idris et al., 2008).

The well-known Universal Distinct Element Code (UDEC) was proposed by Idris et al. (2008 and 2009), based on the Distinct Element Method (DEM), to develop old

tunnel models supported by masonry structures. The mechanical behaviour of masonry blocks (limestone) and joints structures were analysed as well. A simplified micro-modelling strategy was used in the two papers (Idris et al. 2008, 2009).

Idris et al. (2008) used different values of block (limestone) parameters that would define block failure, such as cohesion, tensile strength and friction angle to simulate various stages in the tunnel ageing process for degradations. It also allowed the study of their individual influence on masonry behaviour from elastic to plastic, as well as the effect of the interaction between these factors (using SURFER 8 software, multivariate analysis of variance and multiple linear regressions). Whereas soil and joint properties remained unchanged, block properties such as density, elasticity modulus (Young's modulus) and Poisson's ratio were modified due to underground water penetration.

The following paper (Idris et al., 2009) focussed on the evolution of masonry joints to enhance the database of old tunnel instabilities. The study process was similar to that of the previous paper by changing three joint parameters influencing the mechanical behaviour of joints. In addition, an experimental design dealing with the evolution of the normal stiffness/shear stiffness ratio was proposed based on the UDEC code. Future work could place an emphasis on the study of the influence of the surrounding soil properties on the ageing phenomenon of tunnels.

2) Numerical analysis of masonry bridges

Similar to old masonry tunnels, a large number of arch bridges (see Figure 2.28) in service were built during the 19th century. Therefore, they have shown signs of deterioration.

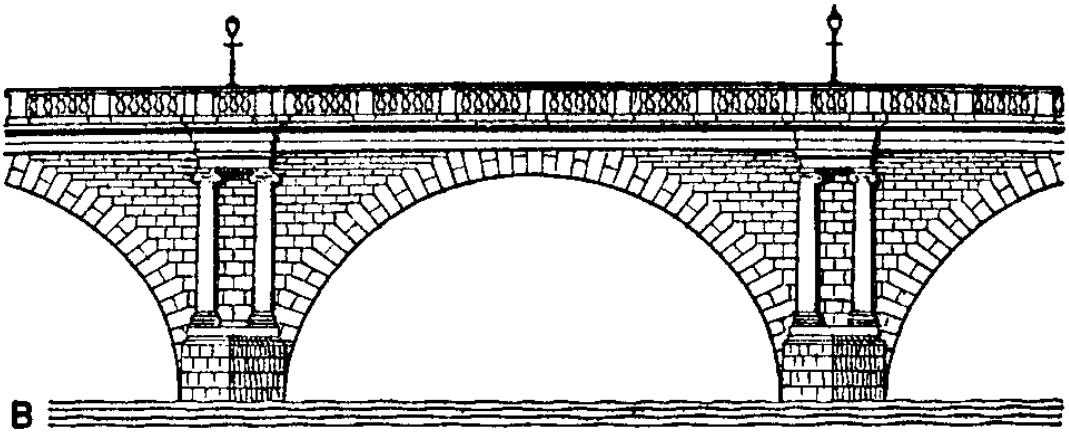

Figure 2.28 A typical multi-ring arch bridge (from Arthurs Clipart, Org., 2012)

Estimation is necessary to assess their actual load carrying capacity and collapse mechanism by setting up numerical models. The non-linear finite element technique (Betti, 2008) and the discrete element method, or a combination of both, showed the final potential of the arch bridges (e.g. see Figure 2.29). The onset of delamination could be predicted.

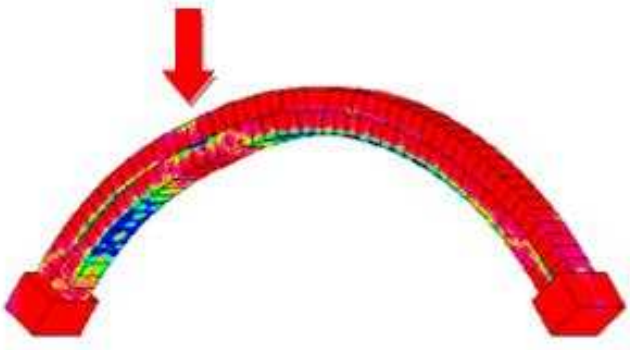

Figure 2.29 Block failure mechanisms of multi-ring arch bridge

3) Numerical analysis of masonry building structures

A series of studies have been conducted by many researchers on historical masonry building structures, which may help to obtain a better understanding of masonry structures using different numerical modelling methods.

Giordano et al. (2002) proposed and compared several numerical approaches to the modelling of historical masonry structures. Namely, the standard finite element method (FEM) modelling strategy was used, assuming homogenized material when the global behaviour of a whole structure was investigated. When study of the structure in detail was required, two approaches were proposed: the finite element method with discontinuous elements (FEMDE) and the discrete element method (DEM) (see Figure 2.30).

Mechanical behaviour of the control of cracking phenomena after structural repointing of the bed joints was analysed by Valluzzi et al. (2005) using finite element models.

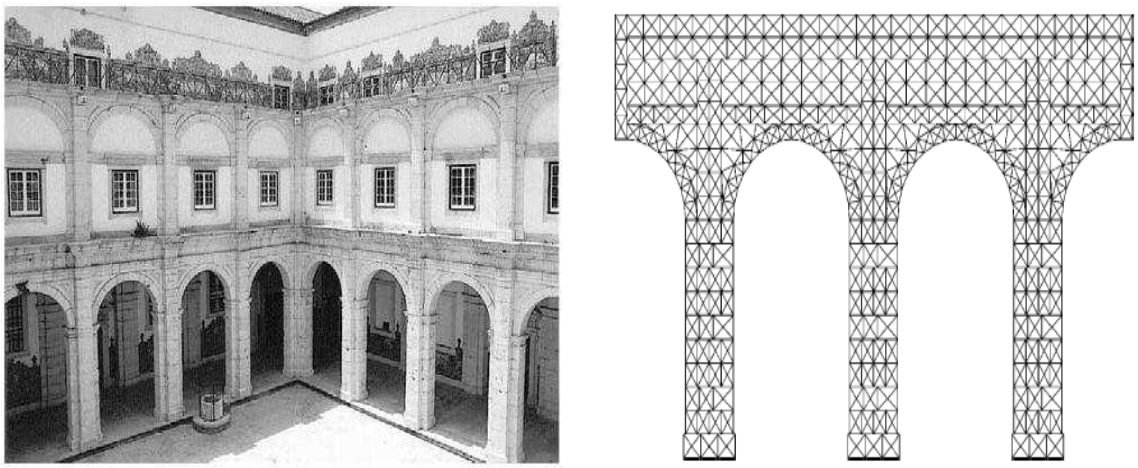

Figure 2.30 (a) Masonry building: Cloister Façade; (b) DEM internal finite element mesh of the lower part of the building (Giordano et al., 2002)

2.6 Chapter summary

This chapter is comprised of the basic literature review relevant to the research work, starting from stability issues of tunnels in which the permanent liners of tunnels and instability phenomena were reviewed, followed by some maintenance methods. Then, the typical monitoring methods in tunnels were introduced and compared with each other in order to find the proper measuring methods for this project. For the purpose of understanding the materials of brick-lined tunnels in this research, masonry structures, especially brickwork, were studied in detail. At the end of this chapter, the numerical modelling strategies were introduced, followed by some reviews of the numerical analysis of masonry structures.

The details of the physical model preparation, installation and loading tests as well as post-processing work of monitoring techniques are shown in Chapter 3.

CHAPTER 3 PHYSICAL MODEL TESTS

3.1 Introduction

Although numerical modelling continues to be widely used for analysing and predicting mechanical behaviour of engineering structures, outputs of the majority of masonry structure simulations have hitherto been unconvincing. It is because of the ambiguous and inconsistent nature at times of the input data for masonry properties, and assumptions such as simplified numerical models and interface issues underlying the models utilised (Jia, 2010). Physical model testing in the laboratory is an invaluable means of masonry research, not only demonstrating the performance of real masonry structures, but also validating and confirming the outputs of numerical models. It is particularly useful to undertake physical model testing prior to undertaking real world tunnel construction for safety and economic reasons.

A review of existing literature revealed that physical model testing of masonry arch bridges is not a new concept. Hogg (1997) assessed the effects of repeated loading on masonry arch bridges (spanning 2.5m) and its implications for serviceability limit state. Furthermore, Alonso (2001) compared the results from similar tests of half-scale physical masonry arch bridges (spanning 1.25m) to Hogg's prototype.

However, there are few publications focussed on the structure analysis of tunnel masonry structures with verification of physical modelling, alongside the numerical modelling. In this investigation, the stability of brick-lined tunnels was assessed via the mechanical testing of physical models constructed in the laboratory under controlled conditions. In other words, tunnel performance was assessed by applying incremental loads until the model tunnels failed.

3.2 Design of physical model tests

The purpose of conducting different physical model tests on small-scale brick-lined tunnels was to primarily gain an understanding of the mechanical behaviour of masonry tunnels in general and in the process determine their respective ultimate loading capacities. With this knowledge, it became possible to develop a numerical model capable of predicting the behaviour of real masonry tunnels. It is noted that the brick-lined tunnels were surrounded by dry sand (soil) to apply surrounding pressure and allow loading from the top the overburden soil. The soil material is easier to be obtained and worked with than the rock material in the laboratory.

Several factors were known beforehand to have potential to significantly influence the outcome of the tests on the physical models. These included brick bond pattern, the water content of the surrounding soil, brick variability, mortar variability, surrounding soil type, and load types e.g. concentrated and uniformly distributed loads. This research focussed on studying the effect of varying the mortar mix proportions and loading types while the other aforementioned variables were kept constant for all the different model tests. Details of the variables examined as mortar mix proportions and loading types are shown below.

3.2.1 Mortar mix proportion

For the first model, a comparatively higher strength mortar mix comprising cement, lime and sand in respective proportions of ratio 1:1:6 as prescribed by BS 4451:1980 British Standard for Methods of testing mortars, screeds and plasters was used. For the other physical model tests considered in this study, a mortar mix proportion of

lower strength (1:2:9) was used to study the effects of lower strength of brickwork on the tunnels.

3.2.2 Loading style

In order to simulate the behaviour of both deep seated (e.g. mountain tunnels) and shallow tunnels subjected to traffic load, the physical model tests were subjected to static uniform and concentrated load applied to the surface of the overburden soil.

3.2.3 Test variations

As mentioned above, three physical models with varying mortar mixes (1:1:6/1:2:9) were designed and conducted. The models were monotonically loaded to failure with uniform and concentrated loads, separately.

Table 3.1 below shows the different combinations of variables investigated for the three physical model tests conducted.

Table 3.1 Different physical model tests

	Mortar mix proportion	**loading style**
Physical model test 1	1:1:6 (higher strength)	Uniform load
Physical model test 2	1:2:9 (lower strength)	Uniform load
Physical model test 3	1:2:9 (lower strength)	Concentrated load

3.3 Design of a physical model

3.3.1 General introduction

In this research, the design of a physical model includes the selection of tunnel bricks and their bond pattern, dimensions, restrained boundary conditions.

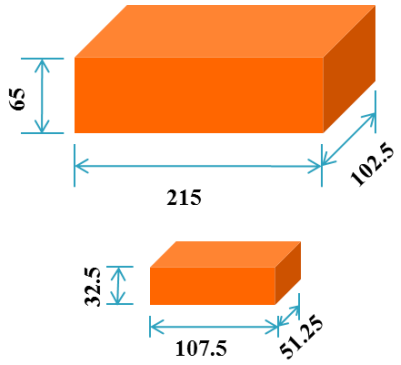

Figure 3.1 Original and half-scale Mellowed red stock bricks

The small-scale brick-lined physical tunnel model designed and constructed was subject to spatial limitations in the laboratory. The small-scale modelling of masonry structures such as masonry arch bridges has been proved to be a reliable solution by Davies et al (1998) and Alonso (2001).

In this investigation, bricks used in constructing the physical models were half-scale (see Figure 3.1). Namely, they were half the size of a full-size 'Mellowed red stock brick' (see later in Section 3.3.1) and had dimensions of 107.5 × 51.25 × 32.5 mm (L × W × H). Thus the dimension of the brick-lined tunnel profile was designed to be 690 × 887.5 mm (L × H), shown in Figure 3.2.

3.3.2 Brick bond pattern

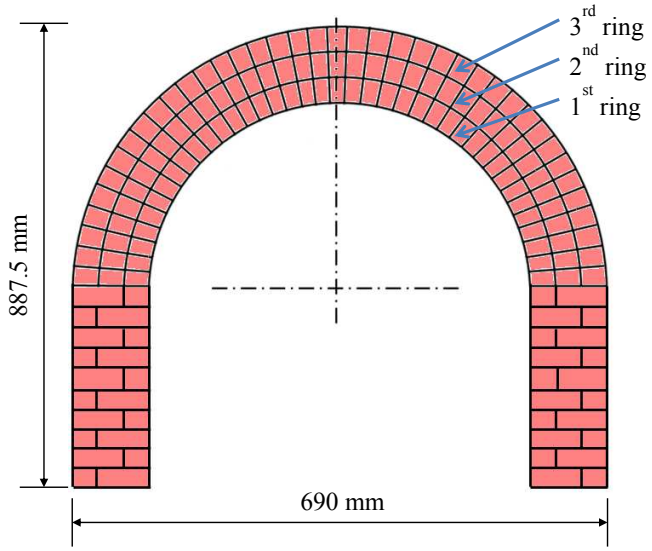

Figure 3.2 Front view of the brickwork liner

The tunnel's brick lining, having the profile of a horseshoe was built with the aid of a wood arch support. As shown in Figure 3.2, the tunnel consists of three layers of bricks situated at the arched region with each layer having bricks of similar size. The sidewalls, on the other hand, comprise one and a half bricks juxtaposed to each other but layered alternately. Each brick piece was separated by a 5 mm mortar joint. The tunnel was not constructed with any wedge-shaped bespoke bricks, in line with the construction pattern of many existing ancient brick-lined tunnels.

Although various brick bond patterns are used in reality for tunnel construction (see Section 2.4.2 in details), for consistency this research utilised the stretcher bond along the width of the entire tunnel.

3.3.3 Rigid box

A rigid support fashioned mainly from wood was utilised to support the soil surrounding the brick liner and to behave like a boundary restriction. The support

was in the form of a box of the dimensions shown in Figure 3.3, and with the exposed faces of the second and the third ring of the brickwork tunnel covered with Perspex. It can be seen from Figure 3.3, brick liner is placed into the box (see Section 3.2 and 3.5 for more details).

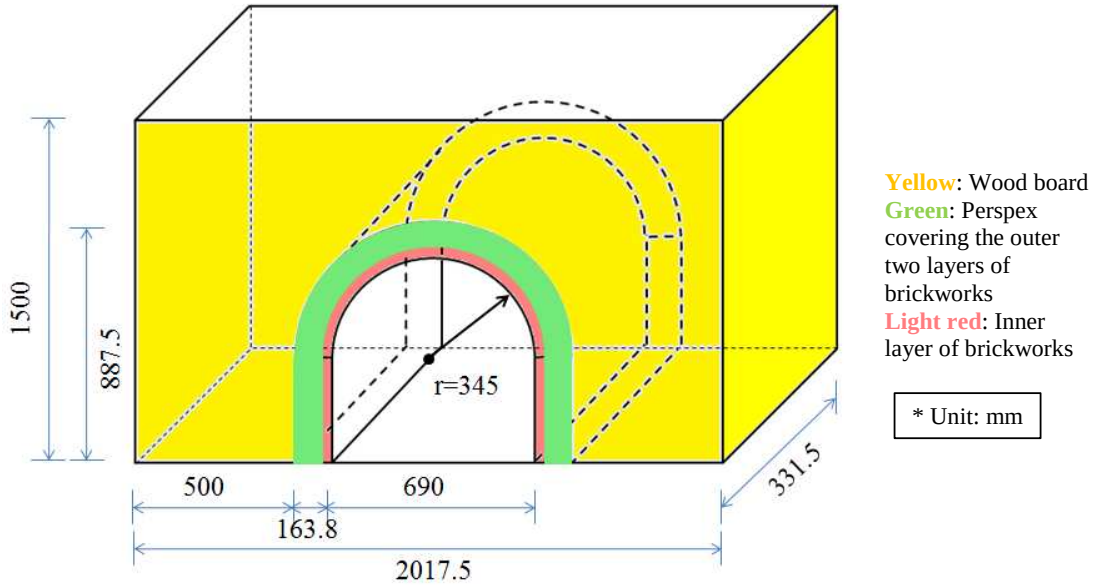

Figure 3.3 The rigid box surrounding the brick-lined tunnel

3.4 Physical model materials

Three specified materials may largely influence the structural strength and mechanical behaviour during the tests, i.e. brick, mortar, and surrounding soil. The details of each material are shown.

3.4.1 Brick

In accordance to the ancient masonry arch bridge tested by Hogg (1997) and Alonso (2001), 'Mellowed red stock brick' sourced from Wienerberger Ltd. was utilised for physical models tested in this investigation. Technical details of the bricks are shown in Table 3.2.

Table 3.2 Technical details of the brick (Alonso, 2001)

Brick name	Mellowed red sovereign stock
Brick type	Solid fired clay - facing brick
Standard work size	215 × 102.5 × 65 mm
Dry weight	2.5 kg (typically)
Appearance	A stock of oranges and red shades
Minimum compressive strength	>21 N/mm^2

3.4.2 Mortar

The mortar mix utilised comprised High strength Portland cement, hydrated lime and sand. While the cement and lime conformed to British standard specifications, BS EN 197-1-CEMI 52.5N and BS EN 459-1:200, the red builder's sand supplied was determined to be poorly graded. This was found when a representative sample of the sand material was sieved in accordance to BS 1377-2:1990. The proportions of the different particle sizes are shown in Table 3.3 and the particle size distribution is illustrated in Figure 3.4.

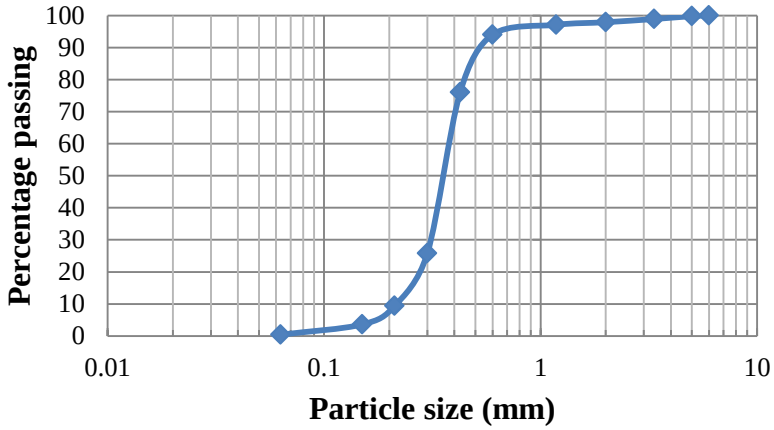

Figure 3.4 Particle size distribution (PSD) of red builder's sand

Table 3.3 Grading data for mortar sand

BS Sieve Size	% Passing by Mass
6.3 mm	100
5 mm	99.8
3.35 mm	98.9
2 mm	97.9
1.18 mm	97.1
600 µm	94
425 µm	76
300 µm	25.8
212 µm	9.4
150 µm	3.6
63 µm	0.4

3.4.3 Surrounding soil

Being a vital part of the physical tunnel model, the surrounding soil such as overburden soil cannot be neglected. In this study, this is represented by a compacted poorly graded Portaway sand (normal building sand), which was not subjected to any hydrostatic effects throughout the testing programme.

The sand's relative particle proportions and PSD was determined as prescribed by BS 1377-2:1990 and is shown in Table 3.4 and Figure 3.5 respectively.

Table 3.4 Grading data for surrounding soil

BS Sieve Size	% Passing by Mass
5 mm	100
3.35 mm	98.6
2 mm	85.6
1.18 mm	72.5
600 µm	50.2
425 µm	29.4
300 µm	11.8
212 µm	6.2
150 µm	3.5
63 µm	0.4

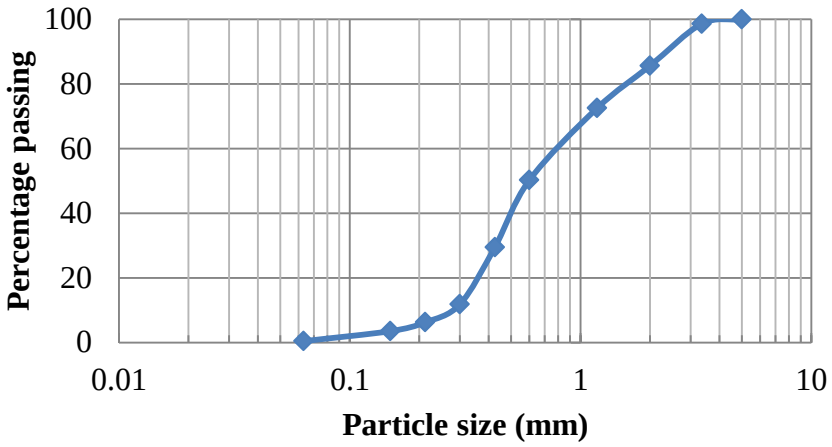

Figure 3.5 Particle size distribution chart of surrounding soil

3.5 Model construction and loading process

All the physical models investigated in this study followed an identical construction process to ensure consistency and comparability. The key elements of the

construction process were the brickwork liner, rigid box, plastic sheeting, and surrounding soil.

3.5.1 Construction of brickwork liner

The bricks used to construct the liner comprised approximately 500 bricks of half-scale bricks and ‘half bat’ (see Table 3.5 for details) cut beforehand by electrical saw. The fabrication process commenced with the construction of two symmetrical sidewalls comprising 10 layers separated by 5 mm mortar joints to prevent asymmetrical loading of the structure. The sidewalls were followed by the arch which comprised three layers of brickwork formed with the assistance of the wood arch support (see Figure 3.6 (a)). To separate the brickwork from the wooden support, a polythene sheet was placed at the interface of the brickwork and the wooden support, and was removed later when the mortar had sufficiently cured.

Figure 3.6 (a) Building process with wood arch support; (b) The small-scale brickwork liner of the tunnel

The stretcher bond pattern of the tunnel arch was formed using 50 half-scale bricks cut into half as ‘half bat’ and installed to form the 3 consecutive arch rings. The first,

second, and third arch rings required 30, 32 and 34 courses of bricks respectively to complete, as can be seen in Figure 3.6 (b).

Table 3.5 Dimensions of bricks used in the construction

Scale	Length (mm)	Width (mm)	Depth (mm)
Original	215	102.5	65
Half	107.5	51.25	32.5
Half bat*	53.75	51.25	32.5

Half bat*: A brick cut in half across its length.

Although it was supposed to maintain a 5 mm mortar joint thickness it varied between 4 mm and 10 mm due to the geometric limitations to the formation of the brickwork at the tunnel arch. In addition, workmanship error was made especially when building the arch and towards the crown. The outer side of the arch went up to 12 mm at some points.

In total, it took 7 working days to finish the first brick-lined tunnel, around 56 hours together. Then, the wood arch support was taken out after 7 days and the tunnel became self-supporting.

After the removal of the wood support, repointing work was done especially underneath the arch and at the sidewalls with the same proportion of mortar mix to prevent any crack generation or defect. A minimum of 28 days curing period was considered while the accomplishment of the rigid box could be done.

3.5.2 Rigid box

The wood board and Perspex were cut following the design size and sealed with clear silicone sealant. In addition, several steel angles were fixed at each box edge to strengthen the box.

After a full analysis of potential loads, deflections and factors of safety, a set of hot finished square and rectangular hollow section steel beams were designed and bolted at the front and back of the box. It consisted of six short hollow beams and one long hollow beam at each face (see Figure 3.7). Details of the hollow beams are in Table 3.6. The hollow beams were connected with steel packing of 50 mm thickness, bolted with steelrods (Φ 25 mm). They worked effectively to increase the stiffness of the box.

An additional set of wood wedges was at the position of 1/3 and 2/3 of the long beam against ‘A’ framesbolted on the robust floor, which supported and increased the bending capacity of the long beams (see Figure 3.8).

The two sides of the box were also be strengthened against the loading frame by wood wedges.

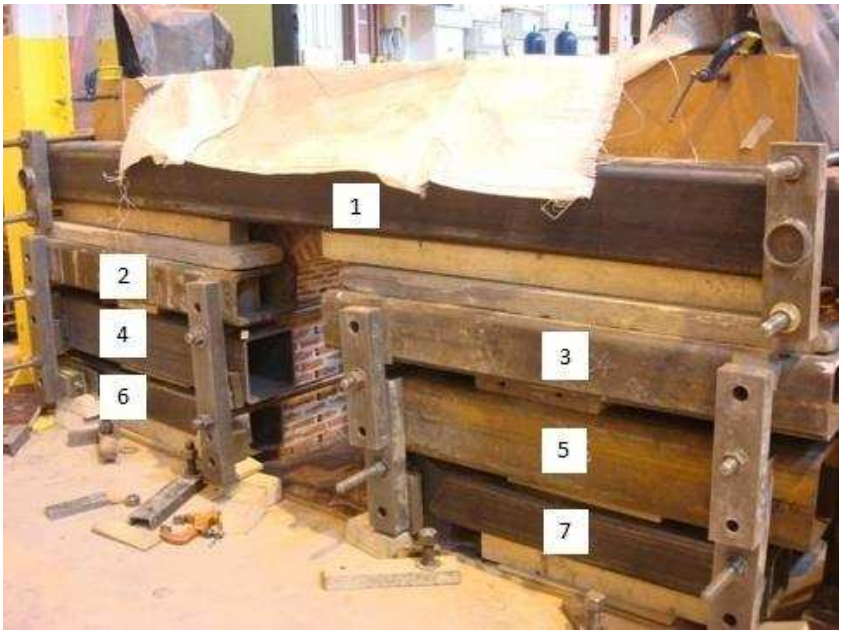

Figure 3.7 The rigid box of the first physical model

Figure 3.8 Wood wedges on the long beams against 'A' frames

Table 3.6 Dimension of hollow section beams

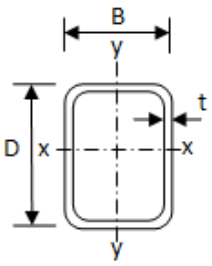

Dimension	NO. 1	NO. 2 & 3	NO. 4 & 5	NO. 6 & 7
B (mm)	200	150	200	150
D (mm)	200	250	200	150
t (mm)	12	16	10	8.8
Length (mm)	2800	1220	1130	1000

3.5.3 Plastic sheeting

To avoid the surrounding soil slipping out of the box through the Perspex and brickwork gap up to 2 mm while loading, the tunnel was covered with white plastic sheeting all around the rigid box (see Figure 3.7) before filling the surrounding soil. Moreover, plastic sheeting played an important role in reducing the friction between the soil and the box when loading occurred.

3.5.4 Surrounding soil

The placement of the fill sand commenced just before the loading test as it represented a heavy dead load. The Portaway sand was placed and compacted in layers. Each layer was approximately 125 mm thick with a standard 2.5 kg compaction test drop hammer for 20 times, up to 1075 mm depth from the box bottom. Care was taken during surrounding sand compaction, especially close to the tunnel arch where the fill was less.

The density of 1832 kg/m^3 (see Section 4.2.4 for details) and the depth of 1075 mm for surrounding soil from the tunnel toe were kept the same for all physical model tests.

3.5.5 Loading system installation

1) Uniform load

Monotonic (Static) load tests were run through the research. For these tests, load equipment consisted of one loading frame and a long cross beam to hang two hand-operated ‘Enerpac’ jacking systems associated with two load cells (Capacity was 500 kN each), to properly distribute the point load on top of the model and measure the imposed load. The load capacity of one hadraulic jack was 1000 kN and the maximum movement was 150 mm. (see Figure 3.9)

The load from two jacks was applied evenly on the whole surface of the overburden soil by a load spreader beam (1690 × 150 × 250 mm, L × W × H) with 5 point loading rollers (equally distributed along the length of the box), and a 20 mm thick steel plate of 1950 mm long and 300 mm wide underneath, as can be seen in Figure 3.10.

Figure 3.9 Loading system installation for uniform load

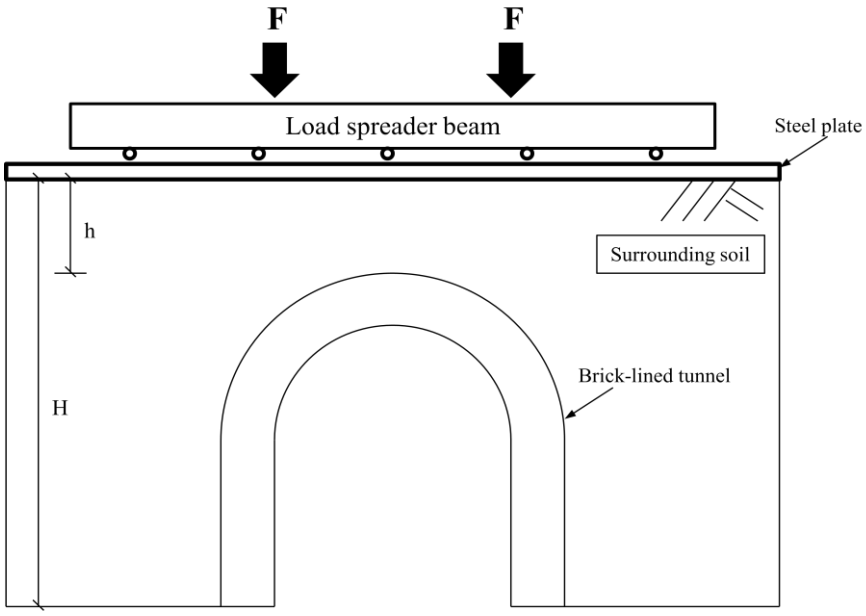

Figure 3.10 Load distribution design from two jacking systems

2) Concentrated load

Figure 3.11 Concentrated load jacking system

For the concentrated load test, the same loading system was used with one hand-operated jack and one load cell (Capacity was 1000 kN) to distribute the point load by a 30 mm thick steel plate of 330 mm wide and 300 mm long, on the surface of the overburden soil just above the tunnel crown. The hydraulic jack was the same as uniform load test with 1000 kN capacity and 150 mm maximum movement. (see Figure 3.11 and Figure 3.12)

Once a test was completed, the brick-lined tunnel was demolished and the Portaway sand was removed. The rigid box and wood arch support were cleared and made ready for the next model building. The duration for each physical model test from construction, mortar curing, loading to demolition was around 7 weeks.

Figure 3.12 Loading system installation for concentrated load

3.5.6 Loading procedures

Loading from 0 kN was initiated using hand pumps connected to hydraulic jacks and load increments of 40 kN were maintained for the majority of the time for each test. As the load accumulated on the structure and the failure load was imminent, the load interval was reduced to 10 kN until the structure failed at its ultimate load. It would be seen from the instantaneous recorded data of potentiometers (details in Section 3.7) shown on the monitor screen that the load versus crown displacement curve started to behave from linear to non-linear, which is a symbol of upcoming structural failure.

In most instances, load increments were sustained for one to two minutes to allow for logging of potentiometer data, the capture of digital photos and the laser scanning. Photogrammetry undertaken in the between load increments involved capturing images at different positions in both ‘portrait’ and ‘landscape’ orientations.

3.6 Tunnel monitoring instrumentation

It is imperative in any tunnel examination to monitor tunnel distortions/deformations in addition to other physical defects in the entire tunnel shell, such as leaks, cracks, and corrosion. Traditionally, this has been achieved with the use of physical-contact techniques such as steel tapes and tape extensometers. More recently, however highly precise and non-intrusive methods have been employed to achieve the aforementioned purpose. Both the traditional and modern methods of monitoring were utilised in this investigation and are the subject of discussion in the forthcoming section.

3.6.1 Advanced monitoring techniques

Due to the limitations of traditional monitoring methods (details in Section 2.3), two advanced, non-intrusive techniques, namely the laser scanning and photogrammetry were used to monitor the distortion and ascertain the evolution of defects on the tunnel shells in this study. The calculation methods used in analysing the outputs of both techniques were similar to each other. The sections below introduce the instrumentation of the advanced techniques.

1) Laser scanner

The FARO Focus^{3D}, a light and user-friendly laser scanner was used for monitoring work (see Figure 3.13). It was relatively a very small 3D scanner, with a size of only 240 × 200 × 100 mm and a body weight of 5 kg. This laser scanner has a touch screen to control all scanning functions and is extremely easy to use. The scanning process takes only a few minutes, saving up to 50% of scan time compared to other scanners. The laser scanning process required no special preparation prior to the start and the scan.

Figure 3.13 The front view of the laser scanner FARO Focus^{3D} (Faro Ltd., 2011)

Table 3.7 below displays more technical specifications. (Faro Ltd., 2011)

Table 3.7 Technical specifications of the laser scanner

Main Features	The Laser Scanner FARO Focus^{3D}
Measurement Range	0.6 m - 120 m
Vertical field of view	305°
Horizontal field of view	360°
Max. vertical scan speed	97 Hz
Ambient temperature	5° - 40° C

The physical model was scanned after each load increment and a 3D image obtained by assembling the millions of 'clouds of points' with coordinates. Via post-processing work of the point cloud data, it was possible to determine the extent of deformation at specific locations on the tunnel structure. Details of the post-processing work and subsequent results are illustrated later in Section 3.9.

2) Digital camera

For the photogrammetry work, a Canon EOS-5D Mark Ⅱ Digital SLR camera was used for image recording during the loading tests (see Figure 3.14).

Prior to loading, preparation for photogrammetry required the placement of around 150 reflective markers on the structure. These were stuck to the first lining ring (intrados) at both tunnel openings, to serve as reference points to monitor deformation variations during the tests. Additionally, it ensured that the ambient lighting was sufficient for the process.

Figure 3.14 The top view and the front view of Canon EOS-5D Mark Ⅱ (Imaging Resource, Ltd., 2009)

3.6.2 Potentiometer

The purpose of using potentiometers was to compare their outputs to results from monitoring using the digital camera and the laser scanner. Linear potentiometers were positioned at specific monitoring points on the tunnels' crowns, springing and toes, during the monotonic loading tests to measure horizontal and vertical deflection. With regards to the potentiometer installations, ten light aluminium targets were attached to the specific monitoring positions (crown, springing, and toes) on the first lining ring of the tunnel faces. These targets provide a reactive force to horizontal and vertical potentiometers. Here crown refers to the highest point of an arch layer of the tunnel liner, springing is the level where an arch or vault rises from a support, and toe is the bottom region of the horseshoe tunnel (see Figure 3.15).

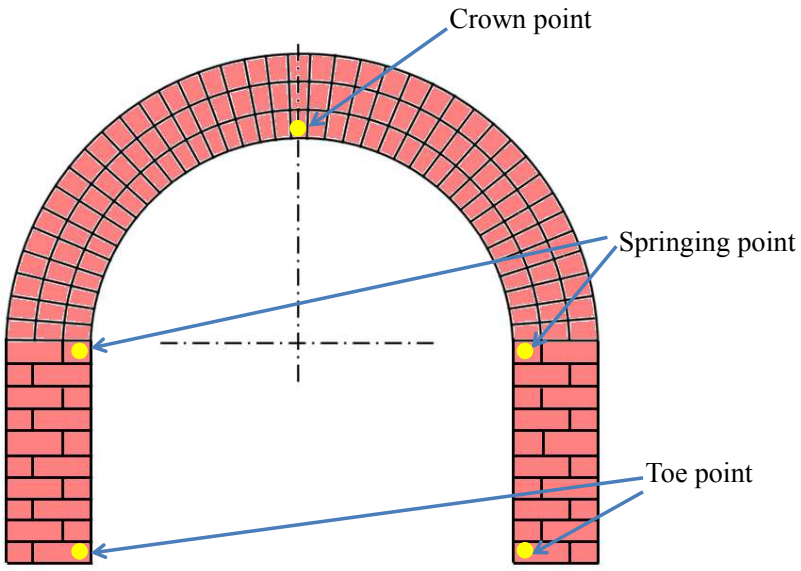

Figure 3.15 Five monitoring points in yellow at each tunnel face

Of the ten linear potentiometers employed, eight had a 30 mm range (see Figure 3.16) and the remaining two mounted on the tunnel crown, a range of 50 mm.

Figure 3.16 Potentiometer with 30 mm range

3.7 Test results of the first and the second models under uniform load

Results from the mechanical testing of the first and second physical models were compared to ascertain the relative effects of the different mortar mix proportions used in the construction of their brick linings. The data obtained proved useful for establishing typical behavioural characteristics for a uniformly loaded tunnel and determining specific tunnel failure criterion. Furthermore, the outputs of the mechanical tests were relevant as reference points for the numerical validation that ensued.

3.7.1 Ultimate load capacity and tunnel mode of failure

Figure 3.17 shows the transmitting path of the uniform load from the steel plate on top of the overburden soil to the tunnel. In this figure, H was the soil depth from the surface to the tunnel's toe, h was the soil depth above the tunnel crown, q was the uniformly distributed load acting on the tunnel arch and e was the horizontal stress acting on the tunnel, from the top to the bottom of the tunnel (e1 to e2). By virtue of its shape, the uniformly distributed load on the arch of the tunnel caused the tunnel to fact as a monolith thereby forcing the applied load to be transmitted to the sidewalls, which led to the shear failure on the tunnel sidewalls as the primary mode of failure.

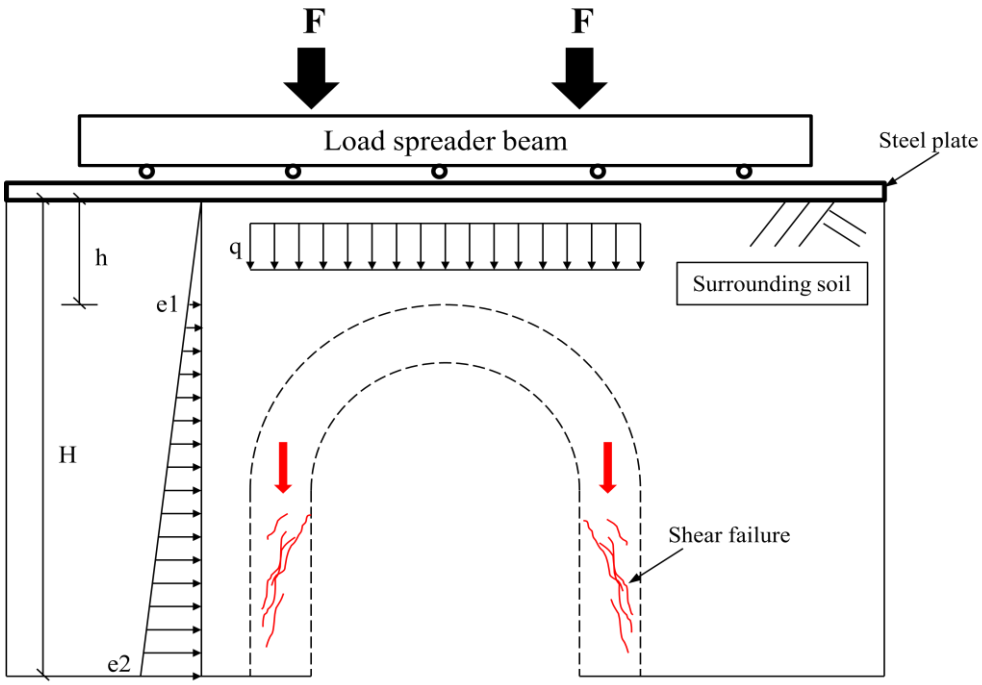

Figure 3.17 Tunnel model of failure under uniform load

The first physical model failed at a load of 995 kN, corresponding to a pressure of 1.49 MPa. The major shear failure was observed on the two sidewalls together with evidence of minor tensile failure on the tunnel's crown. Although a similar failure pattern was observed in the second physical model test, the model's ultimate load at failure was found to be 69.7% of that of the first model, having failed at 694 kN (or equivalent pressure of 1.04 MPa). The test data from these two uniform load tests on the physical models are shown in Table 3.8.

Table 3.8 Outputs from uniform load tests

Physical model	Mortar mix proportion	Failure load	Mode of failure	Location of failure
1	1:1:6 (higher strength)	995 kN	Mainly shear failure, partially tensile failure	Mainly tunnel sidewalls, partially tunnel arch
2	1:2:9 (lower strength)	694 kN	Mainly shear failure, partially tensile failure	Mainly tunnel sidewalls, partially tunnel arch

The result is consistent with the comparatively higher compressive strength of the brickwork in the first physical model (More details are shown in Chapter 4). It also suggests a correlation between compressive strength of constituent brickwork and the tunnels' ultimate load capacities, in that the tunnel comprising brickwork of higher strength failed later than its counterpart when both were subject to identical load regimes. The result is consistent with previous research by Hogg (1997), the first physical model could withstand a larger uniform load than the second physical model, possibly because it comprised brickwork of higher compressive strength.

3.7.2 Deflection behaviour

It is shown in Figure 3.18 that the tunnel under uniform load deforms inwards with the tunnel arch transferring the imposed uniform load downwards to the sidewalls, resulting in a crushing phenomenon near the arch springing (see Figure 3.22 (b)).

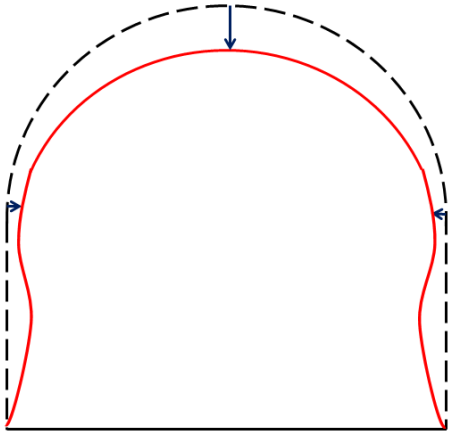

Figure 3.18 Deformation tendency of the tunnel under uniform load

From averaged outputs of the two vertical linear potentiometers located midpoint of the tunnel's crown and the eight potentiometers at the springing and toes of two tunnel faces, the pressure-deflection curves shown in Figure 3.19 and Figure 3.20 were produced for the tunnel's crown and the springing.

The pressure-crown deflection relationship in Figure 3.19 presents similar arch structural stiffness of the two brick-lined tunnels. It suggests that the stiffness of the brickworks, such as Young's modulus of the brickworks, does not have significant effect on the brick-lined tunnels, which is consistent with the parametric study of numerical simulations in Chapter 4. However, the first physical model test with comparatively stronger ultimate load capacity corresponded with more deformation (62.3 mm) at failure, while the crown displacement at failure of the second physical model test was 46.2 mm as 67.6% of that of the former test.

It is observed from Figure 3.20 that the springing structural stiffness of the second physical model reduced to around 3/4 of that of the first physical model. It indicated that the brickwork stiffness of the second model had a great influence on the springing structural stiffness when the lateral load from the surrounding soil was parallel to the bed joints (horizontal joint in masonry).

The smaller development of the springing deformation at the same load level in the first physical model test implied that the springing of the tunnel arch connected to the sidewall started to crush early than that in the second physical model test, which slowed down the movement of the springing.

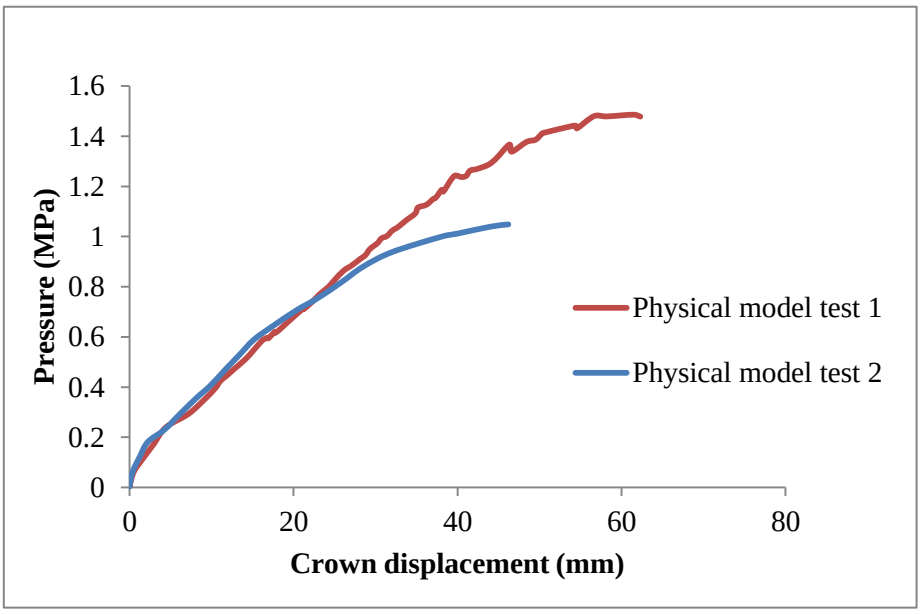

Figure 3.19 Pressure-crown displacement (vertically) curves under uniform load

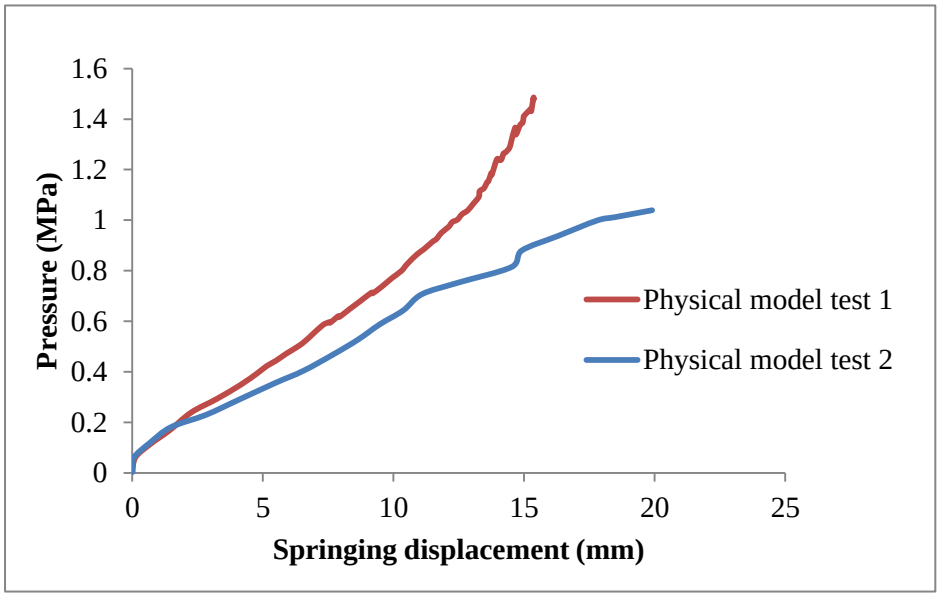

Figure 3.20 Pressure-springing displacement (horizontally) curves under uniform load

3.7.3 Cracking behaviour

Initiation of radial and stepped cracking was observed in the outwardly facing mortar joints of the first, second and third arch rings during the process of loading. These were noted to occur at 59% (594 kN) and 56% (392 kN) of the total loading regime for the first and the second physical models respectively.

As the loading progressed, the cracks were noted to propagate at the intrados of the tunnel arch (i.e. the inner surface of the tunnel arch). Subsequently, an increase in growth of radial cracking at the intrados of the tunnel arch was observed (see Figure 3.21).

Additionally, the onset of diagonal cracking cutting through the two tunnel sidewalls and leading to imminent shear failure was observed as evidenced by Figure 3.22.

Figure 3.21 Crack failure under uniform load

Figure 3.22 (a) Shear failure at sidewalls; (b) Crushing phenomenon at the arch springing

3.8 Test results of the third model under concentrated load

The third physical model was subjected to concentrated loading above the centre of the tunnel crown. The mortar of the same mix proportion (1:2:9) as per the second physical model was used in the construction of the third physical model. Consequently, it was possible to compare the mechanical behaviour of the tunnel structures subjected to two different load types i.e. the second physical model under uniform load and the third physical model under concentrated load.

3.8.1 Ultimate capacity and tunnel mode of failure

Figure 3.23 illustrates the third physical model under concentrated load acting on the overburden soil area just above the tunnel crown, transmitted by a steel plate (loading area of 330 × 300 mm, mentioned in Section 3.5.5), where f was the distributed load acting on the centre of the tunnel arch. The failure was due to the development of five structural hinges namely point A to E at the tunnel arch,

occurring since the tunnel arch was subjected to symmetrically distributed loading, which showed an agreement with Page (1993). Theoretically the five structural hinges would appeared at certain position of the tunnel (i.e. 1/6, 2/6, 3/6, 4/6, 5/6 section of the tunnel arch) as shown in Figure 3.23.

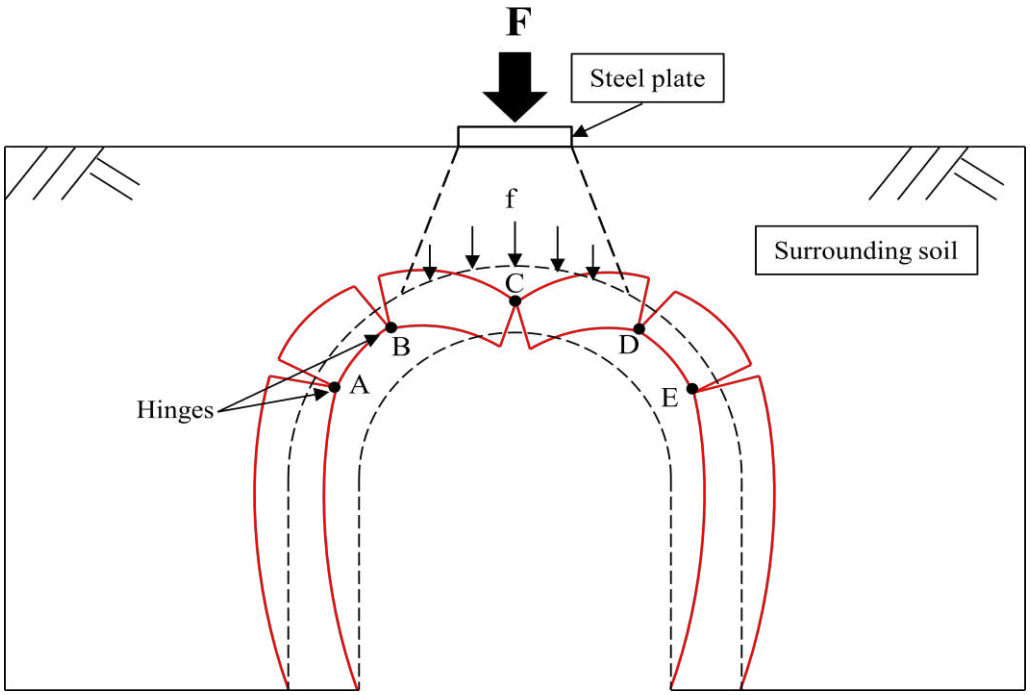

Figure 3.23 Tunnel model of failure under concentrated load

The third physical model experienced a sudden failure at 73 kN, corresponding to the failure pressure of 0.73 MPa on the loading area of 330 × 300 mm which was 70% of the failure pressure of the second physical model test (see Table 3.9). During loading, a five-hinge failure mechanism was observed as shown in Figure 3.24 specially appeared at the second and third rings of the tunnel arch with hinge points A, B, D and E, and through three arch rings with hinge point C. In addition, the collapse of partial ring sections due to ring separation of three arch rings at the tunnel crown, occurred suddenly at the maximum load as can be seen in Figure 3.24. The ring separation would normally occur in a multi-ring masonry arch subjected to

loading (Chen, 2007). The test data from the concentrated load test on the third physical model is shown in Table 3.10.

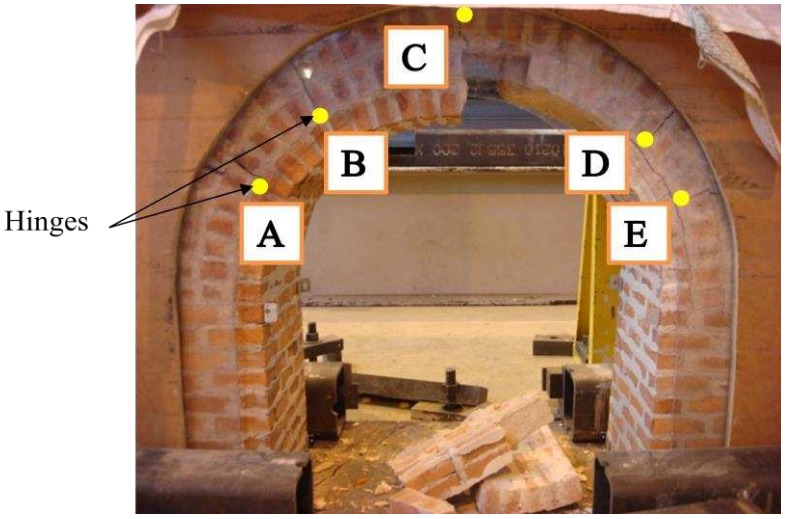

Figure 3.24 Collapse during the physical model test under concentrated load

Table 3.9 Loading outputs from three physical models

Physical model	Loading style	Failure load	Loading area	Failure pressure
1	Uniform load	995 kN	0.67 m^2	1.49 MPa
2	Uniform load	694 kN	0.67 m^2	1.04 MPa
3	Concentrated load	73 kN	0.10 m^2	0.73 MPa

Table 3.10 Outputs from the concentrated load test

Physical model	Mortar mix proportion	Failure load	Mode of failure	Location of failure
3	1:2:9 (lower strength)	73 kN	Mainly five structural hinges, collapsed due to ring separation	Mainly tunnel arch

3.8.2 Deflection behaviour

The deformation trend of the tunnel under concentrated load differed from that under uniform load. The simplistic depiction of the deformation tendency to failure in Figure 3.25 shows the sidewalls as having deformed outwards from the original tunnel profile and the crown at the third ring inwards over the loading period. Figure 3.23 specifically illustrates the deformation tendency to failure in red with structural hinges at the tunnel arch, which separated the tunnel into six sections.

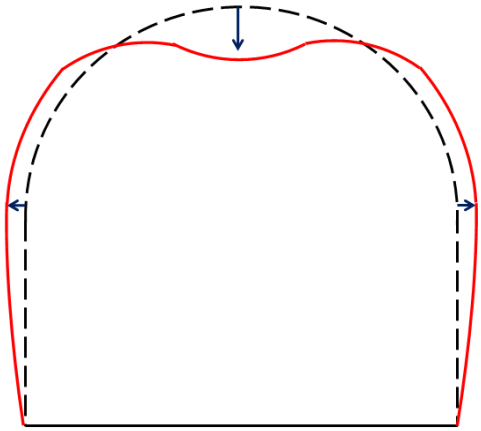

Figure 3.25 Deformation tendency of the tunnel profile under concentrated load

For the same mortar mix ratio of 1:2:9, the third physical model under concentrated load experienced only half vertical movement of the crown at failure, compared to that of the second physical model under uniform load shown in Figure 3.26. Because in the third physical model, the tunnel crown recorded at the first (inner) arch ring deformed diagonally, developing a structural hinge at the third (outer) arch ring and cracks through three arch rings at the tunnel crown (see Figure 3.23), while in the second physical model, the tunnel crown only moved vertically.

With regards to springing deflection at failure, the third physical model had comparable springing displacement within 5% difference from that of the second physical model as can be seen in Figure 3.27.

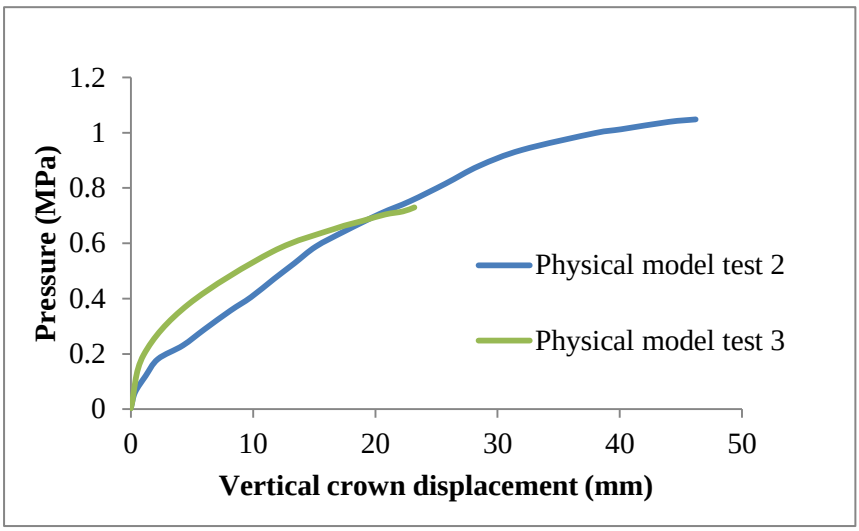

Figure 3.26 Pressure-crown displacement curves under uniform and concentrated load

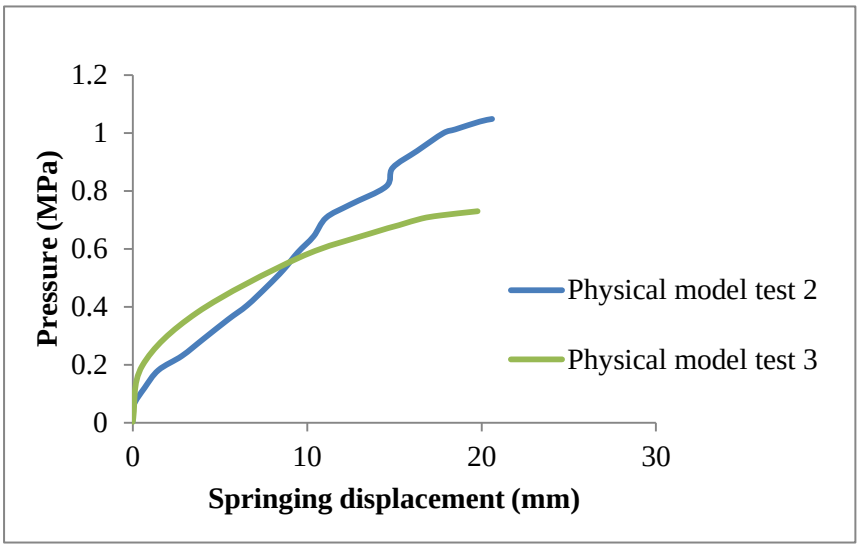

Figure 3.27 Pressure-springing displacement curves under uniform and concentrated load

3.8.3 Cracking behaviour

During the concentrated loading of the third physical model, the formation of structural hinges with cracking was noted at 62% of the loading programme (i.e. load of 45 kN, pressure of 453 kPa). Figure 3.28 shows the major structural hinge with cracking at the tunnel crown whist Figure 3.29 illustrates the five structural hinges as points A to E and cracking development, which were almost symmetrical in the experiment. Furthermore, two springings initiated minor cracks with the potential to develop into structural hinges.

At failure, ring separation with radial cracking occurred among three arch rings at the tunnel crown, which led to collapse of partial tunnel section.

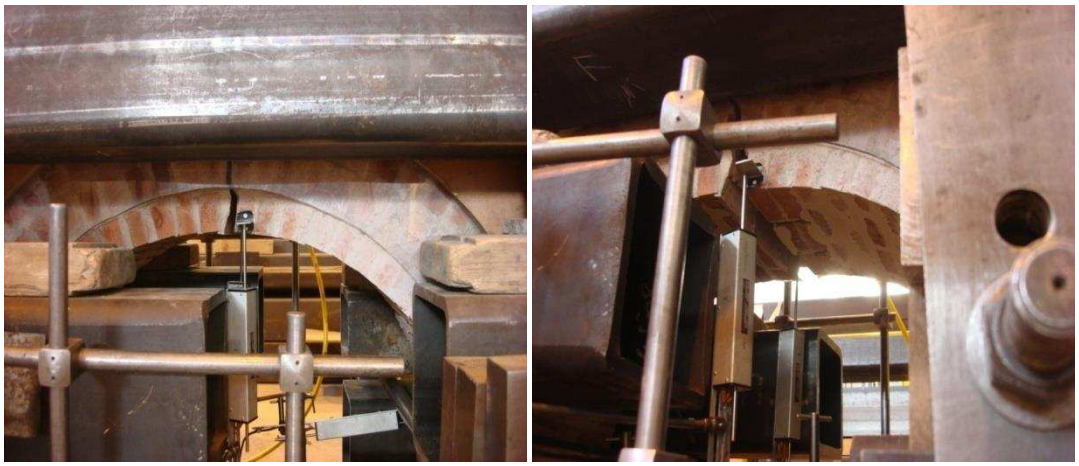

Figure 3.28 Structural hinge at tunnel crown along the width under concentrated load

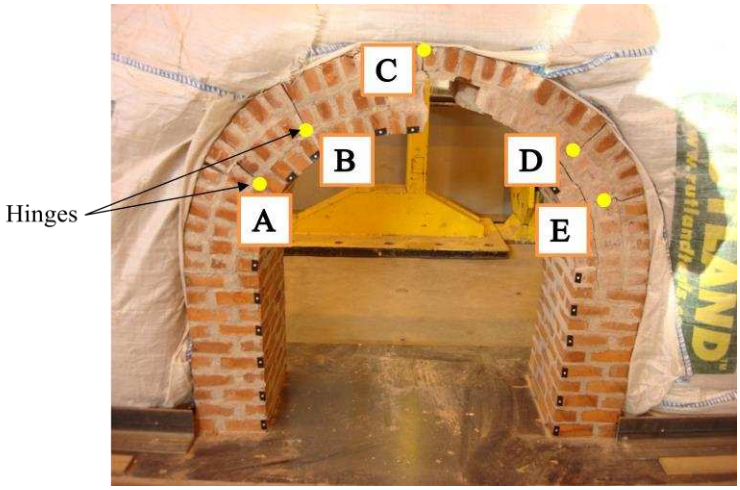

Figure 3.29 Structural hinges with cracking of the tunnel arch under concentrated load

3.9 Post-processing work of advanced monitoring techniques

3.9.1 General introduction

During the loading tests, two advanced techniques (i.e. photogrammetry and the laser scanning system) were used for monitoring tunnel shell distortions and inspecting defects. The raw data from the techniques utilised was post-processed using the commercial software, 'Australis' and 'Geomagic Studio 10' for close-range digital photogrammetry and the laser scanning system respectively. The implementation and output of the techniques with regards to this study are shown in the following sections.

3.9.2 Tunnel monitoring and data processing of measurements using photogrammetry

Australis (Version 7.0) is used to make 3D measurements of numerous targeted points on an object of interest, which in the instance of this investigation are physical

models of tunnels. The targets for measurement points usually comprise retro-reflective dots stuck on the object. Additionally, distinct and retro-reflective coded targets against a dark background are placed nearby the object of interest, to facilitate the automatic measurement, as shown in Figure 3.30.

Figure 3.30 Dots and coded targets in green

The Australis Users' Guide prescribes a process involving measurements, scale setting, coordinate system transformation and exporting points of interest, for successful analysis of photogrammetry raw data.

a) Project set up and manual measurements

Following the guide, a project comprising selected images obtained at the same loading stage but from different image stations was set up. Full measurements (conducted manually) were then made, ensuring that every targeted point appearing in at least two images were matched. Via this process, a 3D photogrammetric

network comprising multiple tunnel images and object points obtained from specific camera stations could be formed and measured.

In Figure 3.31 for example, thumbnails and expanded versions of images obtained from different stations are shown, along with a 3D tunnel point profile of both tunnel openings (shown in green at the right bottom). However, the object of interest i.e. brick-lined tunnel was not scaled in accordance with the real scale at this stage.

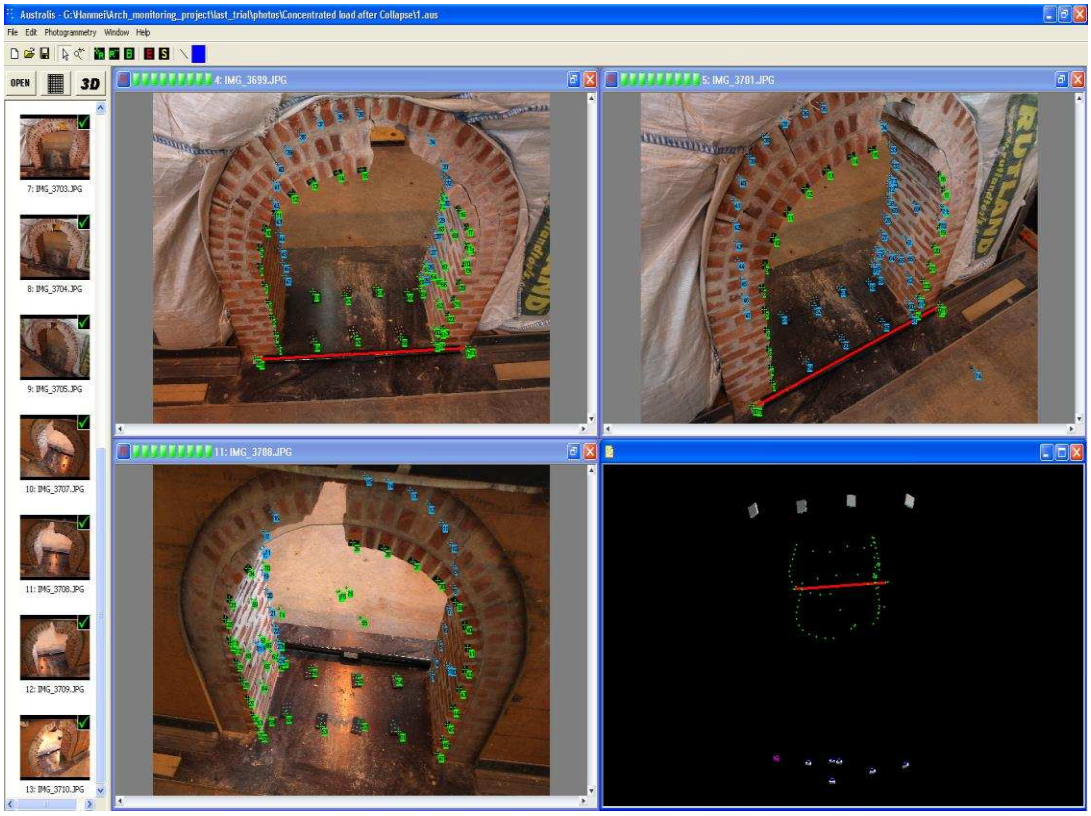

Figure 3.31 3D photogrammetric network of multiple images and the 3D view

b) Setting the scale

In this step, the tunnel measurements were scaled to true size using a scale bar. The process utilises the image of a scale bar of known distance between its two end targets. The scale bar targets are measured and a scale factor is computed and applied. With this registered value, subsequent tunnel point-to-point distances were made in reference to it.

c) Coordinate system transformation using control points

As the 3D images obtained for the tunnels at each load were initially set up in their own local coordinate systems, it was necessary to undertake coordinate transformation to a single Primary Coordinate System. In this study, the coordinate system of the tunnels' original 3D images (without any load) was utilised as the Primary Coordinate System.

The transformation is defined by 'control points' with known coordinates in two Cartesian reference systems: Xc, Yc, Zc coordinates from the existing Primary Coordinate system, and X, Y, Z coordinates from the Secondary Coordinate system. Figure 3.32 illustrates a 2D coordinate transformation, which is similar to 3D transformation.

Given three or more control points that are non co-linear (as Points 2, 10, 11 and 15 here), a 2D transformation can be performed from the specified Secondary XYZ system to the Primary XcYcZc system of the control points.

d) Exporting XcYcZc coordinate points of interest

Finally, the XcYcZc coordinate data is exported for further analysis in Excel.

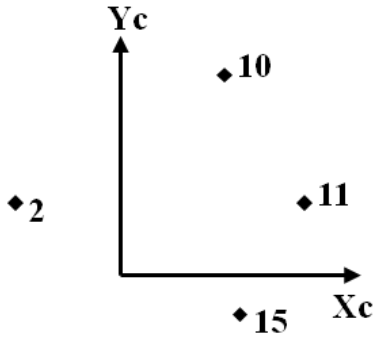

a) Control points in Primary Xc,Yc system (Points 2,10,11 and 15)

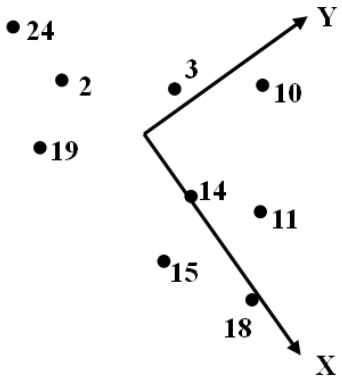

b) Measured points in Secondary X, Y system

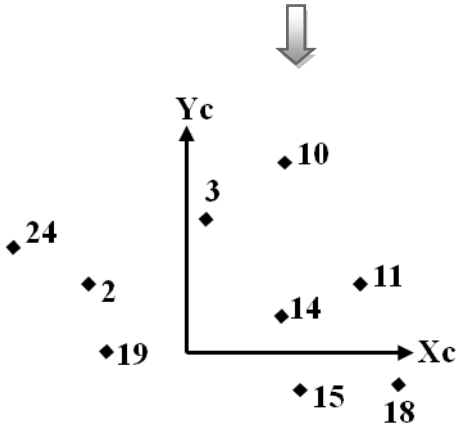

c) Measured points transformed into the Primary Xc, Yc system

Figure 3.32 2D transformation of XY coordinates into Xc, Yc coordinates (after Australis Users' Guide)

3.9.3 Tunnel monitoring and data processing of measurements using the Laser Scanning Technique

'Geomagic Studio 10' software is used to post-process the test data for the close-range laser scanner measurements.

The scanning object exists in 'Point phase' in Geomagic Studio as a collection of scanned points. The Point phase explains the registration and merging of two adjacent points to form a polygon object. The basic workflows of point phase are shown below, taking the scanning of failed physical model after concentrated load as an example:

a) Deleting redundant points and reducing noises

Since the raw data from scanning is of 360 degree, there are a large number of unnecessary points. It is essential to delete unrelated points to minimise the amount of data. After that, 'clouds of points' 3D model of brick-lined tunnel are obtained shown in Figure 3.33.

Some of the redundant points nearby the point cloud tunnel may remain, which are hard to be reduced manually. Those so-called noises could produce sharp edges, or cause smooth curves to become rough when a polygon object is created. Thus, Noise Reduction function is used to reduce the number of errant points, resulting in more uniform arrangement that the polygon object can be formed more smoothly.

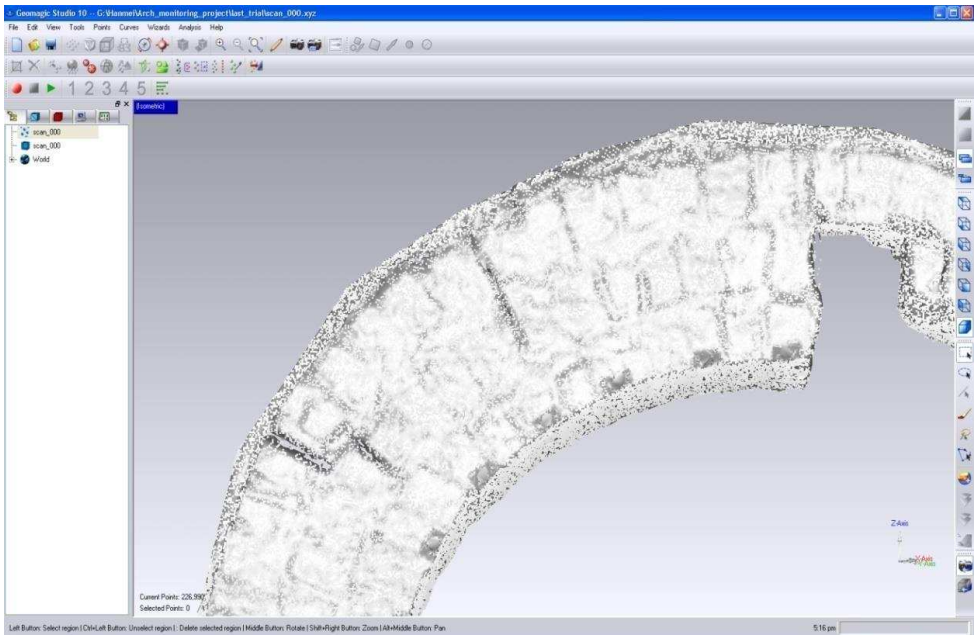

Figure 3.33 Partial 3D model in point clouds

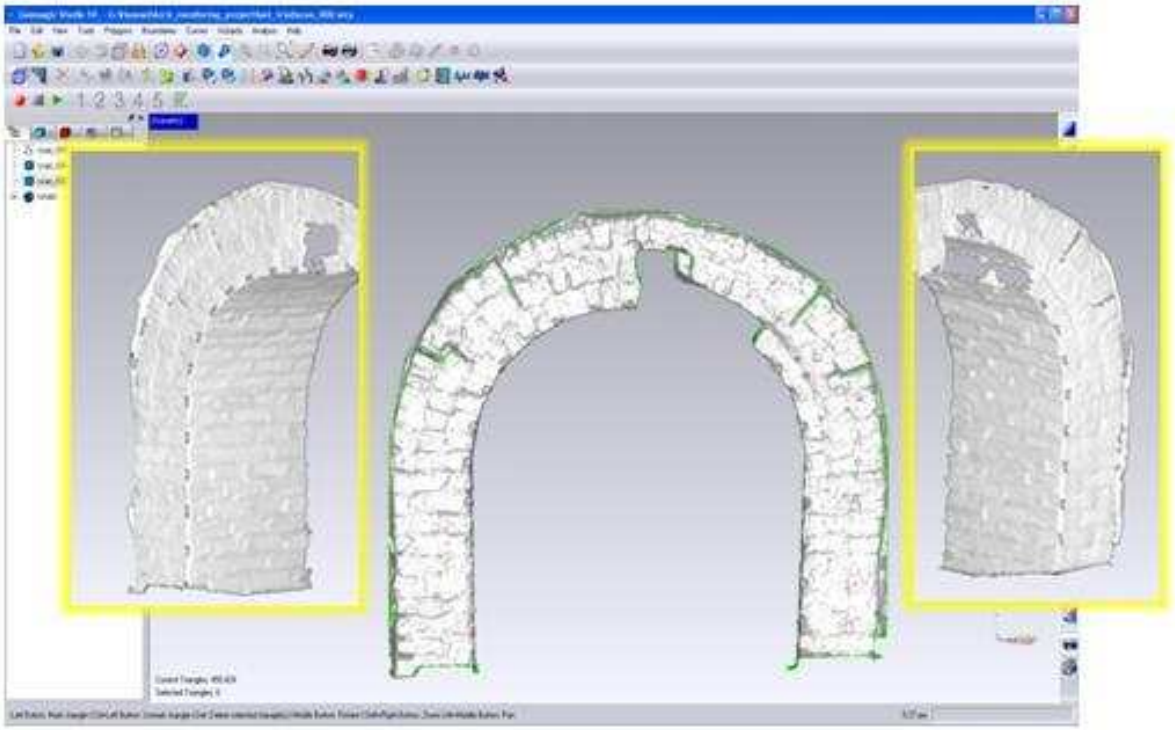

Figure 3.34 3D tunnel model after wrapping

b) Wrapping the tunnel model

Using the Wrap function to create a polygon object: Wrapping performs as stretching plastic sheeting around one point and pulling it to form a polygonal surface, thus changing the 3D model of point clouds into a polygonal object with sided edges as shown in Figure 3.34.

c) Observation for cracks and defects

Figure 3.34 clearly demonstrates the mode of failure and hinges appearing at the arch, from the front view and side views of the scanning model. Even the layout of the brickwork could be seen especially at two sides of the tunnel's inner surface.

d) Distance measurement

Now the original point cloud has become a polygon object, which could be measured using distance measurement. Since several cracks and defects have been observed, it is required to measure the crack width and length (see Figure 3.35). This allows the laser scanning technique to be compared to the conventional vernier calliper.

e) Deformation measurement and Mapping of the differences

An average value for each deformation is determined by analysing the registered point cloud in coordinates.

3D Compare function helps to generate a 3D colour coded mapping of the deformations between two surfaces at different conditions, such as under various loadings. More figures illustrated this function are shown in Appendix B.

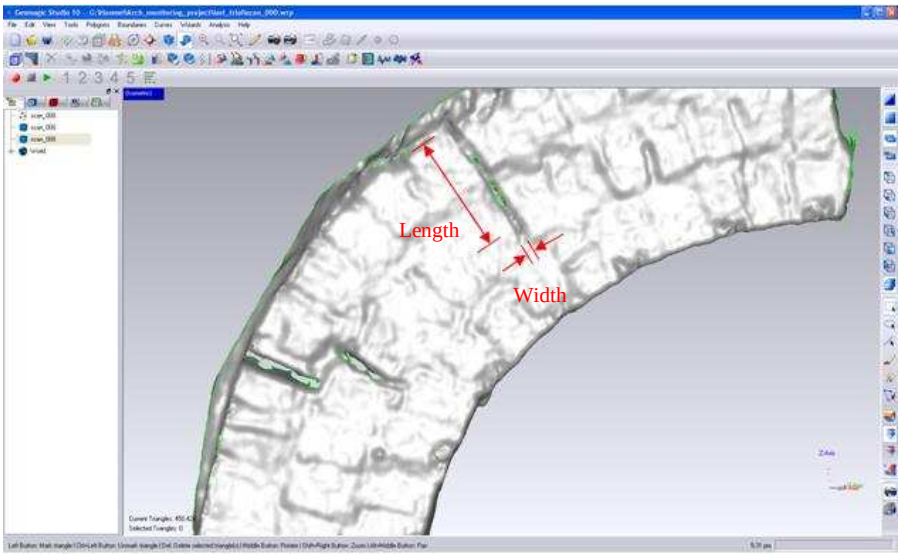

Figure 3.35 Crack width and length measurement

3.9.4 Results and comparison of the monitoring equipment

1) Introduction to measurement comparisons

In order to compare the tunnel crown deformation measuring results of the monitoring equipment (photogrammetry, the laser scanning system and potentiometers), physical model test 1 with a mortar mix proportion of 1:1:6, was used here as an example, at the uniform load of 0 kN and 590 kN.

To compare the distance measuring results (crack width and length) of the monitoring equipment (photogrammetry, the laser scanning system and the vernier calliper), physical model 3 (with a mortar mix proportion of 1:2:9) at failure under concentrated loading, was employed.

2) Deformation measurement by photogrammetry

Through photogrammetry, it was possible to determine deformations at other targeted points of interest, such as those located at a quarter and three quarters of the

span of the tunnels' arches, except the crown deformations of tunnels. They were also important points to monitor the arch behaviour (see Figure 3.36). The centre point of all the target points was maintained using the Centroiding function in Australis for the different loading conditions as seen in Figure 3.37.

For the tunnel of the physical model 1 with a mortar mix proportion of 1:1:6 under the uniform load of 0 kN and 590 kN, vertical crown deformation and diagonal deformation at the target points located at a quarter span of the tunnel arch, have been analysed as shown by the coordinates presented in Table 3.11.

With the help of photogrammetry, the pressure versus displacement curve at a quarter span of the tunnel arch from load 0 kN to 590 kN is shown in Figure 3.38. It would be compared with numerical results in Chapter 4.

The starting point of the coordinate system was set to the first camera station as default.

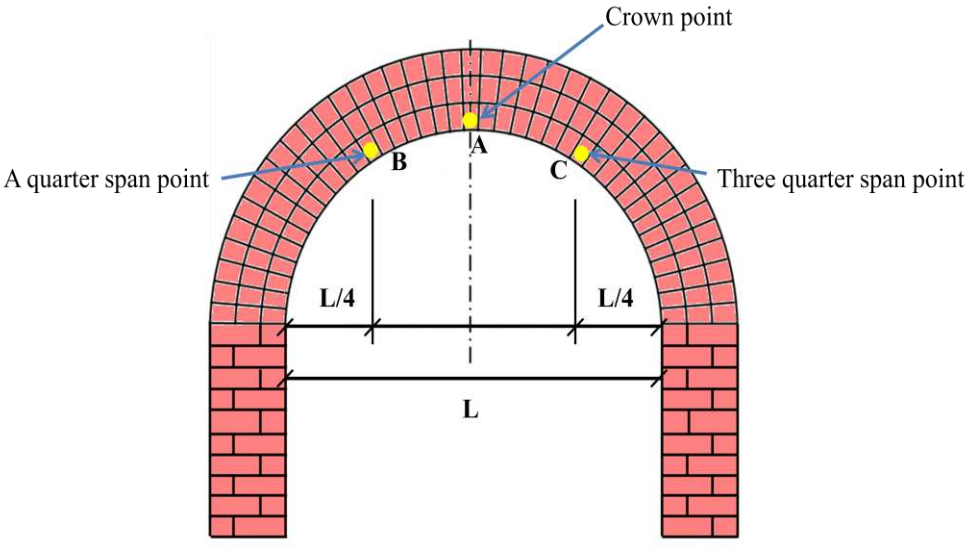

Figure 3.36 Target points in yellow measured via photogrammetry

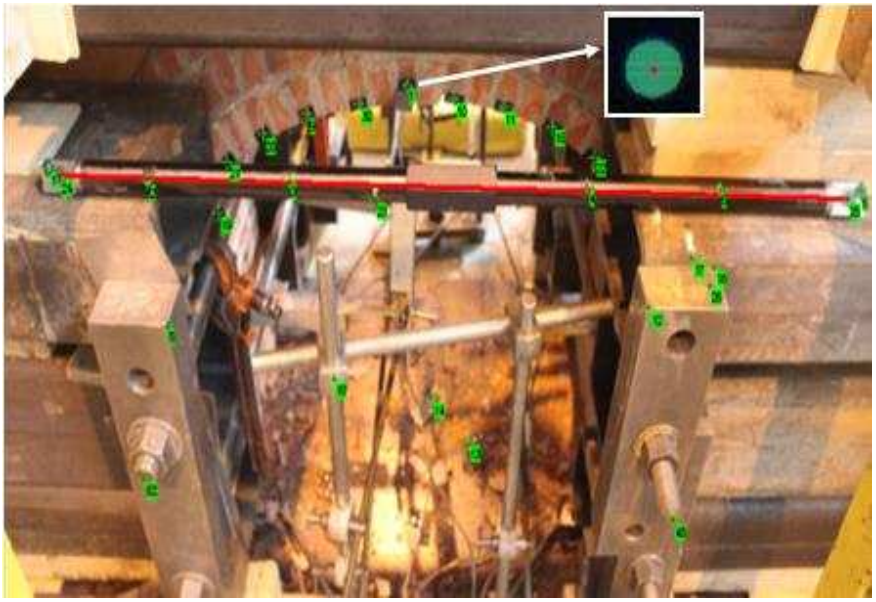

Figure 3.37 Target points used for photogrammetry processing

Table 3.11 Deformation results by photogrammetry

Target point at the crown				
Position No.	Coordinates from two measurement epochs			Deformation (mm)
	X (mm)	Y (mm)	Z (mm)	
A (at 0 kN)	-53.09	1058.14	239.79	35.63
A'' (at 590 kN)	-52.06	1068.80	205.80	
Target point at the a quarter span of the tunnel arch				
Position No.	Coordinates from two measurement epochs			Deformation (mm)
	X (mm)	Y (mm)	Z (mm)	
B (at 0 kN)	-300.00	1064.75	97.10	20.78
B'' (at 590 kN)	-314.54	1052.94	88.11	

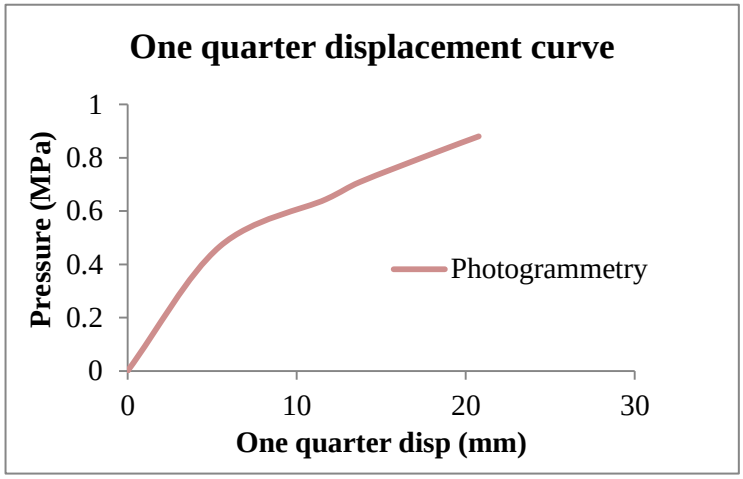

Figure 3.38 A quarter span displacement curve with the aid of photogrammetry

3) Deformation measurement by the laser scanning system

Figure 3.39 and Figure 3.40 demonstrate the 3D deviation of the tunnel crown part in different colours, showing the displacement between images at 0 kN and 551 kN load. The maximum deformation was at the crown around 30 mm. The deformation gradually reduced towards the springing of around a minimum of 2 mm.

The blank parts in the images were due to the covering of the steel bars bolted on the hollow steel beam when scanning. The grey parts were as a result of insufficient data for valid comparison, from the test against the original object. We could also see from Appendix B for more details, the 3D deviation between each two scanning image at different loads.

An average value from three points at the crown was recorded for load 0 kN and 590 kN, shown in Table 3.12. The result was compared with the results of both photogrammetry and potentiometers in the later section, for the same physical model test.

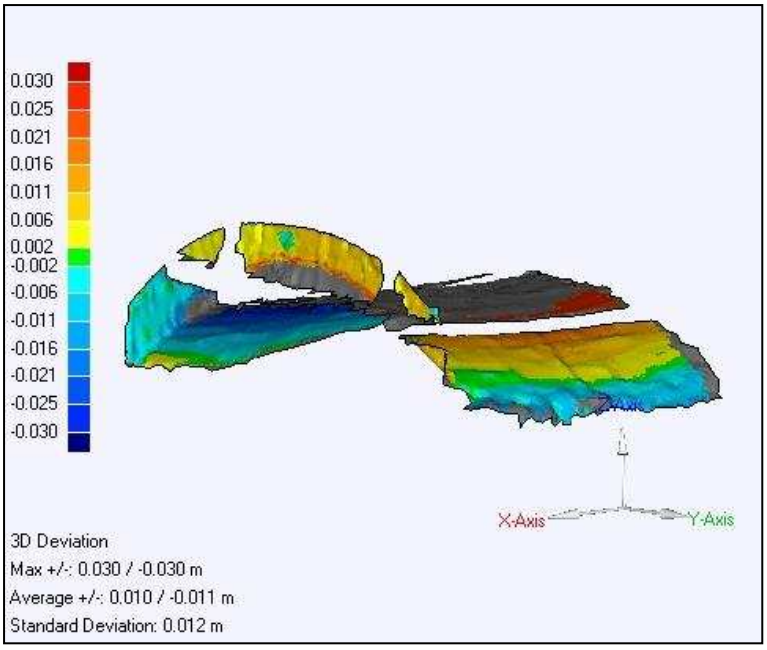

Figure 3.39 The side view of the 3D deviation of the tunnel crown

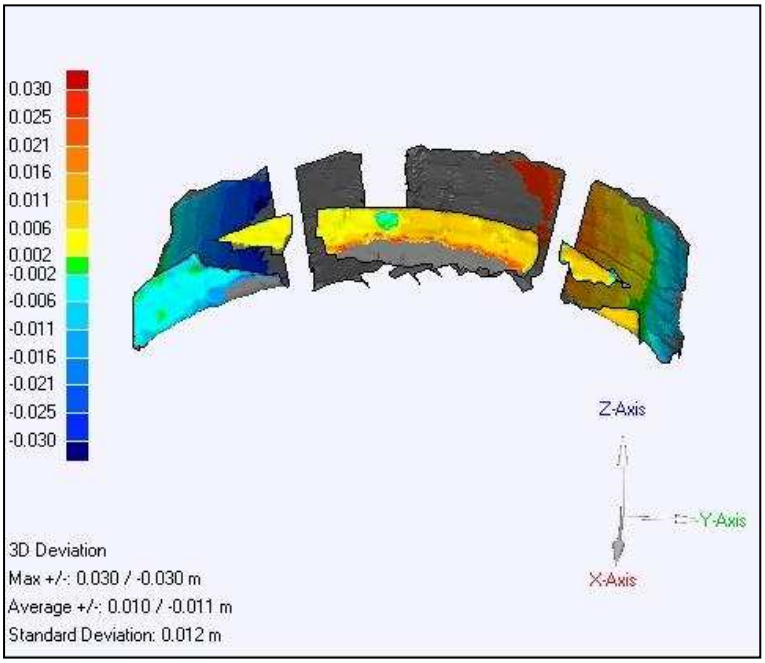

Figure 3.40 The oblique view of the 3D deviation of the tunnel crown

Table 3.12 Deformation results by the laser scanning technique

Position No.	Crown coordinates from two measurement epochs			Deformation (mm)
	X (m)	Y (m)	Z (m)	
1 (at 0 kN)	-1.583638	-0.098053	0.535654	40.10
2 (at 0 kN)	-1.582363	-0.108903	0.534358	
3 (at 0 kN)	-1.582369	-0.121182	0.536781	
Average	-1.582790	-0.109379	0.535598	
1'' (at 590 kN)	-1.575600	-0.092600	0.494900	
2'' (at 590 kN)	-1.575600	-0.104300	0.495100	
3'' (at 590 kN)	-1.578000	-0.116400	0.496100	
Average	-1.576400	-0.104433	0.495367	

4) Distance measurement by photogrammetry

The accuracy of distance measurement by photogrammetry, such as the crack width and length, is of great importance to be figured out for the monitoring work.

Figure 3.41 and Figure 3.42 show the major crack (hinge failure) at one third of the tunnel arch of the physical model 3. An average crack length of three values has been taken; while crack width has been specified and measured from three different locations due to width variations along the crack (the beginning of the crack, the middle of the crack and the end of the crack, position numbered 1 to 3 separately) in Table 3.13. One of the key influence factors would be the processing work of manual measurement operation. For this tunnel arch, the estimated accuracy of 3D point coordinates was shown in Table 3.14, with the overall accuracy of ± 0.45 mm.

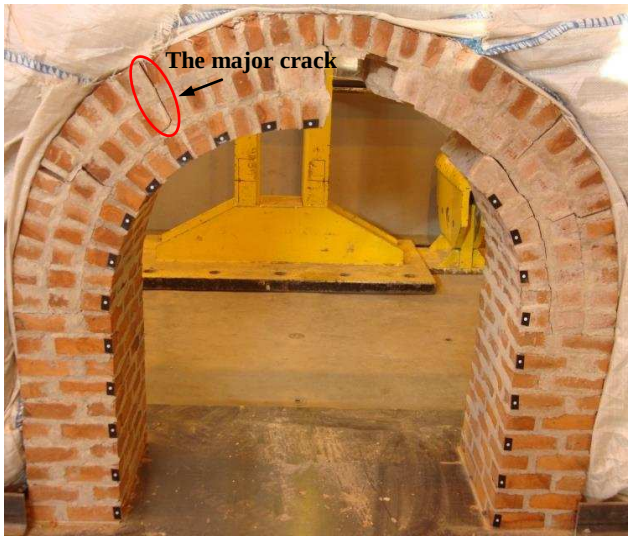

Figure 3.41 The major crack at one third of the tunnel arch of the physical model 3 for the measurement of crack length and width

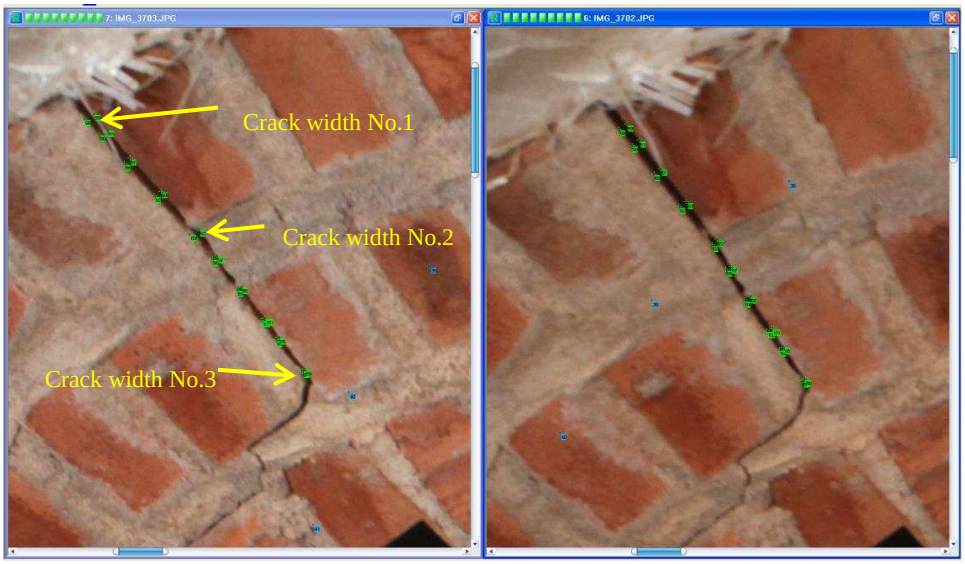

Figure 3.42 Non-targetted points of interest in coordinates along a major crack

Table 3.13 The major crack results by photogrammetry

Crack length No.	Crack length in each coordinate			Crack length (mm)
	∆X (mm)	∆Y (mm)	∆Z (mm)	
1	54.29	58.45	66.15	103.63
2	53.79	59.06	66.32	103.83
3	52.43	60.04	65.99	103.48
Average	53.50	59.18	66.15	103.65
Position No.	Crack width in each coordinate			Crack width (mm)
	∆X (mm)	∆Y (mm)	∆Z (mm)	
1 (The beginning position)	2.03	1.46	1.99	3.20
2 (The middle position)	1.46	2.57	2.34	3.77
3 (The end position)	0.63	1.26	1.35	1.80

Table 3.14 Estimated accuracy of 3D point coordinates

X coordinate (mm)	Y coordinate (mm)	Z coordinate (mm)	Overall (mm)
± 0.279	± 0.673	± 0.402	± 0.450

5) Distance measurement by the laser scanning system

The same crack (hinge failure) at one third of the arch was measured using the laser scanning technique, as that measured using photogrammetry, shown in Figure 3.43.

For crack length (i.e. total distance), average value was taken from three results. For crack width, the beginning, middle and the end of the crack width were taken. Results were shown in Table 3.15.

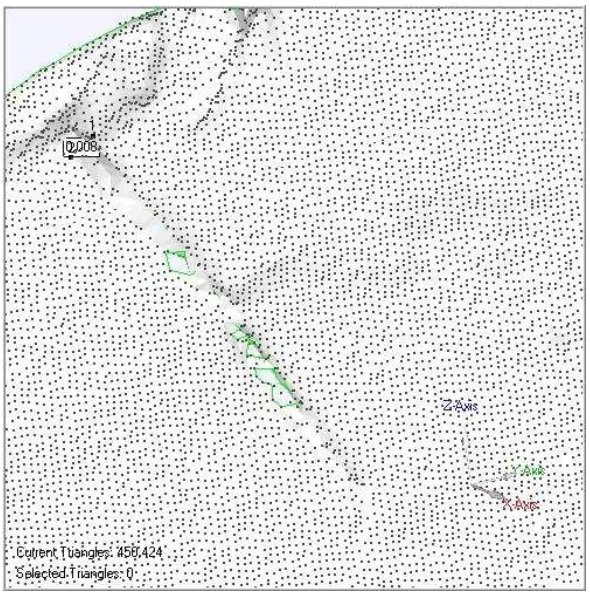

Figure 3.43 Cloud points in coordinates among a major crack from the laser scanning technique

Table 3.15 The major crack by the laser scanning technique

Crack length No.	Crack length in each coordinate			Crack length (mm)
	∆X (mm)	∆Y (mm)	∆Z (mm)	
1	24.98	49.84	87.12	103.43
2	24.37	48.66	87.80	103.30
3	23.17	47.53	88.55	103.13
Average	24.17	48.68	87.82	103.29
Position No.	Crack width in each coordinate			Crack width (mm)
	∆X (mm)	∆Y (mm)	∆Z (mm)	
1 (The beginning position)	4.62	2.09	1.94	5.43
2 (The middle position)	2.44	4.03	2.88	5.52
3 (The end position)	1.78	1.97	0.86	2.79

6) Comparison results

Deformation measurement comparison

The crown deformation measurements from the potentiometers, photogrammetry and the laser scanning system were compared using physical model test 1 with mortar mix proportion 1:1:6, at the uniform load of 0 kN and 590 kN.

Ideally, the measuring method (i.e. potentiometers, photogrammetry and the laser scanning technique) was in the same condition. However, the monitoring work during loading was not simultaneous. During each loading interval, the results of potentiometers were recorded first within 3 seconds, followed by digital images taken for photogrammetry in 30 seconds and finally the scanning work of the laser scanner that took around 1 minute.

During this minute, the tunnel may deform slightly to achieve equilibrium, thus there were some variation in the deformation due to the small time difference in measurement.

As Table 3.16 displays, the results difference between potentiometers and photogrammetry was 8.5 mm while difference between potentiometers and the laser scanner was up to 13 mm. For a shorter length of time between photogrammetry and the laser scanner, the variation was smaller at 4.5 mm.

Table 3.16 Deformation results comparison at the crown

Measuring method	Crown coordinates from two measurement epochs			Average deformation (mm)
	X (mm)	Y (mm)	Z (mm)	
POT	N/A			27.14
	N/A			
Photogrammetry	-53.09	1058.14	239.79	35.63
	-52.06	1068.80	205.80	
Laser scanning	-1582.79	-109.38	535.60	40.10
	-1576.40	-104.43	495.37	

Distance measurement comparison

The length and width of the major crack (hinge failure) at one third of the tunnel arch (with mortar mix proportion 1:2:9) under concentrated loading were analysed using a vernier calliper (shown in Table 3.17), photogrammetry and the laser scanning technique.

The measuring results from the vernier calliper were used as a benchmark. The beginning, middle and the end of the crack width were measured by the vernier calliper corresponding to position number 1 to 3 in Table 3.17.

Since this crack was measured after hinge failure and up to a new equilibrium, there should be no more variation of the crack size. In other words, the crack results would not be affected by the sequence of measurement.

Table 3.17 The major crack results by a vernier calliper

Crack length No.	Crack length (mm)
1	103.34
2	103.65
3	103.22
Average	103.40
Position No.	Crack width (mm)
1 (The beginning position)	4.13
2 (The middle position)	4.33
3 (The end position)	2.78

The results comparison was shown in Table 3.18 and Table 3.19 below.

For crack length, the difference between the vernier calliper and photogrammetry was only 0.25 mm while the difference between the vernier calliper and the laser scanner was as small as 0.11 mm. It shows a good comparison from both photogrammetry and the laser scanning techniques within 0.3 mm.

For crack width, the difference between the vernier calliper and photogrammetry at the 3 same positions was only 0.93 mm, 0.56 mm and 0.98 mm while the difference between the vernier calliper and the laser scanner was 1.30 mm, 1.19 mm and 0.01 mm at these 3 positions. Therefore, the photogrammetry result compared was better than the laser scanning.

Table 3.18 The major crack length results comparison

Measuring method	Average crack length in each coordinate			Average crack length (mm)
	∆X (mm)	∆Y (mm)	∆Z (mm)	
Vernier calliper	N/A	N/A	N/A	103.40
Photogrammetry	53.50	59.18	66.15	103.65
Laser scanning	24.17	48.68	87.82	103.29

Table 3.19 The major crack width results comparison

Measuring method	The beginning position (mm)	The middle position (mm)	The end position (mm)
Vernier calliper	4.13	4.33	2.78
Photogrammetry	3.20	3.77	1.80
Laser scanning	5.43	5.52	2.79

3.10 Summary

3.10.1 Design of different physical models

A set of physical models was designed and outlined to represent the brick-lined railway tunnels under different mortar and loading conditions. Half-scale typical bricks were used for building the tunnel. In addition, dimensions, building and installation process, and model materials for the tests were described.

3.10.2 Programme of physical model testing

A programme of physical model tests was conducted which included two static uniform load tests to failure by varying mortar strengths and one static concentrated load test to collapse.

The mode of failure of physical models under uniform and concentrated load differed. The first two physical models, which were under uniform load, failed as a result of shear failure at the sidewalls as the major force was transferred to the sides. The third physical model, which was under concentrated load, failed due to the formation of five structural hinges at the tunnel arch.

The physical model under concentrated load seemed to reduce the ultimate capacity of the tunnel by approximately 30%, comparing with the model under uniform load.

For both first and second physical models under uniform load, built with different mortar mix proportions of the brick-lined tunnels, ultimate capacity was affected by the compressive strength of the tunnel materials.

In summary, the small-scale physical model tests clearly indicated the mechanical behaviour of the brick-lined tunnel with various mortar strengths and under different loadings. The ultimate load capacity and mode of failure were also determined and compared with different models.

The results of three physical models were used to validate the numerical models built in Chapter 4 Numerical Simulation. Details and comparisons of the results between physical models and numerical models are to be found in Chapter 4.

3.10.3 Monitoring techniques

During the loading test, potentiometers and two advanced techniques, photogrammetry and the laser scanning, have been used for monitoring the tunnel deformation. Moreover, inspecting defects (cracks) on the tunnel shells were carried out by the two advanced techniques.

The data was analysed in the post-processing work and some conclusions were drawn as below:

a) Photogrammetry usually works with the help of daylight, or a lighting system in a dark environment, whereas the laser scanning system performs well without any aid of lighting to observe cracks and defects.
b) The observation of defects such as a major crack around 3 to 5 mm wide could be clearly identified in the laser scanning data. The accuracy of the laser scanning technique is within 1.3 mm when compared with the vernier calliper, while the accuracy of photogrammetry is within 1.0 mm. Both of them are suitable to measure the tunnel defects such as major cracks.
c) Photogrammetry shows a strong potential for measuring tunnel deformation with high accuracy with the help of lighting (see a)). The centre point of target points could be easily captured by Centroiding function in the related post-processing software Australis, rather than ambiguous point cloud of the target points in the laser scanning system.

CHAPTER 4 NUMERICAL SIMULATION

4.1 General introduction

Nowadays, numerical modelling has been increasingly used to assess the stability of tunnels and underground caverns. However, an analysis of the mechanical behaviour of existing brick-lined tunnels remains challenging due to the complex material components.

In this research, numerical models are developed using FLAC (Finite Difference Method) and UDEC (Distinct Element Method) programmes to simulate the mechanical behaviour of physical models after loading which were tested in Chapter 3. In other words, physical model tests also act as a validation for numerical simulations. Thus in the future research, these numerical models could be applied to the field study and enable accurate predictions of the actual mechanical behaviour of a masonry tunnel.

4.2 Programme of material testing

4.2.1 General introduction

Due to the uncertainty in the material property database, the selection of material properties is usually one of the most difficult parts in numerical simulation (Jia, 2010).

A series of laboratory tests were carried out to obtain the properties of brick, mortar and soil conventionally. The tests included uni-axial and single stage tri-axial compressive strength tests, direct shear box tests and so on. The following data were

gained from these tests and have been included in Appendix A in this thesis. These properties were used in the numerical simulation:

a) Density (ρ)

b) Young's modulus (E)

c) Uni-axial compressive strength (σ_c)

d) Mohr-Coulomb strength properties (cohesion c and friction angle φ)

e) Tensile strength (Tr)

For the other uncertain properties, an appropriate selection of properties based upon the available database or laboratory tests was conducted in parametric studies, compared with the results from the related physical model tests.

4.2.2 Brick

1) Uni-axial compressive strength test (UCS test)

The brick cylinder samples for the UCS test were cored from full-sized bricks of the same batch. The required dimension was 37 mm in diameter and 74 mm (twice of the diameter) in height. Thus, four samples could be cored from one full-sized brick (see Figure 4.1 (b) & (c)). The tests were conducted by a stiff testing machine in the Nottingham Centre for Geomechanics (NCG) (see Figure 4.1 (a)).

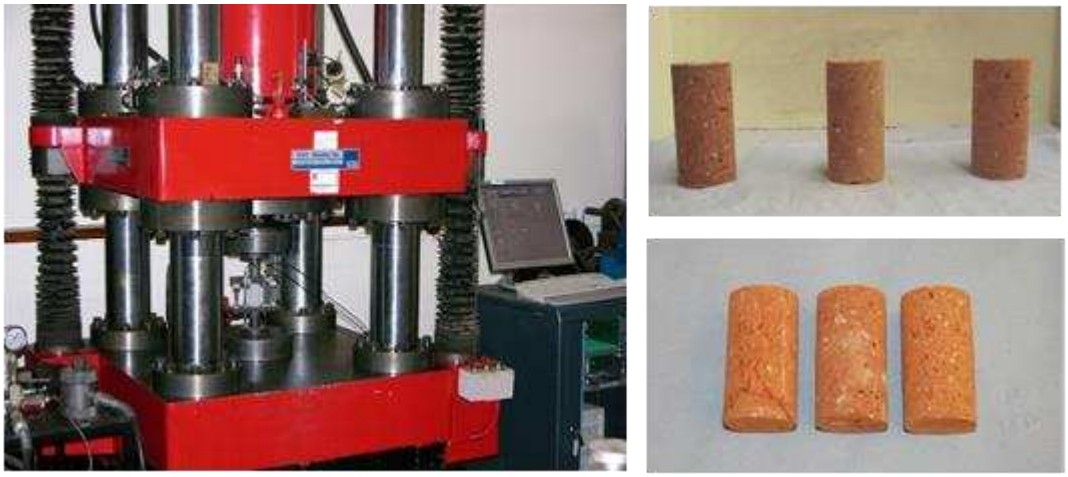

Figure 4.1 (a) Stiff testing machine in NCG; (b) & (c) Brick samples

The uni-axial loading rate was 0.02 mm/s. Initially, four sample tests were carried out. Five more sample tests then followed to obtain the average properties, especially for brick density, ultimate compressive strength and Young's modulus, as shown in Table 4.1.

The load versus displacement curve is also shown Figure 4.2. In general, most samples failed at an average of 28.4 kN around 0.27 mm displacement. However, the load value of sample 8 and sample 9 seemed different from the other samples as their failure load exceeded 40 kN. The higher strength of these two samples is due to the nonuniformity of a single brick during manufacture process. It's one of the natural characteristic of bricks.

Table 4.1 UCS test list of bricks

Sample Reference	Average Length (mm)	Average Diameter (mm)	Sample Density (g/cm^3)	Failure Load (kN)	Ultimate Compressive Strength (MPa)	Young's Modulus (GPa)
Sample 01	74.18	37.02	1.67	27.9	25.9	6.8
Sample 02	74.21	36.99	1.66	24.2	22.5	5.8
Sample 03	74.09	37.01	1.66	21.8	20.3	5.7
Sample 04	74.07	36.98	1.66	23.7	22.1	7.0
Sample 05	73.01	37.39	1.65	22.7	20.6	5.9
Sample 06	72.01	37.47	1.67	23.4	21.2	6.5
Sample 07	74.01	37.41	1.66	25.9	23.5	7.2
Sample 08	74.01	37.48	1.82	44.2	40.1	11.6
Sample 09	73.94	37.44	1.75	41.8	38.0	10.5
Average	**73.73**	**37.24**	**1.69**	**28.4**	**26.0**	**7.5**
Standard Deviation	0.74	0.23	0.06	8.49	7.6	2.1

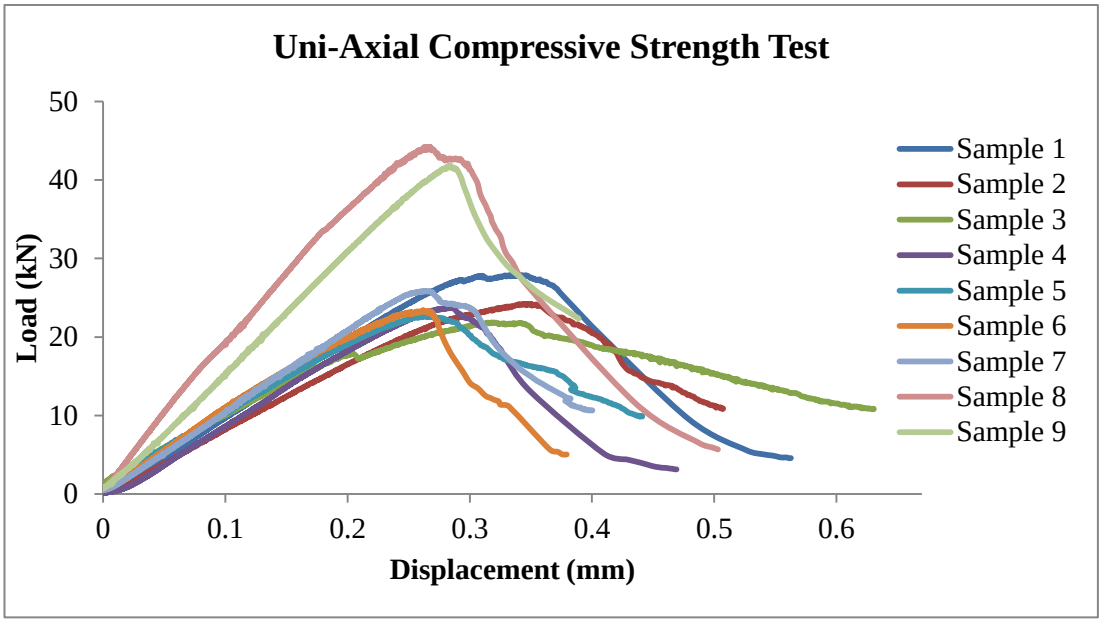

Figure 4.2 Load against displacement of UCS brick property test

2) Tri-axial compressive strength test (σ2 = σ3)

The single stage tri-axial compressive strength tests were carried out using 12 cylinder samples (The same size as the uni-axial test sample) at a confining pressure of around 1, 3, 5 and 10 MPa individually. For each confining pressure, the tri-axial test was repeated three times.

The results of the ultimate compressive strength helped to obtain the brick properties of cohesion and friction angle. The details are shown in Table 4.2. The axial stress versus axial strain curve is also shown in Figure 4.3.

Figure 4.4 shows the average Mohr-Coulomb circles at different confining pressures. Strength envelopes could be drawn between two circles. Thus, the maximum, minimum and medium friction angle and the relative cohesion could be gained as shown below by the strength envelopes. The result details of various Mohr-Coulomb strength envelopes are listed in Table 4.3. In this research, the maximum and

minimum friction angle and cohesion were omitted, the medium ones were chosen for numerical simulation.

Table 4.2 Tri-axial test list of bricks

Sample Reference	**Average Length (mm)**	**Average Diameter (mm)**	**Confining Pressure (MPa)**	**Failure Load (kN)**	**Ultimate Compressive Strength (MPa)**	**Average Ultimate Compressive Strength (MPa)**
Sample 01	74.05	37.42	1.11	29.6	26.9	21.7
Sample 02	74.01	37.46	1.11	20.8	18.8	
Sample 03	74.01	37.36	1.11	21.3	19.5	
Sample 04	74.07	37.42	3.06	40.0	36.3	36.0
Sample 05	74.08	37.46	3.06	38.5	34.9	
Sample 06	73.66	37.46	3.06	40.5	36.7	
Sample 07	73.68	37.42	5.01	40.3	36.6	46.3
Sample 08	74.06	37.45	5.00	65.4	59.4	
Sample 09	74.01	37.46	5.01	47.1	42.8	
Sample 10	73.98	37.45	9.93	76.8	69.7	69.6
Sample 11	73.12	37.42	9.92	69.3	63.0	
Sample 12	73.79	37.45	9.93	83.8	76.1	
Average	**73.88**	**37.44**	-	-	-	-
Standard Deviation	0.28	0.03	-	-	-	-

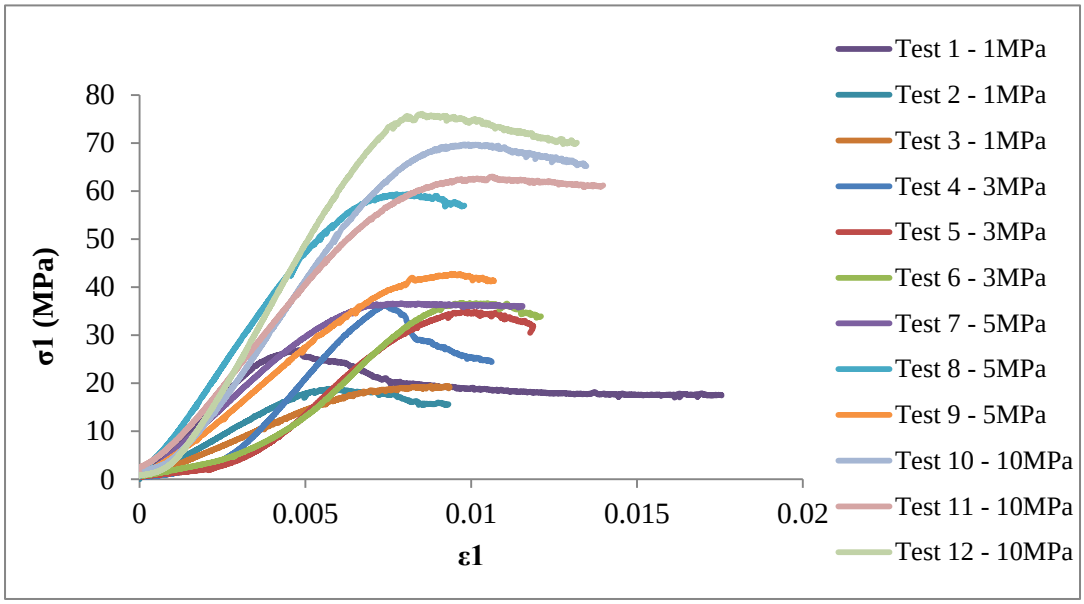

Figure 4.3 Axial stress against axial strain of tri-axial brick property test

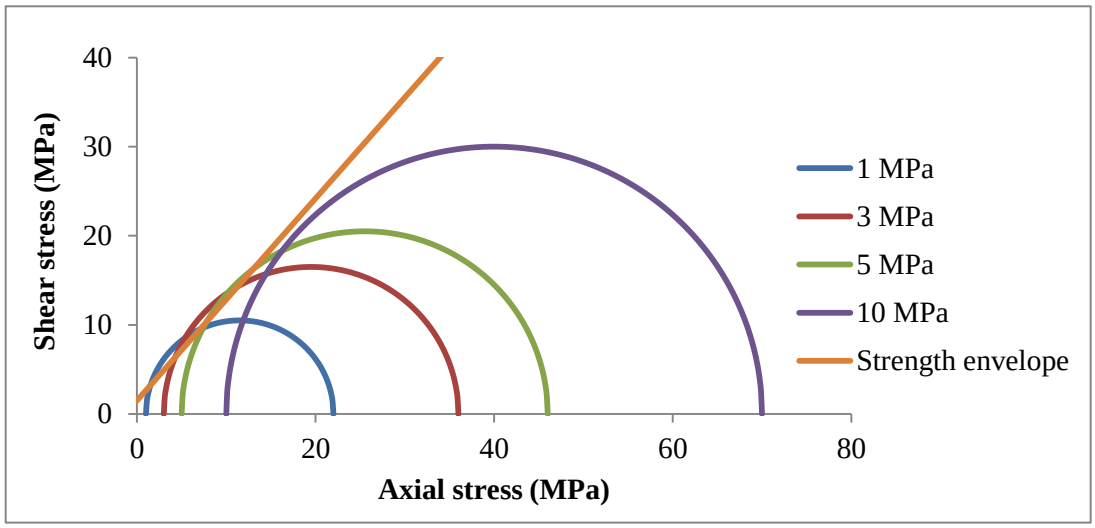

Figure 4.4 Shear stress against axial stress of tri-axial property test

Table 4.3 Results of various Mohr-Coulomb strength envelopes

	Strength Envelope 1	Strength Envelope 2	Strength Envelope 3
Friction angle	44° (Max.)	41° (Min.)	43° (Medium)
Cohesion (MPa)	4.8	9.5	4.3

4.2.3 Mortar

The 20 mortar samples for each mix proportion of cement to lime to sand (1:2:9/1:1:6) were prepared with the help of the mortar moulds (i.e. PVC pipe sections, as shown in Figure 4.5 (a)). The required dimension was the same as the brick cylinder sample for UCS test (Ø 37 × 74 mm). When the mortar was put into the mortar moulds, a vibrating table was used to get the bubbles out of the moulds. When the mortar samples were demoulded after 14 days, they were still low in strength.

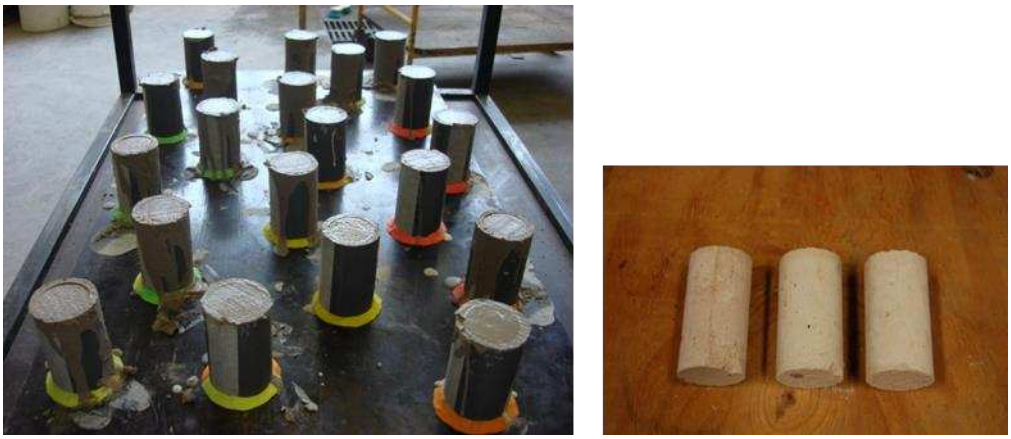

Figure 4.5 (a) PVC pipe sections for mortar sample preparation; (b) Mortar cylinder samples

1) Uni-axial compressive strength test

After 28 days, uni-axial compressive strength tests of mortars in different mix proportions were carried out using a UCS machine. The loading rate was 0.2 mm/min. The results are shown in Table 4.4. A stronger mortar mix proportion of 1:1:6 seems to be stiffer with a higher Young's modulus. The load versus displacement curve obtained from the test data can be seen in Appendix A.

Table 4.4 Average UCS test list of different mortar samples

Mortar samples	Mortar Mix Proportion	Average Length (mm)	Average Diameter (mm)	Failure Load (kN)	Ultimate Compressive Strength (MPa)	Young's Modulus (MPa)
Batch 01	1:2:9	73.93	37.57	3.3	3.1	254
Batch 02	1:1:6	73.97	37.62	4.8	4.4	328

4.2.4 Surrounding soil

1) Shear box tests

Shear box tests (direct shear tests, see Figure 4.6) were utilised to investigate the properties of soil, such as the friction angle.

The shear box could be split horizontally into two halves. A specimen of Portaway sand (60 × 60 mm by 30 mm thick, see Figure 4.7 & Figure 4.8) placed in the box was sheared horizontally by moving the bottom half of the box relative to the top half at a constant rate of 1 mm/min.

A vertical normal stress was applied during shearing and both the vertical displacement of the top of the specimen and the horizontal shear displacement were measured by dial gauges. Failure was prescribed on the plane separating the two halves of the box. The horizontal shear load was applied to the sand in the box with the normal force of 0.5, 1 and 1.5 kN. For each dead weight, the shear test was repeated 3 times; thus, 9 tests were done in total.

The shear force versus horizontal displacement curve at different normal stresses is shown in Figure 4.9. The shear stress versus the normal stress curve is also displayed in Figure 4.10, whilst Figure 4.11 illustrates the average shear stress versus the normal stress curve. The results of the shear box test help to obtain the essential soil properties of the friction angle, as shown in Table 4.5.

Figure 4.6 General view of shear box apparatus

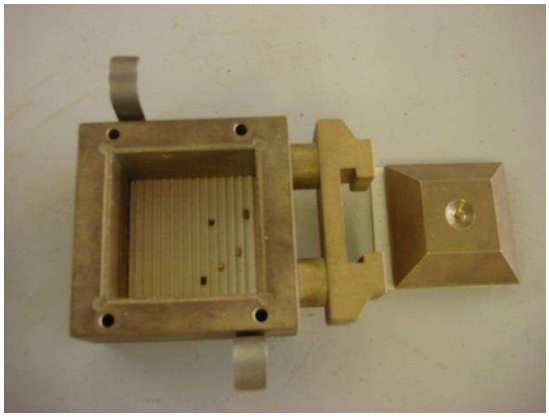

Figure 4.7 Detailed view of shear box sample holder

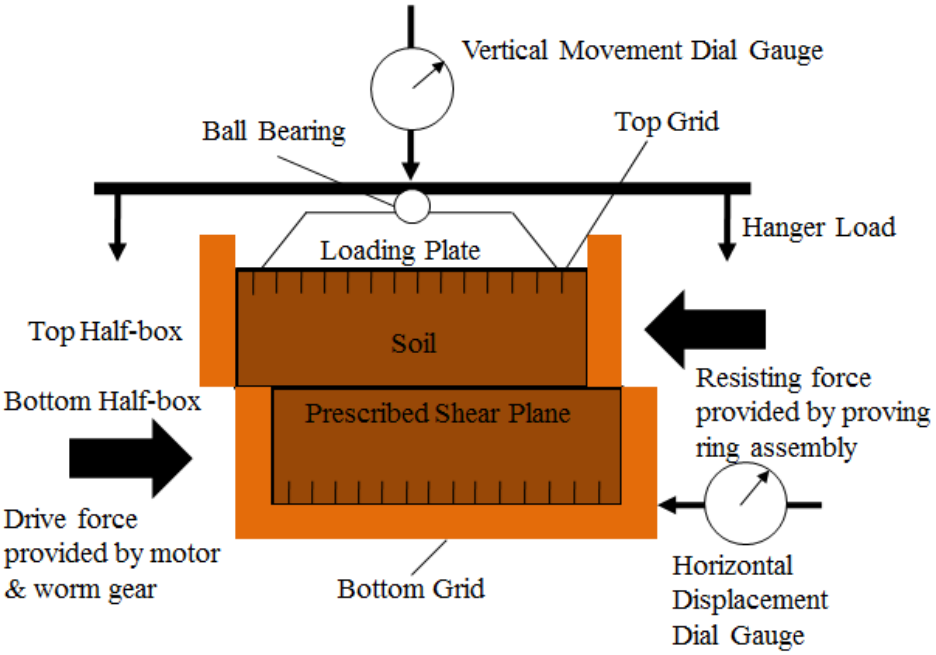

Figure 4.8 Cross section of shear box

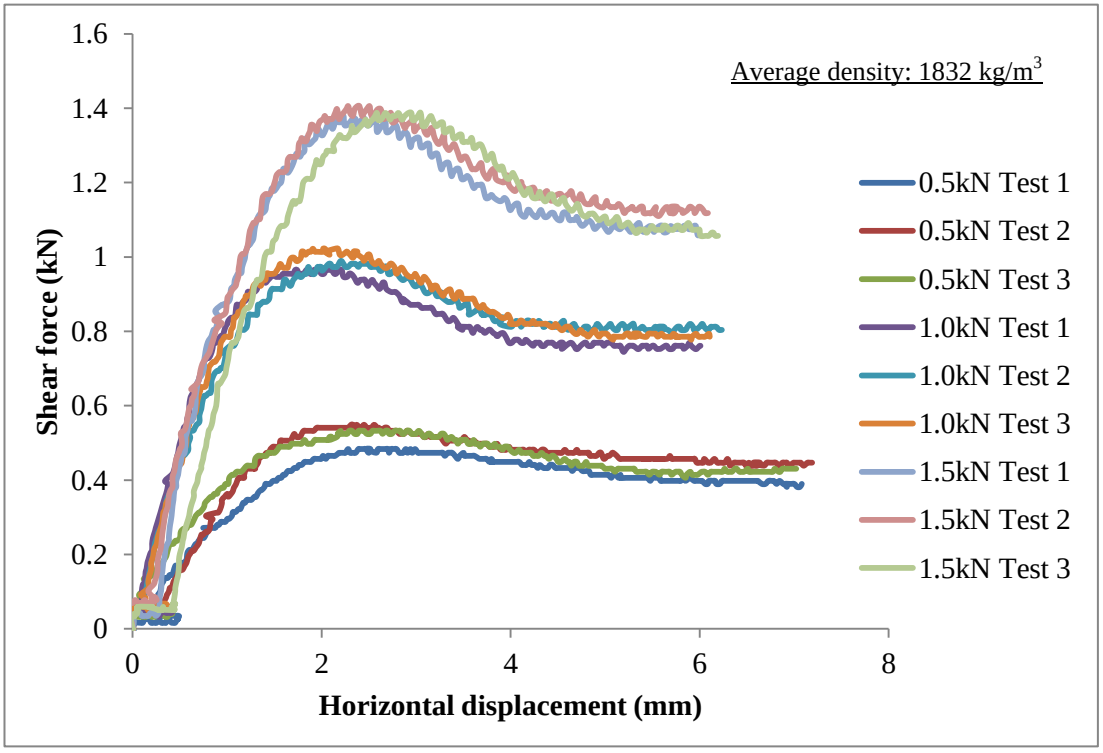

Figure 4.9 Shear force against horizontal displacement in shear box test

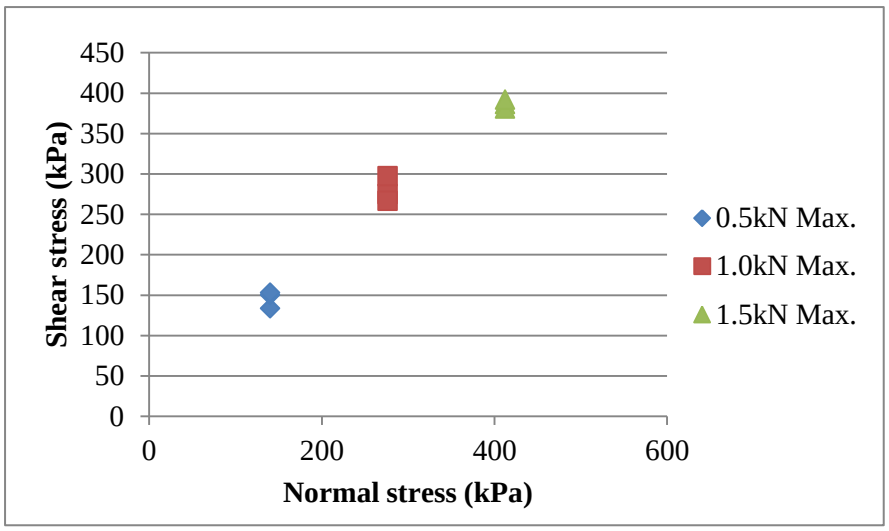

Figure 4.10 Shear stress against normal stress in shear box test

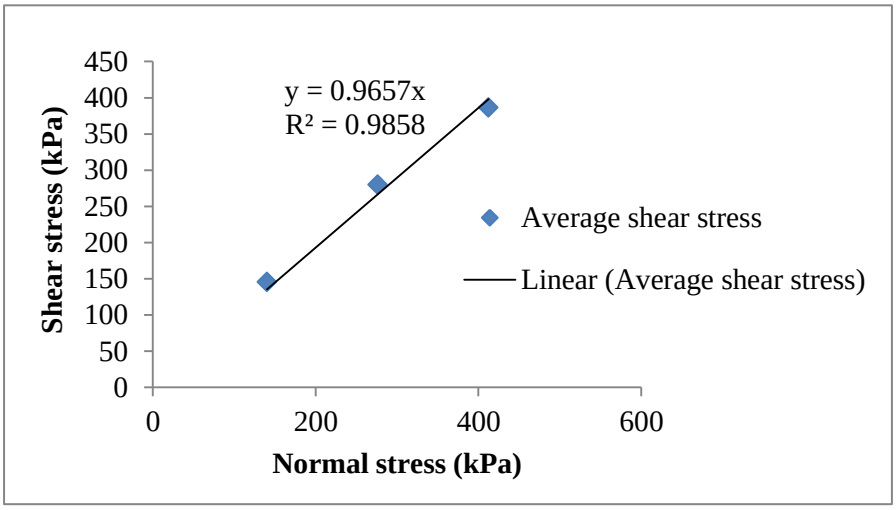

Figure 4.11 Average shear stress against normal stress in shear box test

Table 4.5 Portaway sand partial properties

Soil type	Average density	Cohesion	Friction angle
Portaway sand	1832 kg/m^3	0	44˚

2) Maximum and minimum density test

Since the density of the soil in the physical model may vary during the compaction, the maximum and minimum densities of the soil were tested individually, according

to BS 1377 - 4: 1990. The density of the soil would also affect the value of the friction angle in a numerical simulation. The results are shown below:

$\rho_{min.}$= 1621 kg/m^3

$\rho_{max.}$= 1867 kg/m^3

4.2.5 Brickwork (Triplet / Couplet)

1) Introduction

The format of the brickwork specimen comprised a three half-scale brick triplet sandwich for the UCS test and the shear strength test, with a two half-scale brick couplet for the tensile strength test. The specimens were prepared separately with two mortar mix proportions of cement to lime to sand (1:2:9/1:1:6) and tested at 28 days for quality control purposes. The thickness of the mortar was kept at a constant 5 mm, the same as that in physical models.

2) UCS test

Figure 4.12 The uni-axial compressive strength test of the brickwork

The uni-axial compressive strength tests were carried out using a Universal Testing Machine (UTM) from the Zwick/Roell company, in accordance with BS EN 1052 - 1: 1999 (Determination of compressive strength). The capacity of the UTM is 200 kN.

For each mortar mix proportion, 3 triplet specimens were tested at a loading speed of 0.02 mm/s until failure occurred. As can be seen from Figure 4.12, two LVDTs (Linear Variable Differential Transformer) with a stroke of 10 mm were fixed on two symmetrical faces for each specimen to measure vertical deformations under the applied load.

Calculations

Strength

$$fi = \frac{Fi,max}{Ai} \quad \text{..}\ldots\ldots\ldots\ldots\ldots\ldots\ldots\ldots\ldots\ldots N/mm^2 \ldots\ldots\ldots\ldots\ldots\ldots\ldots\ldots\ldots\ldots\ldots\ldots\ldots\ldots \textbf{(4.1)}$$

Fi,max (N) is the maximum load reached on an individual brickwork specimen, fi (N/mm^2) is the compressive strength of an individual brickwork specimen, and Ai (mm^2) is the loaded cross-section of an individual brickwork specimen. Thus, the mean compressive strength of the brickwork f is obtained.

Modulus of elasticity

$$Ei = \frac{Fi,max}{3 \times \varepsilon i \times Ai} \quad \ldots\ldots\ldots\ldots\ldots\ldots\ldots\ldots\ldots\ldots N/mm^2 \ldots\ldots\ldots\ldots\ldots\ldots\ldots\ldots\ldots\ldots\ldots\ldots\ldots\ldots \textbf{(4.2)}$$

The modulus of elasticity of an individual brickwork specimen is calculated from the mean of all measuring positions occurring at a stress equal to one third of the maximum stress and εi is the mean strain in an individual brickwork specimen at one third of the maximum stress achieved.

The main results of the uni-axial compressive strength tests of the brickwork are shown in Table 4.6 and in Appendix A for figures of load versus displacement.

Table 4.6 UCS test list of various brickwork triplets

Mortar Mix Proportion	Average Length (mm)	Average Height (mm)	Average Width (mm)	Failure Load (kN)	Compressive Strength (MPa)	Young's Modulus (GPa)
1:2:9	99.17	105.67	49.17	33.28	6.83	0.219
1:1:6	104	107.667	48.33	39.30	7.83	0.384

3) Tensile strength test

The bond between brick and mortar is often considered to be the weakest link in brickwork. Thus, the brick-mortar interface is one of the most essential features related to brickwork behaviour.

There are two different failure phenomena occurring in the brick-mortar interface, in the form of tensile failure and shear failure (Lourenco, 1996).

Therefore, a tensile (bond) strength test was carried out associated with tensile failure according to the tensile test by Van Der Pluijm (1992), as seen in Figure 4.13; a shear (bond) strength test was conducted associated with shear failure (see next section for details).

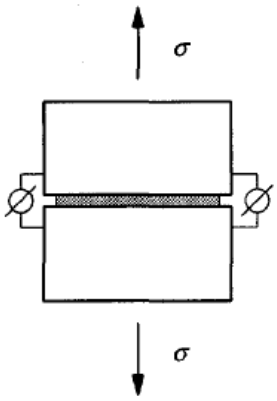

Figure 4.13 Test specimen of tensile strength after Van Der Pluijm (1992)

Calculations

Strength

$$ft = \frac{Fu}{A} \quad \text{N/mm}^2 \quad (\mathbf{4.3})$$

Fu (N) is the ultimate force reached on an individual brickwork specimen, ft (N/mm^2) is the tensile bond strength of an individual brickwork specimen and A (mm^2) is the cross-section area of an individual brickwork specimen where the crack has occurred. (Van Der Pluijm, 1997)

Testing of the couplet

The tensile strength test rig was designed and made in the work shop which enables two bricks to be fixed firmly (see Figure 4.14 (a). The tensile strength tests were carried out using a 'Dual Column Tabletop Universal Testing Machine' (UTM) for mid-range testing from the Instron Company (see Figure 4.15). The capacity of this UTM is 50 kN.

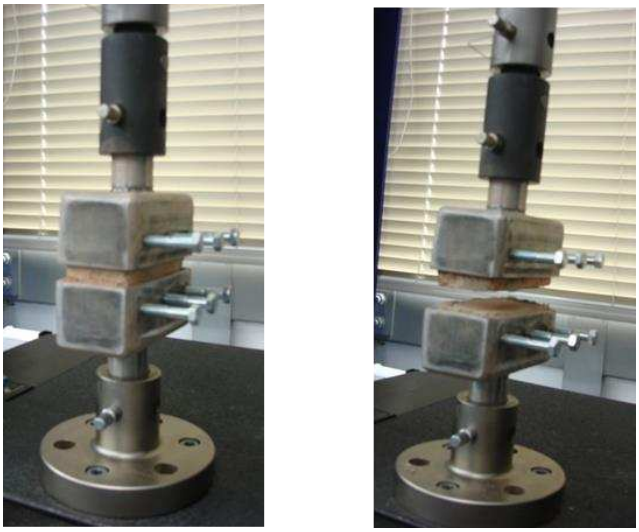

Figure 4.14 (a) The tensile strength test before loading; (b) The tensile strength test after loading

Figure 4.15 The Tabletop Universal Testing Machine after Instron Ltd.

As can be seen from Figure 4.14 (b), after each test the brickwork couplet was separated in the brick / mortar bond area on one or two brick faces (see Figure 4.16). i.e. tensile failure occurred at the brick / mortar interface. It shows a good agreement

with Lenczner (1972), who found that the tensile strength of brickwork was governed by the tensile bond strength.

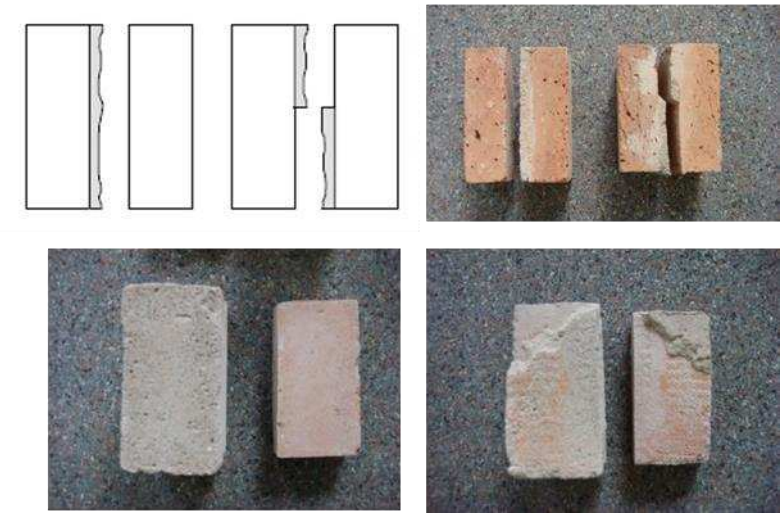

Figure 4.16 Tensile failures at brick / mortar interface

Table 4.7 lists the results of average tensile strength tests which helped to draw Figure 4.17 and shows the tensile strength difference between two mortar mix proportions. Generally speaking, as the strength of mortar mix proportion increased, the tensile strength of brickwork also increased correspondingly. More details of the results are shown in Appendix A.

Table 4.7 The tensile strength test results of brickwork triplets

Brickwork Triplets	Mortar Mix Proportion	Average Length (mm)	Average Width (mm)	Tensile Failure Load (N)	Tensile Strength (MPa)
Batch 01	1:2:9	103.8	45.8	467.09	0.09681
Batch 02	1:1:6	100.367	50.3667	1230.05	0.24369

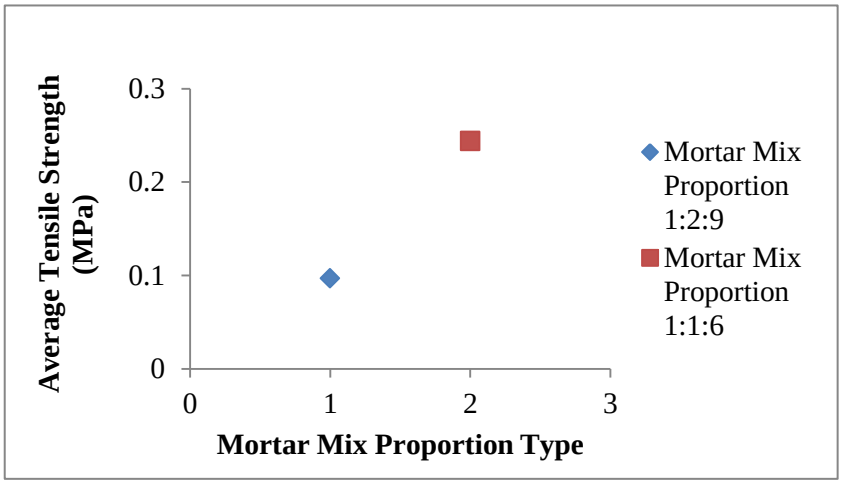

Figure 4.17 Tensile strength of two mortar mix proportions

4) Shear strength test

Figure 4.18 Test rig for shear strength test

The shear strength test was carried out in accordance with the provision of BS EN 1052 - 3: 2002 (Determination of initial shear strength).

A test rig (in Figure 4.18) was especially designed and fabricated for the testing of the half-scale brick triplet specimens. A spring was used to exert and adjust the different applied precompressive forces.

The vertical load was also applied by the same UTM from the Instron Company as used for the tensile strength test.

For this test, the vertical load was at a loading speed of 1 mm/min until shear failure occurred. Vertical displacement was caught automatically by the LVDTs built inside the loading machine.

According to the standard, two steel plates of 6 mm thickness with two steel bars of 6 mm diameter were placed underneath the specimen in a certain position. Meanwhile, two steel bars of 6 mm in diameter were placed between two steel plates of 6 mm thickness above the specimen on which the load was applied (see Figure 4.19).

For each mortar mix proportion, three triplet specimens were tested at each of 3 precompression loads horizontally, which gave precompressive stresses of approximately 0.002 N/mm^2, 0.006 N/mm^2 and 0.01 N/mm^2.

Calculations

Strength

$$fshi = \frac{Fi,max}{2Ai} \quad \text{....N/mm}^2\text{.....(4.4)}$$

$$fpi = \frac{Fpi}{Ai} \quad \text{.....N/mm}^2\text{.....(4.5)}$$

Fi,max (N) is the maximum shear load reached on an individual brickwork specimen, Fpi (N) is the precompressive force, fshi (N/mm^2) and fpi (N/mm^2) are the shear strength and precompressive stress of an individual brickwork specimen respectively, while Ai (mm^2) is the cross-section area of an individual brickwork specimen parallel

to the bed joints. The mean initial shear strength is recorded at zero precompressive stress from the intercept of the fshi against fpi line with the vertical axis. The angle of internal friction and cohesion could also be obtained.

	L (mm)	e (mm)	d (mm)	t (mm)
Mean dimensions	104	6.5	6	6

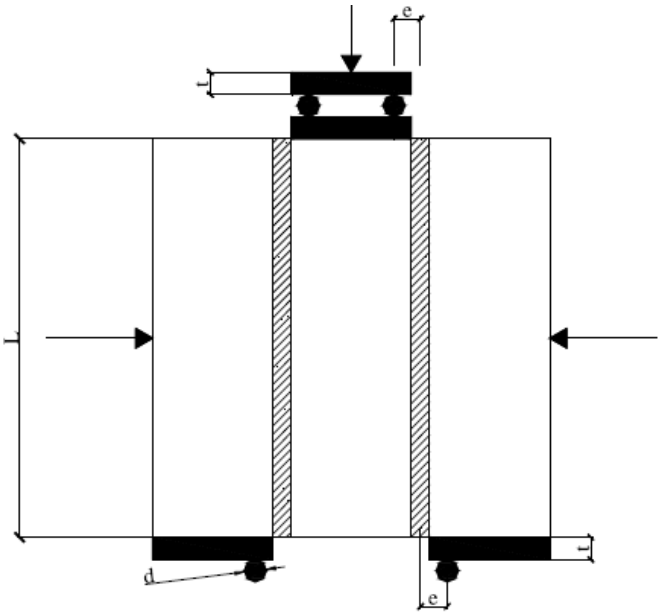

Figure 4.19 Dimensions for shear strength tests (Mohammed, 2006)

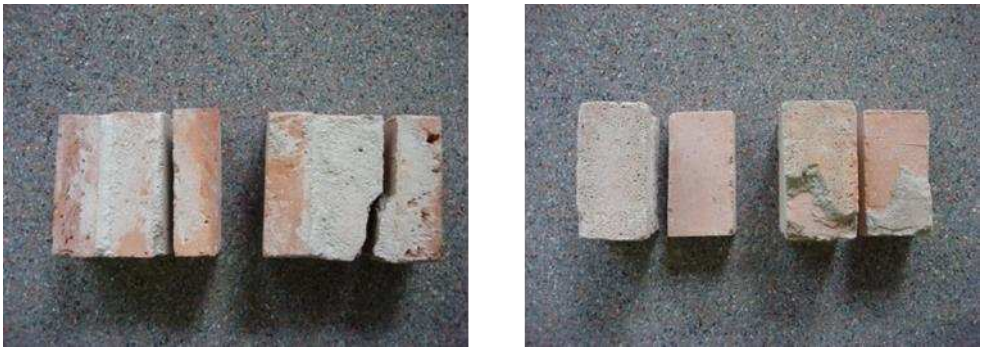

Figure 4.20 Shear failures in the brick / mortar bond area

All the shear failures were in the brick / mortar bond area, either on one or divided between two brick faces, as Figure 4.20 shows.

The main results of the shear strength test are shown in Table 4.8, Figure 4.21, Figure 4.22 and the figures in Appendix A. The ultimate shear strength of brickwork does not increase dramatically as the mortar strength is increased. It proves that the shear bond was normally independent of mortar strength (Lenczner, 1972).

Table 4.8 The shear strength test results of brickwork triplets

Brickwork Triplets	Mortar Mix Proportion	Average Length (mm)	Average Width (mm)	Cohesion (MPa)	Friction Angle
Batch 01	1:2:9	98.55	50.13	0.0389	52°
Batch 02	1:1:6	99.02	50.43	0.1845	55°

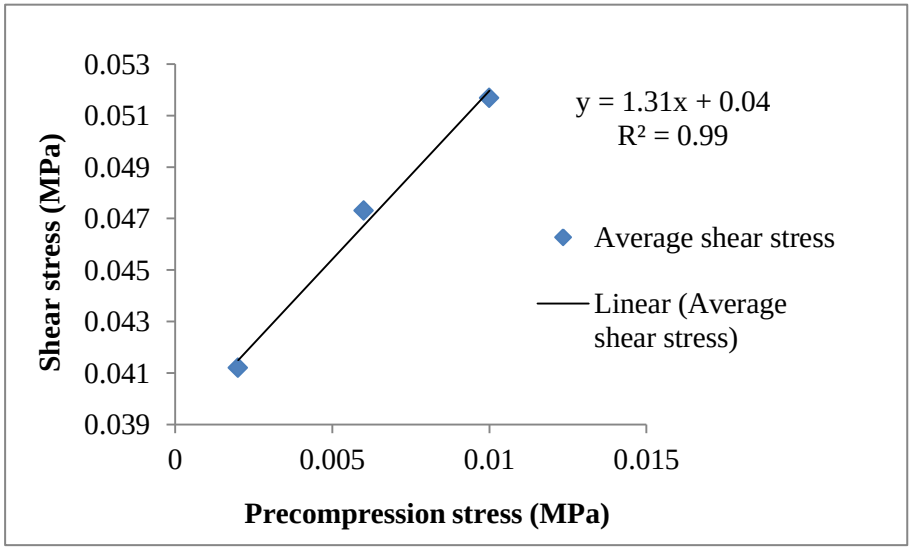

Figure 4.21 Average shear stress against precompression stress of brickwork triplet (1:2:9)

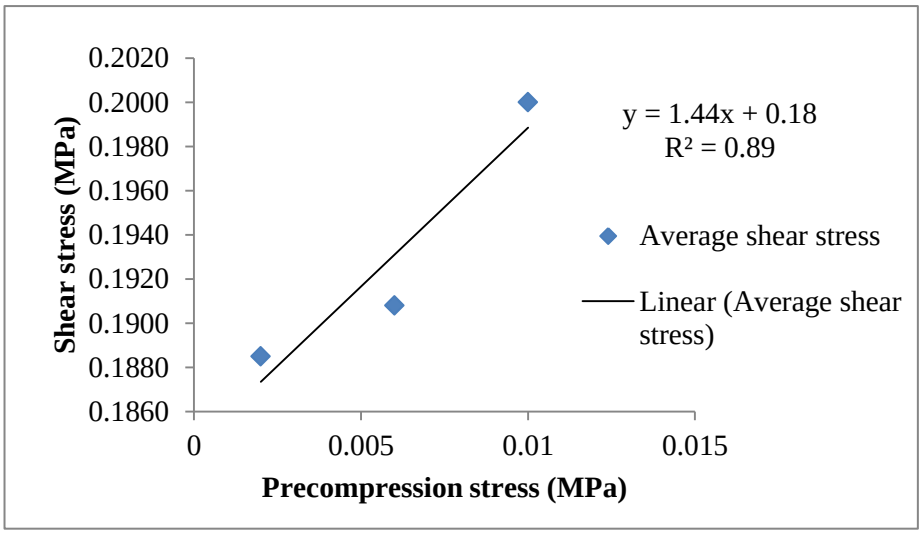

Figure 4.22 Average shear stress against precompression stress of brickwork triplet (1:1:6)

4.3 Modelling issues of brick-lined tunnels

4.3.1 Modelling approaches

Both simplified micro-modelling and macro-modelling strategies are employed in this research and compared with each other.

The finite difference method (FDM) is used in FLAC programme to build numerical models corresponding to a macro-modelling strategy, while a simplified micro-modelling strategy is applied to the UDEC programme (Distinct element method). (see Chapter 2 literature review for more details)

4.4 Introduction to FLAC

4.4.1 General introduction

In this research, the finite difference method (FDM) is mainly used to build numerical models corresponding to the macro-modelling strategy. It is one of the oldest numerical techniques for the solution of differential equations.

FLAC (Fast Lagrangian Analysis of Continua) is a two-dimensional commercial program developed by the Itasca Consulting Group Inc., using the explicit finite difference method. The program was originally developed for mining and geotechnical engineering applications, such as underground construction. It could simulate the nonlinear behaviour of structures built of soil, rock or other materials undergoing plastic collapse and flow when their yield limits in shear or tension are reached.

FLAC is also capable of solving a wide range of complex problems in mechanics with the help of several built-in constitutive models. In FLAC Version 6.0, there are 12 basic constitutive models divided into null, elastic and plastic model groups.

In FLAC, a powerful built-in programming language called FISH enables the user to define new variables, write new functions to extend the application of FLAC or implement one's own constitutive models. FISH was developed to assist users who would like to conduct work that is difficult or unavailable with existing codes.

The main characteristics and implementation of FLAC are presented with reference to the manual of FLAC (Itasca, 2008).

In FLAC, it is not necessary to form a global stiffness matrix. Coordinates at each time step are updated in large-strain mode. As the incremental displacements are added to the coordinates, the grid moves and deforms with the corresponding material. This is termed a 'Lagrangian' formulation. It is different from a formulation called 'Eulerian', in which the material moves and deforms relative to a fixed grid.

4.4.2 Fields of application

FLAC has been used primarily for analysis and design in the fields of mining, underground construction and so on. The analysis of progressive failure and collapse is achievable by its explicit, time-marching solution of the full equations of motion. Some example applications of FLAC are listed below:

a) Evaluation of the influence of fault structures in mine design;
b) Simulation of various rock reinforcement systems, such as rockbolts, steel beams and tunnel liners, as well as soil reinforcement systems such as tiebacks and soil nailing, using structural elements;
c) Studies in salt and potash mine design by establishing the creep model;
d) Research into the process and mechanisms of localisation and the evolution of shear bands in frictional materials;
e) Studies of the performance of deep underground repositories for high-level radioactive waste by setting up the thermal model;
f) Potential applications, including analyses of earth-retaining structures and earthen slopes under drained and undrained loading in addition to calculations of bearing capacity and the settlement of foundations;

g) Analyses in earthquake engineering, such as dam stability, soil structure interaction and liquefaction; studies of the effects of explosive loading, such as underground blasting;

h) In this research, FLAC was used to develop a two-dimensional plane-strain model as its basic formulation.

4.4.3 Comparison with the Finite Element Method

1) Similarities and differences

Over the years, the finite difference method (FDM) has always been compared with the finite element method (FEM) as applied to computer programs for numerical simulation.

Both methods produce a range of algebraic equations to solve. Although these algebraic equations are derived differently in FDM and FEM, the resulting equations are the same.

At the same time, there are some distinctions between these two methods. It should, however, be stressed that these different features are mainly due to established habits. For instance, in finite difference programs, finite difference equations are regenerated at each step for efficiency, while finite element programs usually combine element matrices into a global stiffness matrix. An explicit, time-marching scheme is commonly used in finite difference programs to solve the algebraic equations, while finite element programs often use implicit, matrix-oriented solutions. Table 4.9 compares the explicit and implicit methods.

Table 4.9 Comparison of explicit and implicit solution methods (Itasca, 2008)

Explicit	Implicit
Timestep must be smaller than a critical value for stability.	Timestep can be arbitrarily large, with unconditionally stable schemes.
Small amount of computational effort per timestep.	Large amount of computational effort per timestep.
No significant numerical damping introduced for dynamic solution.	Numerical damping dependent on timestep present with unconditionally stable schemes.
No iterations necessary to follow nonlinear constitutive law.	Iterative procedure necessary to follow nonlinear constitutive law.
Provided that the timestep criterion is always satisfied, nonlinear laws are always followed in a valid physical way.	Always necessary to demonstrate that the abovementioned procedure is: (a) stable; and (b) follows the physically correct path (for path-sensitive problems).
Matrices are never formed. Memory requirements are always at a minimum. No bandwidth limitations.	Stiffness matrices must be stored. Ways must be found to overcome associated problems such as bandwidth. Memory requirements tend to be large.
Since matrices are never formed, large displacements and strains are accommodated without additional computing effort.	Additional computing effort needed to follow large displacements and strains.

2) Advantages and disadvantages

There are several outstanding advantages of FLAC using explicit methods: most importantly, the iteration process is not necessary when computing stresses from strains in an element, whether the constitutive law is linear or nonlinear.

FLAC using explicit methods is better for modelling ill-behaved systems (e.g., nonlinear, large-strain, physical instability); they are not efficient enough for linear, small-strain issues.

FLAC could handle any constitutive model without adjustment to the solution algorithm, whereas many finite element codes need different solution algorithms for different constitutive models.

FLAC elements are in a row-and-column fashion rather than in a sequential fashion, which makes it easier to identify elements.

One significant disadvantage is that FLAC takes a longer time to simulate linear problems than equivalent finite element programs.

4.4.4 General solution procedure

To start with, three fundamental components of a problem must be specified in order to establish and run a numerical model with FLAC.

a) A finite difference grid;
b) Constitutive behaviour and material properties; and
c) Boundary and initial conditions.

After these conditions are defined in a numerical model, the initial equilibrium state is calculated for the model. An alteration is then performed such as excavation or changing boundary conditions; the resulting response of the model is calculated. The general solution procedure, illustrated in Figure 4.23, represents the sequence of processes that occurs in the physical environment.

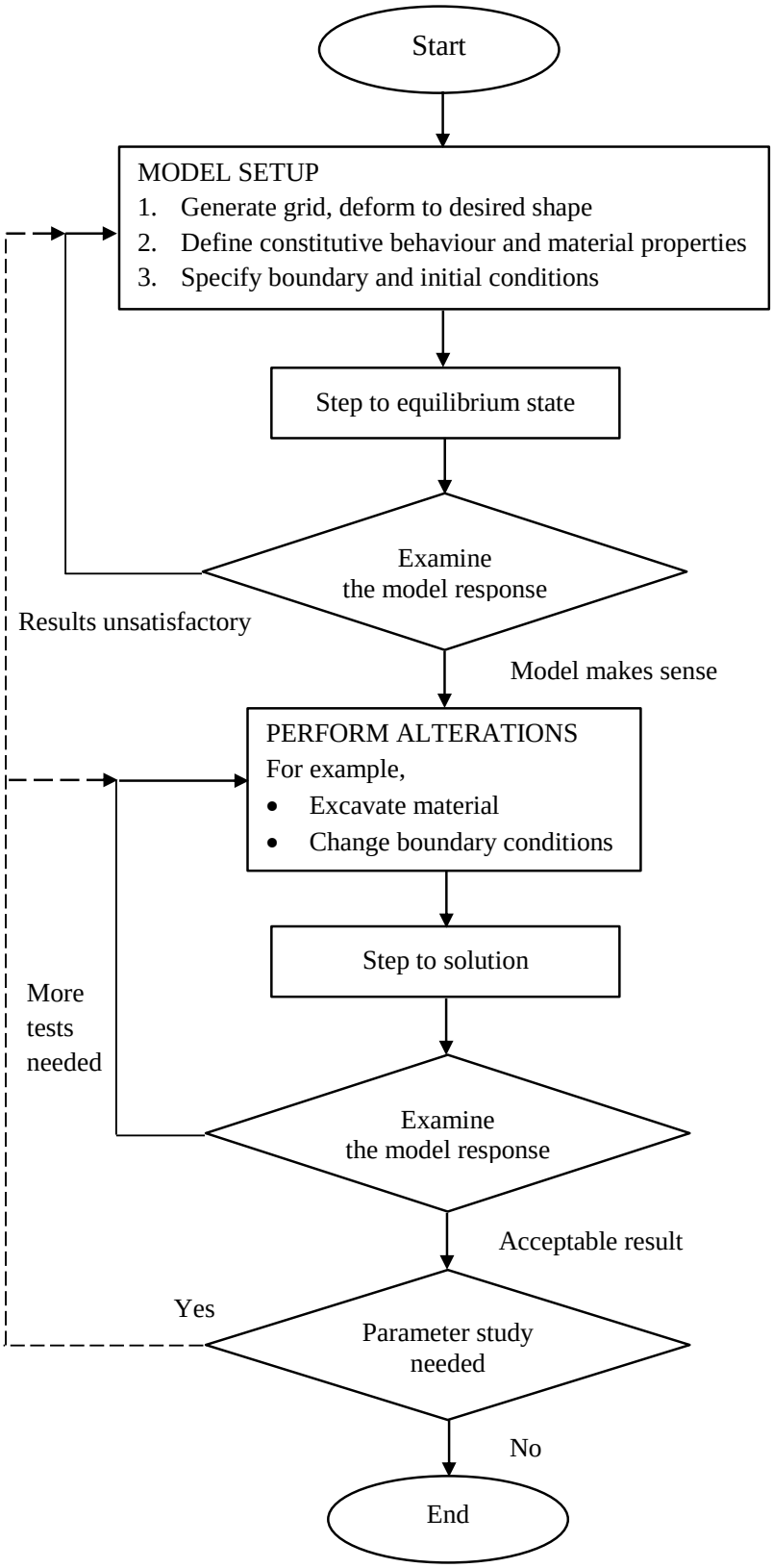

Figure 4.23 General solution procedure (Itasca, 2008)

4.4.5 Further developments

Itasca Consulting Group Inc. has also developed the FLAC^{3D} program based on the well-established FLAC program. Thus, it extends the analysis capability of FLAC into three dimensions, mainly simulating the behaviour of certain three-dimensional geotechnical structures, which FLAC could hardly simulate.

4.5 Numerical modelling of physical models using FLAC

4.5.1 Materials and interface properties

The Mohr-Coulomb constitutive model is used during the numerical modelling of FLAC. Most of the properties needed are derived from laboratory property tests, as mentioned in Section 4.2 Programme of material testing.

Interfaces (Joints) are used to represent planes on which sliding or separation would occur. In particular, the interface has some essential stiffness factors such as normal and shear stiffness (JKn and JKs) between two blocks, which may contact each other. Other important strength factors are cohesion, friction angle and tensile bond strength, etc.

The interface properties are classified into three categories as follows (Itasca, 2008):

a) Glued

Where there is no slip or separation allowed in the interface. Only joint normal and shear stiffness are required.

b) Unglued

- Unbonded: Where the slip is allowed without any tensile bond. Factors of JKn, JKs, cohesion, dilation angle and friction angle are needed.
- Bonded: Where there is no slip or separation allowed unless the strength(s) is exceeded. Factors for the 'unbonded' category and also tensile bond strength are required.

Since a macro-modelling strategy is used in FLAC, only the interfaces between brickwork and the soil belong to 'unbonded' category. Stiffness and strength properties (JKn, JKs, cohesion, dilation and friction angle) are required.

For interfaces used to glue two blocks, i.e. preventing any slip or separation, a good rule-of-thumb for the value of JKn and JKs is to set to ten times the equivalent stiffness of the stiffest neighbouring zone (Itasca, 2008).

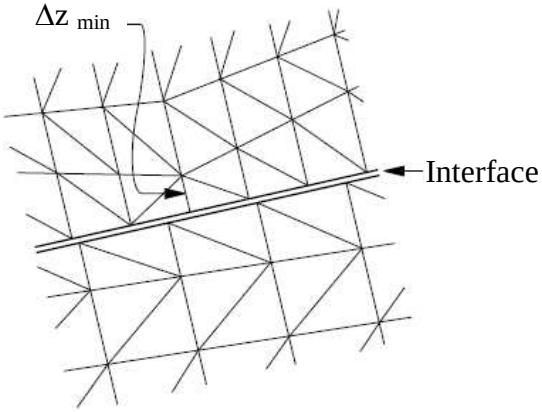

Figure 4.24 Zone dimension used in stiffness calculation

$$JKn = JKs = 10 \max\left[\left(\frac{K + \frac{4}{3}G}{\Delta z \min} \right) \right] \quad \text{(4.6)}$$

$$K = \frac{E}{3(1-2v)} \quad \text{(4.7)}$$

$$G = \frac{E}{2(1+v)} \quad \text{(4.8)}$$

Where K and G are the bulk and shear moduli respectively, Δzmin is the smallest width of an adjoining zone in the normal direction; E is the Young's modulus, while v is the Poisson's ratio. (see Figure 4.24)

In other unglued circumstances, unbonded and bonded, the value of both JKn and JKs could be reduced according to the equivalent stiffness of the neighbouring zone.

In the following sections, the joint stiffness properties have been calculated according to Equations (4.6) to (4.8), and joint strength properties have been estimated from laboratory property tests in Section 4.2 Programme of material testing.

4.5.2 Model generation

The tunnel was subjected to the self weight of the homogeneous surrounding soil.

Grid generation, with very fine meshes as well as proper aspect ratio (ratio of height to width of a zone), was made to fit the physical shape of the model and to pursue more results that are accurate.

The next step was to create and assign materials and their properties to the zones within the grid. Here brickwork properties were assigned in blue while surrounding soil properties were in green, as is shown in Figure 4.25, with both prescribed according to the Mohr-Coulomb model.

Thereafter, boundary conditions for the physical model were assigned so that roller boundary conditions were applied to two sides and along the bottom of the model. Moreover, pinned boundary conditions were also applied to the bottom corners of the tunnel, shown in Figure 4.25. Gravity of 9.81 m/s^2 was set. The model was then

set to equilibrium state, simulating the preparation procedure of the physical model just before loading.

Vertical loading was then added at certain interval until the tunnel failed, in order to simulate the physical model test. That required a change in the boundary conditions as displacement-control loading and a step to the solution. Afterwards, the model response was analysed.

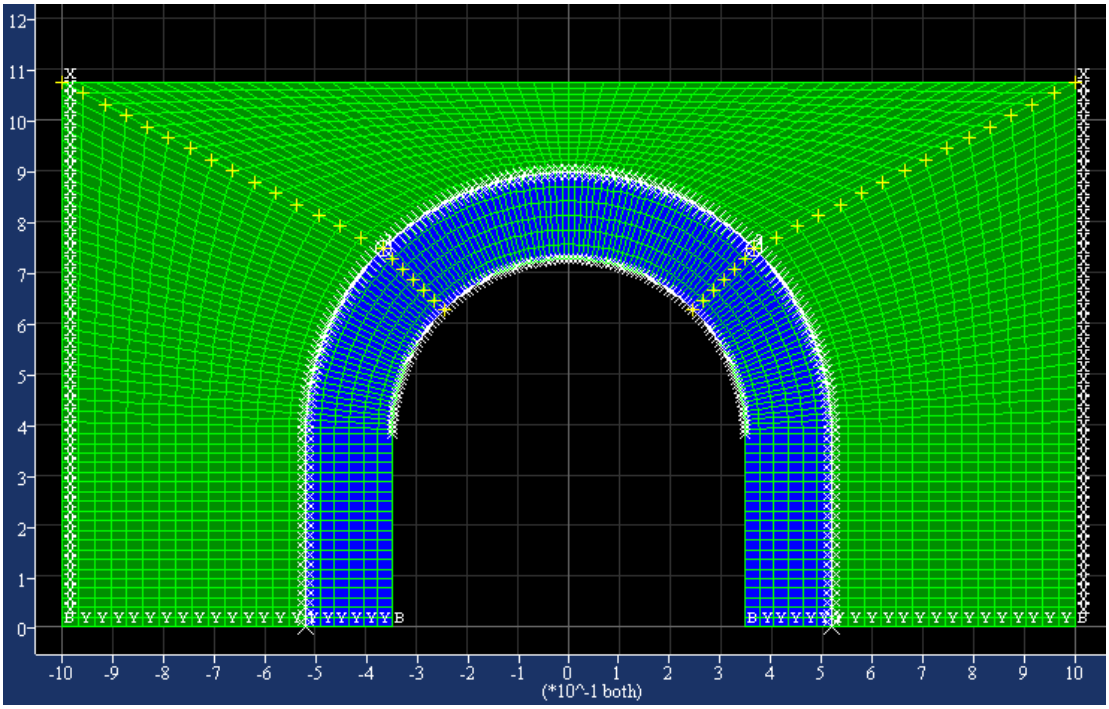

Figure 4.25 FLAC model grids with boundary conditions

4.5.3 Parametric study

In FLAC, a macro-modelling strategy (see Section 2.5.1 for details) is used, which is to consider the brick, mortar and brick / mortar interface smeared out in a homogeneous anisotropic continuum.

Thus, the mechanical properties of brickwork below were selected for the purpose of parametric study: Poisson's ratio (v), Young's modulus (E), cohesion (c), friction angle (φ) and density (ρ).

In addition, the interface properties of brickwork / soil were estimated for use after the parametric study of joint stiffness and joint friction angle.

The effects of these properties on the stress and deformation conditions have been studied with both uniform and concentrated loading until failure.

The properties of surrounding soil were always kept the same during the whole process of numerical simulation, based on the laboratory tests (see Table 4.10).

Table 4.10 Surrounding soil (Portaway sand) properties

Surrounding soil					
ρ (kg/m³)	**E (MPa)**	**v**	**c (MPa)**	**φ**	**Tr (MPa)**
1832	26*	0.3*	0	44°	0*

*:Young's modulus and Poisson's ratio were referring to Juspi, 2008; Tr is the tensile strength.

1) Uniform load

Baseline numerical model (1:1:6)

Table 4.11 lists the mechanical properties assigned to brickwork with mortar mix proportion of 1:1:6 and interface properties of brickwork and soil as a baseline from the laboratory work, Equations (4.6) to (4.8) and some estimation, such as joint friction and joint cohesion. Further adjustment of some estimated properties would be made after the parametric study.

Table 4.11 Brickwork (mix proportion 1:1:6) and brickwork / soil joint properties

Brickwork (1:1:6)					
ρ (kg/m³)	**E (MPa)**	**v**	**c (MPa)**	**φ**	**Tr (MPa)**
1732	384.33	0.2*	0.1845	55°	0.2437
Brickwork / soil joint					
	JKn (GPa/m)	**JKs (GPa/m)**	**Jc (MPa)**	**Jφ**	**JTr (MPa)**
	112.97	112.97	0	25*	0

*: Poisson's ratio of the brickwork and the friction angle of the joint (Jφ) were initially referring to Idris et al., 2008.

Figure 4.26 and Figure 4.27 illustrate the displacement vectors and plastic state of the baseline numerical model individually, with the image in the lower left-hand corner showing the physical model test result. Both of the figures are coincident with the physical model test, with a similar deformation trend and shear failure at the tunnel sides.

The tunnel crown displacement curve of the FLAC baseline numerical model is compared with that of the physical model test 1 in Figure 4.28, which seems to be much stiffer than the physical model result.

Thus, further parametric studies of the mechanical properties are needed to approach the proper simulation of the physical model test 1 in the next part.

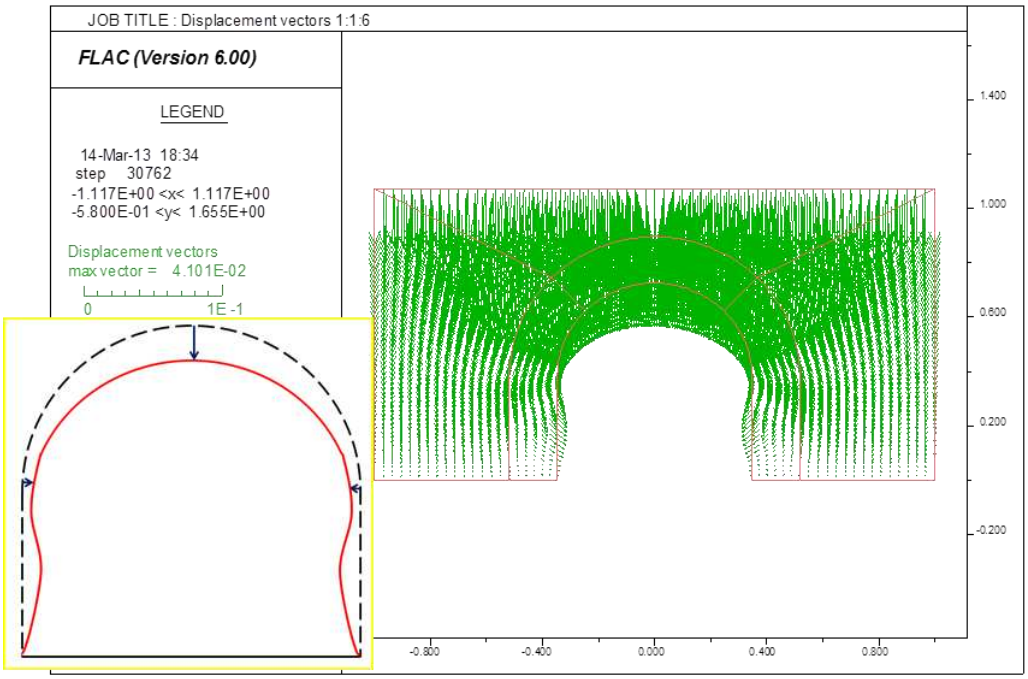

Figure 4.26 Displacement vectors of numerical model (1:1:6) during uniform static load compared with the physical model

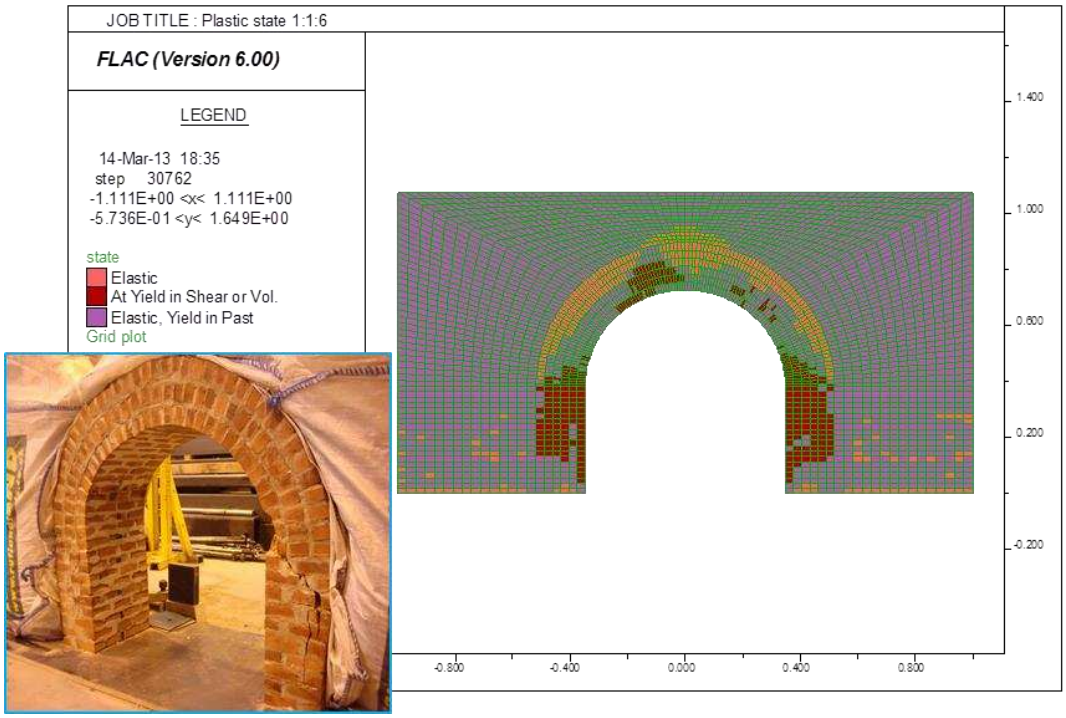

Figure 4.27 Plastic state of numerical model (1:1:6) compared with the physical model

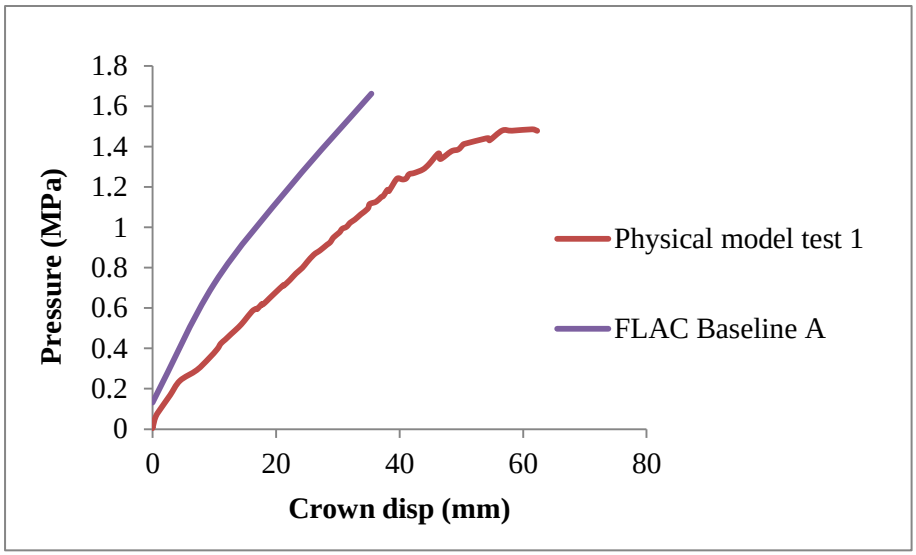

Figure 4.28 Physical model 1 vs. FLAC baseline A curves

Parametric study

FLAC model A1: After increasing the Poisson's ratio of the brickwork to 0.3, there was no significant effect on stiffness (see Figure 4.29). Thus, the Poisson's ratio of 0.2 would be used through the parametric study of the numerical model (1:1:6).

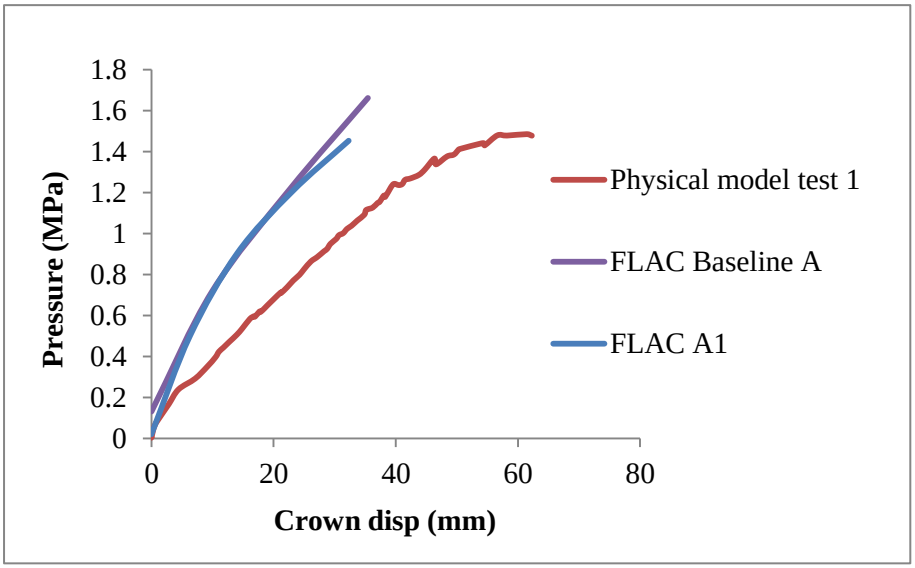

Figure 4.29 Physical model 1 vs. FLAC baseline A & model A1 curves

FLAC models A2 and A3: The maximum and minimum values of Young's modulus (E) obtained from the UCS test of brickwork (1:1:6) were then input in FLAC models A2 and A3, which more or less varied the stiffness (see Figure 4.30).

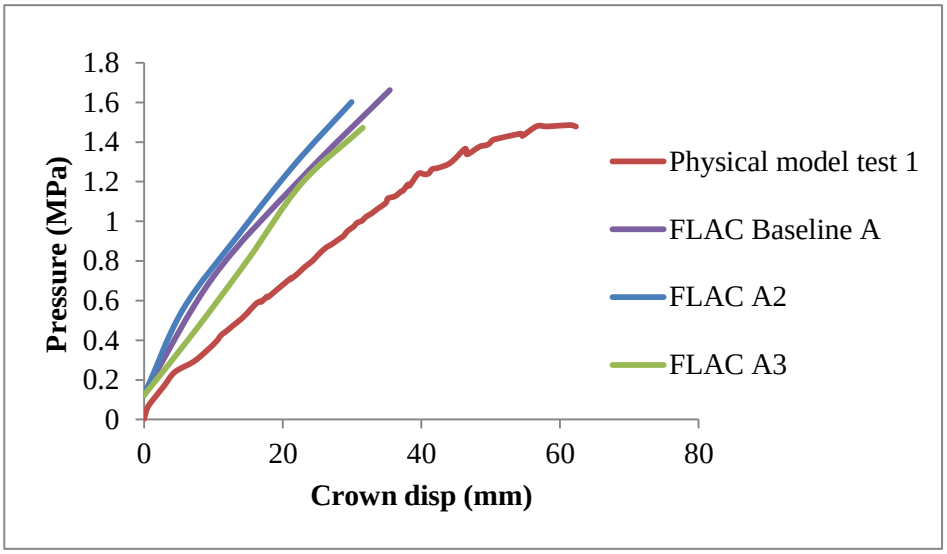

Figure 4.30 Physical model 1 vs. FLAC baseline A & model A2 - A3 curves

FLAC models A4 and A5: The strength of the baseline model seemed to be much stronger than that of the physical model. In order to match the ultimate pressure of the physical model, the friction angle of the brickwork was reduced to 50° and 52° in FLAC models A4 and A5 respectively. FLAC model A4 performed very well and approached the ultimate value and crown displacement as physical model test 1, while FLAC model A5 showed a larger ultimate value in Figure 4.31. Therefore, in the following parametric study, the result of FLAC model A4 would be compared as a new baseline.

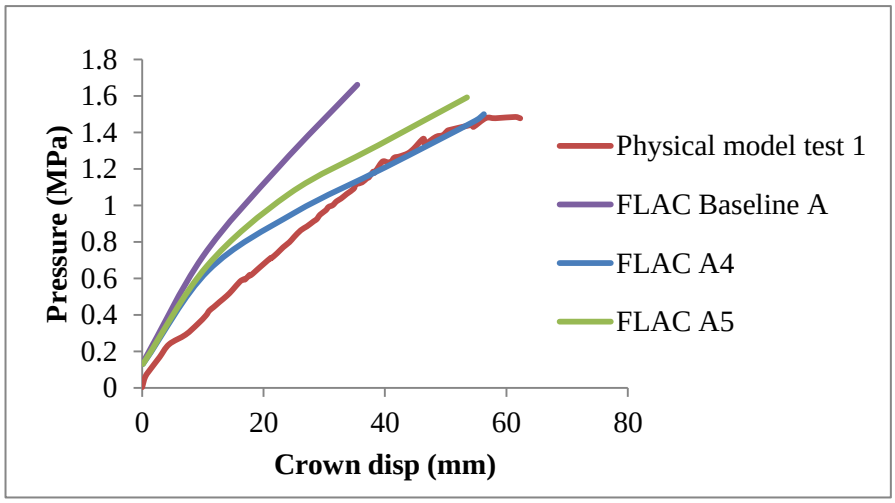

Figure 4.31 Physical model 1 vs. FLAC baseline A & model A4 - A5 curves

FLAC models A6, A7 and A8: Next, the cohesion of the brickwork was varied from 0.14 to 0.2 MPa, up to 24.1% difference from FLAC model A4. The increase in the cohesion also increased the ultimate pressure and the stiffness. As can be seen in Figure 4.32, FLAC model A7 seemed to be closer to the physical model test, where the stiffness was even lower than FLAC model A4. In this case, the new baseline FLAC model A4 was replaced by FLAC model A7.

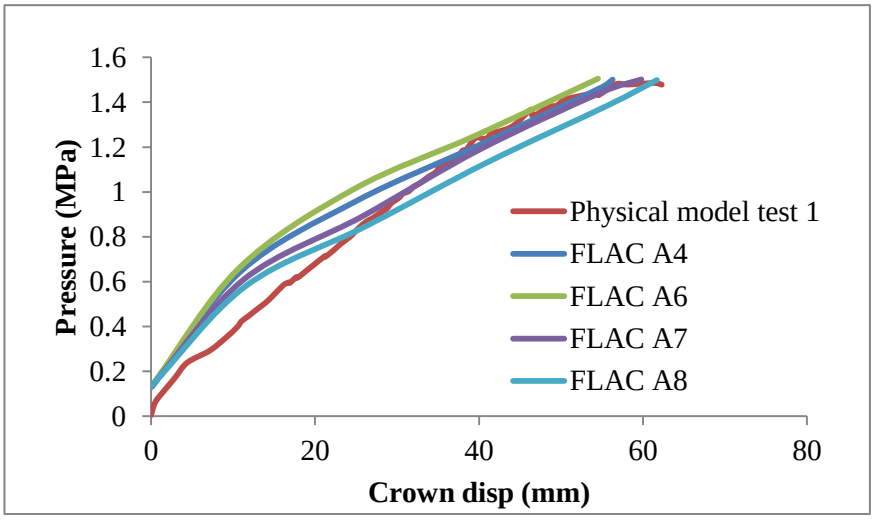

Figure 4.32 Physical model 1 vs. FLAC model A4 & model A6 - A8 curves

FLAC models A9, A10 and A11: Since the friction angle of brickwork / soil interface was estimated with reference to Idris et al., 2008, the parametric study of the friction angle was carried out by increasing the value from 30°, to 35° and then 40°. The stiffness in these models was similar. However, as the friction angle increased, the ultimate pressure also increased. The curve does not match the physical model result and is toward the opposite direction (see Figure 4.33). FLAC model A7 was better than other models in simulating the physical model.

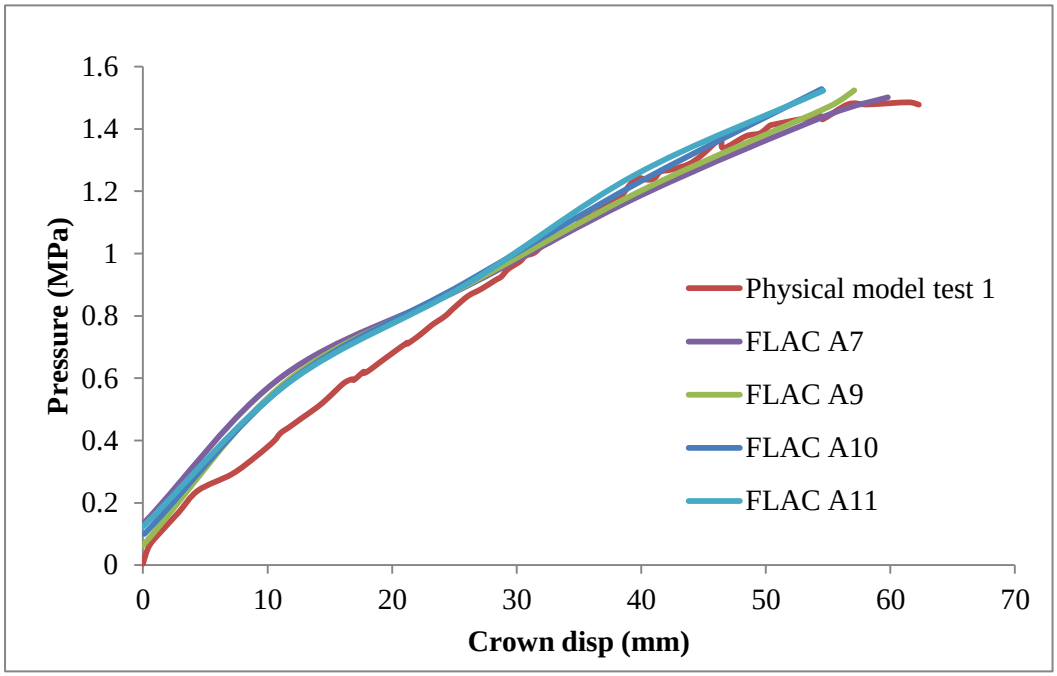

Figure 4.33 Physical model 1 vs. FLAC model A7 & model A9 - A11 curves

FLAC models A12 and A13: Again, the maximum and minimum value of Young's modulus (E) was employed in FLAC models A12 and A13. This time the increased Young's modulus also led to an increase in stiffness and ultimate pressure, while the minimum value resulted in similar stiffness and lower ultimate value (see Figure 4.34). FLAC model A7 was an appropriate model compared with physical model 1.

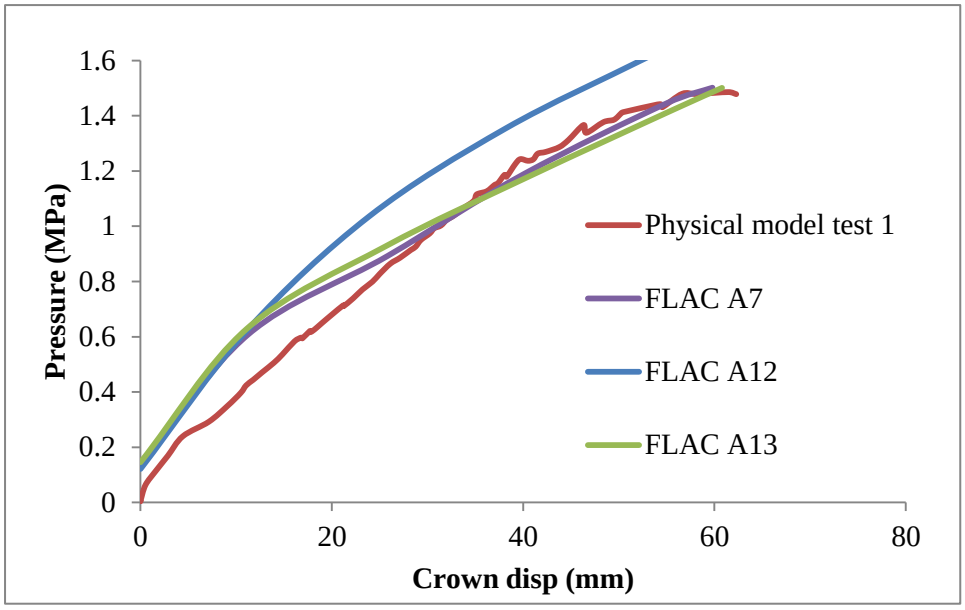

Figure 4.34 Physical model 1 vs. FLAC model A7 & model A12 - A13 curves

FLAC model A14: At last, the joint stiffness was reduced according to Equations (4.6) to (4.8). As can be seen from Figure 4.35, the result of FLAC model A14 seems to be removed from that of physical model test 1.

Ultimately, FLAC model A7 was proved to be the most appropriate one to simulate the physical model test 1 (see Figure 4.36).

In addition, the pressure-displacement curve at one quarter across the tunnel arch obtained by photogrammetry (Figure 3.38 shown in Chapter 3) was compared with the proper FLAC model, as seen in Figure 4.37, from 0 kN to 590 kN load. The curve by photogrammetry shows a slightly higher stiffness, although the displacement difference is within 2.5 mm at the same pressure of 0.89 MPa.

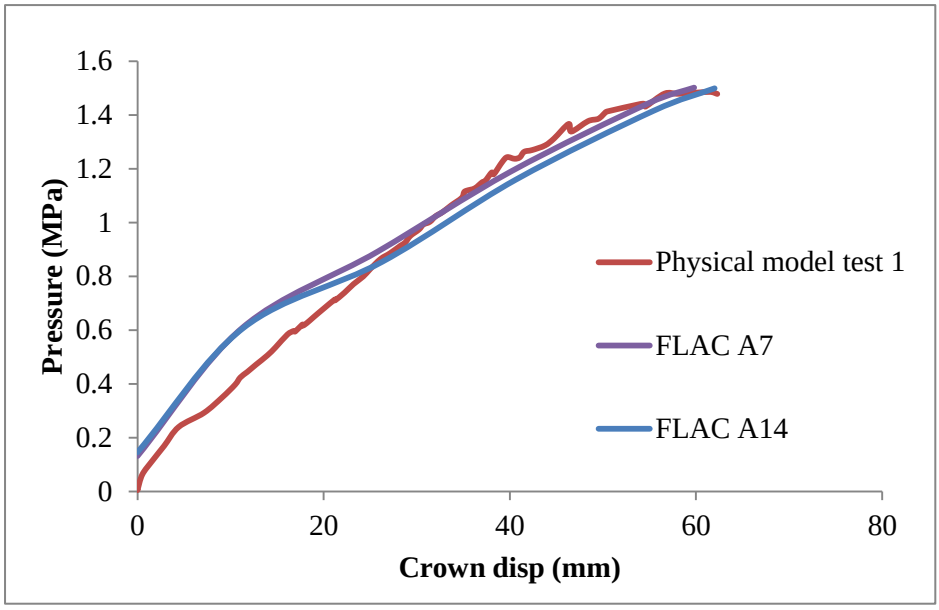

Figure 4.35 Physical model 1 vs. FLAC model A7 & A14 curves

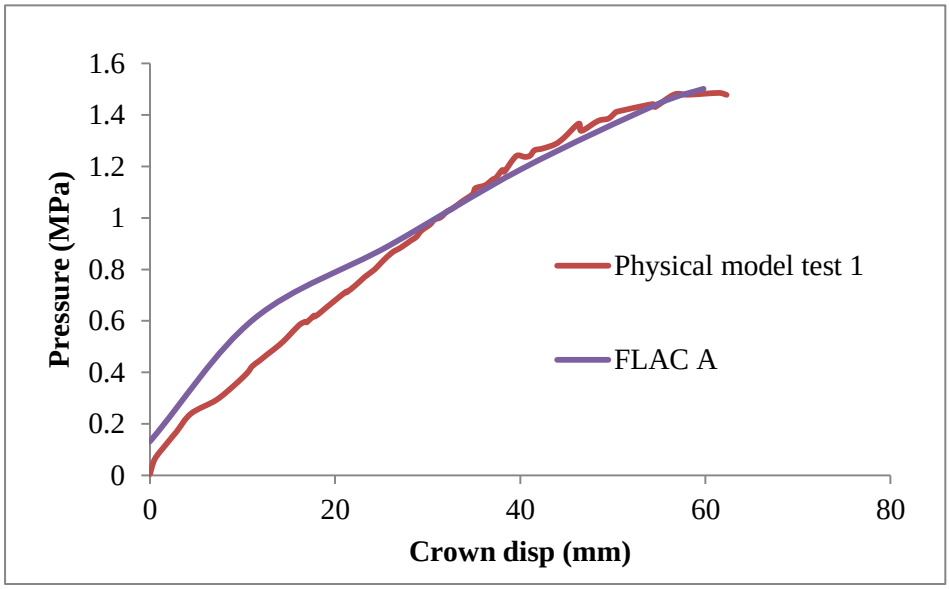

Figure 4.36 Physical model 1 vs. FLAC model A curves

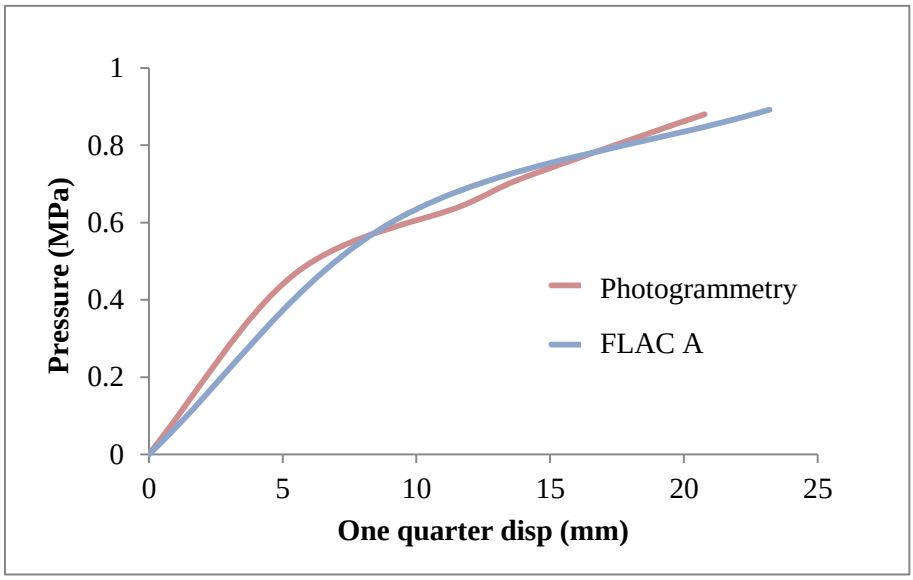

Figure 4.37 Photogrammetry at 1/4 vs. FLAC model A curves

Table 4.12, Table 4.13 and Table 4.14 have clearly displayed the progress of the parametric study.

Table 4.12 Brickwork parametric study of Poisson's ratio, Young's modulus and friction angle (Mix proportion of 1:1:6)

	E (MPa)	v	c (MPa)	φ	JKn = JKs (GPa/m)	Jφ
Baseline A	384.33	0.2	0.1845	55°	112.97	25°
FLAC A1	384.33	0.3	0.1845	55°	136.87	25°
FLAC A2	553	0.2	0.1845	55°	162.55	25°
FLAC A3	249	0.2	0.1845	55°	73.19	25°
FLAC A4	384.33	0.2	0.1845	50°	112.97	25°
FLAC A5	384.33	0.2	0.1845	52°	112.97	25°

Table 4.13 Parametric study of the brickwork cohesion (1:1:6)

	E (MPa)	v	c (MPa)	φ	JKn = JKs (GPa/m)	Jφ
FLAC A4	384.33	0.2	0.1845	50°	112.97	25°
FLAC A6	384.33	0.2	0.2 (8%)	50°	112.97	25°
FLAC A7	384.33	0.2	0.16 (13.3%)	50°	112.97	25°
FLAC A8	384.33	0.2	0.14 (24.1%)	50°	112.97	25°

Table 4.14 Parametric study of brickwork Young's modulus, joint friction angle and stiffness (1:1:6)

	E (MPa)	v	c (MPa)	φ	JKn = JKs (GPa/m)	Jφ
FLAC A7	384.33	0.2	0.16	50°	112.97	25°
FLAC A9	384.33	0.2	0.16	50°	112.97	30°
FLAC A10	384.33	0.2	0.16	50°	112.97	35°
FLAC A11	384.33	0.2	0.16	50°	112.97	40°
FLAC A12	553	0.2	0.16	50°	162.55	25°
FLAC A13	249	0.2	0.16	50°	73.19	25°
FLAC A14	384.33	0.2	0.16	50°	56.49	25°

Baseline numerical model (1:2:9)

As in the numerical modelling of brickwork (1:1:6), the baseline numerical model B was first developed with the properties listed in Table 4.15. Compared with physical model test 2, the FLAC baseline model B is less stiff. Thus, more parametric studies are required to obtain a better simulation of physical model test 2.

Table 4.15 Brickwork (mix proportion of 1:2:9) and brickwork / soil joint properties

Brickwork (1:2:9)					
ρ (kg/m³)	**E (MPa)**	**v**	**c (MPa)**	**φ**	**Tr (MPa)**
1672.5	218.67	0.2*	0.0389	52°	0.0968
Brickwork / soil joint					
	JKn (GPa/m)	**JKs (GPa/m)**	**Jc (MPa)**	**Jφ**	**JTr (MPa)**
	64.28	64.28	0	25*	0

*: Poisson's ratio of the brickwork and the friction angle of the joint (Jφ) were initially referring to Idris et al., 2008.

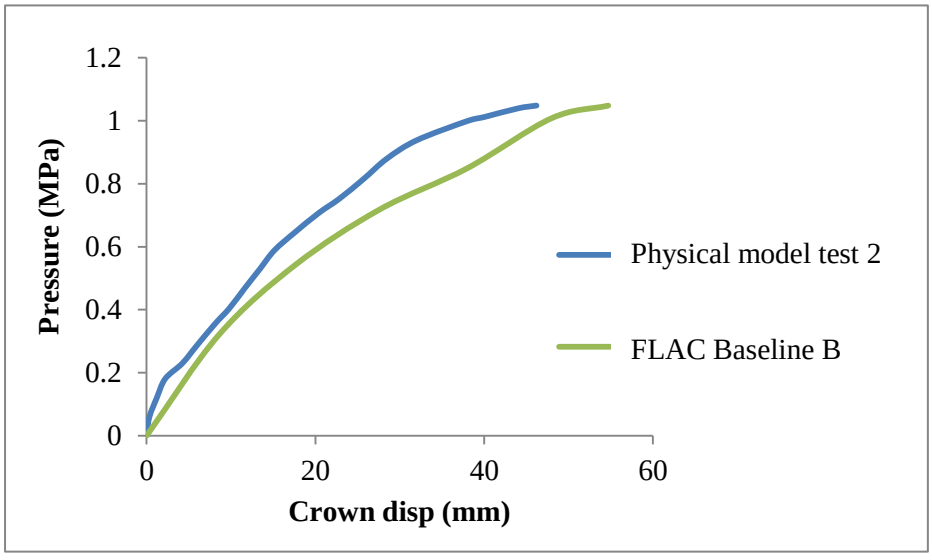

Figure 4.38 Physical model 2 vs. FLAC baseline B curves

Parametric study

FLAC models B1 and B2: The maximum and minimum values of Young's modulus (E) obtained from the UCS test of brickwork (1:2:9) were used to model FLAC B1 and B2. As can been seen in Figure 4.39, the change in Young's modulus has not significantly affected the curve to approach the experiment curve. In this case, the variation in strength properties is studied in the following part.

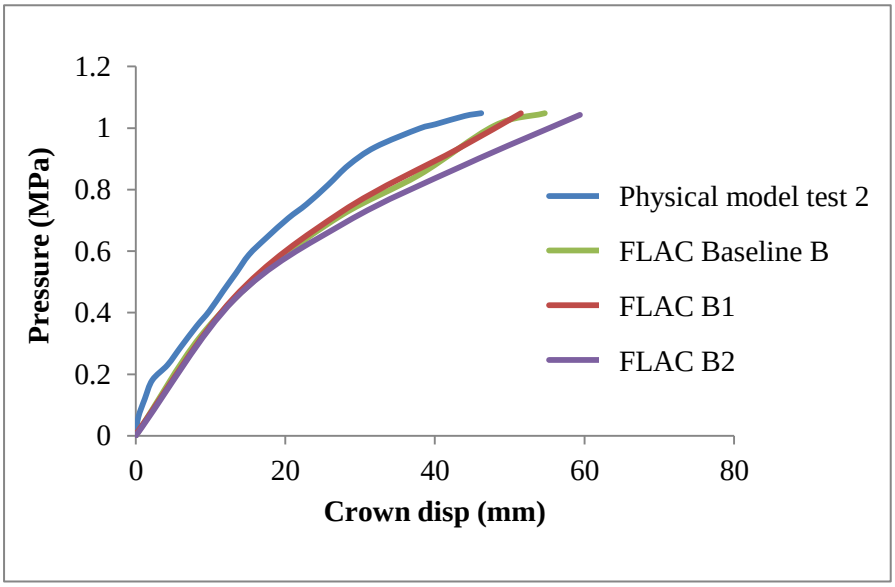

Figure 4.39 Physical model 2 vs. FLAC baseline B & model B1 - B2 curves

FLAC model B3 and B4: The reduction of the friction angle of the brickwork to 50° in FLAC B3 also reduced the stiffness. However, as the friction angle increased to 55° in FLAC B4, there was still a large difference compared to physical model test 2 (see Figure 4.40). It was then necessary to check the cohesion influence.

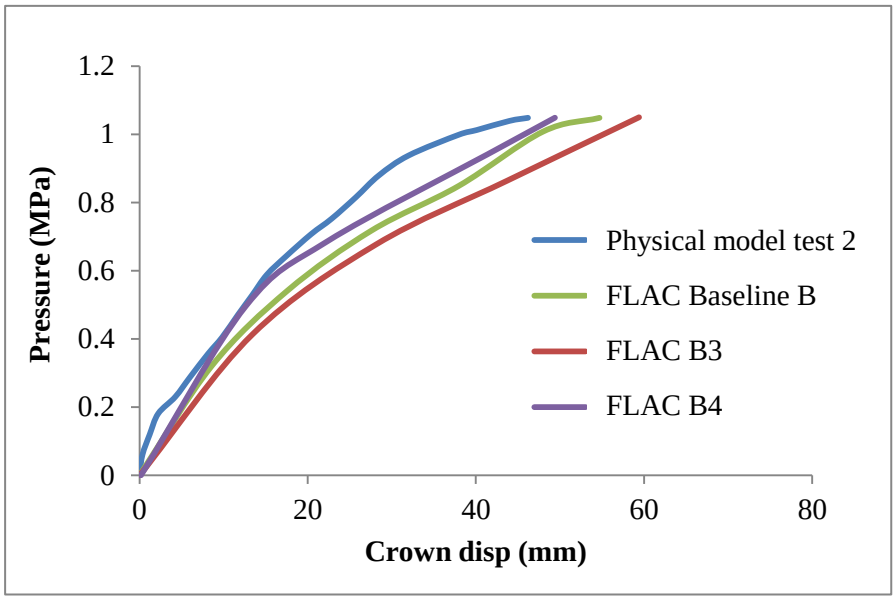

Figure 4.40 Physical model 2 vs. FLAC baseline B & model B3 - B4 curves

FLAC models B5, B6, B7 and B8: The cohesion of the brickwork was increased step by step, from 0.05 MPa to 0.1 MPa (increased by 28.53% to 157.07%, see Table 4.17). Thus the stiffness and the ultimate pressure were increased and to become closer to the experiment result (see Figure 4.41). In these models, FLAC B6 with the increased cohesion of 0.07 MPa (increased by 79.94%) seemed to be better than the FLAC baseline model B. The cohesion value input was not as large as 0.09 MPa or even 0.1 MPa, which increased by more than 100% of the laboratory value. The FLAC baseline B was then replaced by FLAC model B6 as a new baseline.

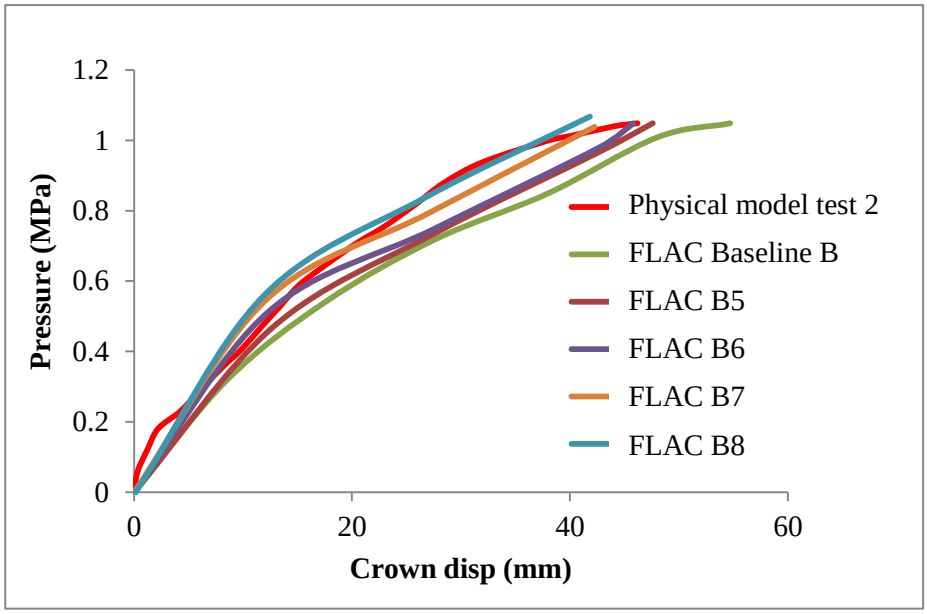

Figure 4.41 Physical model 2 vs. FLAC baseline B & model B5 - B8 curves

FLAC models B9 and B10: Next, the maximum and minimum values of Young's modulus (E) were input in FLAC models B9 and B10. Figure 4.42 illustrates that the variation of Young's modulus did not make a big difference in terms of stiffness and ultimate load.

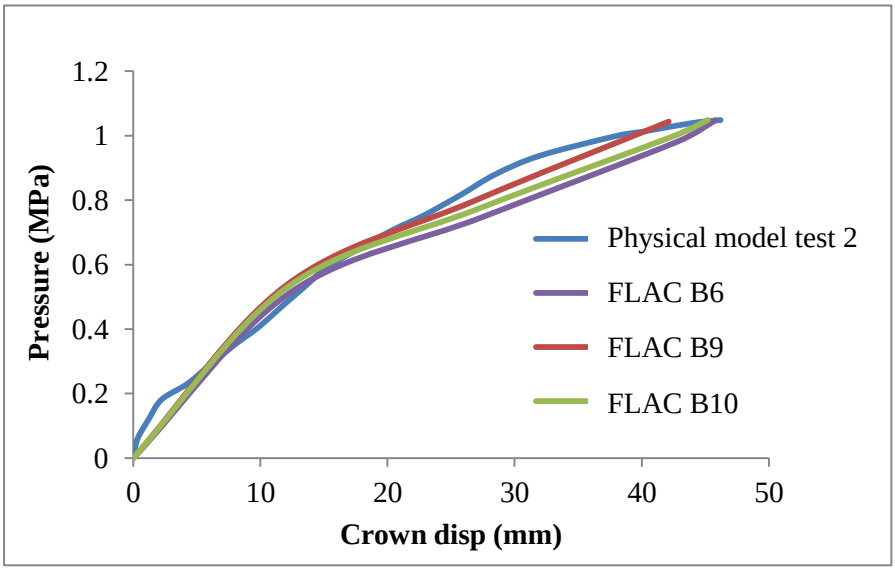

Figure 4.42 Physical model 2 vs. FLAC model B6 & model B9 - B10 curves

FLAC model B11: Finally, the joint stiffness was reduced by 50% in FLAC B11 according to Equations 4.1 to 4.3, which differed from the experiment result (see Figure 4.43).

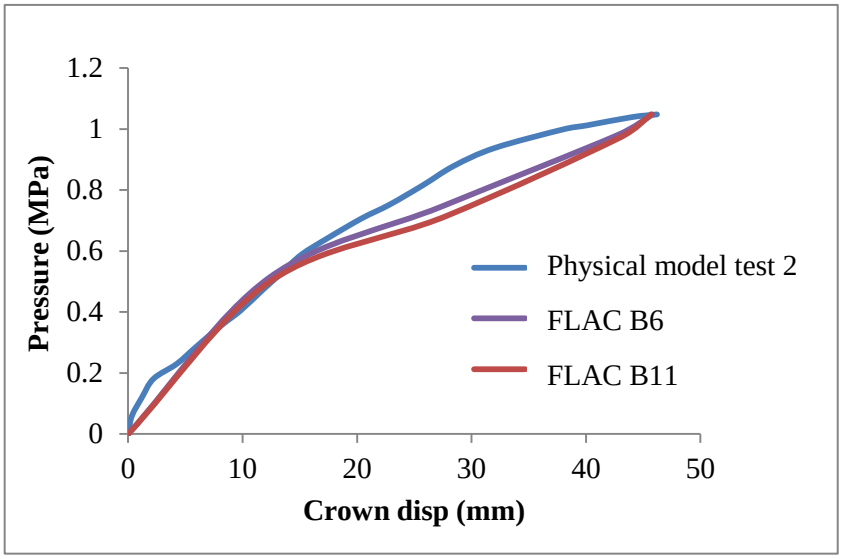

Figure 4.43 Physical model 2 vs. FLAC model B6 & model B11 curves

After the parametric study, FLAC B6 was proved to be the most suitable model to simulate physical model test 2, as shown in Figure 4.44.

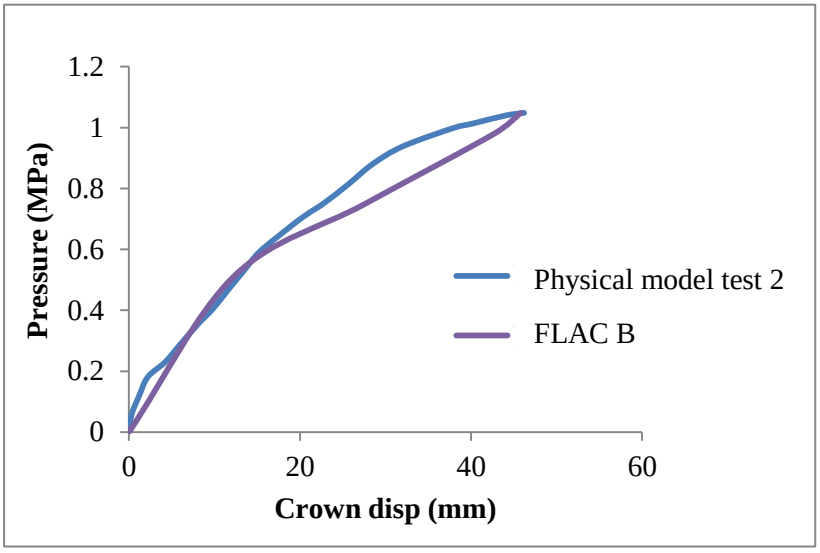

Figure 4.44 Physical model 2 vs. FLAC model B curves

Table 4.16, Table 4.17 and Table 4.18 list the progress of the parametric study as below.

Table 4.16 Brickwork parametric study of Young's modulus and friction angle (Mix proportion of 1:2:9)

	E (MPa)	v	c (MPa)	φ	JKn = JKs (GPa/m)
Baseline B	218.67	0.2	0.0389	52°	64.28
FLAC B1	233	0.2	0.0389	52°	68.49
FLAC B2	211	0.2	0.0389	52°	62.02
FLAC B3	218.67	0.2	0.0389	50°	64.28
FLAC B4	218.67	0.2	0.0389	55°	64.28

Table 4.17 Parametric study of the brickwork cohesion (1:2:9)

	E (MPa)	v	c (MPa)	φ	JKn = JKs (GPa/m)
Baseline	218.67	0.2	0.0389	52°	64.28
FLAC B5	218.67	0.2	0.05 (28.53%)	52°	64.28
FLAC B6	218.67	0.2	0.07 (79.94%)	52°	64.28
FLAC B7	218.67	0.2	0.09 (131.36%)	52°	64.28
FLAC B8	218.67	0.2	0.1 (157.07%)	52°	64.28

Table 4.18 Parametric study of brickwork Young's modulus and joint stiffness (1:2:9)

	E (MPa)	v	c (MPa)	φ	JKn = JKs (GPa/m)
FLAC B6	218.67	0.2	0.07	52°	64.28
FLAC B9	233	0.2	0.07	52°	68.49
FLAC B10	211	0.2	0.07	52°	62.02
FLAC B11	218.67	0.2	0.07	52°	32.14

2) Concentrated load

Baseline numerical model (1:2:9)

The same properties, for baseline model under concentrated load, were used as under uniform load (see Table 4.15). The loading area was 0.3 m wide. The crown displacement curve of the FLAC baseline model C is far removed from that of physical model test 3 (see Figure 4.45).

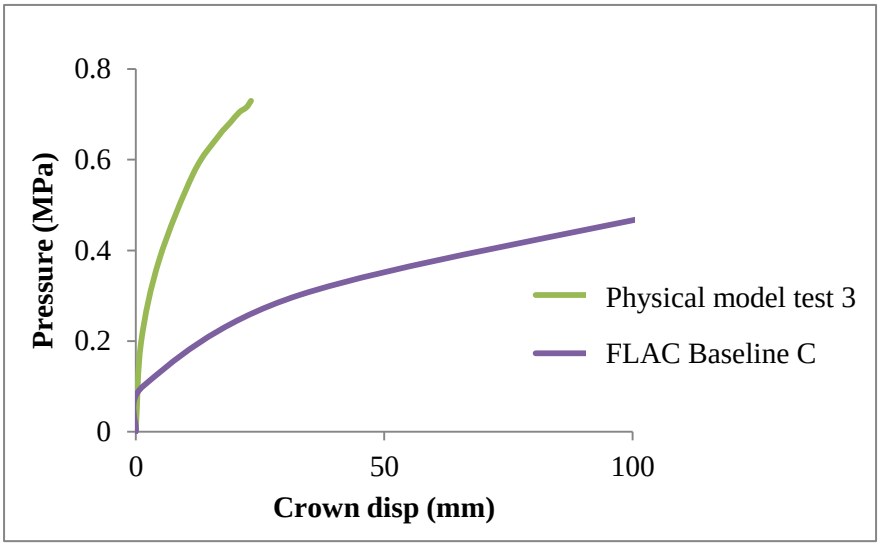

Figure 4.45 Physical model 3 vs. FLAC baseline C curves

Parametric study

FLAC models C1, C2, C3 and C4: From the experience obtained, the cohesion of the brickwork largely influenced the curve behaviour. Therefore, the cohesion was varied at first to approach the experiment curve, from 0.07 MPa to 0.2 MPa. As can be seen from Figure 4.46, an increase in the cohesion also increases the stiffness of the crown displacement curve. The curve of FLAC C4 with 0.2 MPa cohesion was closest to that of the physical model.

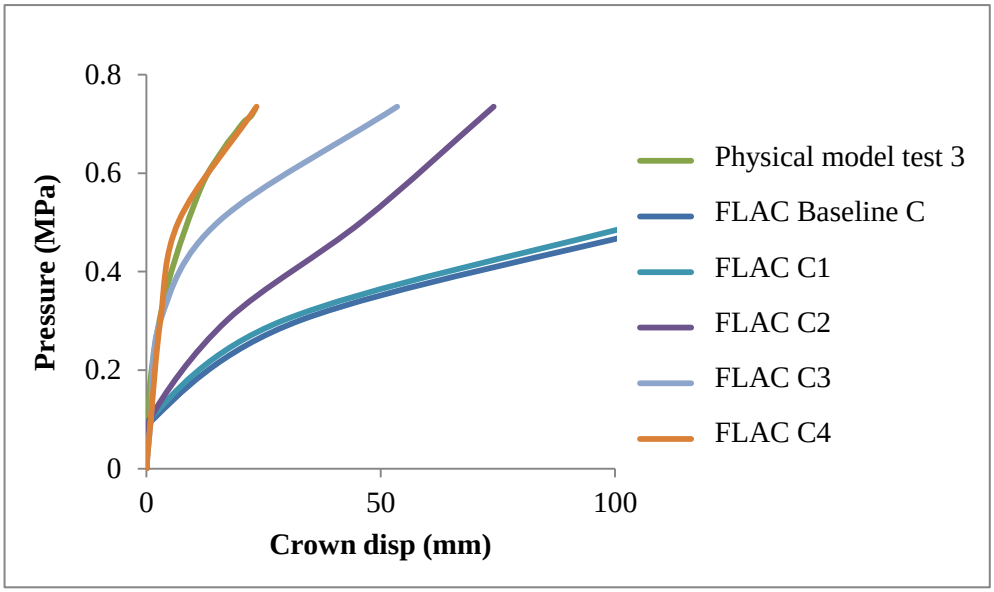

Figure 4.46 Physical model 3 vs. FLAC baseline C & model C1 - C4 curves

Therefore, FLAC C4 was the best model to match the physical model. However, the cohesion used (0.2 MPa) was more than 5 times larger than the laboratory result (0.0389 MPa), shown in Figure 4.47. The reason might be that the FLAC software with macro-modelling was not able to simulate the model under concentrated load very well.

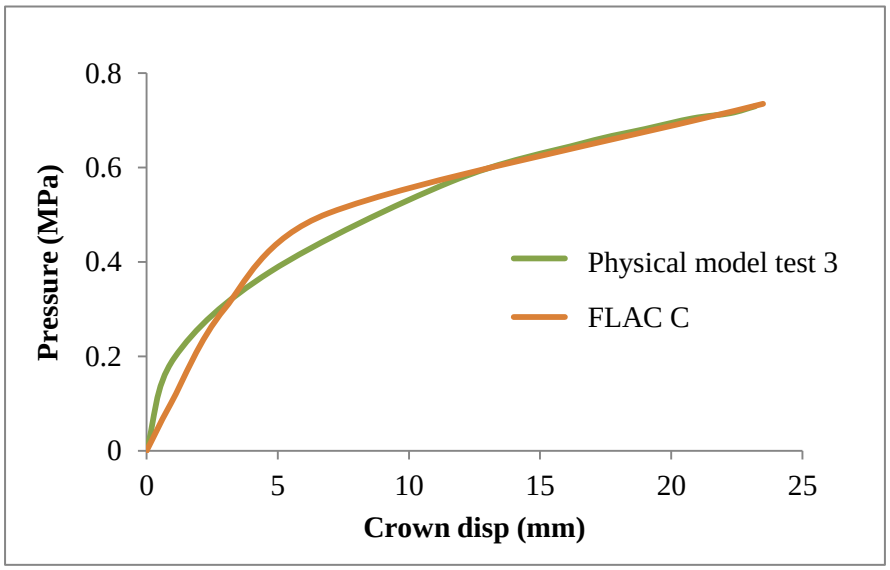

Figure 4.47 Physical model 3 vs. FLAC model C curves

The progress of the parametric study has been displayed in Table 4.19.

Table 4.19 Parametric study of the brickwork cohesion under concentrated load

	E (MPa)	v	c (MPa)	φ	JKn = JKs (GPa/m)	Jφ
Baseline C	218.67	0.2	0.0389	52°	64.28	25°
FLAC C1	218.67	0.2	0.07 (79.94%)	52°	64.28	25°
FLAC C2	218.67	0.2	0.1 (157.07%)	52°	64.28	25°
FLAC C3	218.67	0.2	0.15	52°	64.28	25°
FLAC C4	218.67	0.2	0.2	52°	64.28	25°

4.5.4 Results analysis of the parametric study

As discussed in Section 4.5.3 , parametric studies in the FLAC models for the simulations of physical model tests under distributed and concentrated load have been conducted and presented respectively. They focus on both stiffness and strength properties of the brickwork and the brickwork / soil joint.

1) The effect of stiffness properties

Brickwork stiffness

Taking numerical models (1:1:6) for example, the obtained results have shown that there is little change on the crown displacement due to the increase in the Poisson's ratio; the variation in Young's modulus of the brickwork affects 3.5% to 13% of the crown displacement behaviour, which is compared to the crown displacement of the FLAC baseline A.

Brickwork / soil joint stiffness

The interface stiffness (JKn & JKs) reduction in value to 50% decreases the overall stiffness to some extent, as shown in Figure 4.35.

2) The effect of strength properties

Brickwork strength

As can be seen from Figure 4.31 and Figure 4.32, the decrease of friction angle increases the crown displacement up to 75% of that of the FLAC baseline A, at 1.5MPa loading level; also the cohesion changes largely affect the mechanical behaviour of the brickwork tunnel.

Brickwork / soil joint strength

The increase in joint friction angle slightly changes the crown displacement curve (see Figure 4.33).

3) Comments

The results of the parametric study indicate that both the friction angle and cohesion have a remarkable influence on the brick-lined tunnel mechanical behaviour and the most important parameter is the cohesion. It shows a good agreement with Idris et al. (2008) on the property study of masonry blocks.

The rest of the factors considered (Poisson's ratio, Young's modulus of the brickwork, joint stiffness and friction angle) do not have a significant influence on the mechanical behaviour of the brick-lined tunnel.

4.5.5 Modelling results

1) Uniform load

Numerical model (1:1:6)

The mechanical behaviour of the chosen FLAC model A (FLAC A7) at certain loading level (displacement vectors and plastic state) is shown in Figure 4.48 and Figure 4.49, which reasonably simulated the physical model test 1.

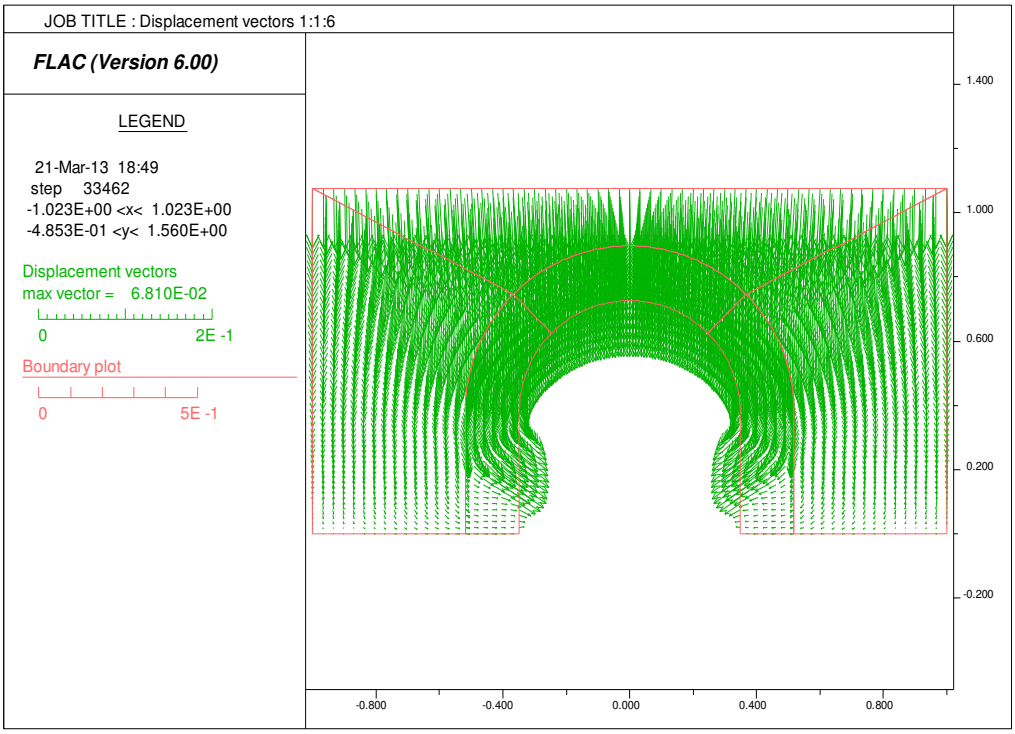

Figure 4.48 Displacement vectors of FLAC model A (1:1:6)

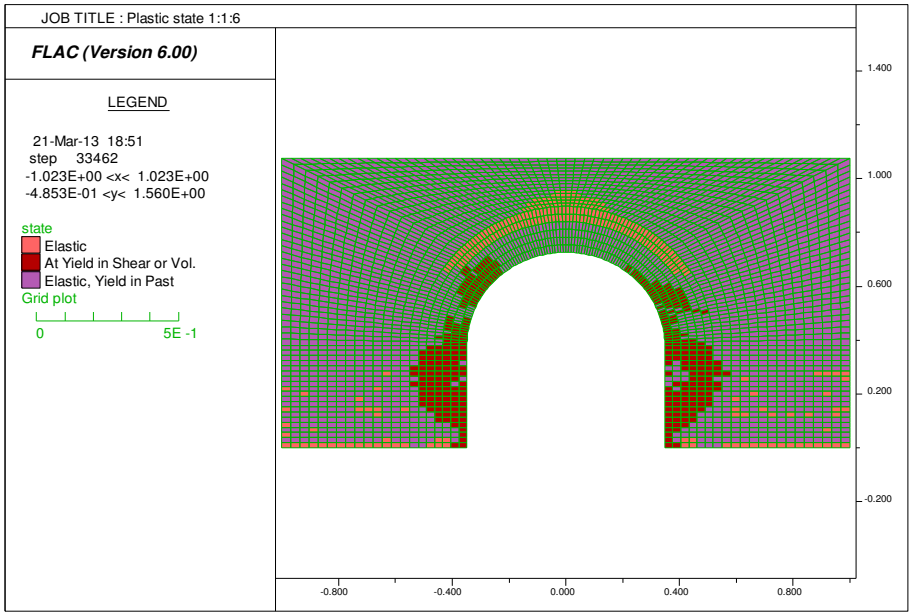

Figure 4.49 Plastic state of FLAC model A (1:1:6)

Numerical model (1:2:9)

Similarly, the mechanical behaviour of the chosen FLAC model B (FLAC B6) at certain loading level (displacement vectors and plastic state) is shown in Figure 4.50 and Figure 4.51, which reasonably simulated the physical model test 2.

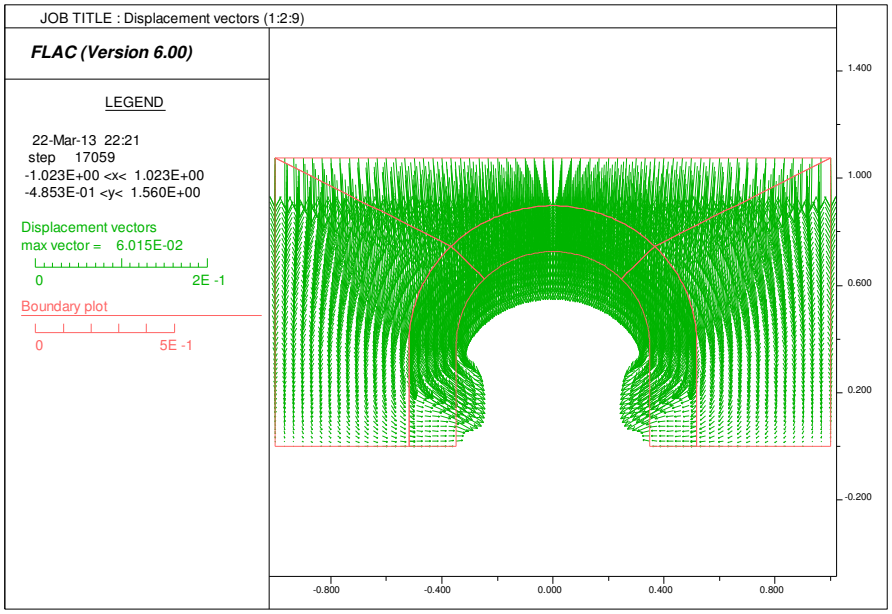

Figure 4.50 Displacement vectors of FLAC model B (1:2:9)

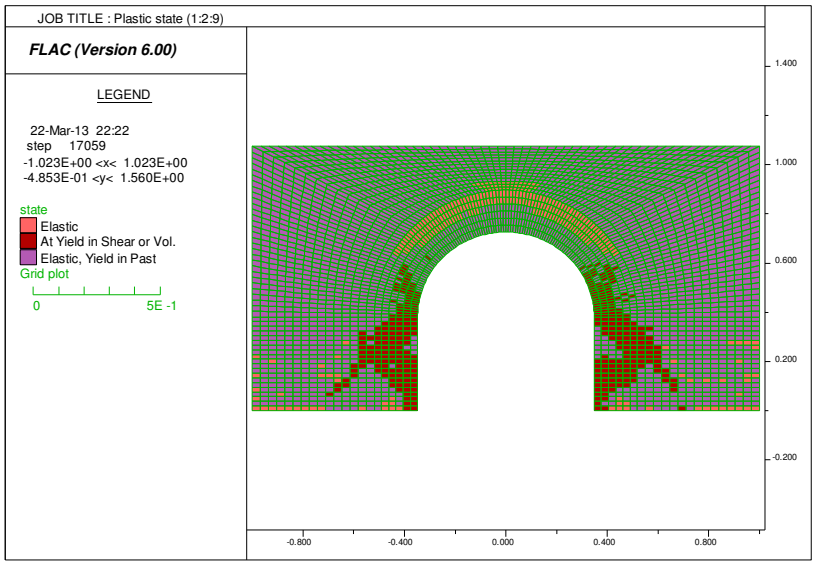

Figure 4.51 Plastic state of FLAC model B (1:2:9)

2) Concentrated load

Additionally, the mechanical behaviour of the FLAC model C (FLAC C4) at certain loading level (for displacement vectors and plastic state, see Figure 4.52 and Figure 4.53) may not represent the real behaviour, as shown in physical model test 3.

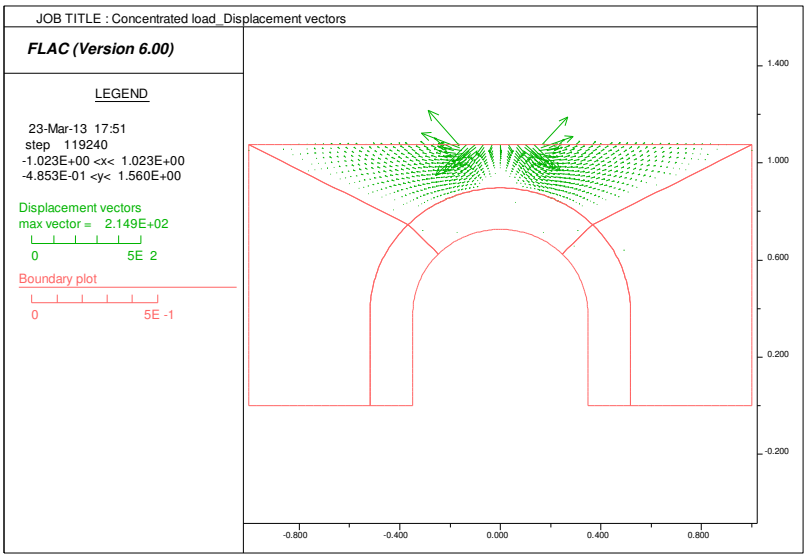

Figure 4.52 Displacement vectors of FLAC model C (1:2:9) under concentrated load

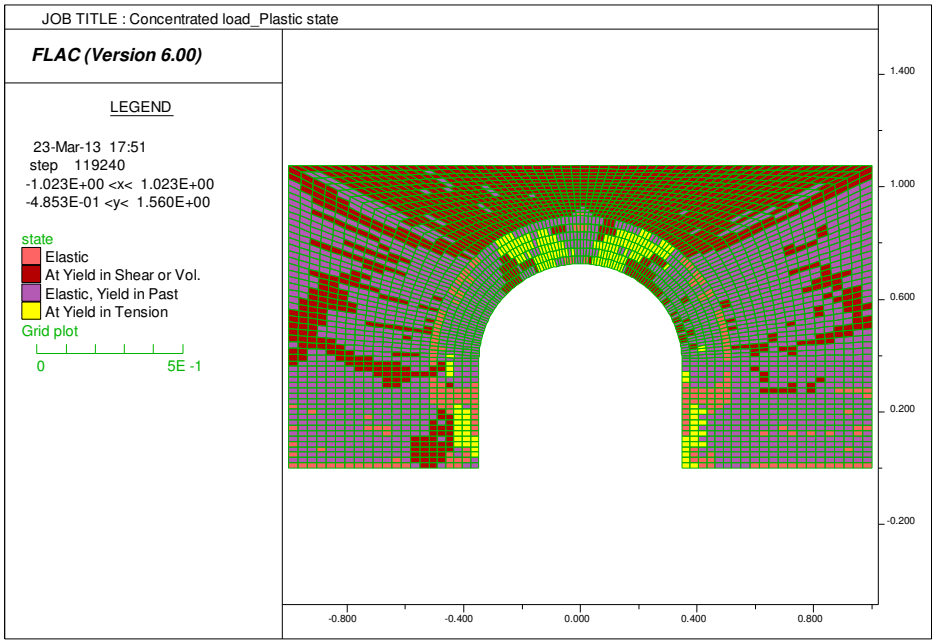

Figure 4.53 Plastic state of FLAC model C (1:2:9) under concentrated load

4.6 Introduction to UDEC

4.6.1 General introduction

In this research, a simplified micro-modelling strategy is applied to the UDEC programme.

UDEC (Universal Distinct Element Code) is a two-dimensional numerical program also developed by Itasca Consulting Group Inc., based on the distinct element method (DEM) for discontinuum modelling. UDEC could simulate the behaviour of discontinuous media, such as a jointed rock mass and an assemblage of discrete masonry blocks subjected to static or dynamic loading. UDEC is based on a "Lagrangian" calculation scheme, which is well-suited to model the large movements and rotations of a blocky system.

Deformable blocks could be subdivided into a mesh of finite-difference elements, with each element responding according to a prescribed linear or nonlinear stress-strain law. Linear or nonlinear force-displacement relations for movement both in the normal and shear direction also govern the relative motion of the discontinuities.

Similar to FLAC, UDEC also contains FISH to define new variables and functions. FISH permits (UDEC Manual, 2005):

a) Custom property variations in the grid (e.g., nonlinear increase of strength with depth);
b) Plotting and printing of user-prescribed variables;
c) Implementation of special joint generators;
d) Specification of unusual boundary conditions; variations in time and space;
e) Automation of parameter studies.

4.6.2 Fields of application

The nature of a jointed rock mass (i.e., the internal structure and initial stress state) is unknown and unknowable to a large extent. Thus, it would be impossible to make an identical model of a rock mass system by UDEC. Nevertheless, an understanding of the response of a jointed rock mass can be achieved using UDEC. Thus, it could improve the engineering understanding of the relative impact of various phenomena on rock mechanics design. In this way, the engineer could investigate and predict potential failure mechanisms associated with a jointed rock mass.

The analysis was conducted primarily in the field of rock engineering, ranging from studies of the progressive failure of rock slopes to evaluations of the influence of rock joints, faults, bedding planes, etc. on underground excavations and rock

foundations. Various rock reinforcement systems, such as grouted rockbolting and shotcrete, have been simulated using a structural element set in the program.

UDEC has been applied mostly in studies related to mining engineering, such as static and dynamic analyses of deep underground mined openings. Another application is the study of the response of reinforced concrete. The breaking of bonds between blocks could simulate the progressive failure with crack propagation and spalling.

A potential application area of UDEC is in studies related to earthquake engineering. For example, the program may be used to explain some phenomena, like fault movement.

4.6.3 Comparison with other methods

1) Differentiation

A general question is asked about UDEC: 'Is UDEC a distinct element or a discrete element program?'

The term *'discrete element method'* applies to a computer program when it: (a) could allow finite displacements and rotations of discrete bodies, even complete detachment; and (b) could recognise new contacts automatically in progress.

The name *'distinct element method'* refers to a particular discrete element scheme. Distinct Element Programs use deformable contacts and an explicit, time-domain solution of the equations of motion directly; bodies may be rigid or deformable by subdivision into elements. UDEC falls in this category (UDEC Manual, 2005).

2) Characteristics

In order to simulate the behaviour of a discontinuous medium, many finite elements, boundary elements and Lagrangian finite difference programs have developed interface elements or slide lines to a limited extent only. For instance, their formulation is usually restricted to small displacements and rotation; the logic may break down when many intersecting interfaces are used. That is to say, the above programs are more suited to dealing with continuum features rather than large discontinuous media; UDEC is ideally suited to the study of potential modes of failure directly related to the presence of discontinuous features.

4.6.4 General solution procedure

In this research, UDEC is used to simulate a set of physical models with hundreds of discrete masonry bricks under static loading.

Firstly, to set up a model in UDEC, three fundamental components must be specified as:

a) A distinct-element model block with cuts to create problem geometry;
b) Constitutive behaviour and material properties;
c) Boundary and initial conditions.

After these conditions have been defined in UDEC, an alteration is then performed (such as excavating material or changing material properties), and the resulting response of the model is calculated.

The general solution procedure for static analysis with UDEC is illustrated in Figure 4.54. This procedure represents the sequence of processes that occurs in the physical environment.

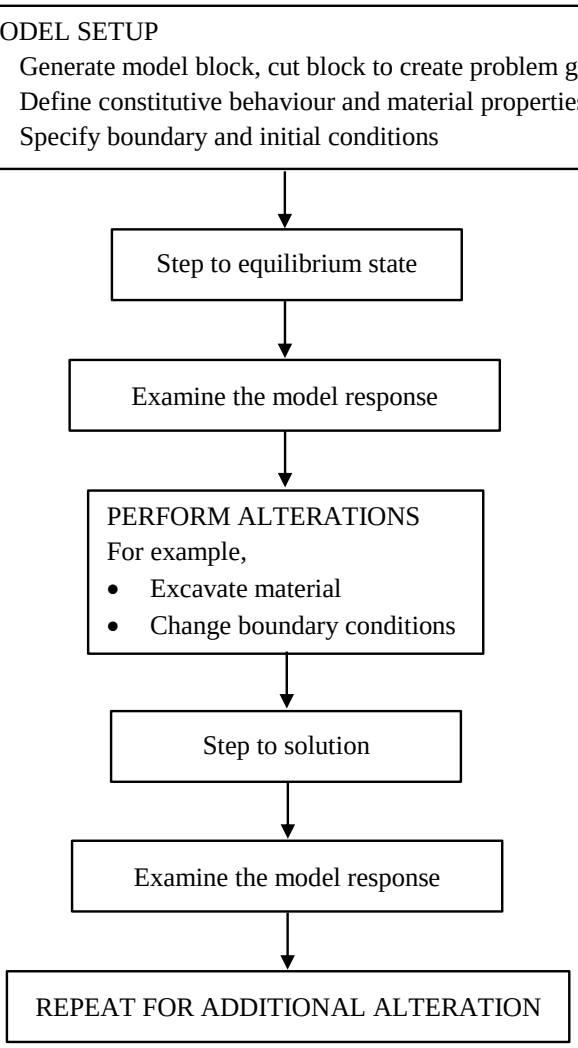

Figure 4.54 General solution procedure for static analysis (Itasca, 2005)

4.6.5 Further developments

Since UDEC is a two-dimensional program, the three-dimensional geometry of a joint structure cannot be represented, except for special orientations.

In order to evaluate the importance of three-dimensional geometry on the response of a system, a three-dimensional numerical program, such as the Itasca code 3DEC or PFC^{3D}, is required.

4.7 Numerical modelling of physical models using UDEC

4.7.1 Materials and interface properties

The Mohr-Coulomb constitutive model is also employed for numerical modelling in UDEC. Similar to FLAC modelling, most of the material properties are obtained in the laboratory, as mentioned in Section 4.2 Programme of material testing.

In terms of interfaces, UDEC is specially designed to model interacting bodies and would replace FLAC in terms of more complicated interface problems such as brickwork block (including mortar) joints.

In particular, the interface has two essential factors of normal and shear stiffness between two blocks, which may contact each other. Figure 4.55 illustrates the joint model, in which two blocks are connected by shear and normal stiffness springs, joint tensile strength, joint friction angle and joint cohesion (Goodman et al., 1968).

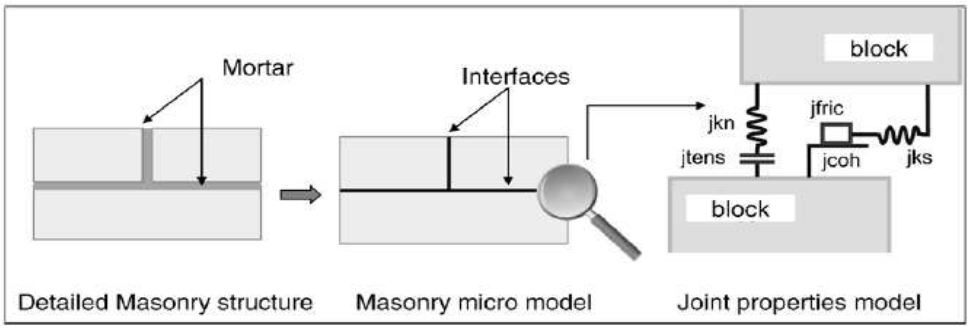

Figure 4.55 Interface model in the UDEC code (Idris et al. 2009)

The values of Jkn and Jks depend on the contact area ratio, the relevant properties of the joint filling material and blocks and the roughness of the joint surface. There are two ways to determine the value of Jkn and Jks.

1° Rule-of-thumb (see Section 4.5.1)

2° After CUR (1994)

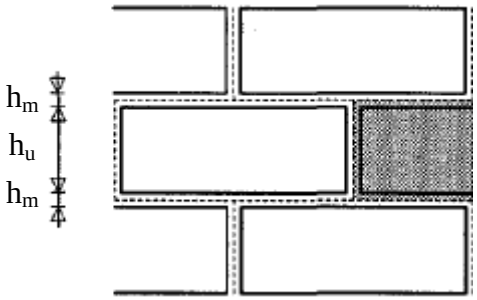

Figure 4.56 Model using Micro-modelling strategy

With the assumption of stack bond and uniform stress distributions in both brick and mortar, the components of the elastic stiffness matrix D read, (Lourenco, 1996; CUR, 1994),

$$kn = \frac{EbEm}{hm(Eb - Em)} \quad \text{(4.9)}$$

$$ks = \frac{GbGm}{hm(Gb - Gm)} \quad \text{(4.10)}$$

Where E_u and E_m are the Young's moduli, G_u and G_m are the shear moduli, respectively, for brick and mortar and h_m is the actual thickness of the joint.

4.7.2 Model generation

Similar to the model generation using FLAC, the first step was to specify the shape of the whole model using several pieces of block. The procedure continued to split the initial blocks of brick-lined tunnels into smaller blocks with the purpose of generating interfaces between individual bricks (the thin mortar between bricks was simplified and combined with brick as a whole). The blocks were then made deformable by creating finite-difference triangular zones in each block (see Figure 4.57).

Next, the same boundary conditions and gravity were set as those in FLAC. The material properties were assigned for the blocks and interfaces: the soil properties were in blue, whilst brick combined with mortar properties were in green, as shown in Figure 4.57 and as prescribed in the Mohr-Coulomb model. After setting to an equilibrium state, vertical loading was then added until failure occurred. Thus, the boundary conditions of the initial physical model were changed.

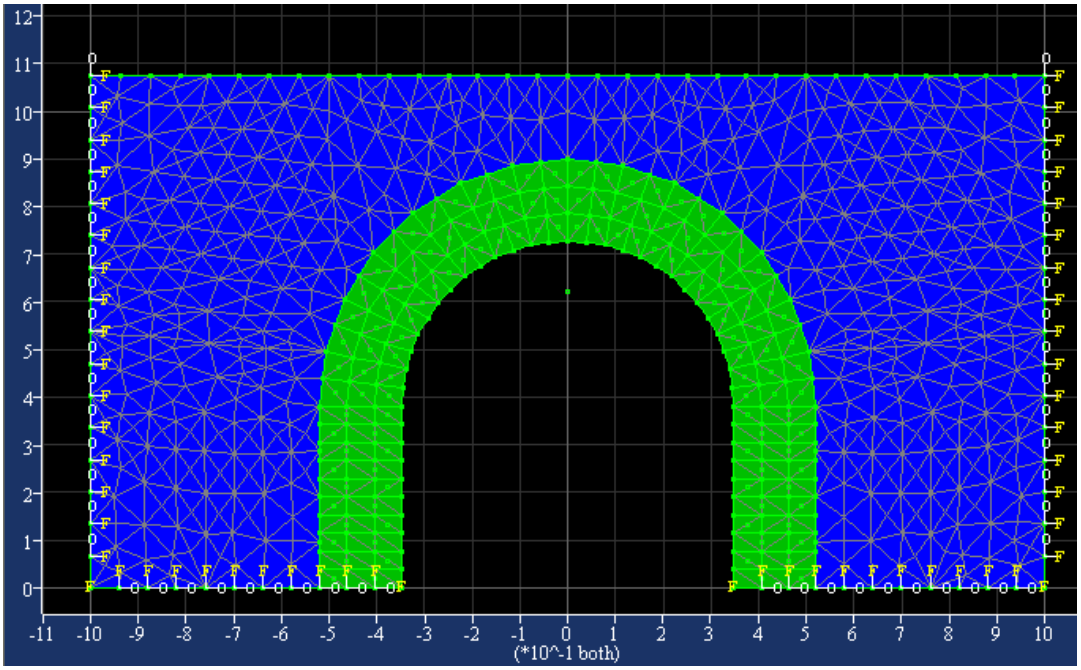

Figure 4.57 UDEC model grids with boundary conditions

4.7.3 Parametric study

Parametric studies of different variables were conducted by UDEC to simulate the evolution of the mechanical properties of the materials and interfaces used. The variations of the different parameters are shown below.

1) Uniform load

Baseline numerical model (1:1:6)

The properties of brickwork and brickwork / soil joints listed in Table 4.20 are the same as those in FLAC baseline model A (1:1:6), whilst brickwork block joint properties are displayed at the end. The pressure versus crown displacement curve of the baseline model is compared with the variations of properties in the parametric study.

Table 4.20 Brickwork block (mix proportion 1:1:6), brickwork / soil and brickwork block joint properties

Brickwork block (1:1:6)					
ρ (kg/m³)	**E (MPa)**	**v**	**c (MPa)**	**φ**	**Tr (MPa)**
1732	384.33	0.2*	0.1845	55°	0.2437
Brickwork / soil joint					
	JKn_1 (GPa/m)	**JKs_1 (GPa/m)**	**Jc_1 (MPa)**	**$J\varphi_1$**	**JTr_1 (MPa)**
	112.97	112.97	0	25*	0
Brickwork block joints					
	JKn_2 (GPa/m)	**JKs_2 (GPa/m)**	**Jc_2 (MPa)**	**$J\varphi_2$**	**JTr_2 (MPa)**
	112.97	112.97	0.1521	25*	0.218

*: Poisson's ratio of the brickwork and the friction angle of the joint (Jφ) were initially referring to Idris et al., 2008.

Parametric study

UDEC baseline A, models A1 - A4: Initially the friction angle of the brickwork block was decreased to 50° and 52° in UDEC A1 and A2 separately. As we could see from Figure 4.58, the reducing values of the friction show a gradual decrease in the slope, which is closer to the experiment result. In UDEC A3, the cohesion was dropped to 0.16 MPa, as in the FLAC modelling. Thus, the crown displacement was similar to the experiment curve at the ultimate load. The values of joint normal and shear stiffness were both calculated in two ways (see Section 4.7.1). The above models used the first method, while UDEC A4 changed to the second method with which the crown displacement increased at ultimate load. After study, UDEC A3 was determined to be the most appropriate model to simulate physical model test 1.

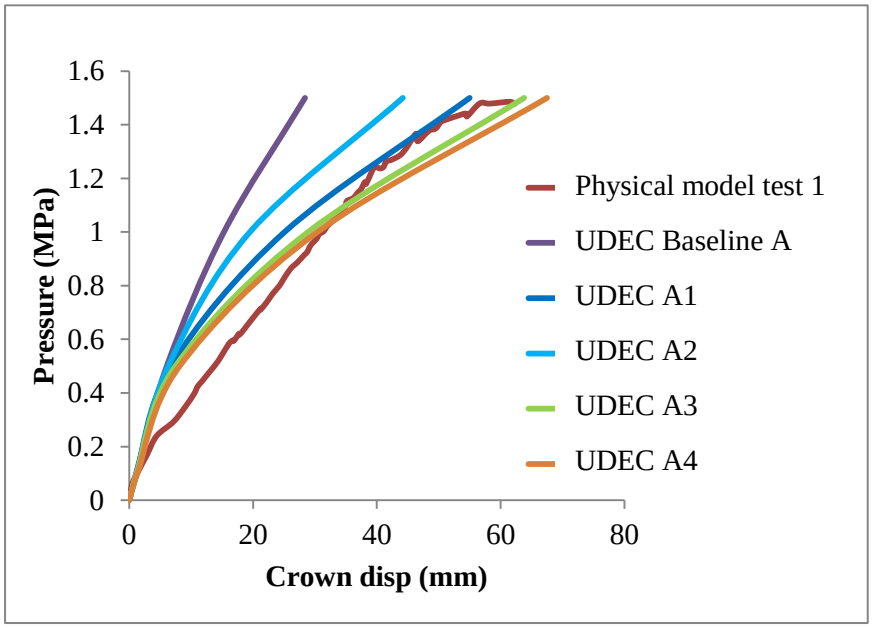

Figure 4.58 Physical model 1 vs. UDEC model A curves

Table 4.21 shows the values of the parametric study.

Table 4.21 Brickwork parametric study (1:1:6)

	E (MPa)	v	c (MPa)	φ	JKs_2 (GPa/m)	JKn_2 (GPa/m)	$J\varphi_2$
Baseline A	384.33	0.2	0.1845	55°	112.97	112.97	25°
UDEC A1	384.33	0.2	0.1845	50°	112.97	112.97	25°
UDEC A2	384.33	0.2	0.1845	52°	112.97	112.97	25°
UDEC A3	384.33	0.2	0.16	50°	112.97	112.97	25°
UDEC A4	384.33	0.2	0.16	50°	28.83	69.18	25°

Baseline numerical model (1:2:9)

The properties listed in Table 4.22 were used for the UDEC baseline model B (1:2:9). The crown displacement curve of the baseline model was compared with other UDEC models in the parametric study.

Table 4.22 Brickwork block (mix proportion 1:2:9), brickwork / soil and brickwork block joint properties

Brickwork (1:2:9)					
ρ (kg/m³)	**E (MPa)**	**v**	**c (MPa)**	**φ**	**Tr (MPa)**
1672.5	218.67	0.2*	0.0389	52°	0.0968
Brickwork / soil joint					
	JKn_1 (GPa/m)	**JKs_1 (GPa/m)**	**Jc_1 (MPa)**	**$J\varphi_1$**	**JTr_1 (MPa)**
	64.28	64.28	0	25*	0
Brickwork block joints					
	JKn_2 (GPa/m)	**JKs_2 (GPa/m)**	**Jc_2 (MPa)**	**$J\varphi_2$**	**JTr_2 (MPa)**
	64.28	64.28	0.0449	25*	0.066

*: Poisson's ratio of the brickwork and the friction angle of the joint (Jφ) were initially with reference to Idris et al., 2008.

Parametric study

UDEC baseline B, models B1 - B3: Figure 4.59 clearly illustrates the influence of brickwork cohesion as well as the stiffness of brickwork block joints, where UDEC B2 with the increase of cohesion up to 0.1 MPa could best represent the displacement curve of physical model test 2. The stiffness of the brickwork block joints using method 2 in UDEC B3 did not show any difference compared to UDEC B2 using method 1. Thus, UDEC B2 was considered as the appropriate model here. All the values of parametric study are shown in Table 4.23.

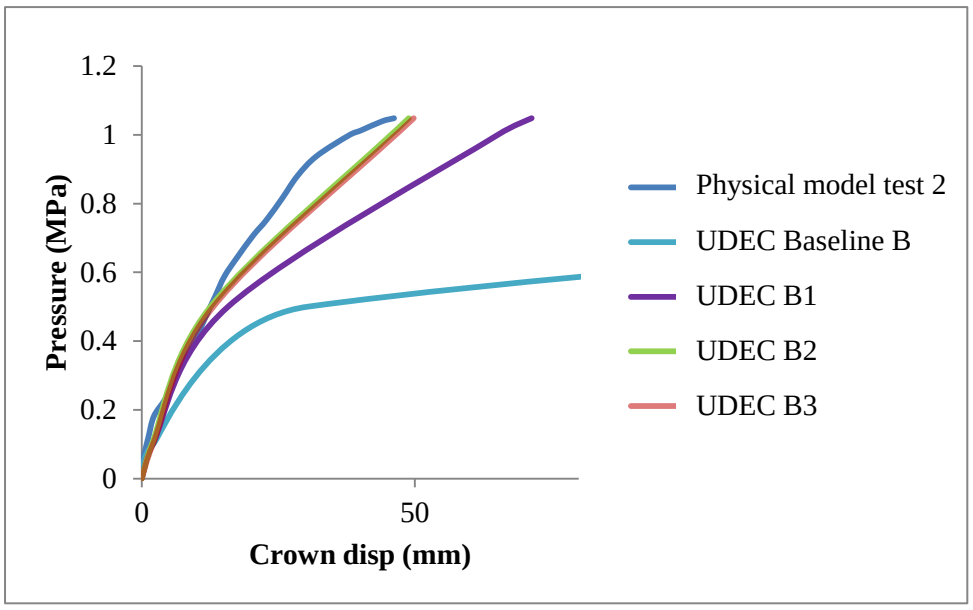

Figure 4.59 Physical model 2 vs. UDEC model B curves

Table 4.23 Brickwork block parametric study (1:2:9)

	E (MPa)	v	c (MPa)	φ	JKs_1 (GPa/m)	JKn_2 (GPa/m)	$J\varphi_2$
Baseline B	218.67	0.2	0.0389	52°	64.28	64.28	25°
UDEC B1	218.67	0.2	0.07 (79.94%)	52°	64.28	64.28	25°
UDEC B2	218.67	0.2	0.1 (157.07%)	52°	64.28	64.28	25°
UDEC B3	218.67	0.2	0.1	52°	22.05	52.92	25°

2) Concentrated load

Baseline numerical model (1:2:9)

Again, the properties listed in Table 4.22 were used for the UDEC baseline model C (1:2:9) under concentrated load. The crown displacement curve of baseline model C was compared with other UDEC models in the parametric study in the next part.

Parametric study

UDEC baseline C, models C1 - C3: The cohesion of the brickwork was increased to approach the experiment curve, from 0.1 MPa to 0.3 MPa. The increase of the cohesion to 0.3 MPa was finally satisfied, as can be seen from Figure 4.60.

UDEC models C4 - C6: In models C4 to C6, the joint stiffness, cohesion and tensile strength were varied separately to find out their influence on the numerical modelling, compared to model C2 with the same cohesion of brickwork. Figure 4.61 demonstrates that the joint cohesion would not have much effect on the brickwork block behaviour, while both joint tensile strength and joint stiffness show remarkable influences on brickwork behaviour. However, these models would not represent physical model test 3.

UDEC model C7: Finally, model C7 with 0.1 MPa joint tensile strength and brickwork block cohesion was compared to model C3 with 0.066 MPa joint tensile strength. The increased joint tensile strength leads to less stiffness of the crown displacement curve shown in Figure 4.62.

In other words, The UDEC model C3 with 0.3 MPa cohesion was the best one to represent physical model 3.

Table 4.24 Brickwork block parametric study (1:2:9) under concentrated load

	E (MPa)	c (MPa)	JKs_1 (GPa/m)	JKn_2 (GPa/m)	Jc	JTr_2 (MPa)
Baseline C	218.67	0.0389	64.28	64.28	0.0449	0.066
UDEC C1	218.67	0.1	64.28	64.28	0.0449	0.066
UDEC C2	218.67	0.2	64.28	64.28	0.0449	0.066
UDEC C3	218.67	0.3	64.28	64.28	0.0449	0.066
UDEC C4	218.67	0.2	64.28	64.28	0.1	0.066
UDEC C5	218.67	0.2	64.28	64.28	0.0449	0.1
UDEC C6	218.67	0.2	22.05	52.92	0.0449	0.066
UDEC C7	218.67	0.3	64.28	64.28	0.0449	0.1

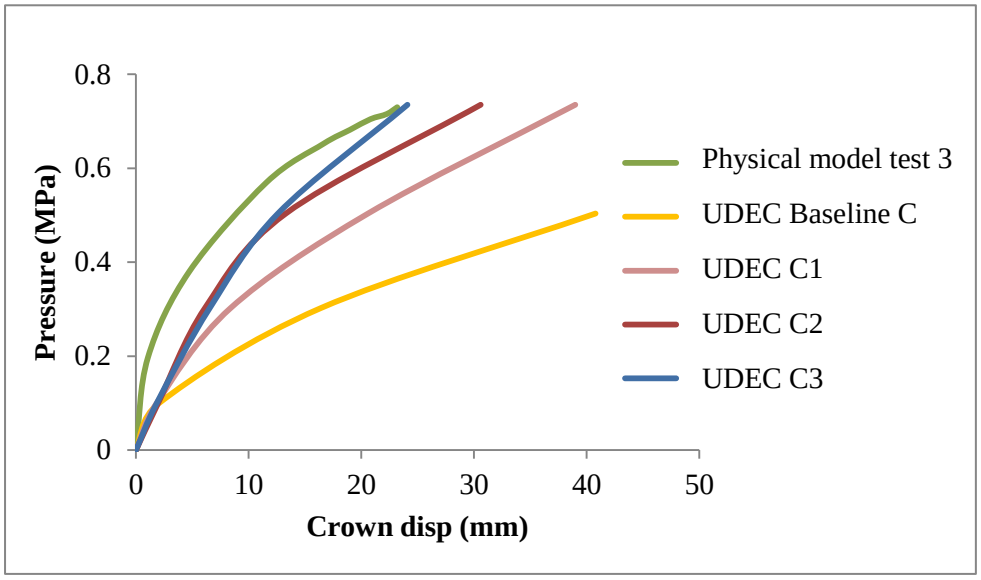

Figure 4.60 Physical model 3 vs. UDEC baseline C & model C1 - C3 curves

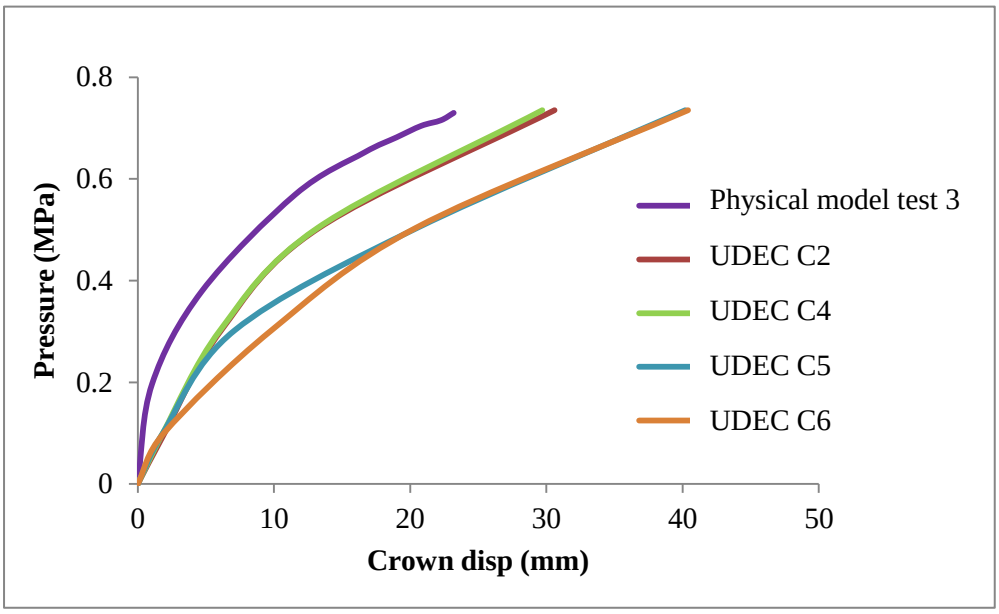

Figure 4.61 Physical model 3 vs. UDEC model C2 & C4 - C6 curves

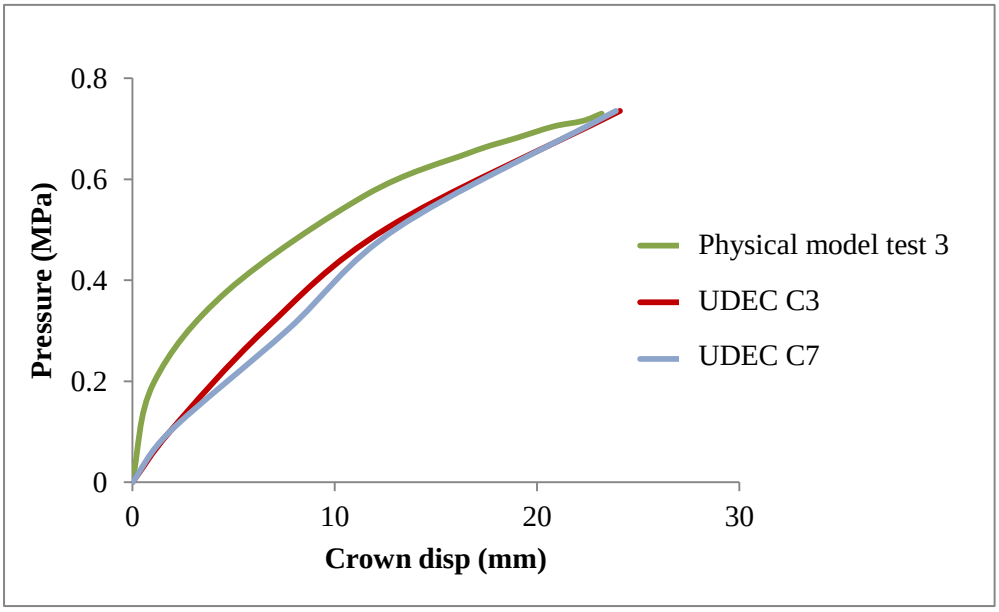

Figure 4.62 Physical model 3 vs. UDEC model C3 & C7 curves

4.7.4 Results analysis of the parametric study

Parametric studies in the UDEC models have also been carried out in the last section 4.7.3; the discussions and comments are shown here.

1) The effect of strength properties

Brickwork block strength

As shown in Figure 4.58, for numerical models (1:1:6) the variation in the friction angle of the brickwork blocks leads to large changes to the crown displacement curve, whilst the decrease in the cohesion increases the crown displacement at failure. This is closer to the physical model test result.

Brickwork block joint strength

In particular, the brickwork block joint strength parameters are studied for numerical models under concentrated load in UDEC. The increase in brickwork block joint cohesion only changes the crown displacement curve slightly. However, the increase in joint tensile strength shows a large drop in the overall stiffness in Figure 4.61. The reason may be that the stronger the joint tensile strength is, the more the tunnel behaves like a continuum, leading to a shear failure at a lower load. The reduction in the overall stiffness is also displayed in Figure 4.62 for the increase in joint tensile strength (0.1 MPa) with increased brickwork block cohesion of 0.3 MPa.

2) The effect of stiffness properties

Brickwork block joint stiffness

Two calculation methods of joint stiffness with different values were used and input into the numerical models. Under uniform load, the model with smaller values slightly increases the crown displacement at the ultimate load. In contrast, the reduction in joint stiffness shows a big change in the crown displacement curve for the model under concentrated load. That is because the crown deforms much more

than other parts under concentrated load, where joint stiffness plays an important role.

3) Comments

The UDEC modelling results imply that the cohesion of brickwork blocks seems to be the predominant factor over others, followed by the friction angle of brickwork blocks and, finally, joint tensile strength.

Neither joint cohesion or joint stiffness show a noticeable influence on the mechanical behaviour of a brick-lined tunnel.

4.7.5 Modelling results

1) Uniform load

Numerical model (1:1:6)

The figures followed demonstrate the displacement and plastic state of the chosen UDEC model A (UDEC A3) at certain loading level, simulating the results of physical model test 1.

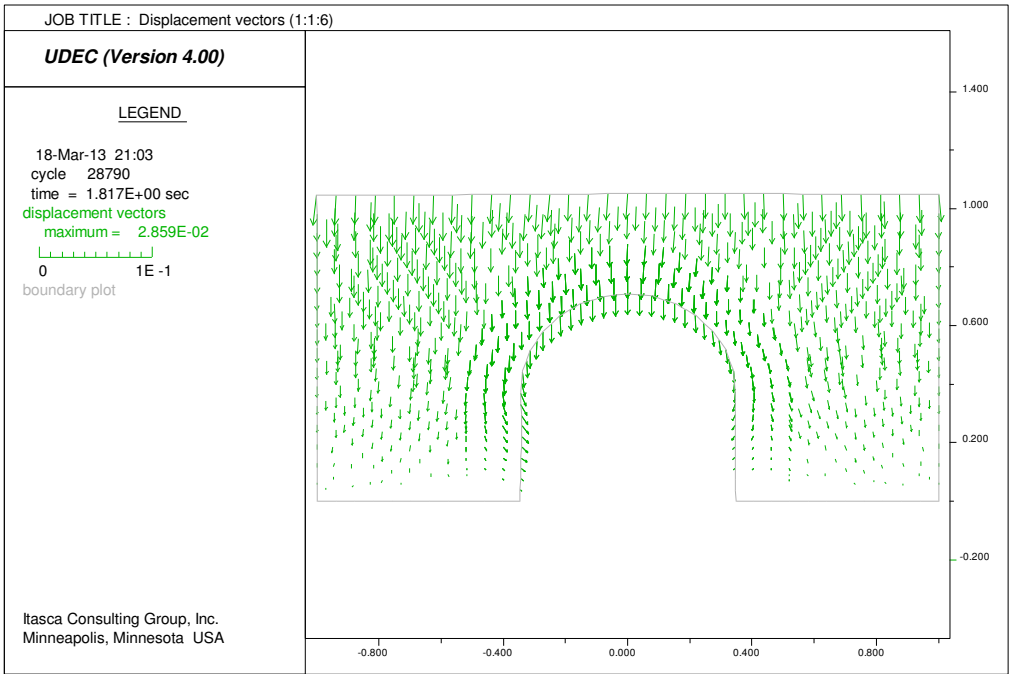

Figure 4.63 Displacement vectors of UDEC model A (1:1:6)

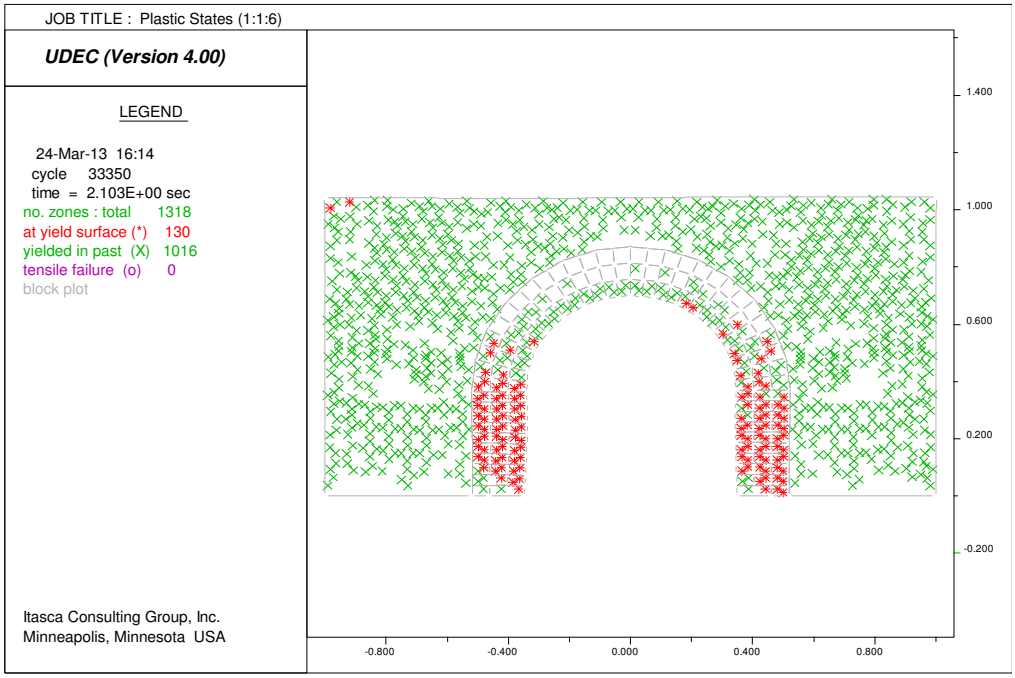

Figure 4.64 Plastic state of UDEC model A (1:1:6)

Numerical model (1:2:9)

The displacement and plastic state of the chosen UDEC model B (UDEC B2) at certain loading level were displayed in Figure 4.65 and Figure 4.66.

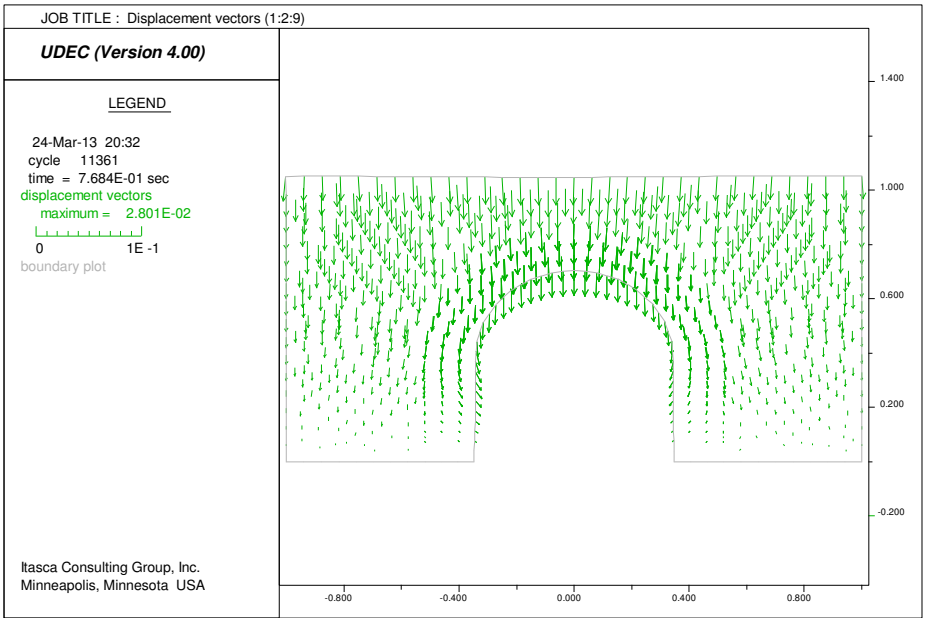

Figure 4.65 Displacement vectors of UDEC model B (1:2:9)

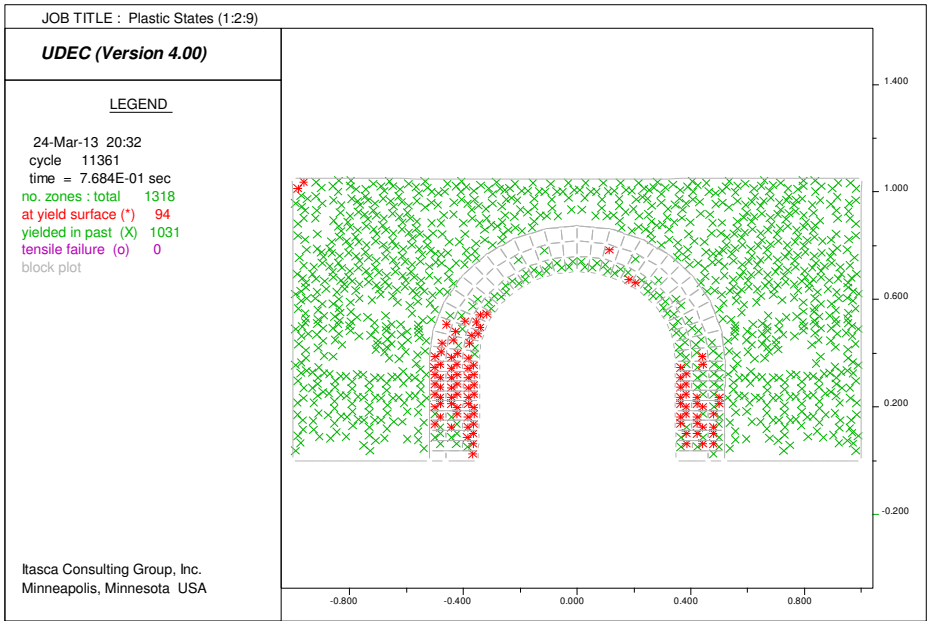

Figure 4.66 Plastic state of UDEC model B (1:2:9)

2) Concentrated load

Figure 4.67, Figure 4.68 and Figure 4.69 display the mechanical behaviour of the UDEC model C (UDEC C3) at certain loading level (displacement vectors and plastic state). In particular, tensile failure at the tunnel arch in Figure 4.68 shows a good agreement with the experimental result, whilst failure pattern of the UDEC model C in Figure 4.69 demonstrates the hinges and cracks at certain positions of the tunnel arch.

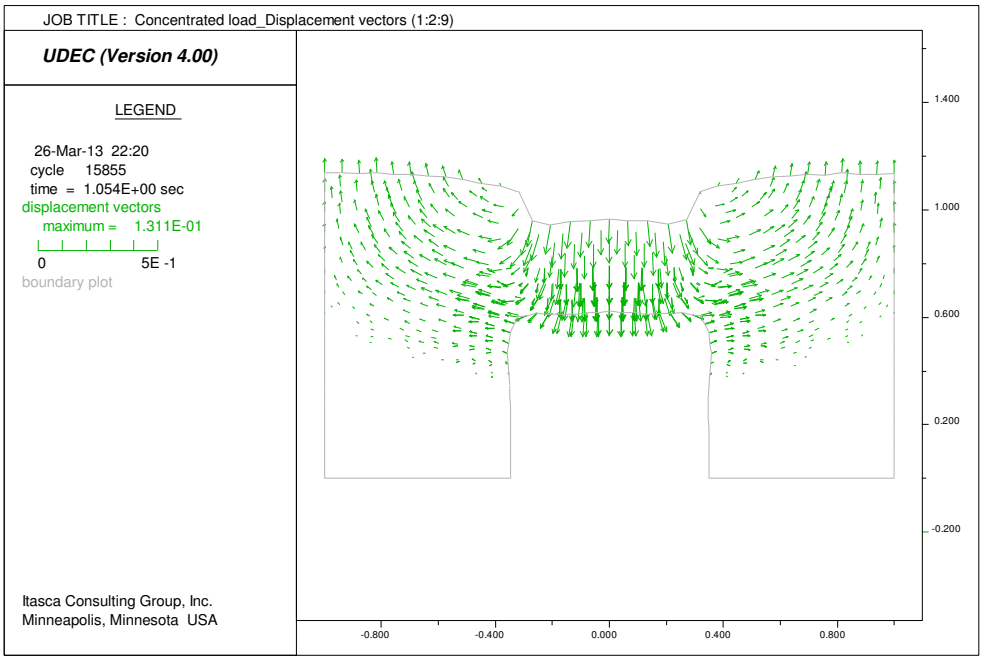

Figure 4.67 Displacement vectors of UDEC model C (1:2:9) under concentrated load

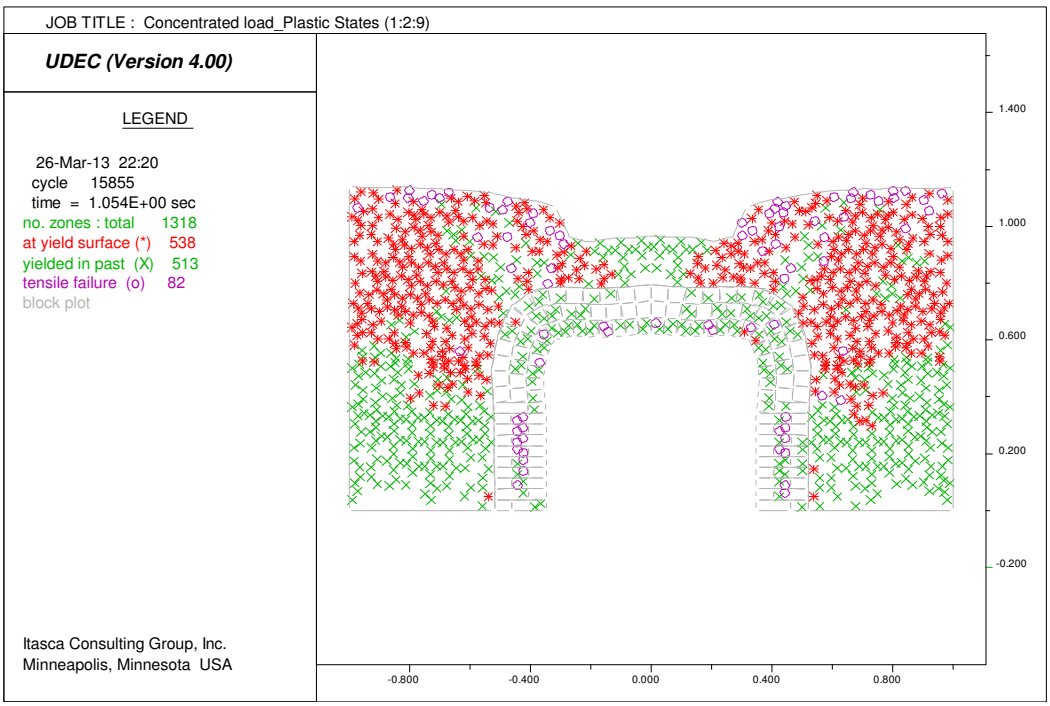

Figure 4.68 Plastic state of UDEC model C (1:2:9) under concentrated load

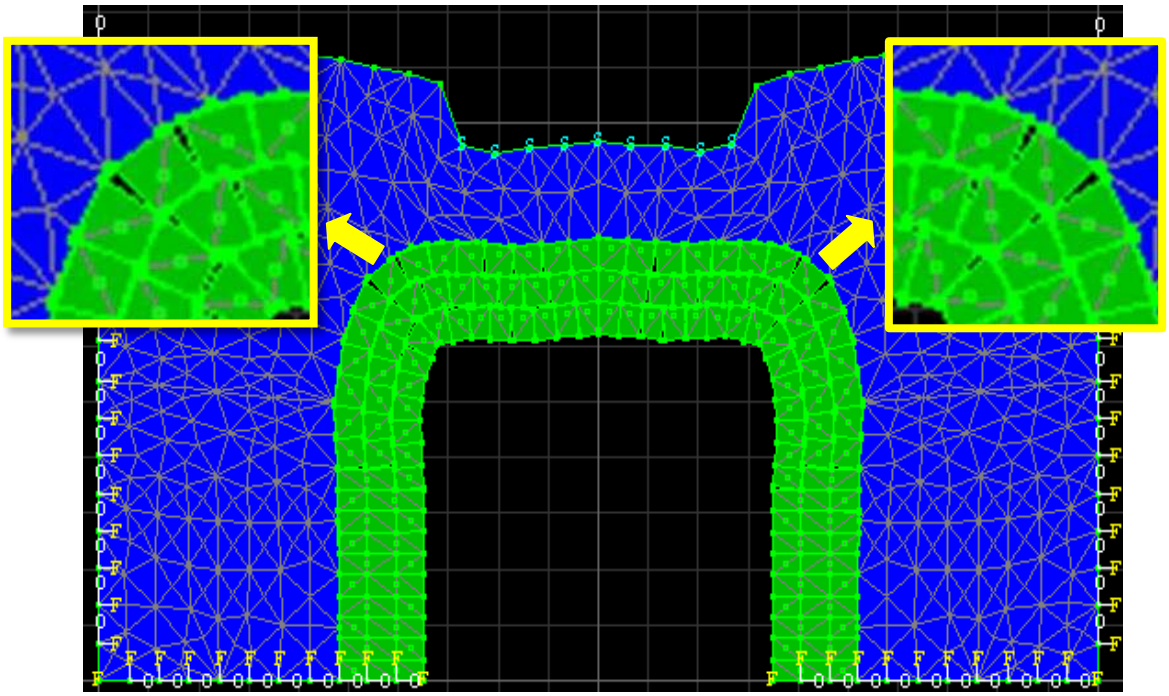

Figure 4.69 Failure pattern of UDEC model C (1:2:9) under concentrated load showing hinges

4.8 Discussion

4.8.1 Comparison with physical model tests

Numerical modelling results were analysed and compared with physical model tests of brick-lined tunnels, as shown from Figure 4.70 to Figure 4.73.

The numerical modelling results have a good agreement with the mechanical behaviour of the physical model tests in terms of both deformation characteristics and failure pattern, thus proving that they could be effectively used in the study of masonry tunnel stability.

These good agreements with physical model tests 1 - 3 encourage further predictions of numerical modelling under various conditions, as discussed in the next section, 4.9.

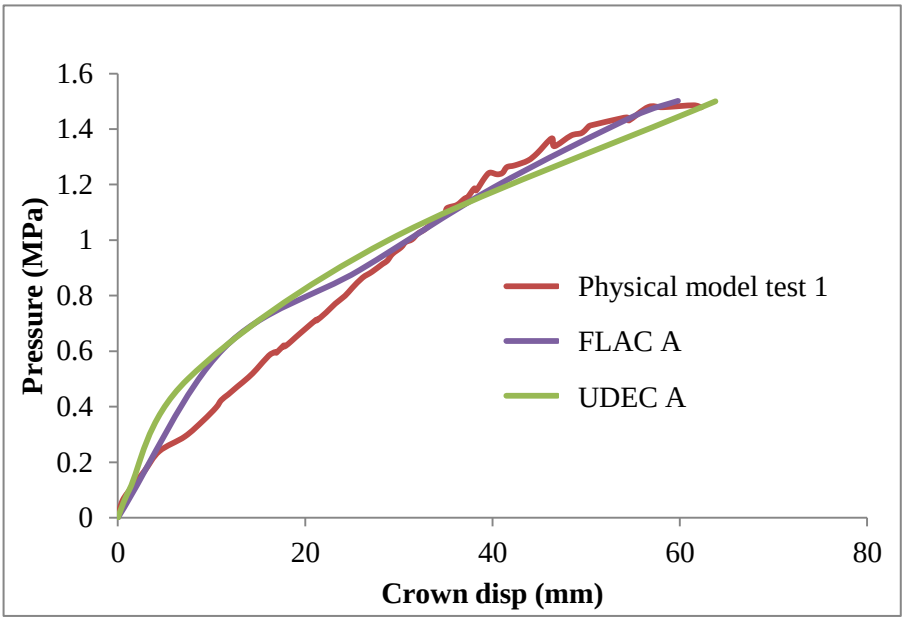

Figure 4.70 Physical model test 1 vs. numerical curves

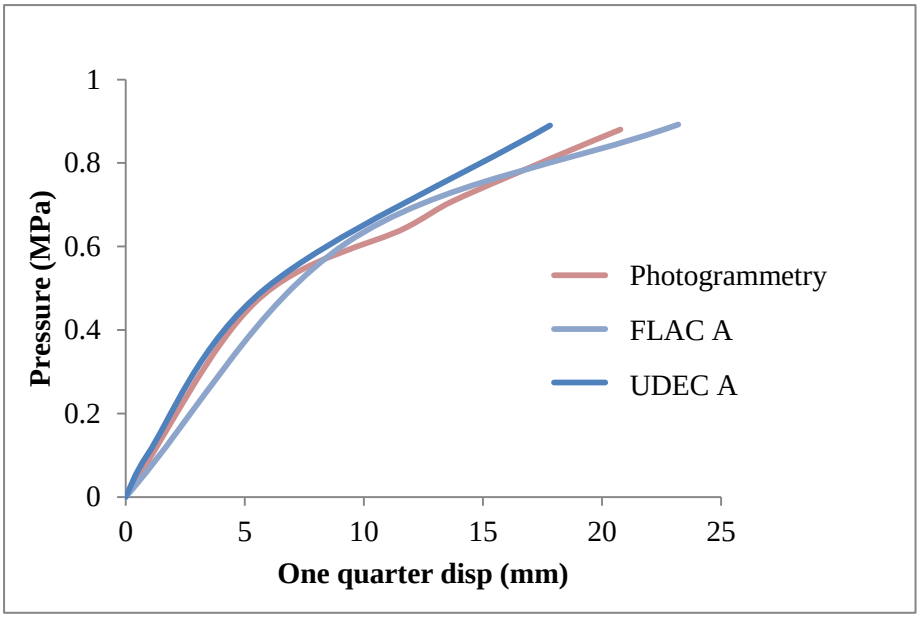

Figure 4.71 Physical model test 1 at 1/4 tunnel arch vs. numerical curves

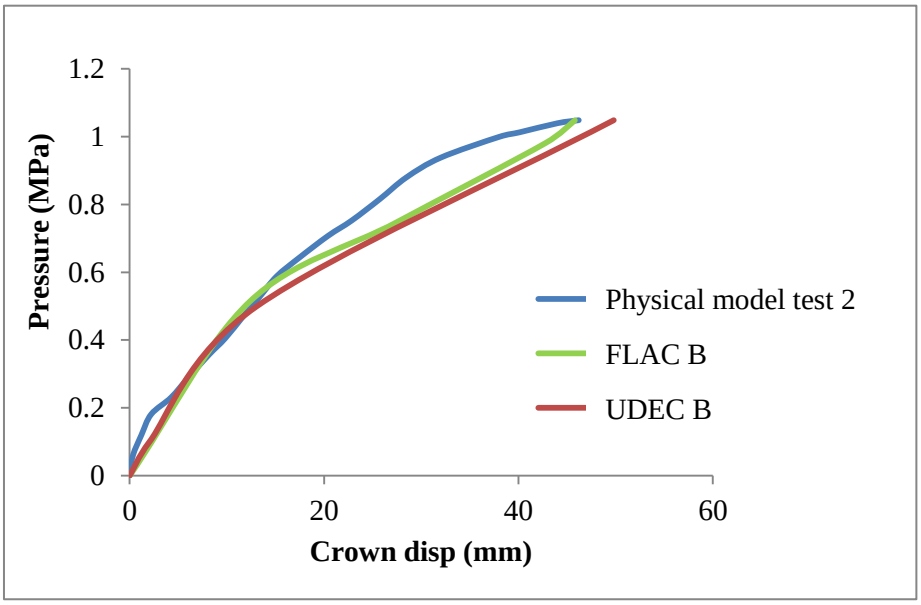

Figure 4.72 Physical model test 2 vs. numerical curves

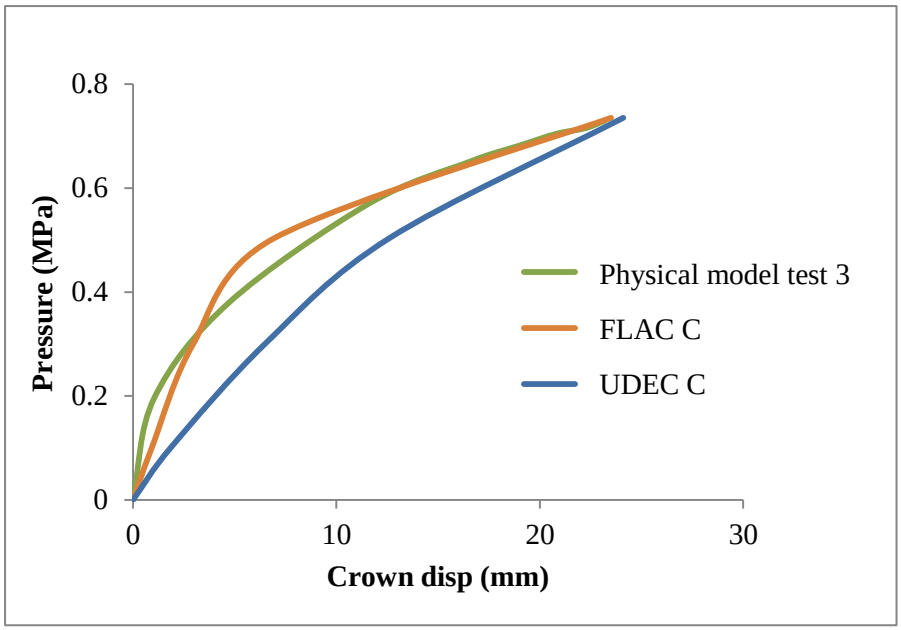

Figure 4.73 Physical model test 3 vs. numerical curves

4.8.2 Comments

Notably, the value of brickwork cohesion of the FLAC numerical model was normally smaller than the brickwork block cohesion in the UDEC model. The reason might be that the brickwork in FLAC (containing mortar and the interface) should be weaker than the brickwork block in UDEC (containing only mortar).

Taking the simulation of physical model 3 for an example, the FLAC numerical model C used 0.2 MPa cohesion of brickwork that was about 5 times larger than the laboratory result (0.0389 MPa), while in UDEC 0.3 MPa cohesion of brickwork block was employed to match the physical model.

For the numerical models under uniform load that reached shear failure, the mechanical behaviour of both the FLAC and UDEC models were very similar to each other.

For the numerical models under concentrated load, hinge failure occurred at the ultimate load. UDEC modelling enabled the local and sophisticated mechanical behaviour of discrete elements such as the cracking among brickwork blocks to be shown.

In general, a micro-modelling strategy could give a better understanding of the local failure behaviour of brickwork structures, whilst macro-modelling could simulate deformation characteristics slightly better.

4.9 Prediction of numerical simulations

4.9.1 Introduction

Based on the proper numerical modelling, the deformation characteristics, mechanical behaviour and probable failure mechanisms of the brick-lined tunnels under different conditions are predicted by the combination of FLAC and UDEC software.

In order to figure out the interaction of the overburden soil, brick-lined tunnel and the soil depth effect on the tunnel, various soil depths (from the tunnel bottom) are used in numerical modelling, from 980 mm to 1455 mm. 95 mm or 190 mm depth may be added each time, as can be seen in Table 4.25.

Numerical models at different locations under concentrated load are then developed to simulate the failure mechanism of 'Brickwork Bridge' under pavement.

Table 4.25 Prediction of numerical models under uniform and concentrated load

Numerical model No.	Overburden soil depth (mm)	Depth difference (mm)	loading style	Mortar mix proportion
1	980		Uniform load	1:1:6 (higher strength)
2	1075	95		
3	1265	190		
4	1455	190		
7	980		Concentrated load	1:2:9 (weaker strength)
8	1075	95		
9	1170	95		
10	1265	95		

4.9.2 Overburden soil depth

1) Uniform load test (1:1:6)

As can be seen in Figure 4.74, the increase in soil depth gradually decreases the overall stiffness and failure load of the brick-lined tunnel. The shear failure not only occurs at the tunnel sidewalls, but also extends to the tunnel arch as the soil depth rises (see Appendix C).

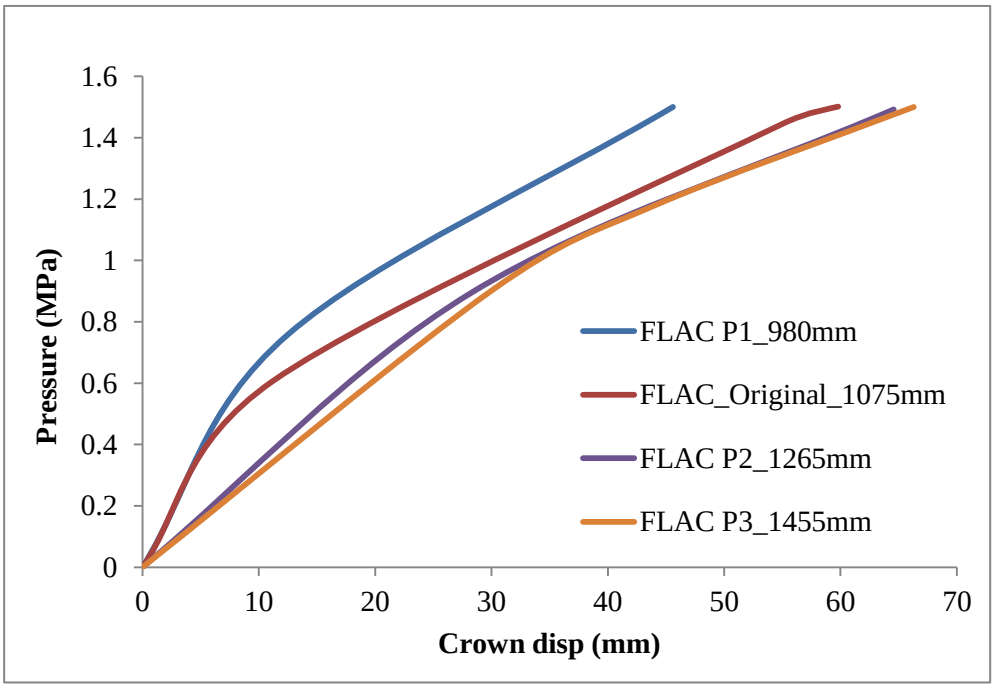

Figure 4.74 Prediction of crown displacement curves under uniform load

2) Concentrated load test (1:2:9)

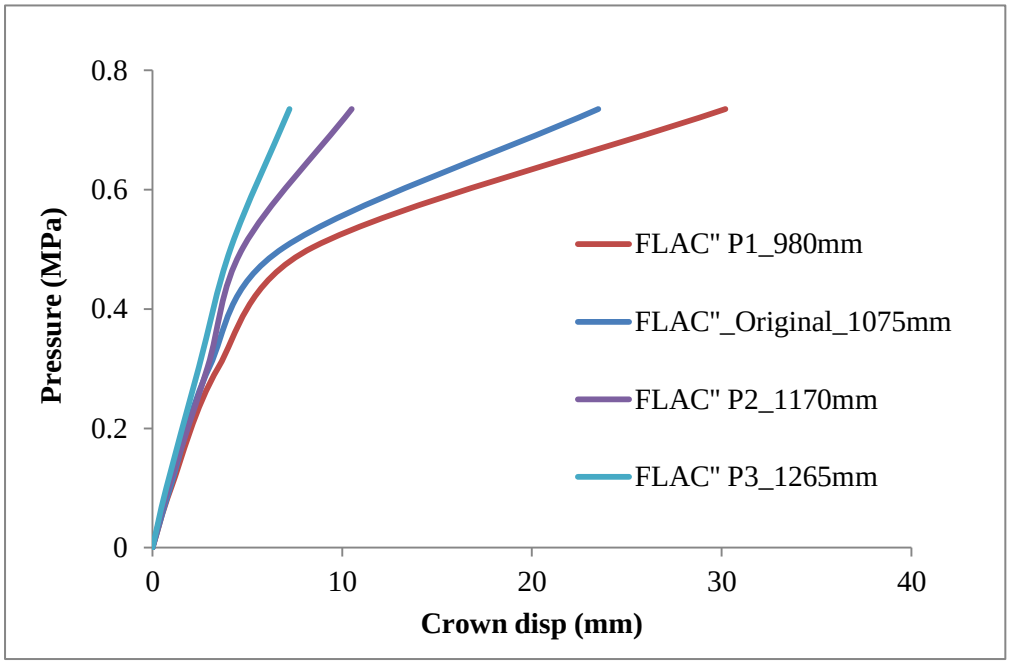

Figure 4.75 Prediction of crown displacement curves under concentrated load

Unlike the model under uniform load, an increase in the soil depth also increases the overall stiffness of the brick-lined tunnel dramatically under concentrated load (see Figure 4.75). Beyond a soil depth of 1265 mm, it is very hard to disperse the concentrated load to the tunnel since most of the concentrated load would only be dispersed to the soil below (see Appendix C).

4.9.3 Concentrated load

The performance of numerical modelling under concentrated load at different positions is predicted as below, especially at one quarter across and at the middle of the tunnel arch. The loading area is 0.1 m wide. UDEC modelling is used to predict better local mechanical behaviour.

1) At one quarter across the tunnel arch

As an application of 'Brickwork Bridge' under pavement, Figure 4.76 demonstrates the failure pattern and deformation of the UDEC model under concentrated load at 1/4 across the tunnel.

2) At the middle of the tunnel arch

Compared to the concentrated load at one quarter across the arch, where some part of the load has been transferred to one side of the tunnel, the failure load at the middle of the arch is smaller due to the direct tensile failure at the crown (see Figure 4.77).

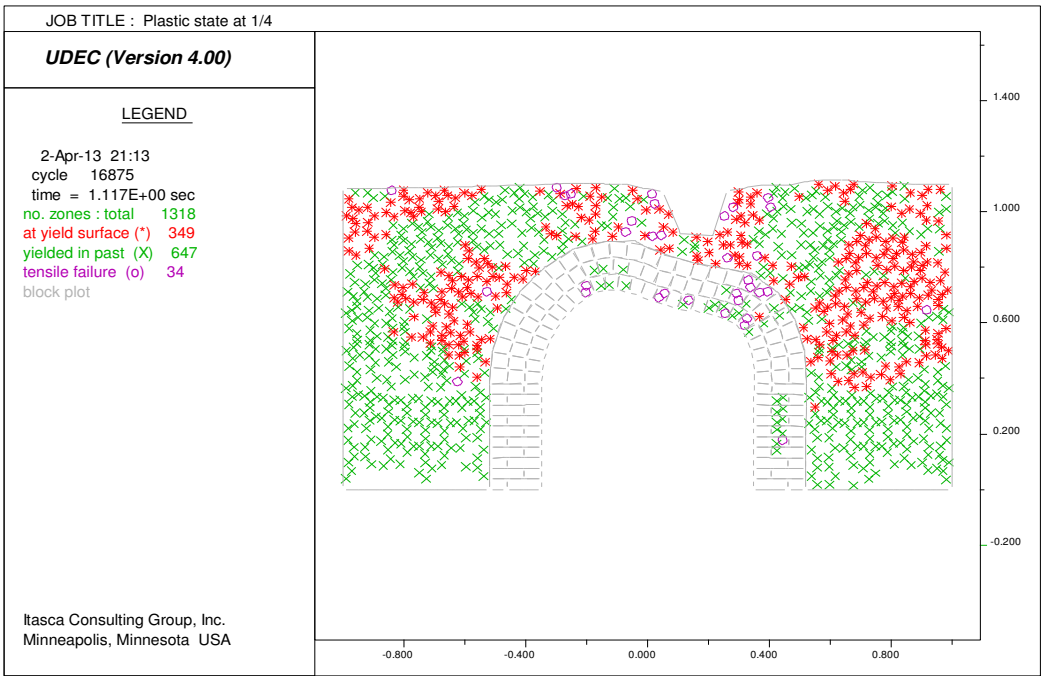

Figure 4.76 Prediction of plastic state under concentrated load at 1/4 of the arch

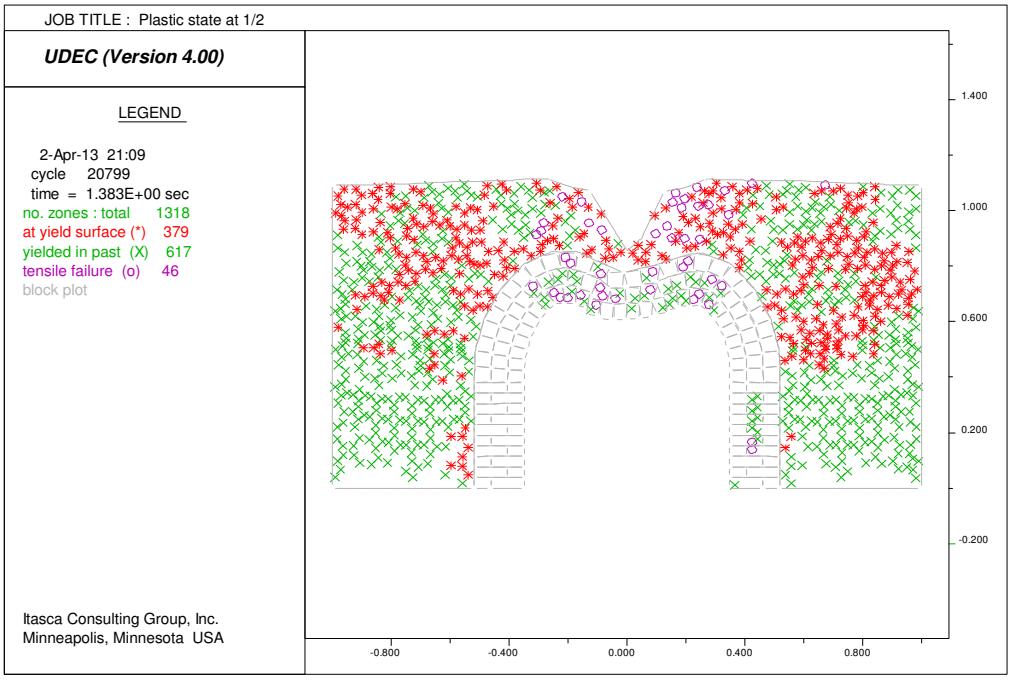

Figure 4.77 Prediction of plastic state under concentrated load at 1/2 of the arch

4.10 Chapter summary

4.10.1 Programme of material testing

A series of laboratory material tests have been conducted as a major reference to the numerical modelling work that followed, including brick, mortar, soil and their interface properties.

4.10.2 FLAC and UDEC models

In order to analyse the mechanical behaviour of the brick-lined tunnels, numerical models of physical model tests were developed with both the finite difference method (in FLAC software) and the distinct element method (in UDEC software) respectively. Their numerical results were then compared with the physical model test data, giving reasonable results as well as revealing drawbacks.

4.10.3 Prediction of numerical modelling

After validation by physical model tests, the numerical simulation has developed and predicted models at various soil depths under uniform load to show the interaction between a brick-lined tunnel and the overburden soil at different locations under concentrated load as a link to the engineering application of a ‘Brickwork Bridge’ under the pavement.

CHAPTER 5 CONCLUSIONS AND RECOMMENDATIONS

5.1 Conclusions

The aim of this PhD research was to develop a numerical approach for a series of small-scale physical models under extreme loading, using finite difference method (FLAC software) and distinct element method (UDEC software) separately. The stability of brick-lined tunnels has been assessed through both physical test models and numerical models in this thesis. The research combines experimental, monitoring and numerical modelling works together.

A comprehensive literature review has been carried out, concentrating on stability issues of tunnels, tunnel monitoring methods, previous masonry structure research and various numerical simulation approaches. Based on the literature review and new laboratory tests of materials, the database of material properties (e.g. bricks, mortar, surrounding soil and brickwork) corresponding to this research have been built.

There were three small-scale physical tunnel models being designed and tested, varying the mortar mix proportions. The mortar mix proportions were from comparatively higher strength mortar mix comprising cement, lime and sand in respective proportions of ratio 1:1:6 in the first physical tunnel model, to a mortar mix proportion of lower strength (1:2:9) in the other two physical models. In addition, the first and second physical tunnel models were under static uniform load to simulate deep seated tunnels while the third model was under concentrated load to simulate shallow tunnels subjected to traffic load.

Numerical modelling of three physical model tests was then carried out with the help of the database of material properties, validated by the physical model results. Parametric studies on the effects of stiffness properties and strength properties (e.g. the Poisson's ratio, Young's modulus, friction angle and cohesion of the brickwork, brickwork / soil interface stiffness and brickwork / soil joint friction angle) have been conducted in the numerical models.

According to the physical model test results presented in Chapter 3, the following conclusions can be drawn:

a) The physical tunnel model tests clearly indicated the mechanical behaviour of the brick-lined tunnels under both uniform and concentrated loads until failure.
b) The failure pattern of physical models under uniform and concentrated load differed. The first two physical models, which were under uniform load, failed as a result of shear failure at the sidewalls as the major force was transferred to the sides. The third physical model, which was under concentrated load, failed due to the formation of five structural hinges at the tunnel arch.
c) The ultimate load capacity and mode of failure were also determined and compared with different models. For both the first and the second physical models under uniform load, built with different mortar mix proportions of the brick-lined tunnels, ultimate capacity was affected by the compressive strength of the tunnel materials.
d) The comparatively higher compressive strength of the brickwork in the first physical model resulted in a higher ultimate load capacity than that of the second physical model. It suggests a correlation between compressive strength of constituent brickwork and ultimate load capacities of the tunnels. That the tunnel

comprising brickwork of higher strength failed later than its counterpart when both were subject to identical load regimes.

e) The third physical model under concentrated load reduced the ultimate capacity of the tunnel by approximately 30%, comparing with the model under uniform load. A significant reason for the lower ultimate capacity of the third tunnel model is due to uniaxial point loading. Comparatively, the first two physical models under uniform load were subjected to the confining pressure from the surrounding soil especially at sidewalls, which increased the ultimate capacity of the brick-lined tunnels.

According to the tunnel monitoring results presented in Chapter 3, some conclusions are drawn below:

f) Potentiometers were used to monitor tunnel deformation during the physical model loading tests, providing a reference for tunnel monitoring work. In addition, two advanced techniques — photogrammetry and a laser scanning system were employed to carry out monitoring tunnel deformation and inspecting brickwork defects during the physical model loading tests.

g) Both advanced techniques are suitable for measuring tunnel defects, such as major cracks on tunnel shells of around 3 to 5 mm wide. The accuracy of the laser scanning technique is within 1.3 mm when compared with the vernier calliper, while the accuracy of photogrammetry is within 1.0 mm.

h) Photogrammetry usually works with the help of daylight, or a lighting system in a dark environment, whereas the laser scanning system performs well without any aid of lighting to observe cracks and defects.

i) Photogrammetry shows a strong potential for measuring tunnel deformation with high accuracy with the help of lighting. The centre point of target points can be easily captured by Centroiding function in the related post-processing software Australis, rather than ambiguous point cloud of the target points in the laser scanning system.

According to the numerical modelling results presented in Chapter 4, some conclusions are drawn as follows:

j) The numerical models have been built and validated by the three physical model tests. The numerical modelling results have a good agreement with the mechanical behaviour of the physical model tests in terms of both deformation characteristics and failure pattern, thus proving that they could be effectively used in the study of the stability of masonry tunnels.

k) The value of the brickwork cohesion of the FLAC numerical model was smaller than the brickwork block cohesion in the UDEC model. The reason may be that the brickwork in FLAC (containing mortar and the interface) should be weaker than the brickwork block in UDEC (containing only mortar).

l) For the numerical models under uniform load that reached shear failure, the mechanical behaviour of both the FLAC and UDEC models were very similar to each other.

m) Generally, the micro-modelling strategy (used in UDEC) shows a better agreement with the physical model test of the local failure behaviour of brickwork structures. The failure pattern of the UDEC model under concentrated load clearly demonstrates the hinges and cracks at certain positions of the tunnel arch.

n) In another way, the macro-modelling strategy (applied in FLAC) reasonably simulates the deformation characteristics and shows a good agreement with the three physical model tests.

o) Results from the analysis confirmed that, in both numerical methods, the cohesion of brickwork (blocks in UDEC) was the predominant factor, followed by the friction angle of brickwork. These results agreed with the findings of Idris et al. (2008). However, numerical models were not very sensitive to the Poisson's ratio, Young's modulus of the brickwork, joint stiffness, joint cohesion or the joint friction angle.

p) Prediction of numerical models at various soil depths under uniform load was to show the interaction between a brick-lined tunnel and the overburdened soil; prediction at different locations under concentrated load was linked to the engineering application of a 'Brickwork Bridge' under the pavement. It was shown that, under uniform load, shear failure not only occurred at the tunnel sidewalls, but also extended to the tunnel arch. As the soil depth increased, the concentrated load at the middle of the arch failed easily due to direct tensile failure at the crown, compared to the load one quarter across the arch.

5.2 Recommendations for future research

Although the research work presented in this thesis has attempted to enhance the understanding of the mechanical behaviour of brick-lined tunnels subjected to uniform and concentrated loading conditions, several studies are recommended for further investigation.

In further research, old tunnel structures, such as weathered or deteriorated brickwork from the field, could be tested to obtain specific properties and these could be input into numerical models.

As a recommendation for further modelling work, it is worth trying to introduce other constitutive models related to masonry structures and simulate the longer term deformation and stress conditions of brick-lined tunnels after years of degradation. More realistic conditions could be applied, such as tunnels surrounded by anisotropic geotechnical materials and cyclic loading, representing moving vehicles on the road.

In addition, 3D modelling using FLAC^{3D} and 3DEC could be used to develop a better understanding of the actual interaction of bricks and mortar, and of the mechanical behaviour of brick-lined tunnels.

It would also be possible to study mobile monitoring techniques combined with Global Position System (GPS) in order to increase the efficiency of the investigation.

REFERENCE

ADAMS, J. & CHANDLER, J. (2003) Evaluation of lidar and medium scale photogrammetry for detecting soft-cliff coastal change. The Photogrammetric Record, 17, 405-418.

ALONSO, E. (2001) Small scale modelling of masonry arch bridges, MPhil Thesis. Department of Civil Engineering. University of Nottingham.

BETTI, M., DROSOPOULOS, G. A. & STAVROULAKIS, G. E. (2008) Two non-linear finite element models developed for the assessment of failure of masonry arches. Comptes Rendus Mécanique, 336 (1-2), 42-53.

BITELLI, G., DUBBINI, M. & ZANUTTA, A. (2004) Terrestrial laser scanning and digital photogrammetry techniques to monitor landslide bodies.

BS1377-2:1990 (1990) Methods of test for soils for civil engineering purposes - Part 2: Classification tests. London: British Standards Institution.

BS1377-4:1990 (1990) Methods of test for soils for civil engineering purposes - Part 4: Compaction-related tests London: British Standards Institution.

BS4551:1980 (1980) Methods of testing mortars, screeds and plasters. London: British Standards Institution.

BSEN197-1:2011 (2011) Cement - Part 1: Composition, specifications and conformity criteria for common cements. London: British Standards Institution.

BSEN459-1:2001 (2001) Building lime - Part 1: Definitions, specifications and conformity criteria. London: British Standards Institution.

BSEN1052-1:1999 (1999) Methods of test for masonry - Part 1: Determination of compressive strength London: British Standards Institution.

BSEN1052-3:2002 (2002) Methods of test for masonry - Part 3: Determination of initial shear strength. London: British Standards Institution.

CLARKE, T. & LINDSEY, N. (1992) Profiling methods reviewed[cross-section measurement by contact and non-contact methods]. Tunnels and Tunnelling, 24, 29-31.

CUR (1994) Structural masonry: a experimental/numerical basis for practical design rules (in Dutch). Report 171.

GIORDANO, A., MELE, E. & DE LUCA, A. (2002) Modelling of historical masonry structures: comparison of different approaches through a case study. Engineering Structures, 24, 1057-1069.

GOODMAN, R. E., TAYLOR, R. L. & BREKKE, T. L. (1968) A model for the mechanics of jointed rock. Journal of Soil Mechanics & Foundations Div, ASCE 94 SM3, 637-659.

GUARNIERI, A., VETTORE, A. & REMONDINO, F. (2004) Photogrammetry and ground-based laser scanning: assessment of metric accuracy of the 3D model of Pozzoveggiani church. FIG Working Week 2004, 22-27.

HAACK, A., SCHREYER, J. & JACKEL, G. (1995) State-of-the-art of Non-destructive Testing Methods for Determining the State of a Tunnel Lining. Tunneling and Underground Space Technology, 10, 413-431.

HAMPEL, U. & MAAS, H. (2003) Application of digital photogrammetry for measuring deformation and cracks during load tests in civil engineering material testing, Optical 3-D Measurement TechniquesVI, Volume II, pp. 80–88..

HENDRY, A. (1998) Structural masonry, Macmillan Press Ltd.

HOGG, V. (1997) Effects of repeated loading on masonry arch bridges and implications for the serviceability limit state, Ph.D. Thesis, Department of Civil Engineering, Universtiy of Nottingham.

IDRIS, J., AL-HEIB, M. & VERDEL, T. (2009) Numerical modelling of masonry joints degradation in built tunnels. Tunnelling and Underground Space Technology, 24, 617-626.

IDRIS, J., VERDEL, T. & AL-HEIB, M. (2008) Numerical modelling and mechanical behaviour analysis of ancient tunnel masonry structures. Tunnelling and Underground Space Technology, 23, 251-263.

ITASCA CONSULTING GROUP, Inc. (2005) UDEC, Universal Distinct Element Code, version 4.0. Minnesota,USA, ITASCA Consulting Group.

ITASCA CONSULTING GROUP, Inc. (2008) FLAC, Fast Lagrangian Analysis of Continua, Version 6.0. Minnesota,USA, ITASCA Consulting Group.

JIA, Y.D. (2010) Numerical modelling of shaft lining stability, Ph.D. Thesis, Department of Civil Engineering, University of Nottingham.

JUSPI, S. (2007) Experimental validation of the shakedown concept for pavement analysis and design, Ph.D. Thesis, Department of Civil Engineering, University of Nottingham.

KAVVADAS, M. J. (2005) Monitoring ground deformation in tunnelling: Current practice in transportation tunnels. Engineering Geology, 79, 93-113.

KOLYMBAS, D. (2005) Tunelling and tunnel mechanics: a rational approach to tunnelling. ISBN 978-3-540-25196-5, Springer.

LEE, Y. J. & BASSETT, R. H. (2006) Application of a photogrammetric technique to a model tunnel. Tunnelling and Underground Space Technology, 21, 79-95.

LENCZNER, D. (1972) Elements of loadbearing brickwork. Pergamon Press, Oxford.

LOURENÇO, P.B. (1996) Computational strategies for masonry structures, Ph.D. Thesis, Department of Civil Engineering, Delft University of Technology.

LOURENÇO, P.B. (1998) Experimental and numerical issues in the modelling of the mechanical behaviour of masonry, In: ROCA, P., GONZÁLEZ, J. L., OÑATE, E. & LOURENÇO, P.B, editors. Structural analysis of historical constructions II. Possibilities of numerical and experimental techniques. CIMNE, 57-92.

MARTIN, C. D., TANNANT, D. D. & LAN, H. (2007) Comparison of terrestrial-based, high resolution, LiDAR and digital photogrammetry surveys of a rock slope. Rock Mechanics: Meeting Society's Challenges and Demands, Two Volume Set. May 2007, 37 - 44.

MCGLONE, J., MIKHAIL, E. M., BETHEL, J., S., MULLEN, R. (2004) Manual of Photogrammetry, 5th edition, American Society of Photogrammetry and Remote Sensing. ISBN 1-57083-071-1.

MCKAY, W. B. & MCKAY, J. K. (1968) Brickwork, by W.B. McKay. 2nd ed., by J.K. McKay, Harlow, Longmans.

MEGAW, T. & BARTLETT, J. (1981) Tunnels: planning, design and construction. Volume 1. Ellis Horwood Ltd. Chichester, Sussex, 284.

NG, C., SIMONS, N. & MENZIES, B. (2004) A short course in soil-structure engineering of deep foundations, excavations and tunnels. Thomas Telford Services Ltd.

PEASE, B., GEIKER, M., STANG, H. & WEISS, J. (2006) Photogrammetric assessment of flexure induced cracking of reinforced concrete beams under service loads. In: Proceedings of the Second International RILEM Symposium: Advances in Concrete through Science and Engineering, Quebec City, Québec, Canada.

PÉQUIGNOT, C. (1963) Tunnels and tunnelling, Hutchinson.

SCHULZ, T., LEMY, F. & YONG, S. (2005) Laser scanning technology for rock engineering applications. Optical 3-D Measurement Techniques VII (Eds.: Grün, Kahmen), Vienna, 50-59.

SUTCLIFFE, D. (2003) Masonry shear walls: a limit analysis approach, Ph.D. Thesis, Discipline of Civil, Surveying and Environmental Engineering, University of Newcastle, Australia.

SZÉCHY, K. (1967) The art of tunnelling. Akademiai Kiado. Budapest, 1st English edn.

TATIYA, R. (2005) Civil excavations and tunnelling, Thomas Telford.

TURNER, A., KEMENY, J., SLOB, S. & HACK, R. (2006) Evaluation, and management of unstable rock slopes by 3-D laser scanning. International Association for Engineering Geology and the Environment (IAEG), paper no. 404, Geol. Soc. London, pp. 1–11.

VALLUZZI, M. R., BINDA, L. & MODENA, C. (2005) Mechanical behaviour of historic masonry structures strengthened by bed joints structural repointing. Construction and Building Materials, 19, 63-73.

VAN DER PLUIJM, R. (1992) Material properties of masonry and its components under tension and shear. In: Proceedings of the 6 th Canadian Masonry Symposium. University of Saskatchevan, Canada, pp 675-686.

VERMELTFOORT, A., MARTENS, D., KLEINMAN, C. & ZIJL, G. (2005) Brick-mortar interaction in masonry under compression. Ph.D. thesis. Eindhoven University of Technology, Eindhoven, the Netherlands. Available from alexandria.tue.nl/extra2/200510997.pdf.

WANG, T.-T., JAW, J.-J., HSU, C.-H. & JENG, F.-S. (2010) Profile-image method for measuring tunnel profile - Improvements and procedures. Tunnelling and Underground Space Technology, 25, 78-90.

WANG, T., JAW, J., CHANG, Y. & JENG, F. (2009) Application and validation of profile-image method for measuring deformation of tunnel wall. Tunnelling and Underground Space Technology, 24, 136-147.

PICTURES AND TECHNIQUE SHEET REFERENCES

ARTHURS CLIPART, Org. (2012)

From: http://www.arthursclipart.org/bridges/bridges/arch%20bridge%204.gif.

BALFOUR BEATTY RAIL, Ltd. (2006) LaserFleX™ - New Generation of High Performance Infrastructure Measurement System.

ENVIRONMENTAL SYSTEMS & SERVICES (ES&S), Ltd. (2009) From: http://www.esands.com/pdf/Geotech/GEO_Tape_Extensometer_07.09_web.pdf.

FARO, Ltd. (2011) Laser Scanner Focus^{3D} Technique Sheet.

GEODETIC SYSTEMS, Ltd (2013). From: http://www.geodetic.com/v-stars/what-is-photogrammetry.aspx.

IMAGING RESOURCE, Ltd.. (2009) From: http://www.imaging-resource.com/PRODS/E5D2/E5D2A.HTM.

LEICA GEOSYSTEMS, Ltd. (2009) From: http://www.leica-geosystems.com/downloads123/zz/tps/tps1200/brochures/Leica_TPS1200+_brochure_en.pdf.

PHOTOMETRIX (2007) User Manual for Australis, Version 7.0. Australia.

PLASSER AMERICAN Ltd. (2010) From:

http://www.plasseramerican.com/en/p_recording/ncms.htm.

http://www.plasseramerican.com/en/p_recording/messfahrzeuge.htm.

WIKIPEDIA (2013) From: http://en.wikipedia.org/wiki/Marc_Isambard_Brunel.

APPENDIX A LABORATORY TEST RESULTS

Table A.1 UCS test list of different mortar samples

Mortar Mix Proportion 1:2:9						
Sample Reference	**Average Length (mm)**	**Average Diameter (mm)**	**Sample Density (g/cm^3)**	**Failure Load (kN)**	**Ultimate Compressive Strength (MPa)**	**Young's Modulus (GPa)**
Sample 01	**73.95**	**37.43**	**1.61**	**3.1**	**2.86**	**0.21**
Sample 02	**73.85**	**37.69**	**1.61**	**3.3**	**3.04**	**0.25**
Sample 03	**74.00**	**37.60**	**1.63**	**3.5**	**3.25**	**0.30**
Average	**73.93**	**37.57**	**1.62**	**3.3**	**3.05**	**0.25**
Standard Deviation	**0.08**	**0.13**	**0.01**	**0.20**	**0.20**	**0.044**
Mortar Mix Proportion 1:1:6						
Sample Reference	**Average Length (mm)**	**Average Height (mm)**	**Sample Density (g/cm^3)**	**Failure Load (kN)**	**Ultimate Compressive Strength (MPa)**	**Young's Modulus (GPa)**
Sample 01	**74.17**	**37.50**	**1.67**	**5.1**	**4.73**	**0.39**
Sample 02	**73.86**	**37.76**	**1.62**	**4.6**	**4.26**	**0.31**
Sample 03	**73.88**	**37.60**	**1.64**	**4.6**	**4.25**	**0.29**
Average	**73.97**	**37.62**	**1.64**	**4.8**	**4.41**	**0.33**
Standard Deviation	**0.17**	**0.13**	**0.03**	**0.27**	**0.27**	**0.052**

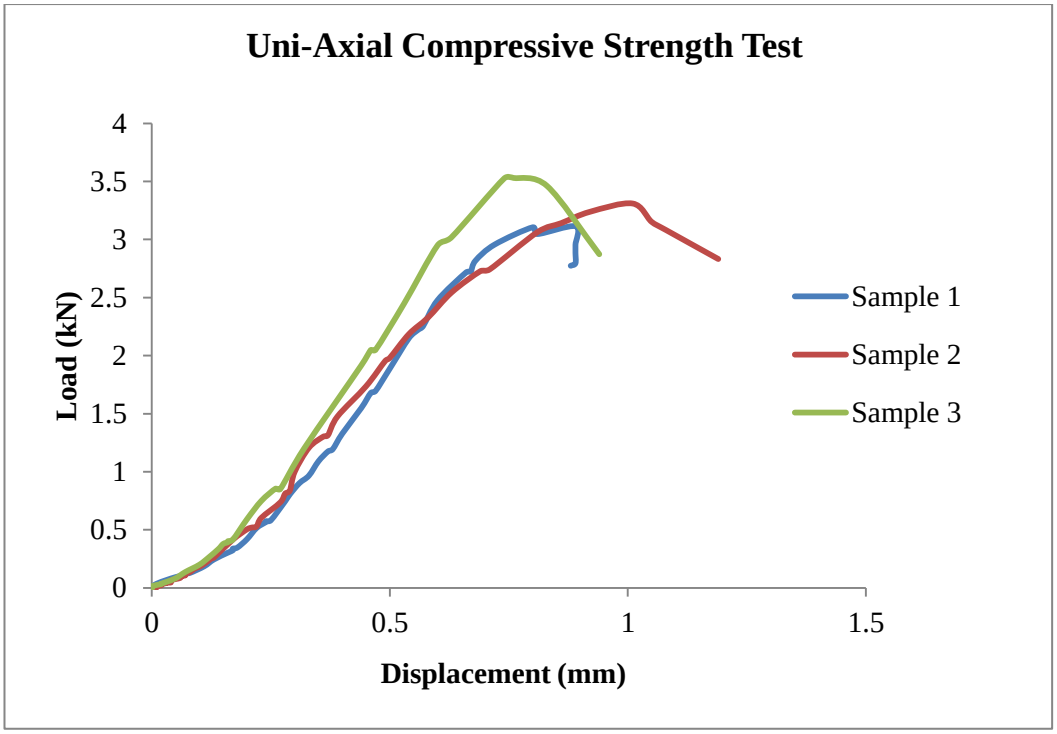

Figure A.1 Load versus displacement curve of mortar mix 1:2:9

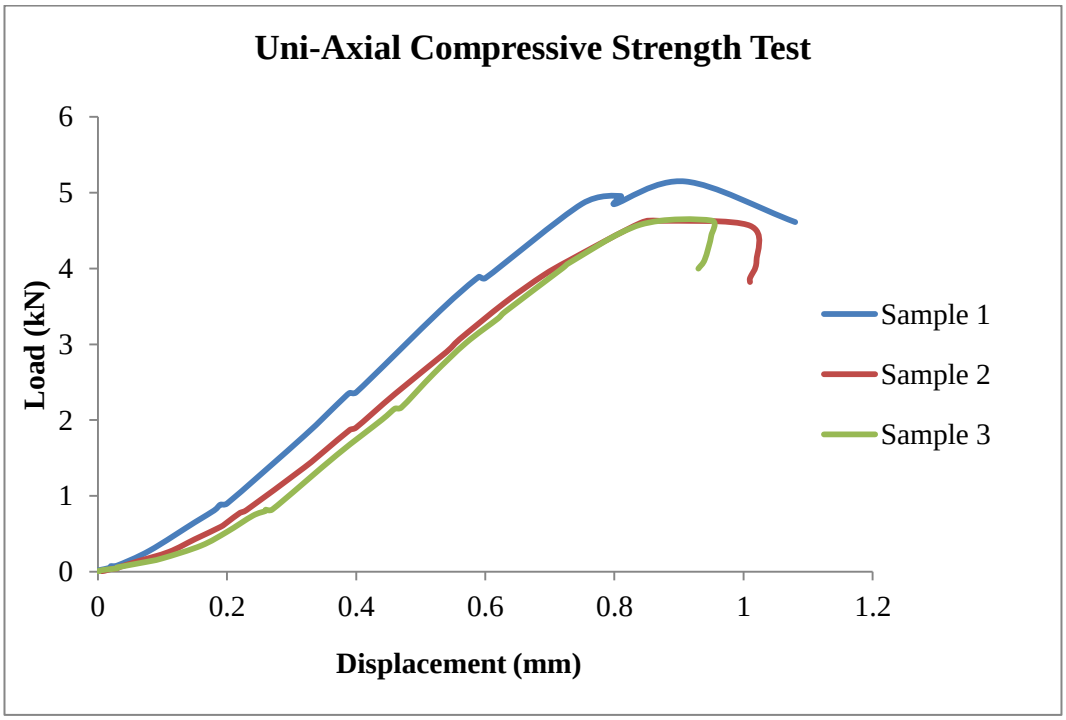

Figure A.2 Load versus displacement curve of mortar mix 1:1:6

Table A.2 UCS test list of brickwork triplets

Brickwork with Mortar Mix Proportion 1:2:9							
Sample Reference	**Average Length (mm)**	**Average Height (mm)**	**Average Width (mm)**	**Sample Density (g/cm^3)**	**Failure Load (kN)**	**Ultimate Compressive Strength (MPa)**	**Young's Modulus (GPa)**
Sample 01	**99**	**104**	**49**	**1.7631**	**29.94**	**6.18**	**0.233**
Sample 02	**98.5**	**105**	**49**	**1.7325**	**34.66**	**7.19**	**0.211**
Sample 03	**100**	**108**	**49.5**	**1.7022**	**35.25**	**7.13**	**0.212**
Average	**99.1667**	**105.667**	**49.1667**	**1.7326**	**33.2833**	**6.83333**	**0.21867**
Standard Deviation	**0.76376**	**2.08167**	**0.28868**	**0.03045**	**2.9104**	**0.5666**	**0.01242**
Brickwork with Mortar Mix Proportion 1:1:6							
Sample Reference	**Average Length (mm)**	**Average Height (mm)**	**Average Width (mm)**	**Sample Density (g/cm^3)**	**Failure Load (kN)**	**Ultimate Compressive Strength (MPa)**	**Young's Modulus (GPa)**
Sample 01	**102**	**109**	**48**	**1.6981**	**43.01**	**8.79**	**0.351**
Sample 02	**108**	**105**	**48**	**1.6803**	**37.62**	**7.26**	**0.249**
Sample 03	**102**	**109**	**49**	**1.6434**	**37.26**	**7.46**	**0.553**
Average	**104**	**107.667**	**48.3333**	**1.6739**	**39.2967**	**7.8367**	**0.38433**
Standard Deviation	**3.4641**	**2.3094**	**0.57735**	**0.02789**	**3.22087**	**0.83164**	**0.15472**

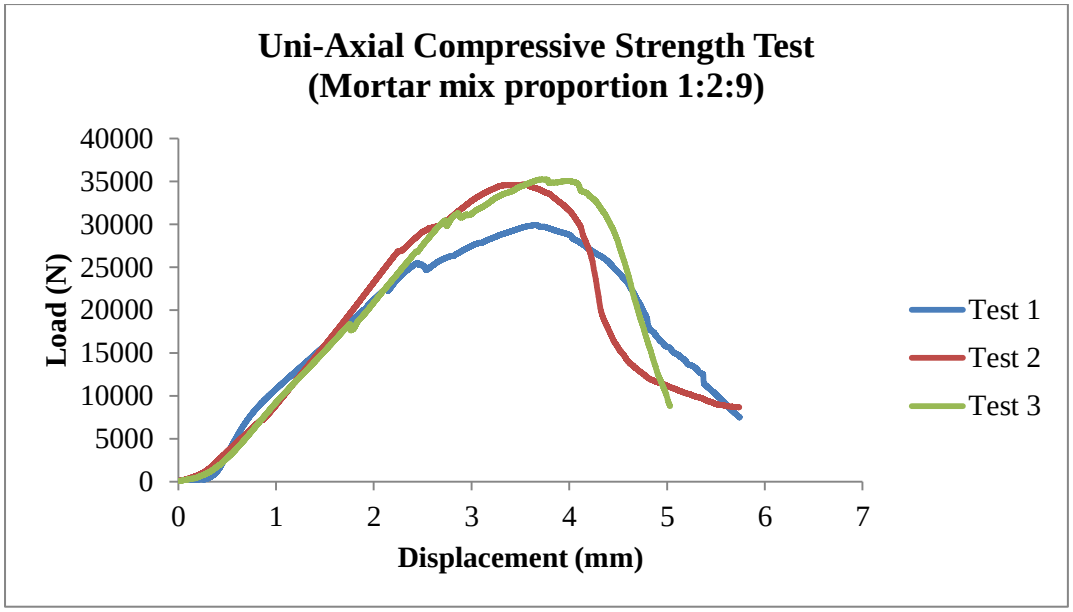

Figure A.3 Load versus displacement curve (brickwork triplet within mortar mix proportion 1:2:9)

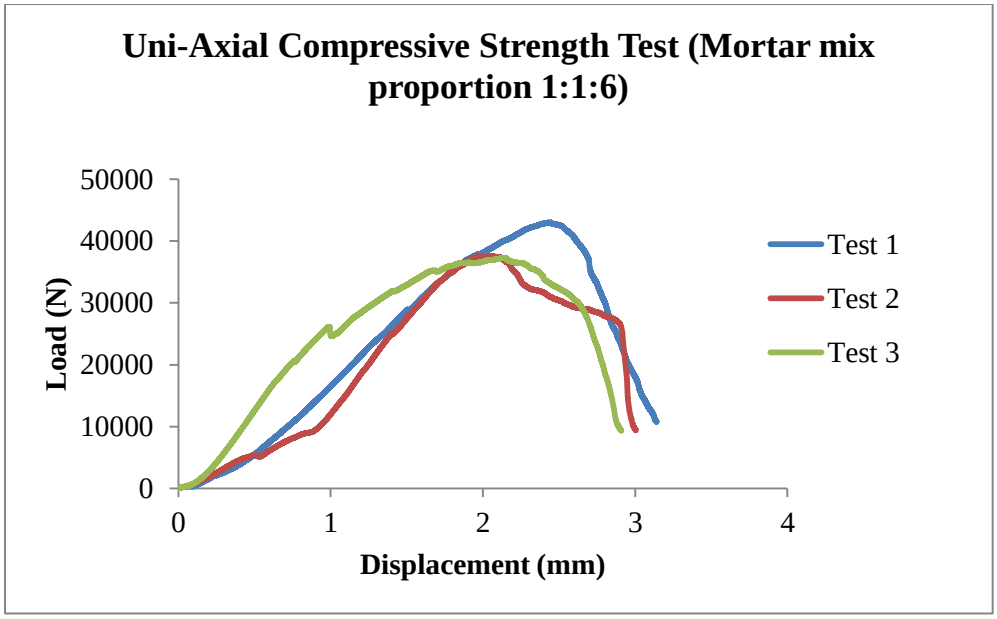

Figure A.4 Load versus displacement curve (brickwork triplet within mortar mix proportion 1:1:6)

Table A.3 The tensile strength test list of brickwork triplets

Mortar Mix Proportion 1:2:9				
Sample Reference	**Average Length (mm)**	**Average Width (mm)**	**Tensile Failure Load (N)**	**Tensile Strength (MPa)**
Sample 01	**103.3**	**48.3**	**413.385**	**0.0829**
Sample 02	**103.9**	**41.4**	**282.297**	**0.0656**
Sample 03	**104.2**	**47.7**	**705.588**	**0.1420**
Average	**103.8**	**45.8**	**467.09**	**0.0968**
Standard Deviation	**0.45826**	**3.8223**	**216.696**	**0.0400**
Mortar Mix Proportion 1:1:6				
Sample Reference	**Average Length (mm)**	**Average Width (mm)**	**Tensile Failure Load (N)**	**Tensile Strength (MPa)**
Sample 01	**99.6**	**50**	**1455.38**	**0.2922**
Sample 02	**99.5**	**50.2**	**1104.35**	**0.2211**
Sample 03	**102**	**50.9**	**1130.43**	**0.2177**
Average	**100.367**	**50.3667**	**1230.05**	**0.2437**
Standard Deviation	**1.41539**	**0.47258**	**195.576**	**0.0421**

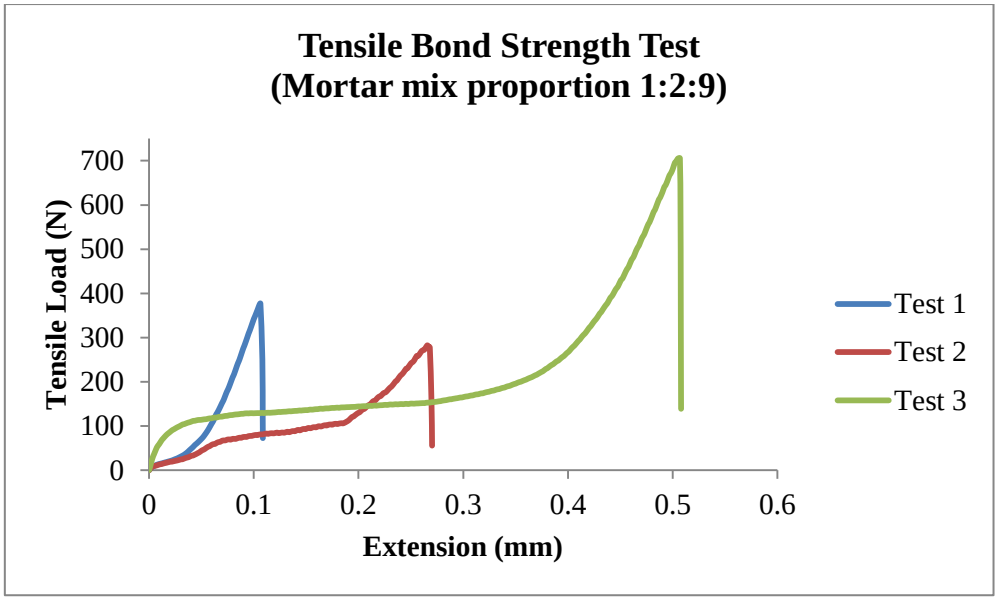

Figure A.5 Tensile load versus extension curve (brickwork triplet within mortar mix proportion 1:2:9)

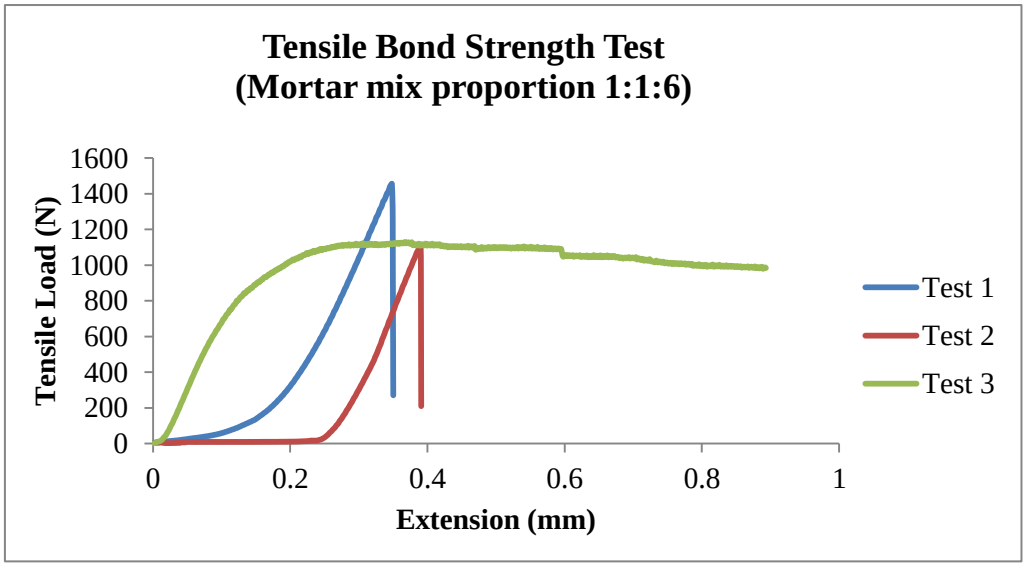

Figure A.6 Tensile load versus extension curve (brickwork triplet within mortar mix proportion 1:1:6)

Table A.4 The shear strength test list of brickwork triplets

Mortar Mix Proportion 1:2:9					
Sample Reference	**Average Length (mm)**	**Average Width (mm)**	**Pre-compressive Stress (MPa)**	**Failure Load (kN)**	**Ultimate Shear Strength (MPa)**
Sample 01	**99.00**	**48.30**	**0.002**	**0.48**	**0.05**
Sample 02	**99.70**	**51.50**	**0.002**	**0.33**	**0.03**
Sample 03	**99.20**	**51.50**	**0.002**	**0.70**	**0.07**
Sample 04	**97.50**	**51.00**	**0.006**	**0.54**	**0.05**
Sample 05	**98.40**	**49.90**	**0.006**	**0.47**	**0.05**
Sample 06	**98.25**	**50.06**	**0.006**	**0.70**	**0.07**
Sample 07	**98.20**	**48.80**	**0.010**	**0.72**	**0.08**
Sample 08	**98.00**	**49.00**	**0.010**	**0.77**	**0.08**
Sample 09	**98.70**	**51.10**	**0.010**	**0.52**	**0.05**
Average	**98.55**	**50.13**	**-**	**-**	**-**
Standard Deviation	**0.67**	**1.22**	**-**	**-**	**-**
Mortar Mix Proportion 1:1:6					
Sample Reference	**Average Length (mm)**	**Average Width (mm)**	**Pre-compressive Stress (MPa)**	**Failure Load (kN)**	**Ultimate Shear Strength (MPa)**
Sample 01	**99.20**	**50.20**	**0.002**	**1.73**	**0.17**
Sample 02	**98.90**	**51.00**	**0.002**	**1.64**	**0.16**
Sample 03	**99.70**	**50.80**	**0.002**	**2.39**	**0.24**
Sample 04	**98.80**	**50.70**	**0.006**	**1.60**	**0.16**
Sample 05	**98.24**	**49.98**	**0.006**	**1.44**	**0.15**
Sample 06	**98.00**	**50.00**	**0.006**	**1.87**	**0.19**
Sample 07	**98.30**	**50.88**	**0.010**	**2.45**	**0.24**
Sample 08	**101.00**	**49.30**	**0.010**	**2.23**	**0.22**
Sample 09	**99.00**	**51.00**	**0.010**	**2.06**	**0.20**
Average	**99.02**	**50.43**	**-**	**-**	**-**
Standard Deviation	**0.91**	**0.59**	**-**	**-**	**-**

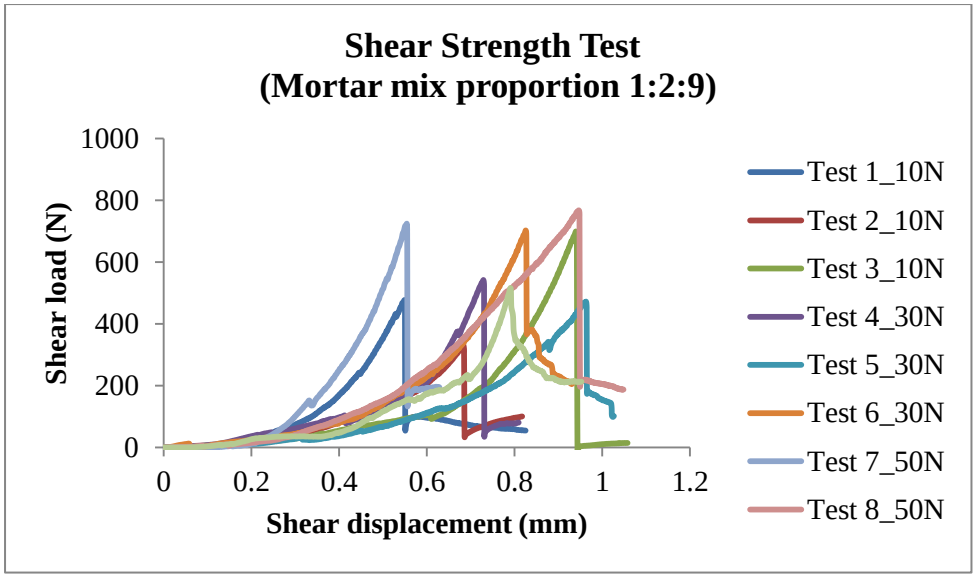

Figure A.7 Shear load versus displacement curve (brickwork triplet within mortar mix proportion 1:2:9)

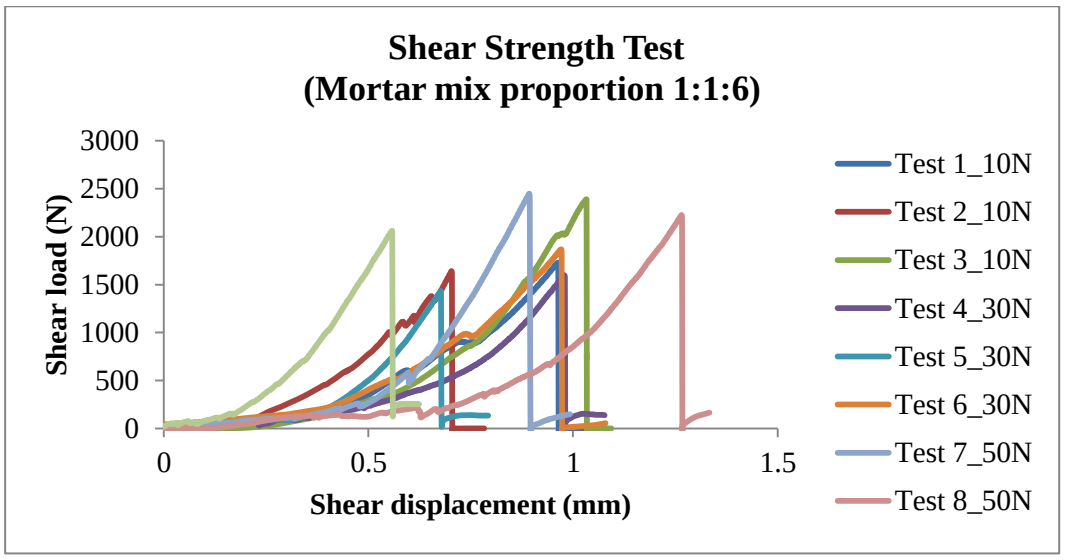

Figure A.8 Shear load versus displacement curve (brickwork triplet within mortar mix proportion 1:1:6)

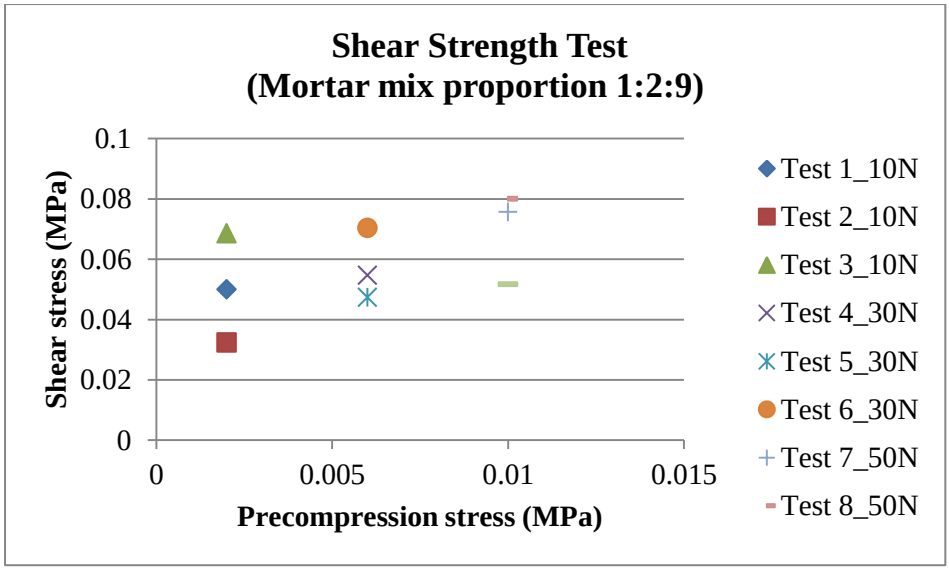

Figure A.9 Shear stress against precompression of brickwork triplet (1:2:9)

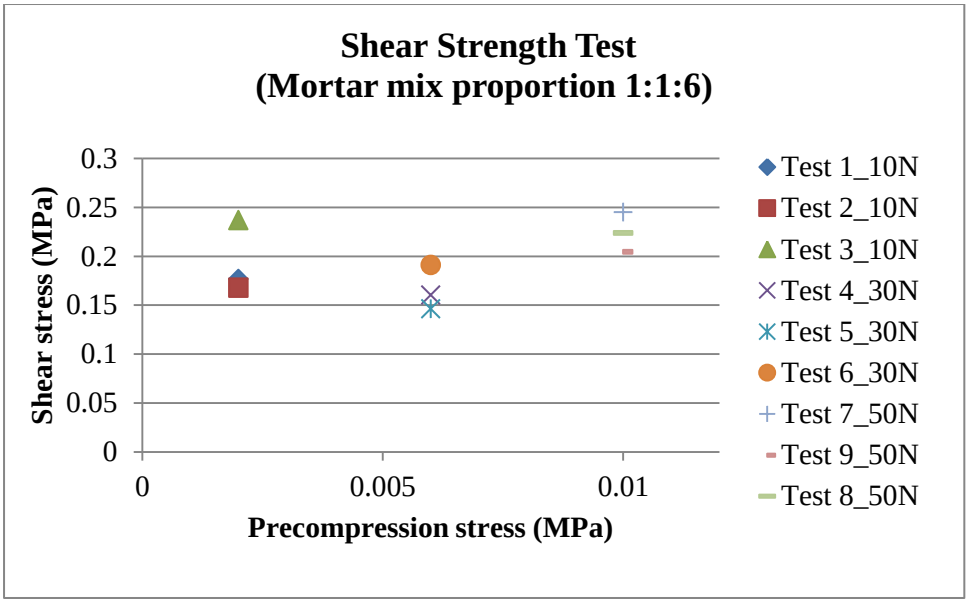

Figure A.10 Shear stress against precompression stress of brickwork triplet (1:1:6)

APPENDIX B POST-PROCESSING WORK OF MONITORING

5_6

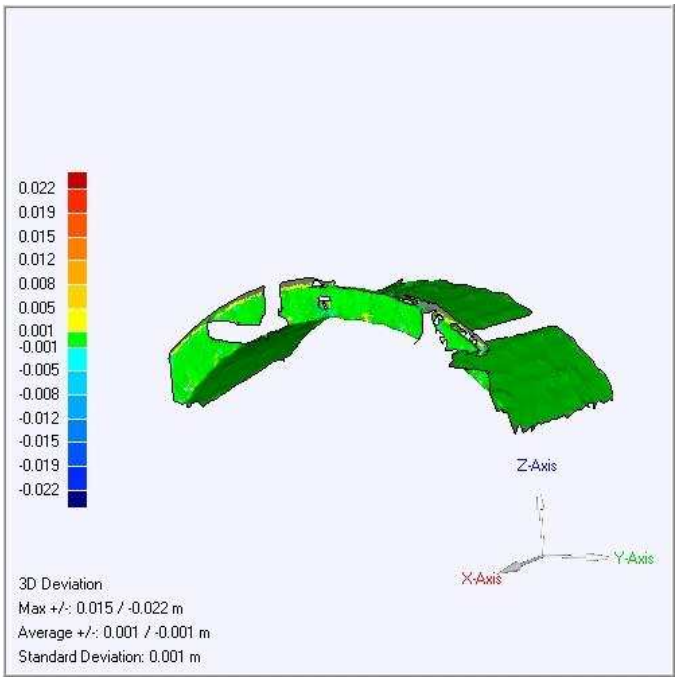

6_7

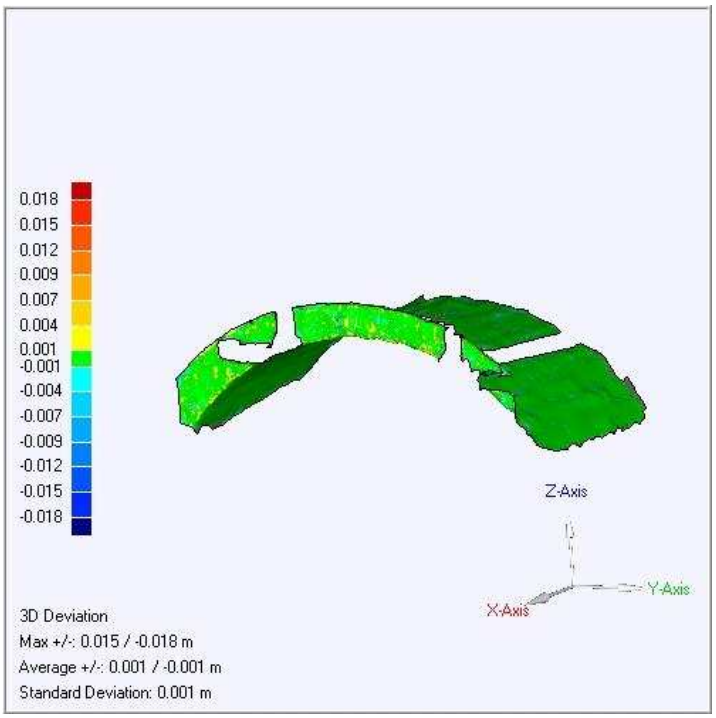

7_8

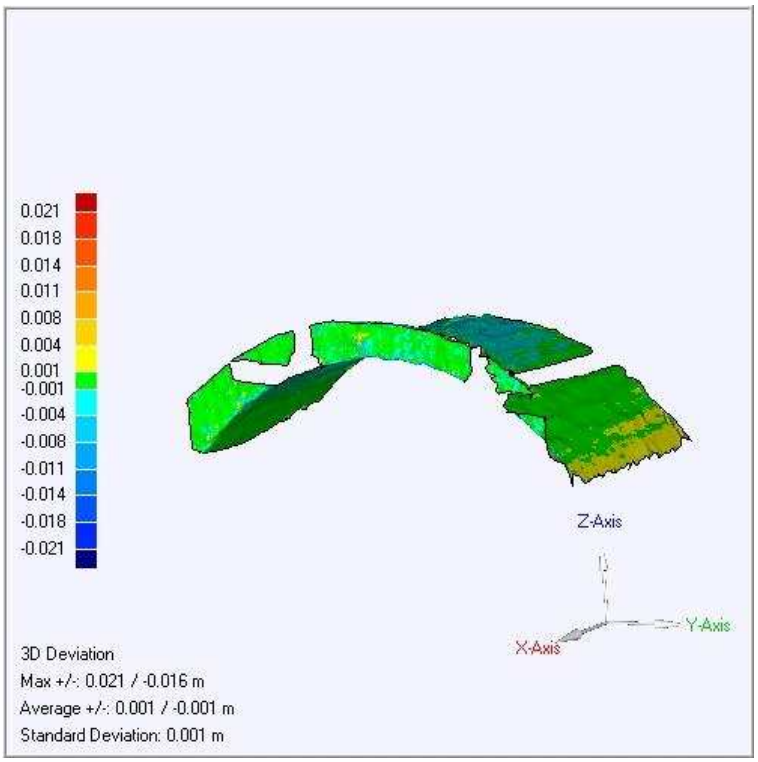
0.021
0.018
0.014
0.011
0.008
0.004
0.001
-0.001
-0.004
-0.008
-0.011
-0.014
-0.018
-0.021
Z-Axis
Y-Axis
X-Axis
3D Deviation
Max +/-: 0.021 / -0.016 m
Average +/-: 0.001 / -0.001 m
Standard Deviation: 0.001 m

8_9

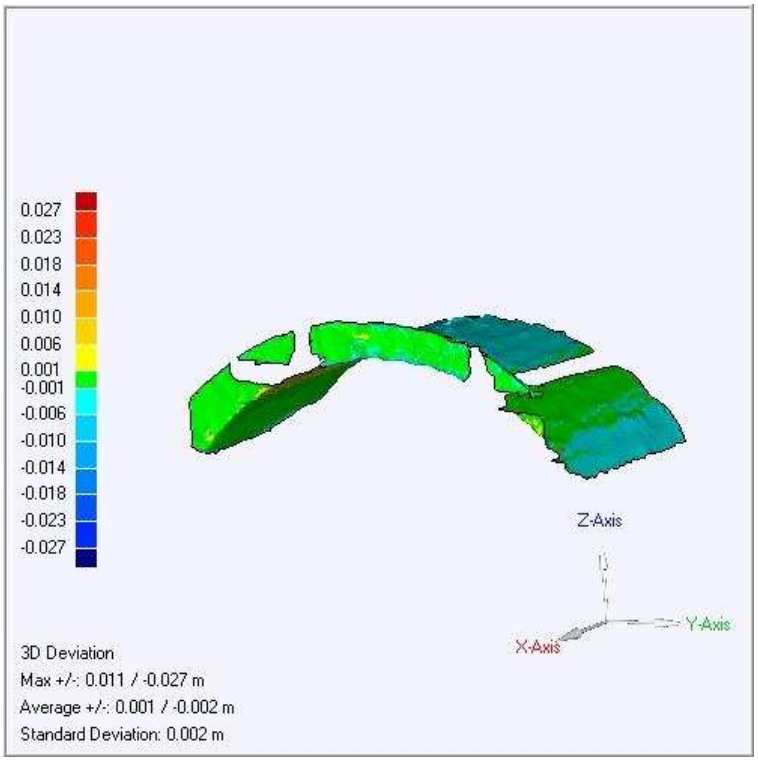
0.027
0.023
0.018
0.014
0.010
0.006
0.001
-0.001
-0.006
-0.010
-0.014
-0.018
-0.023
-0.027
Z-Axis
Y-Axis
X-Axis
3D Deviation
Max +/-: 0.011 / -0.027 m
Average +/-: 0.001 / -0.002 m
Standard Deviation: 0.002 m

9_10

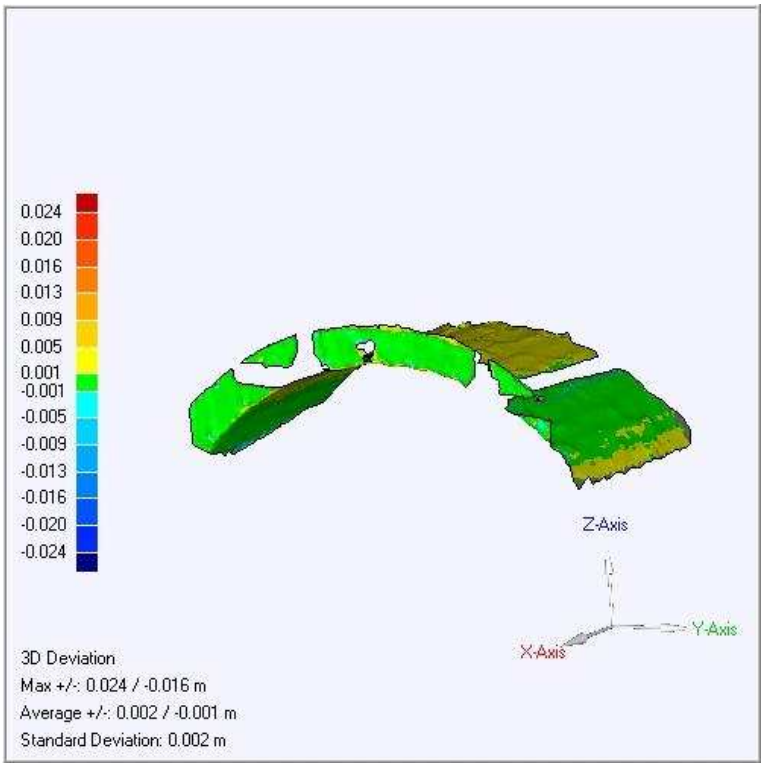
0.024
0.020
0.016
0.013
0.009
0.005
0.001
-0.001
-0.005
-0.009
-0.013
-0.016
-0.020
-0.024
Z-Axis
Y-Axis
X-Axis
3D Deviation
Max +/-: 0.024 / -0.016 m
Average +/-: 0.002 / -0.001 m
Standard Deviation: 0.002 m

10_11

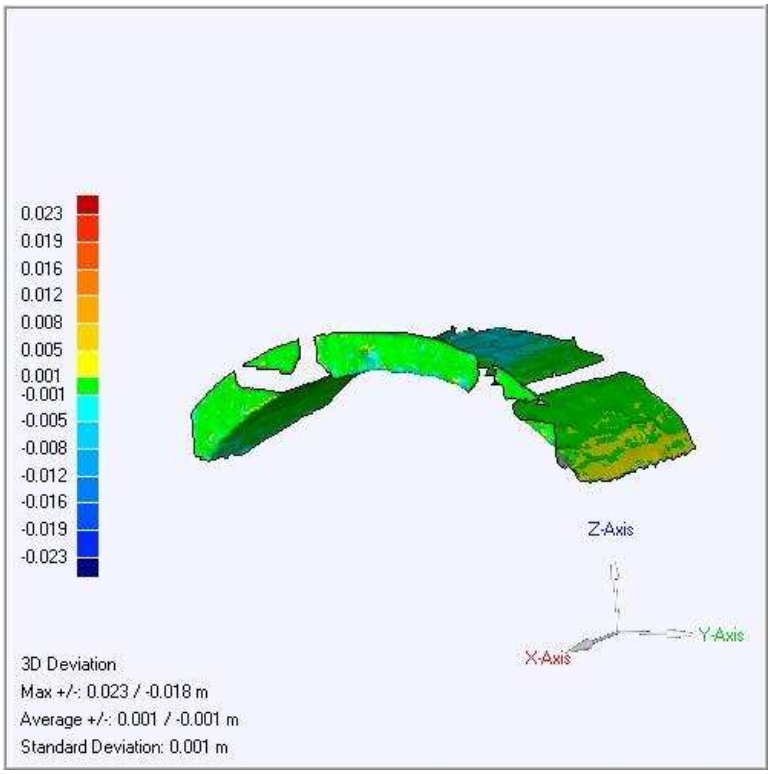
0.023
0.019
0.016
0.012
0.008
0.005
0.001
-0.001
-0.005
-0.008
-0.012
-0.016
-0.019
-0.023
Z-Axis
Y-Axis
X-Axis
3D Deviation
Max +/-: 0.023 / -0.018 m
Average +/-: 0.001 / -0.001 m
Standard Deviation: 0.001 m

11_12

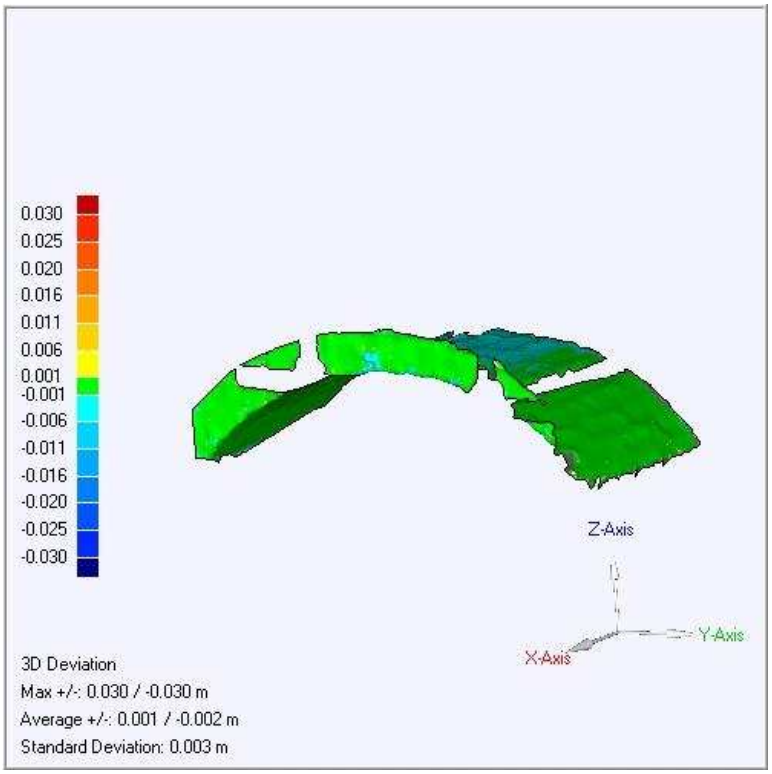
0.030
0.025
0.020
0.016
0.011
0.006
0.001
-0.001
-0.006
-0.011
-0.016
-0.020
-0.025
-0.030
Z-Axis
Y-Axis
X-Axis
3D Deviation
Max +/-: 0.030 / -0.030 m
Average +/-: 0.001 / -0.002 m
Standard Deviation: 0.003 m

12_13

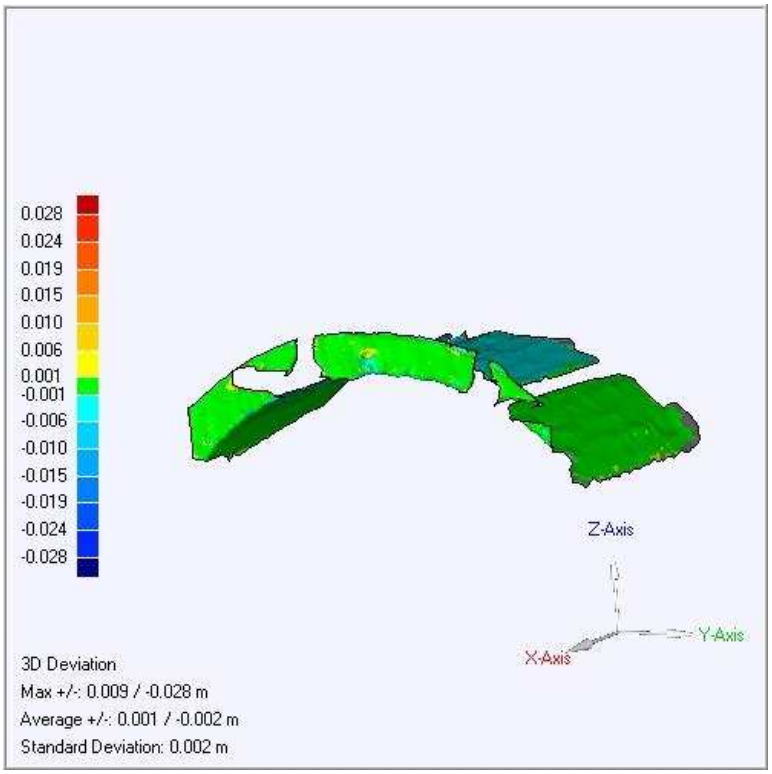
0.028
0.024
0.019
0.015
0.010
0.006
0.001
-0.001
-0.006
-0.010
-0.015
-0.019
-0.024
-0.028
Z-Axis
Y-Axis
X-Axis
3D Deviation
Max +/-: 0.009 / -0.028 m
Average +/-: 0.001 / -0.002 m
Standard Deviation: 0.002 m

13_14

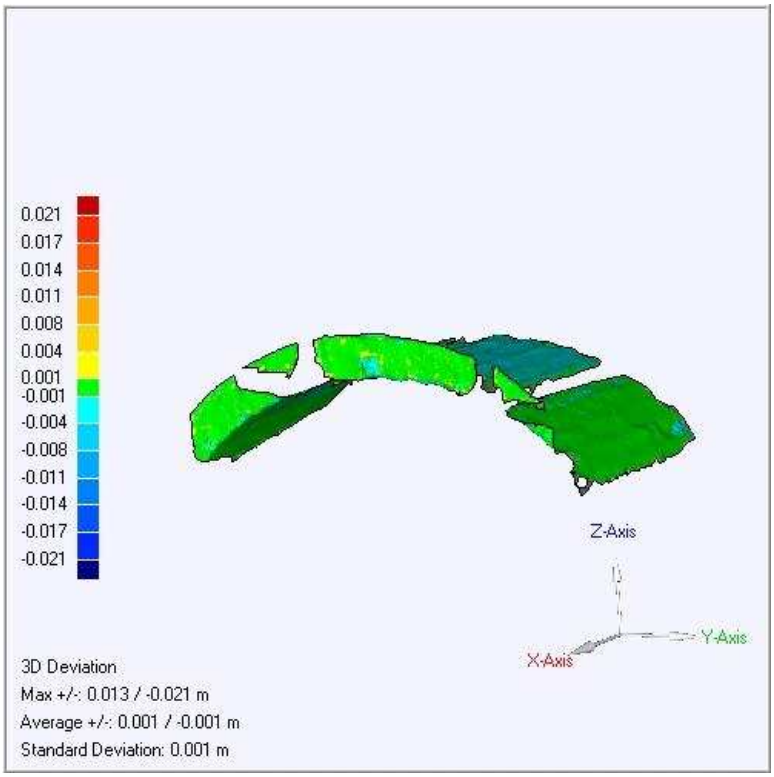
0.021
0.017
0.014
0.011
0.008
0.004
0.001
-0.001
-0.004
-0.008
-0.011
-0.014
-0.017
-0.021
Z-Axis
Y-Axis
X-Axis
3D Deviation
Max +/-: 0.013 / -0.021 m
Average +/-: 0.001 / -0.001 m
Standard Deviation: 0.001 m

14_15

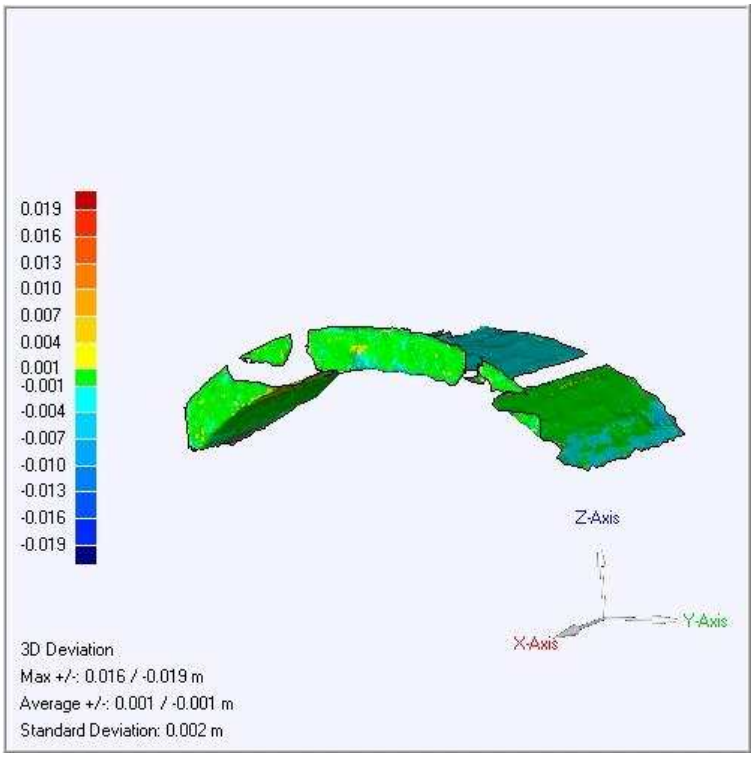
0.019
0.016
0.013
0.010
0.007
0.004
0.001
-0.001
-0.004
-0.007
-0.010
-0.013
-0.016
-0.019
Z-Axis
Y-Axis
X-Axis
3D Deviation
Max +/-: 0.016 / -0.019 m
Average +/-: 0.001 / -0.001 m
Standard Deviation: 0.002 m

15_16

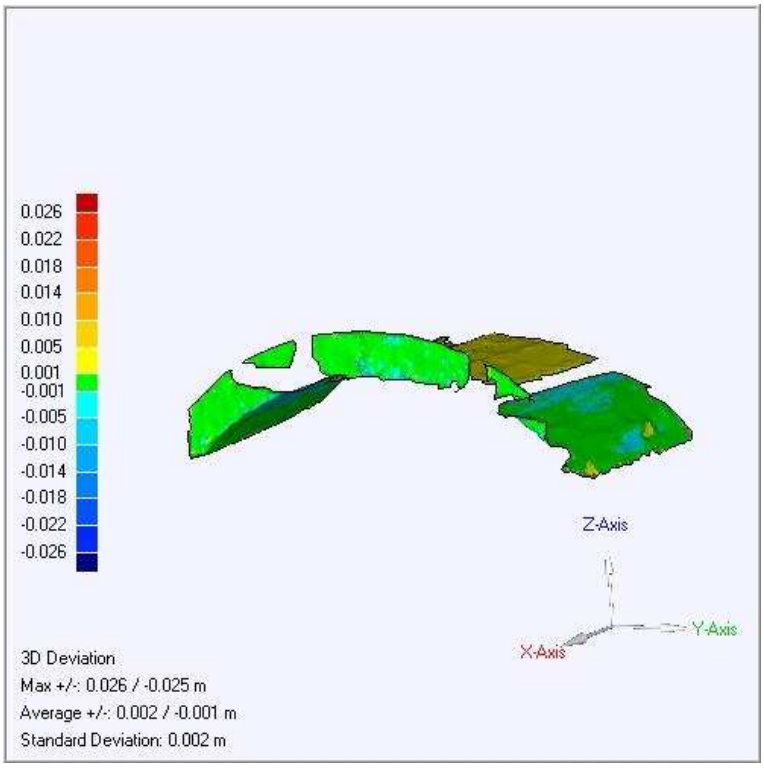
0.026
0.022
0.018
0.014
0.010
0.005
0.001
-0.001
-0.005
-0.010
-0.014
-0.018
-0.022
-0.026
Z-Axis
Y-Axis
X-Axis
3D Deviation
Max +/-: 0.026 / -0.025 m
Average +/-: 0.002 / -0.001 m
Standard Deviation: 0.002 m

16_17

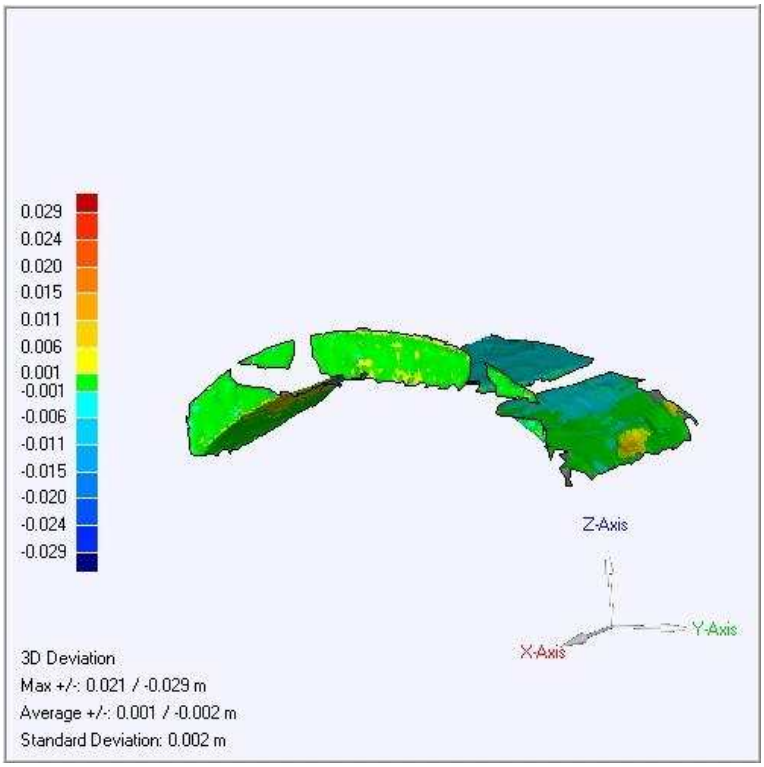
0.029
0.024
0.020
0.015
0.011
0.006
0.001
-0.001
-0.006
-0.011
-0.015
-0.020
-0.024
-0.029
Z-Axis
Y-Axis
X-Axis
3D Deviation
Max +/-: 0.021 / -0.029 m
Average +/-: 0.001 / -0.002 m
Standard Deviation: 0.002 m

17_18

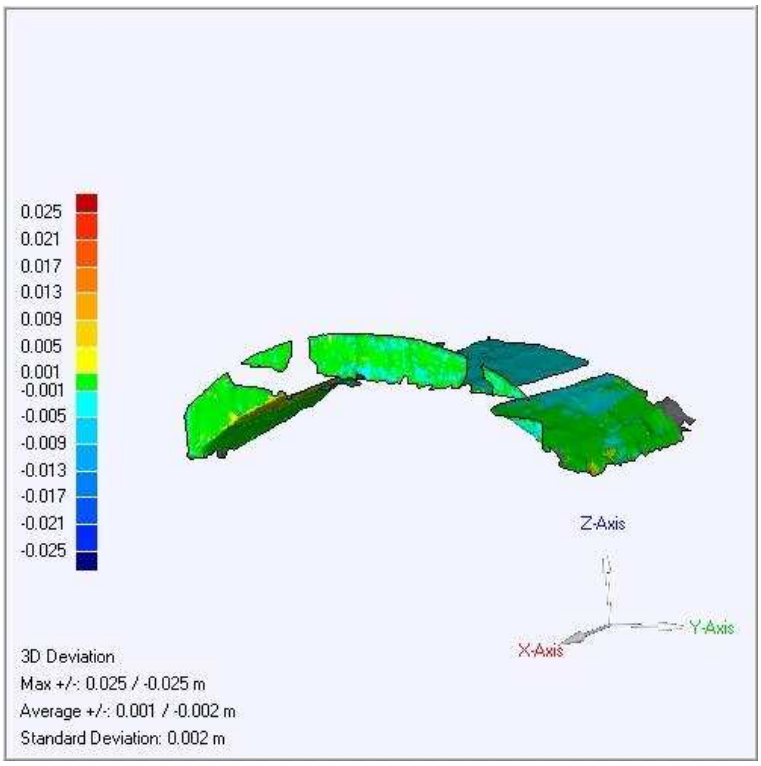
0.025
0.021
0.017
0.013
0.009
0.005
0.001
-0.001
-0.005
-0.009
-0.013
-0.017
-0.021
-0.025
Z-Axis
Y-Axis
X-Axis
3D Deviation
Max +/-: 0.025 / -0.025 m
Average +/-: 0.001 / -0.002 m
Standard Deviation: 0.002 m

18_19

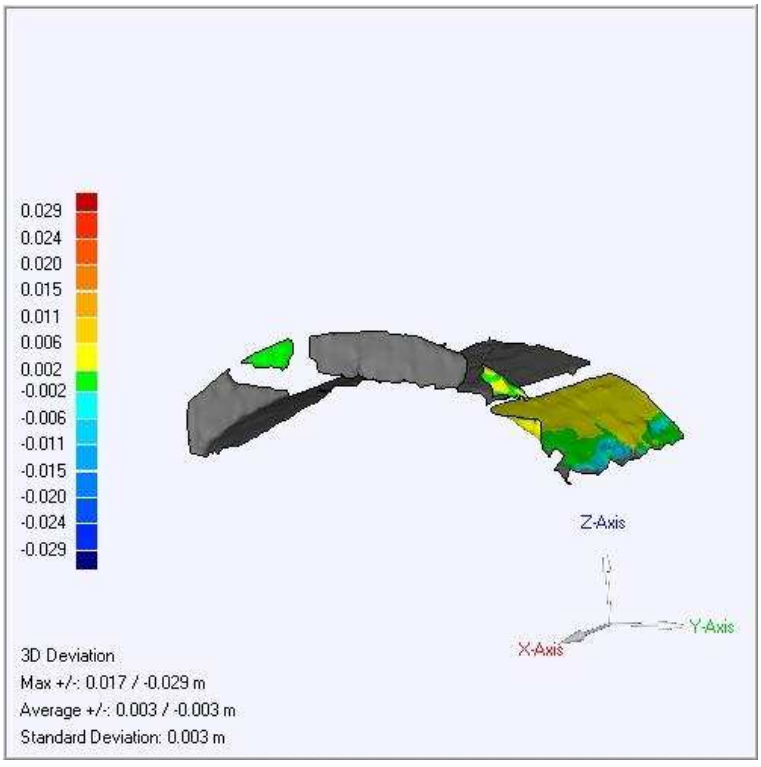
0.029
0.024
0.020
0.015
0.011
0.006
0.002
-0.002
-0.006
-0.011
-0.015
-0.020
-0.024
-0.029
Z-Axis
Y-Axis
X-Axis
3D Deviation
Max +/-: 0.017 / -0.029 m
Average +/-: 0.003 / -0.003 m
Standard Deviation: 0.003 m

19_20

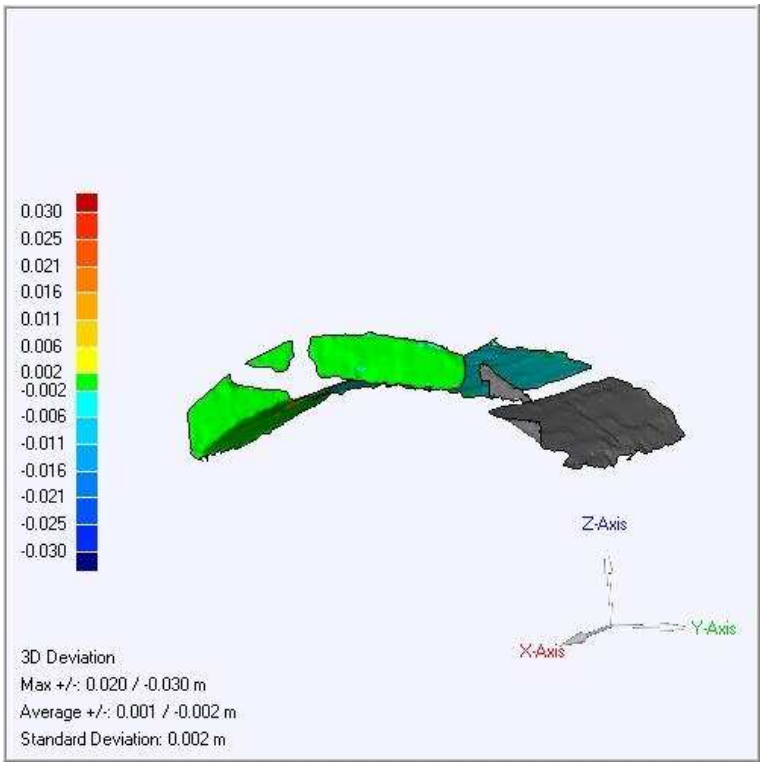
0.030
0.025
0.021
0.016
0.011
0.006
0.002
-0.002
-0.006
-0.011
-0.016
-0.021
-0.025
-0.030
Z-Axis
Y-Axis
X-Axis
3D Deviation
Max +/-: 0.020 / -0.030 m
Average +/-: 0.001 / -0.002 m
Standard Deviation: 0.002 m

20_21

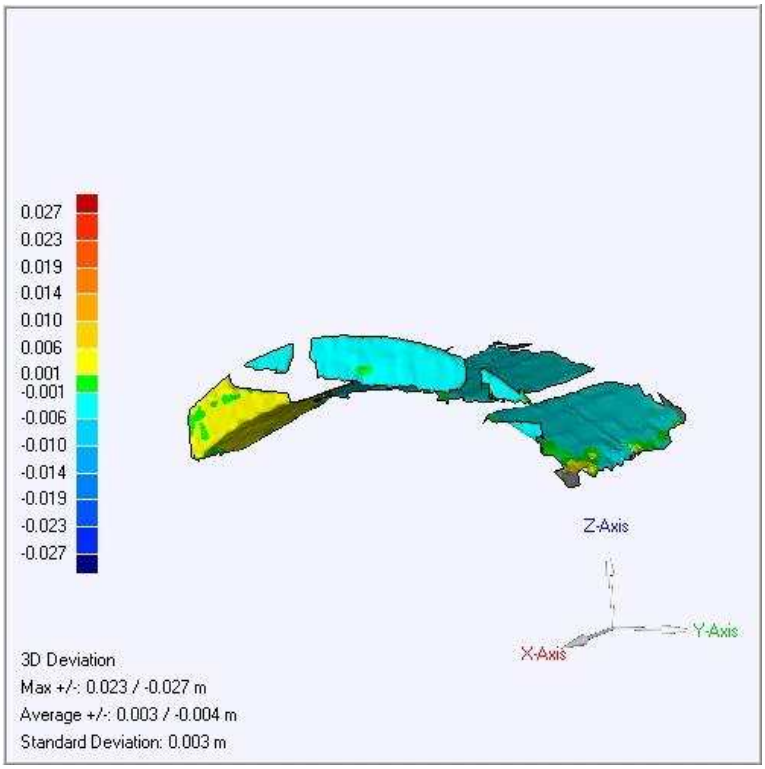
0.027
0.023
0.019
0.014
0.010
0.006
0.001
-0.001
-0.006
-0.010
-0.014
-0.019
-0.023
-0.027
Z-Axis
Y-Axis
X-Axis
3D Deviation
Max +/-: 0.023 / -0.027 m
Average +/-: 0.003 / -0.004 m
Standard Deviation: 0.003 m

APPENDIX C NUMERICAL MODELLING RESULTS OF PREDICTION

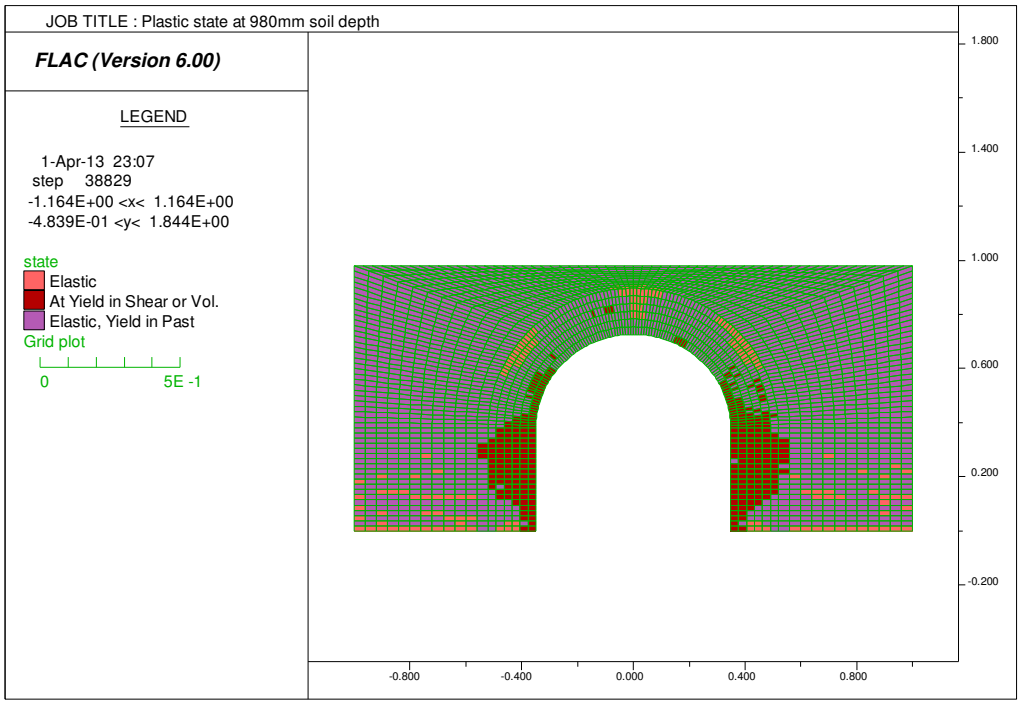

Figure C.1 Plastic state of FLAC model (1:1:6) under uniform load at 980 mm soil depth

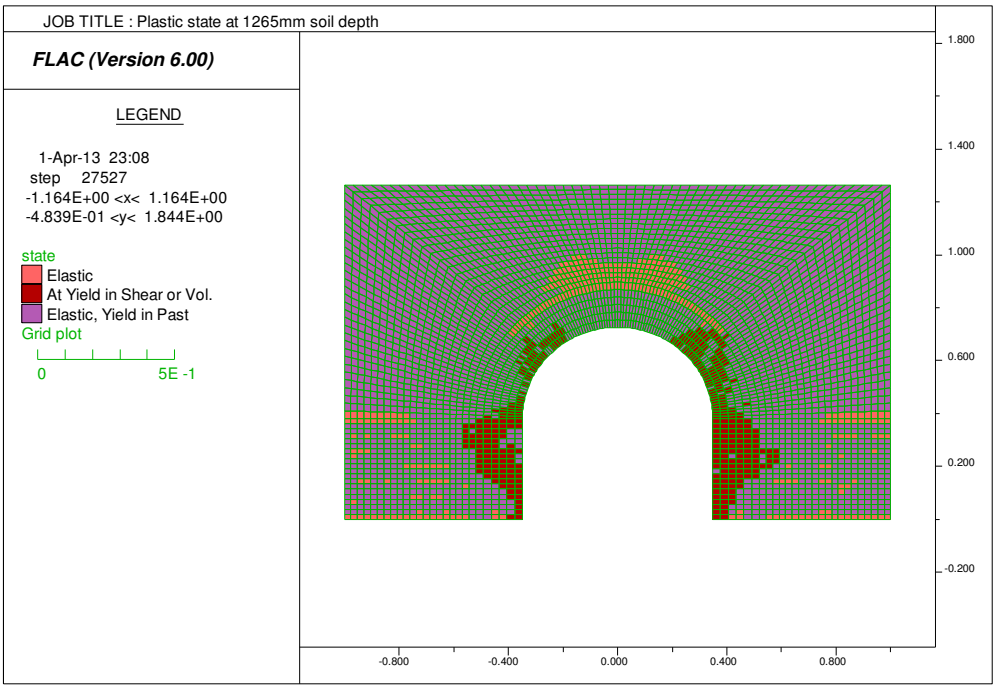

Figure C.2 Plastic state of FLAC model (1:1:6) under uniform load at 1265 mm soil depth

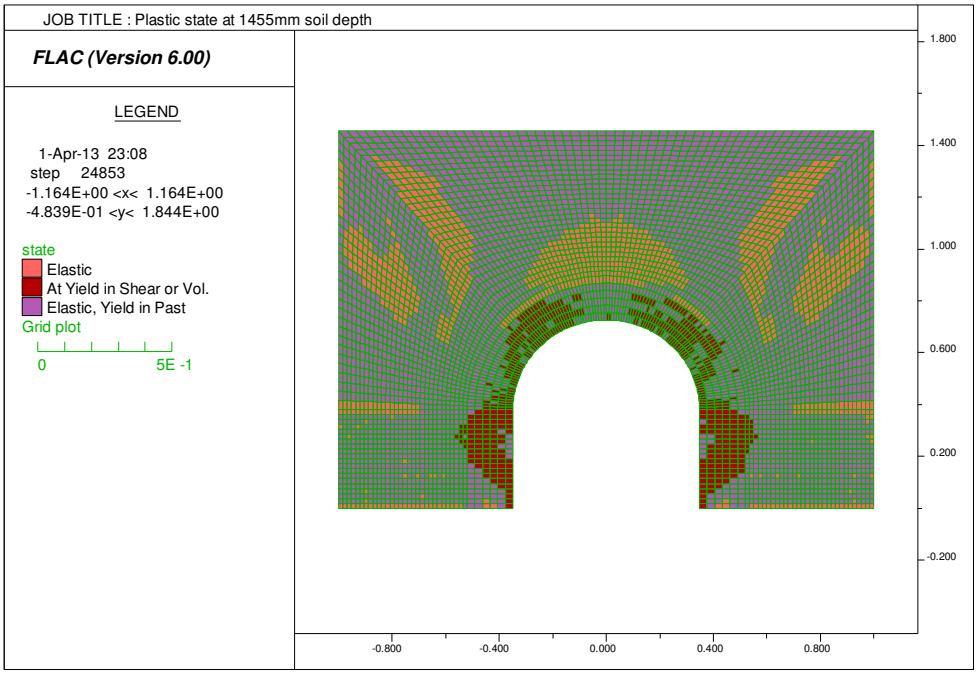

Figure C.3 Plastic state of FLAC model (1:1:6) under uniform load at 1455 mm soil depth

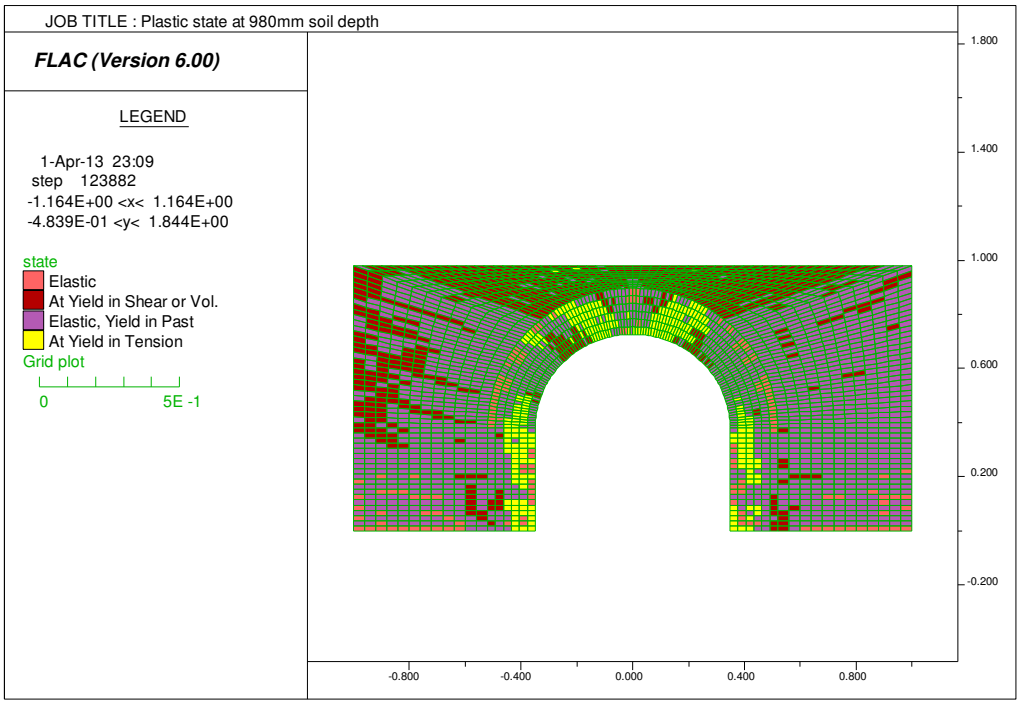

Figure C.4 Plastic state of FLAC model (1:2:9) under concentrated load at 980 mm soil depth

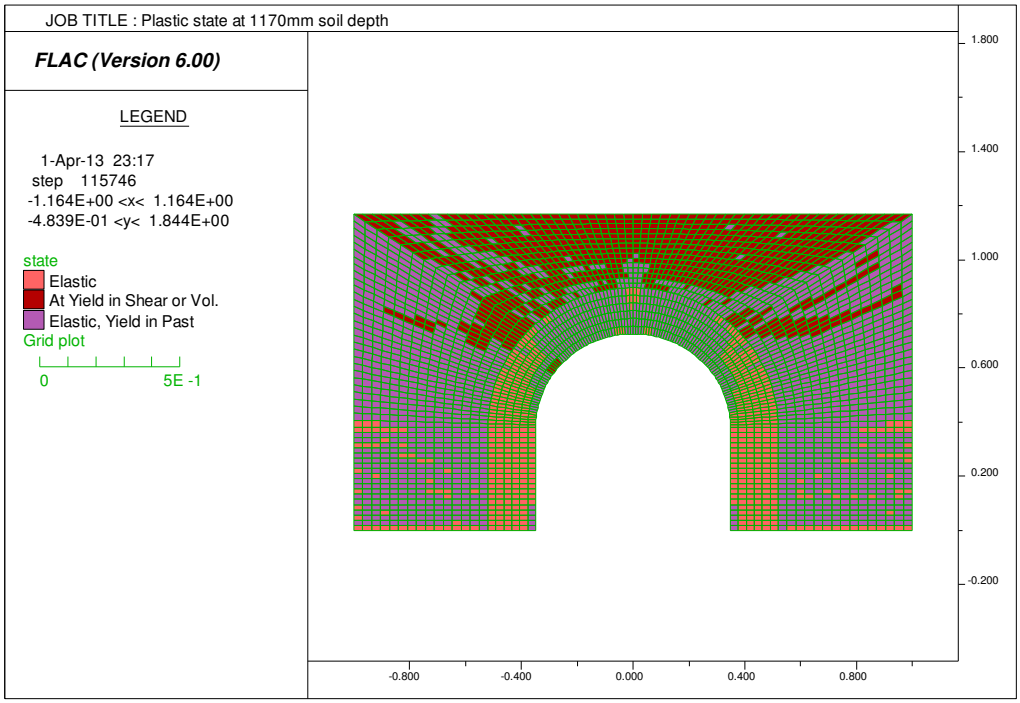

Figure C.5 Plastic state of FLAC model (1:2:9) under concentrated load at 1170 mm soil depth

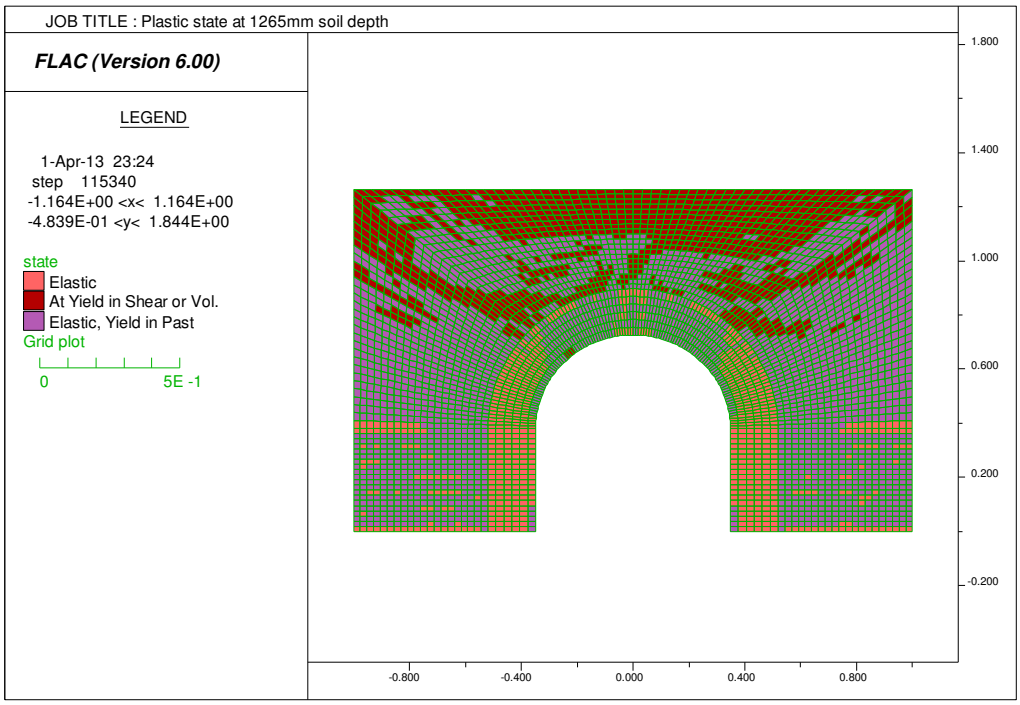

Figure C.6 Plastic state of FLAC model (1:2:9) under concentrated load at 1265 mm soil depth